UNIVERSITÉ DE STRASBOURG

ÉCOLE DOCTORALE de Physique et Chimie-Physique

U1121 Biomatériaux et Bioingénierie

THÈSE présentée par :

Gaëtan LUTZWEILER

soutenue le : **18 Septembre 2019**

pour obtenir le grade de : **Docteur de l'université de Strasbourg**

Discipline/ Spécialité : Biophysique

Matériaux poreux à base de polyuréthane pour l'ingénierie tissulaire

THÈSE dirigée par :

M. Pierre Schaaf	Professeur, Université de Strasbourg
Mme. Wiebke Drenckhan	Directrice de recherche, CNRS

RAPPORTEURS :

Mme. Cosima Stubenrauch	Professeur, Université de Stuttgart
M. Guy Ladam	Professeur, Université de Rouen

AUTRES MEMBRES DU JURY :

M. Guy Schlatter	Professeur, Université de Strasbourg

« Dans la vie, rien est à craindre, tout est à comprendre »

Marie Curie

Remerciements

Je tiens tout d'abord à remercier Pierre Schaaf de m'avoir accueilli dans son équipe et son laboratoire ainsi que de m'avoir permis de réaliser ma thèse sous sa direction. Il a su être disponible et ses conseils ont toujours été précieux. J'ai pu bénéficier de son soutien et de ses nombreuses connaissances au quotidien et je lui suis vraiment reconnaissant pour cela.

Je tiens à remercier également Wiebke Drenckhan pour avoir accepté de codiriger cette thèse. J'ai énormément appris à ses côtés, tant au niveau de la rigueur que sur le plan scientifique. Elle a su s'impliquer énormément et toujours en gardant toujours sa bonne humeur bien que mon sujet ne concernait finalement pas beaucoup les mousses. J'ai pu bénéficier d'un cadre de travail et d'échange idéal au sein de son laboratoire.

Mes remerciements vont également à Engin Nihal Vrana qui a suivi et guidé cette thèse dans son ensemble. Il m'a toujours soutenu dans mes idées et a su me partager sa vision du domaine scientifique et industriel. Je le remercie aussi pour ses conseils concernant mon orientation professionnelle.

Mes remerciements chaleureux aux membres de mon jury Guy Ladam, Guy Schlatter et Cosima Stubenrauch pour avoir accepté d'évaluer ces travaux.

Je remercie aussi Julien Barthes pour son soutien, et ses nombreux conseils tous le long de cette thèse.

Je remercie également Géraldine Koenig, qui m'a formé à la culture cellulaire alors que je n'y connaissais rien ainsi qu'à de nombreuses techniques de biologie. Elle s'est investie dans mon projet et ses idées ont toujours été pertinentes. Entre deux mails plus incendiaires, nous avons eu beaucoup de fou rires et de bon moments.

Je remercie aussi Michel Rawiso pour ses analyses WAXS/SAXS mais aussi pour avoir pris le temps de m'expliquer la théorie sous-jacente. Sa vision de la science en général et son humour me manqueront.

Je tiens à remercier aussi les autres chercheurs du laboratoire, Philippe Lavalle, Florent Meyer, Bernard Senger (notamment pour nos discussions footballistiques) qui ont toujours été agréables. Je remercie tout particulièrement Vincent Ball avec qui j'ai pu avoir plusieurs discussions scientifiques et ses conseils ont toujours été précieux.

Je tiens à remercier Dominique Vautier, Christine Affolter- Zbaraszczuk, Karim Benmlih et Christiane Bouthier et Eric Mathieu pour leur bienveillance, leur aide et nos discussions scientifiques/sportives.

Je remercie aussi mes autres collègues de l'unité 1121 avec qui j'ai aussi passé de bons moments Céline, Elena, Lorène, Cynthia, Emine, Morgane, Ludivine, Claire, François, Manon, Estéban et Léa avec qui j'ai aussi eu de bons moments et je m'excuse pour ceux que j'aurais oublié de citer...

Je remercie aussi chaleureusement Marc Schmutz qui m'a formé au MEB ainsi qu'Alain Carvalho pour nos discussions ainsi que Damien Favier et Christophe Contal.

Mes remerciements vont aussi à Jean Farago pour avoir rédigé toute la partie théorique ainsi que pour sa sympathie.

Je tiens à remercier aussi Léandro Jacomine qui m'a aussi aidé et conseillé pendant ces travaux notamment en rhéologie.

Je tiens à remercier mes collègues de l'ICS également, notamment Aouatef Testouri et Robin Bollache, avec qui j'ai partagé ces trois années pour son aide, et nos bons moments. Je remercie aussi Claire, Sébastien, Gaël, Imen, Martin et les stagiaires, Ozan et Emeline.

Je remercie également Fouzia Boulmedais et Loic Jierry pour nos échanges agréables.

Je remercie aussi Alexandre Collard avec qui j'ai discuté de chimie, d'histoire et d'autres sujets plaisants autour d'un café.

Je remercie enfin tous les membres de ma famille pour leur soutien pendant toutes ces années sans qui je ne serais probablement pas parvenu jusqu'ici.

Merci aussi à Marie qui m'accompagne et me soutient depuis maintenant 6 ans et j'espère pour longtemps encore.

Main Abbreviations

%freeNCO*: free percentage of isocyanate*
ASTM*: American Society for Testing and Materials*
BD*: 1,4 butane diol*
BMSCs*: bone marrow mesenchymal stem cells*
DAPI*: 4’,6 diamidino-2-phenylindole*
E.S*: Elementary Scatterer*
EBM*: electron beam melting*
ECM*: Extra-Cellular Matrix*
ED*: Ethylene diamine*
EDTA*: ethylene diamine tetraacetic acid*
EO*: Ethylene oxyde*
EW*: Equivalent weight*
FBS*: Fetal Bovine Serum*
FDA*: Food and Drug Administration*
GAGs*: Glycosaminoglycans*
HA*: hydroxyapatite*
HUVECs*: Human umbilical vein endothelial cells*
IOL*: intraocular lenses*
MDI*: diphenylmethane diisocyanate*
MMP*: Matrix Metalloproteinase*
MSCs*: mesenchymal stem cells*
MW: Molecular Weight
PCL*: poly(ε-caprolactone)*
PDMS*: polydimethylsiloxane*
PEG*: poly(ethylene) glycol*
PET*: poly(ethylene terephthalate)*
pHEMA*: poly(2-hydroxyethyl methacrylate)*
pHEMA-co-MAA*: poly(hydroxyethyl methacrylate-co-methacrylic acid)*
PLA*: polylactic acid*
PLGA*: poly(lactic-co-glycolic)*
PMMA*: poly(methyl methacrylate)*
PO*: Propylene oxyde*
polyMDI*: polymethylene polyphenylisocyanate*
PPF*: poly(propylene fumarate)*
PU*: polyurethane*
SAP*: Self-assembled peptide*
SDS*: Sodium Dodecyl Sulfate*
SFF*: solid free form*
SLM*: Laser Beam Melting*
TDI*: Toluene methyl diisocyanate*
TE*: Tissue Engineering*
VAS*: Analogue Scale for Pain*
WJMSCs*: Wharton’s Jelly derived mesenchymal stem cells*
XPS*: X-ray photoelectron spectroscopy*

French summary of the thesis

Introduction

L'ingénierie tissulaire est un domaine émergeant qui a pour but de « restaurer, maintenir ou améliorer les fonctions d'un organe ou d'un tissu ». Par le passé, la plupart des implants remplaçaient certains organes ou tissus, tout en restant le plus inerte possible vis-à-vis du corps afin de limiter la réaction inflammatoire engendrée par le corps étranger. Grâce aux progrès, la connaissance de l'interaction entre un matériau (naturel ou synthétique) et le corps a permis de fabriquer de nouveaux matériaux qui interagissent avec leur environnement. Ce sont les avancées conjointes dans les domaines de la biologie, de la physico-chimie et de l'ingénierie qui ont permis de connaître davantage les phénomènes à l'interface entre un matériau et un tissu biologique. Ces nouveaux matériaux ont ouvert une nouvelle approche qui consiste à remplacer temporairement une partie du corps endommagée, de la restaurer, voir même de jouer un rôle thérapeutique. Les matériaux poreux entrent dans ce cadre. En effet, leur volume « vide » peut-être colonisé par les cellules environnantes et permettre à celles-ci de reconstituer un tissue au sein du matériau. Enfin, si ce matériau est biodégradable, le néo-tissu croît en même temps que le matériau se dégrade ce qui permet d'obtenir finalement un nouveau tissu. De nombreuses approches existent pour générer ces matériaux.

Dans le cadre de cette thèse, les objectifs consistent d'une part à générer des matériaux poreux dans lesquels les paramètres architecturaux sont contrôlés. Nous nous sommes focalisés à la fois sur la taille des pores, qui est reconnue comme ayant une influence sur le devenir cellulaire, mais surtout sur la taille des interconnexions entre les pores qui est nettement moins étudiée dans la littérature.
En parallèle, nous avons également étudié la relation entre la chimie du matériau (dans notre cas, du polyuréthane), et la capacité d'adhésion des cellules.
Enfin, nous avons évalué l'impact des paramètres géométriques et chimiques sur la réponse cellulaire (sécrétion de matrice, organisation, prolifération).
Deux types de cellules ont été utilisés : des fibroblastes, et des cellules souches mésenchymateuses. Finalement, nous avons cherché à promouvoir la différenciation des cellules souches au sein des matériaux en intégrant d'abord les cellules dans un hydrogel de peptides. Les peptides sont des enchaînements d'acides aminés que l'on retrouve dans les protéines et les protéines constituent les composants majeurs de la matrice extracellulaire dans laquelle reposent les cellules dans les tissus.

Résultats

La génération des matériaux a été faite par la méthode de « Sphere templating » (Chapitre 3). Celle-ci consiste à utiliser des agents sacrificiels, (dans notre cas il s'agit de microbilles de paraffine) qui sont compactés puis frittés dans un four afin de les fritter. Des images de ces microbilles obtenues par microscopie électronique à balayage (MEB) sont montrées sur la Figure 1-1. Le frittage permet de former un « cou » entre deux billes adjacentes, le diamètre de celui-ci pouvant être ajusté par le temps et la température de chauffage. Une fois le frittage terminé, le polymère est laissé s'infiltrer entre les billes, où il se solidifie. Les billes sont sélectivement dissoutes laissant place à un matériau poreux interconnecté (Figure 1-1b). La taille des pores est ainsi donnée par la tailles des billes, la taille des interconnexions est donnée par la taille du cou. Nous avons aussi pu déterminer quel modèle théorique pouvait décrire le mieux la croissance de ce cou (et donc des interconnexions) afin de pouvoir produire un poreux dont la taille des interconnexions est prédictible.

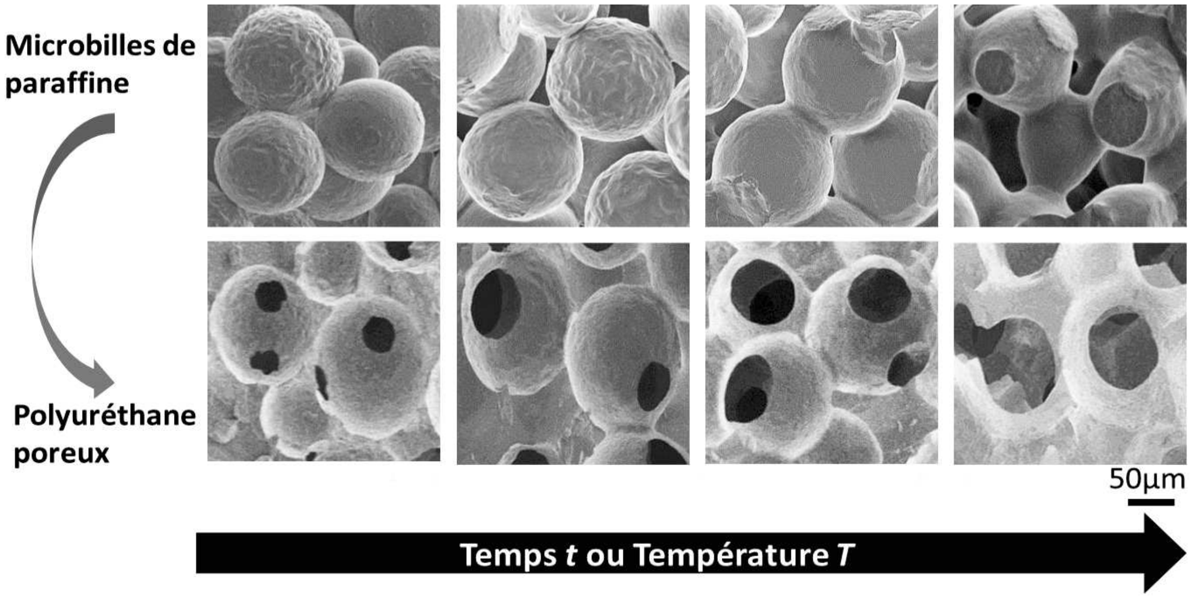

Figure 1-1: Evolution du frittage des billes de paraffine à différents temps/température d'avancement du frittage (colonne du haut) ; poreux résultants de la dissolution des billes de paraffine avec différentes tailles d'interconnexions (colonne du bas) pour une taille de bille donnée.

Nous sommes ainsi parvenus à générer des matériaux poreux, avec une taille de pores et une taille d'interconnexions contrôlables de manière indépendante et prédictible. Cette approche est également simple et peu coûteuse ce qui est un avantage pour d'éventuelles applications en médecine.

Nous avons ensuite évalué la relation entre la taille des interconnexions (Section 4.1), et la capacité des cellules à survivre, coloniser et reproduire un environnement semblable à un tissu au sein du matériau. Nous avons formulé des poreux avec une taille de pore constante (i.e. 133 µm) mais avec deux tailles d'interconnexions (27 et 52 µm). Lors de résultats préliminaires nous avons constaté que le polyuréthane était hydrophobe. Cet effet était renforcé par la nature poreuse de l'échantillon. Nous avons donc testé différentes modifications de surface afin de rendre le matériau plus hydrophile.

Le premier traitement appliqué est le traitement plasma. Celui-ci consiste à accélérer des ions ou des radicaux à la surface du polymère afin de provoquer une scission des chaînes. Cela forme en surface des espèces très réactives telles que des peroxydes qui réagissent à l'air pour former des groupements carboxyles ou hydroxyles.

L'autre approche consiste à appliquer un revêtement de polydopamine (PDA) en surface du matériau. La polydopamine possède un motif moléculaire semblable à celui d'une partie des protéines des fils de byssus des moules (qui leur permettent d'adhérer aux surfaces). Celles-ci peuvent adhérer sur quasi tous les types de surfaces. La polydopamine est reconnue comme biocompatible.

Les résultats pour les cellules souches sont montrés sur la Figure 1-2. Après 21 jours de culture, on peut voir (Figure 1-2a) que les cellules sont grandement affectées par la structure et par le traitement de surface. Le traitement par la polydopamine semble néfaste pour les cellules. Seules quelques cellules sont visibles sur les structures avec de PETITES interconnexions, mais elles sont arrondies ce qui signifie qu'elles n'adhérent pas bien. A l'inverse, le traitement plasma démontre une bien meilleure colonisation, le matériau est quasiment rempli de cellules et celles-ci sont organisées de manière tridimensionnelle ce qui est proche de l'organisation retrouvée dans les tissus natifs. La quantification d'ADN montrée Figure 1-2b démontre un effet immédiat du traitement de surface appliqué. Après seulement 7 jours, la quantité d'ADN (i.e. le nombre de cellules) est significativement plus élevé dans les matériaux traités au plasma comparé à ceux traités à la polydopamine. L'impact des interconnexions quant à lui est plus visible après 21 jours où l'on peut voir que le nombre de cellules est plus important lorsque les interconnexions sont GRANDES. Cela peut s'expliquer par les limitations dans le transport des nutriments et de l'oxygène lorsque les interconnexions sont PETITES.

Pour les fibroblastes, les résultats ont montré une réponse contraire à celui des cellules souches concernant le traitement de surface. En effet, la polydopamine semble favoriser davantage la colonisation et la survie des fibroblastes que le traitement plasma.

Dans les deux cas, l'influence de la taille des interconnexions a été démontrée. Les interconnections de GRANDE taille favorisent la survie à long terme des deux types de cellules, notamment par les propriétés de transport de masse (perméabilité hydraulique) qui étaient d'un ordre de grandeur plus importantes, mais aussi parce que les GRANDES interconnections favorisent la formation de contacts entre les cellules, ce qui est important dans leur capacité de survie et de colonisation.

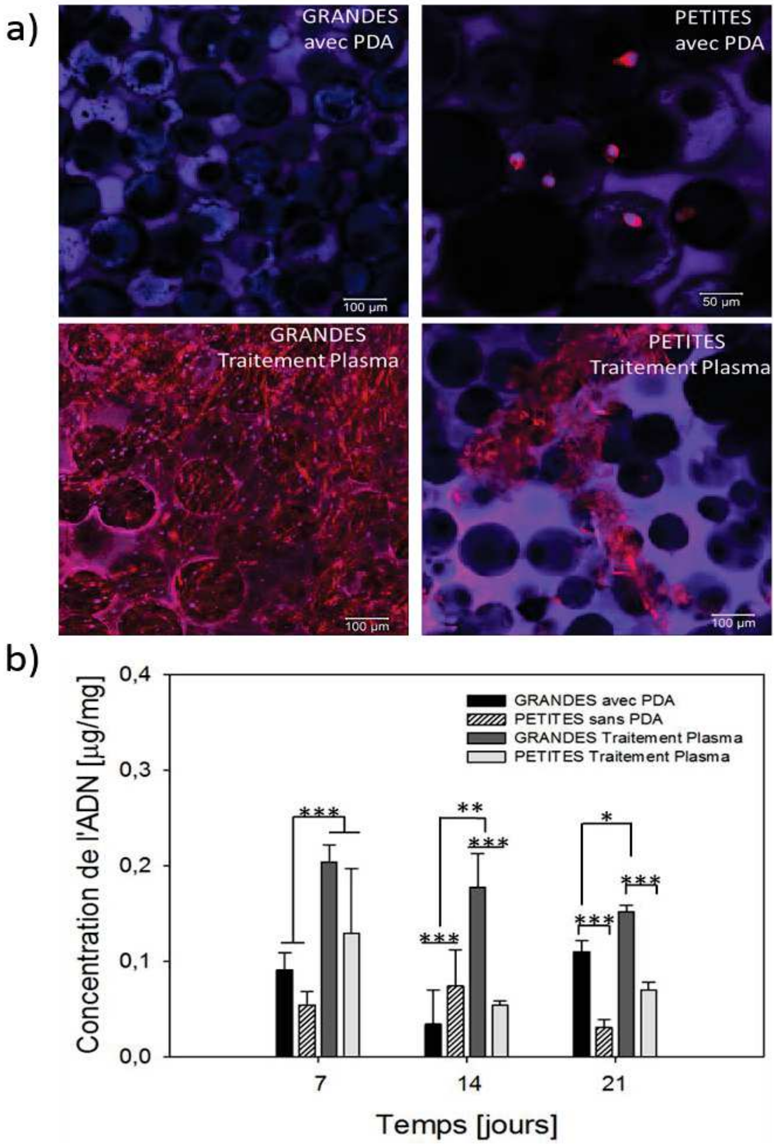

Figure 1-2: a) Images prises en microcopie confocale de cellules souches mésenchymateuses après 21 jours de culture, les cellules sont marquées avec de la phalloïdine pour faire apparaître les filaments d'actine en rouge, et avec du DAPI pour faire apparaître les noyaux en bleu. Les deux structures avec des GRANDES (27 µm) et PETITES (52 µm) interconnexions sont représentées, avec leurs différents traitements en surface ; la polydopamine (PDA) ou le Traitement Plasma. b) Quantification de la concentration en ADN dans les poreux après 7, 14 et 21 jours de culture pour les différents traitements appliqués et structures.

Concernant la relation entre la chimie du matériau et la modulation de l'adhésion cellulaire, nous avons fait varier le ratio d'isocyanate utilisé dans la synthèse du polyuréthane. Le polyuréthane étant obtenu par la réaction de polyols avec de l'isocyanate formant un copolymère dans les cas les plus simples. Le ratio entre fonctions isocyanates et fonctions hydroxyles contenues dans le polyol, est appelé « l'indice d'isocyanate ». Il est par convention de 100 lorsque le ratio entre groupement isocyanate, et fonction alcool est de 1. Nous avons fait varier cet indice dans la Section 4.2. Les images Figure 1-3 montrent un palier entre un indice d'isocyanate de 200 et 300 quel que soit le type de cellule. Nous avons démontré une séparation de phase au sein de la matrice dans laquelle les monomères issus du précurseur isocyanate se regroupent en nano-domaines. Nous avons montré un lien entre le degré de séparation de phase et la capacité d'attachement des cellules au matériau. Ces changements dans la formulation du polymère sont un moyen simple de contrôler les capacités d'adhésion des cellules.

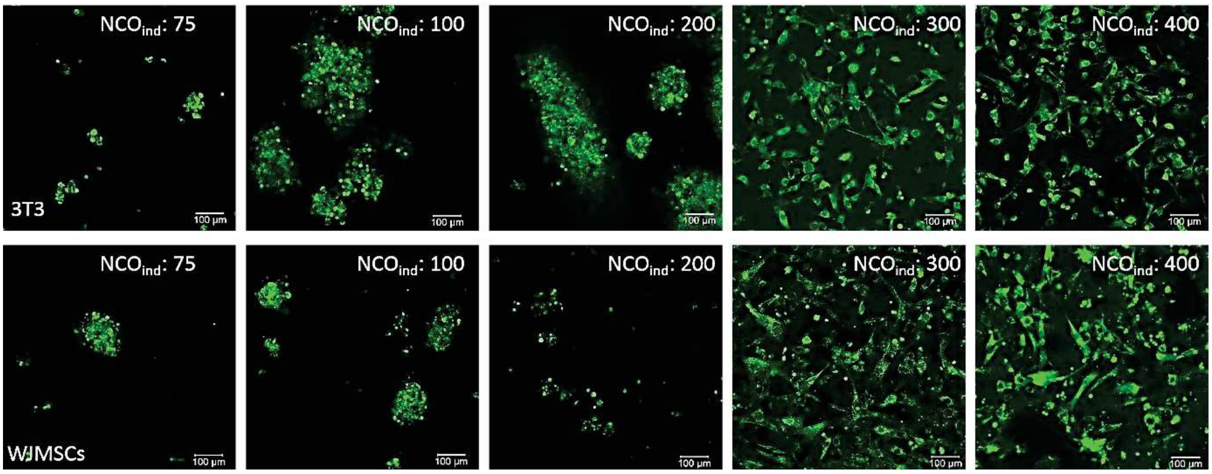

Figure 1-3: Evolution de l'adhésion des Fibroblastes NIH 3T3 (ligne du haut) et des cellules souches (WJMSCs) (ligne du bas) pour un film de polyuréthane avec des indices d'isocyanate de 75, 100,200,300 et 400. Les cellules sont marquées en vert avec de la calcéine. Les images sont prises après 24h de culture.

Conclusion

Nous avons pu générer des poreux à base de polyuréthane dans lesquels l'architecture est contrôlée. S'il est admis que la taille des pores a une influence sur la capacité des cellules à coloniser, voire à se différencier dans un matériau, nous avons démontré que la taille des interconnexions joue également un rôle central dans l'organisation des cellules au sein du matériau, mais aussi dans leur capacité de survie sur le long terme.

Le traitement de surface appliqué au matériau pour augmenter l'adhésion des cellules favorise ou empêche l'adhésion selon le type de cellule. Ceci implique qu'il est possible de discriminer un type cellulaire dans un matériau donné.

En parallèle, nous avons modifié la quantité d'isocyanate ajoutée dans la formulation du polyuréthane. Nous avons démontré qu'à partir d'un indice d'isocyanate de 300, les cellules pouvaient adhérer au matériau alors qu'elles formaient des agrégats pour des indices plus faibles.

Nous avons également mis un gel formé de peptides auto-assemblés dans les pores des matériaux (Chapitre 5). Celui-ci procure un environnement proche de celui de la matrice extracellulaire. La combinaison du gel avec les poreux a favorisé la prolifération des cellules souches ainsi que potentiellement leur différenciation en chondrocytes ce qui ouvre des perspectives intéressantes pour utiliser ces matériaux pour la régénération de cartilage.

En perspectives, il est envisagé de faire la culture cellulaire de façon dynamique, donc de perfuser le milieu de culture pour augmenter l'apport des nutriments aux cellules dans le matériau. La différentiation des cellules souches via des facteurs de croissance est aussi une suite intéressante car elle permet d'obtenir des cellules d'intérêt pour la régénération de cartilage.

Liste des publications

- ***Lutzweiler, G***.; Barthès, J.; Koenig, G.; Kerdjoudj, H.; Mayingi, J.; Boulmedais, F.; Schaaf, P.; Drenckhan, W.; Vrana, N. E. Modulation of Cellular Colonization of Porous Polyurethane Scaffolds via the Control of Pore Interconnection Size and Nanoscale Surface Modifications. ACS Appl. Mater. Interfaces 2019.

- ***Lutzweiler, G***., Oliveira, E., Erverdi, O., Farago, J., Jacomine, L., Vrana, E.N., Schaaf, P. Drenckhan,W. (2019). Controlled Sintering of Paraffin Spheres for the Generation of Porous Polyurethanes with Finely Tuned Morphology. *ACS, Langmuir* **soumis**

- ***Lutzweiler, G***.; Barthes, J., Schaaf, P.; Drenckhan, W.; … Nihal, Vrana, E,. (2019). Adjustment of Cell Adhesion and Eleastic Modulus of Polyurethane Structures with Controlled Hard/Soft Segment Ratio with Constant Surface Chemistry **en preparation**

Table of content

Chapter 1. General introduction

1.1 A brief history of biomaterials and tissue engineering

Implants are "devices or tissues that are placed inside or on the surface of the body" according to the U.S. Food and Drug Administration[1]. *Prosthetics* are a sub category of implants which are only intended to replace a missing part of the body. Other implants are used for therapeutic applications such as drug delivery. Medical implants have been around for thousands of years. Even in the mythology, Tantalus, son of Zeus, wanted to test if the gods were omniscient and by giving his son, Pelops, as an offering at a god feast. However, the gods noticed the trickery and brought him back to life. Only Pelops's shoulder was eaten by Demeter. The shoulder was replaced by a prosthesis made from ivory[2]. Another famous tale where an "implant" or a "prosthesis" (although these terms were not employed) was mentioned is that of the Egyptian god Osiris, who was slaughtered by his brother and cut into several pieces that were thrown into the Nile. Osiris sister collected all the pieces to bring back him to life, except the phallus which was eaten by a fish. The story tells that his sister, Isis, made him a new one made from gold[2]. Furthermore, Nuada, who was an Irish god, left one of his hand in a combat against Sreng. His hand was replaced by a silver implant[3].

Back to real history, an artificial toe named the "Cairo toe" was found on an Egyptian mummy dated between 1550 and 700 BC. This prosthetic toe was made of wood and leather and was believed to have been functional. A human scale dental carving was also found in an Egyptian cemetery being more than 5500 years old[4]. Beside, an artificial eye was discovered in Iran, in the skull bone of a woman. This eye was coated with a thin gold layer, and is expected to have been worn during the women's lifetime estimated around 2900 BC[5].

The first definition of a *biomaterial* was given at the European Society for Biomaterials (ESB) in 1976, as "a nonviable material used in a medical device, intended to interact with biological systems"[6]. It evolved to "material intended to interface with biological systems to evaluate, treat, augment or replace any tissue, organ or function of the body". The main classes of biomaterials are ceramics, metals and polymers that will be described in detail in Section 1.2.3 and this thesis will be focussed on polymeric biomaterials. Despite the fact that humans used biomaterials for a long time, the insufficient knowledge regarding the inflammatory response, and more generaly, the material/organism interaction led to many failures. The first milestone in the biomaterial field was reached during World War II. Harold Riley, an ophthalmologist, realized that pilots who received plastic projections such as poly(methyl methacrylate) (PMMA) in their eyes during fights did not show signs of inflammatory reaction. Following this observation, he designed the first intraocular lens (IOL)[7]which was successfully implanted in 1949. In the same period, others made major contributions. For example, Kolff who built the first dialyser[8] and Charnley developed hip implants in the late 1950s[9].

Ratner *et al.*[7] made a clear and relevant distinction between "traditional biomaterials" and the "new generation of biomaterials". Traditional biomaterials aim to be as inert as possible in the body in order to avoid interactions between the material and the organism. This may be explained by the fact that the cascade of events arising after implantation is quite complex and thus, difficult to control. One of the most challenging steps to overcome is the set of complications due to chronicle inflammations and, in consequence, poor healing. Basically, traditional biomaterials are mostly employed for mechanical and optical support mostly. Moreover, reproducing materials with equivalent mechanical properties as the original tissue is quite difficult and the implant may undergo fatigue. Another example of complication arising after implantation is "stress shielding"[10]. For example, when a bone is replaced by a prosthesis, this prosthesis may support the mechanical load more than the remaining native bone. Consequently, the native bone loses in density and becomes fragile[11]. Thanks to common progress in material science, biology and chemistry, the "new generation of biomaterials", as described by Ratner, are designed to better control the biological response and increase the healing capacity of the implant. The technical and scientific advances allowed to germinate the idea that a material could allow not only to replace, but also accompanying the regeneration of an organ or a tissue.

The term *Tissue Engineering* was given at the National Science Foundation workshop in 1988 to mean "the application of principles and methods of engineering and life sciences toward the fundamental understanding of structure-function relationships in normal and pathological mammalian tissues and the development of biological substitutes to restore, maintain or improve tissue function"[12].In 1993, Langer *et al.* [13] gave a summary of several cases where cells were combined with a biomaterial to restore several types of tissues. Among the cited examples, we can find cartilage, muscle, bone or pancreas.

Tissue engineering aims to provide an alternative to organ transplantations or grafts since the number of available organs is below the current needs and grafts require a second surgery which is accompanied by morbidity, and the amount of available tissues may be limited[14]. Figure 1-1 illustrates the basic philosophy of tissue engineering. First, the desired cell source is harvested, preferably from the patient himself. Then, cells are cultured in vitro to proliferate prior to be seeded in a porous scaffold which provides a three dimensional environment to the cells which is closer to the native tissue organisation. Once the scaffold is fully colonised, it is implanted back into the patient. The market of tissue engineering is constantly growing and gains increasing attention from researchers. It is expected to reach USD 11,5 billion by 2022[15].

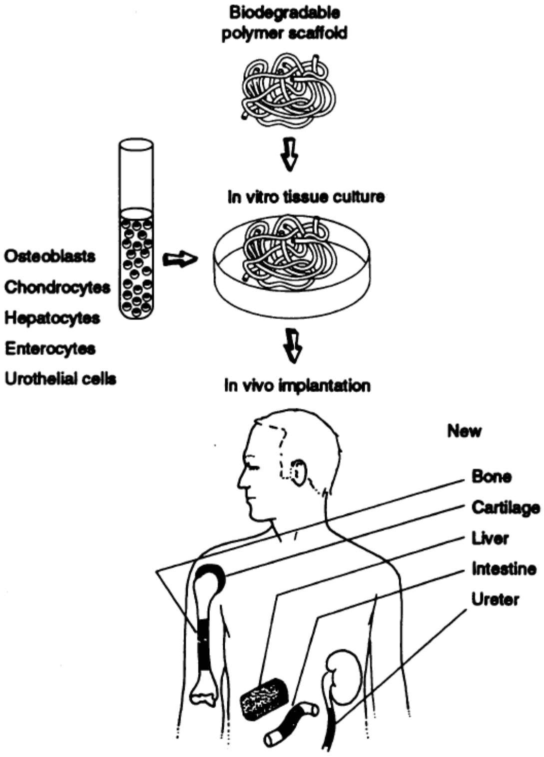

Figure 1-1: Drawing of the tissue engineering concept. Cells are harvested from the donor patient, and cultured in vitro in a porous scaffold prior to be implanted (from Langer et al.[13]*).*

1.2 Main requirements of biomaterials

1.2.1 Biocompatibility

Each material subject to implantation has to be non-toxic. Materials should not alter cell life and their activity. Signs of toxicity may occur via direct contact or indirectly if the material releases toxic compounds. *Biocompatibility* has been defined as "the ability of a material to perform with an appropriate host response in a specific application"[16]. However, this definition is still vague and may vary depending on which tissue is targeted and on other parameters such as the patient-to-patient variability. For instance, blood-contacting devices may prevent thrombus formation[14], IOLs can play a role in the posterior capsule opacification formation which is a complication that can occur after cataract surgery[17]. Furthermore, biodegradable polymers must show a reliable degradation rate and degradation products have to be eliminated without promoting an unacceptable host response[18]. The biomaterial which is universally biocompatible may not exist with regard to the great diversity of materials used, the different sites of implantation, the duration of the implantations, as well as the different responses of the organism associated with them[19]. In spite of everything, B. Ratner[20] recently proposed an equation for the concept of biocompatibility defined as

$$\beta = (A)(\frac{1}{C_t})(\frac{1}{C_d})(M)(M_2 / M_1)(O) , \qquad (1)$$

where ß is the 'biocompatibility number', *A* is the angiogenesis or the density of blood vessels, C_t the capsule thickness, C_d *the* capsule collagen density, M is the number of macrophages, and M_2/M_1 the ratio of M_2 to M_1 macrophages (see Section 1.2.3) and *O* is a term for the other cell types which was not specified. This equation shows the willingness to find a way to mathematically define or even predict if the integration of a material in the body can be successful or not.

Biocompatibility is a term more appropriate to describe a material/host interaction and their outcomes. In this Thesis, all the experiments are carried out in-vitro. Thereby, we will not define our material as biocompatible but we will rather define it as "cytocompatible" which implies that it does not cause the death of cells. This attribution is due to the fact that in-vitro studies do not correctly describe the complex environment that would be encountered in-vivo.

1.2.2 Physical properties

Another challenge for biomaterials is the ability to generate them with mechanical properties equivalent to the native tissue. We provide here a few examples of common tissues on which tissue engineering focused on namely muscles, bones and cartilage and we will discuss particularly the case of trachea which is main field of research in our lab. Muscles have a Young modulus around 100 kPa, and dissipate energy to avoid overstretching[21]. The *Young's modulus E* is defined as the slope of the stress-strain curve in the linear regime[22]. The word "stiffness" is also widely employed, when a load is applied to a given material, and the corresponding strain is measured in the same direction as the applied load, often, one can assimilate the stiffness as the Young modulus[23]. Muscles undergo cyclic strains which promote fatigue. *Fatigue* is defined as the weakening of a material which undergoes cyclic loads[24]. Bones are strong and rigid. For example the modulus of a trabecular bone can range from 10 to 1500 MPa[25]. Lin *et al.*[26] used an algorithm called "general layout optimization" to design a biomaterial with both anisotropic stiffness and equivalent porosity as native trabecular bone. Afterward, they generated the computed structure using solid free form fabrication (SFF).

Trachea is composed among others of hyaline cartilage rings, which show non-linear mechanical behaviour displaying higher stress in compression than in traction[27]. This demonstrates the versatility of the body parts. One must notice that mechanical properties of a part of the body may evolve with the age of the patient. Thus, the development of the ideal material must be almost tailor-made to achieve an optimal integration in the patient. Moreover, implants must have an acceptable durability. A catheter may stay only for a few days whereas an artificial heart valve should stay for years and must bear cyclic constraints.

Some words may be said on the physical properties that biomaterials must fulfill. As an example, implants at the joints have to guarantee a good lubrication to avoid abrasion, since the presence of some debris may trigger inflammations[28]. We can also mention lenses, that must have a good transparency. Last but not least, Locatelli *et al* showed that the hydraulic permeability of dialysis membranes is a key factor to patient survival.[29]

1.2.3 Inflammatory response

Describing the set of events that arise after implantation, one sees the importance of controlling properties of a material[30]. A schematic representation is shown in Figure 1-2. The first event is protein adsorption from blood to the material surface. Fibrinogen is one protein known to be heavily involved in the coagulation cascade and the clot formation which serves as an anchorage site for platelets for instance. Platelets secrete signaling molecules such as chemokines to further recruit neutrophils at the early stages after injury and then monocytes which differentiate into macrophages. Macrophages play two main roles: firstly, eliminate foreign bodies, bacteria and so on. Secondly, macrophages secrete signaling molecules like growth factors to recruit endothelial cells which in turn promote the angiogenesis to improve the transport of oxygen and nutrients to the site of injury. Growth factors also recruit fibroblasts which transform the clot into a primary extra-cellular matrix (ECM)[31]. Together, endothelial cells and fibroblasts allow to form a highly vascularised tissue or "granulation tissue" which will be finally remodeled into a new functional tissue. However, depending on the size and the site of the injury, granulation tissue can evolve into scar tissue.

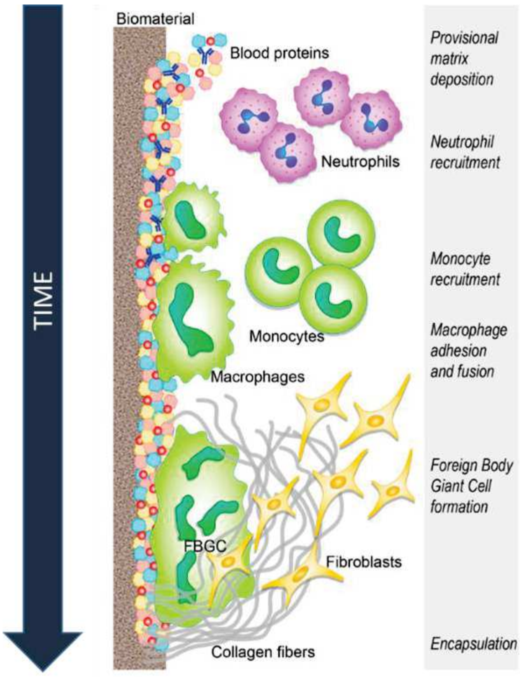

Figure 1-2 : Representation of the evolution with time of biological response of the body to an implant (sketched from Mariani et al.[30])

Unlike classical injuries, the wound healing process is different in the case of biomaterials. For example, early protein adsorption becomes non-specific, and protein conformation is tightly linked to the properties of the material surface[32,33]. Indeed, proteins undergo some conformational changes or are denatured and thus, the exposed binding or signaling motifs can alter the specific recognition of cells leading to an up-regulation of cytokines and other signaling molecules, which, in turn, triggers the inflammatory process[34]. This phenomenon is called the "foreign body reaction" (FBR)[35], which, when it is not controlled, can cause several complications such as acute or chronic inflammation or avascular fibrous capsule formation (Figure 1-2). The FBR leads to poor healing with the formation of a non-functional fibrous tissue. Without entering deeper into detail, we can understand the needs to tailor the material features to guide the FBR towards a pro-healing process instead of pro-inflammatory one. More recently, studies demonstrated that biomaterials could, for instance, modulate the polarization of macrophages, from the M_1 (pro-inflammatory) to the M_2 type which is pro-healing[36,37] as already seen in Equ. 1.

1.3 Classes of materials used in tissue engineering

Many different materials are used in tissue engineering. These include polymers (Section 1.3.1), ceramics (Section 1.3.3) and metals (Section 1.3.4). This section provides a brief overview of the main classes of materials and their key features. We also provide a more detailed section on polyurethane since it is this material that is used in this Thesis (Section 1.3.1.2).

1.3.1 Polymers

Polymers are widespread in the medical field due to their cost-effective production and the vast amount of possibilities they offer which is the essential prerequisites for their use in tissue engineering. Polymers interact with biological systems either at the molecular scale where their structure (i.e. crosslink density, chemical functionality, molecular weight etc.) can directly interact with proteins, cells or enzymes or at the macroscopic scale through their mechanical properties, shape or viscosity to interact directly with the whole tissue. Two main classes of polymers are generally used: synthetic or natural polymers. We will provide here a brief summary of what can be found in the literature. For a more detailed description, the reader can refer to the review of Tian *et al.* [38] and Nair *et al*.[39].

1.3.1.1 Synthetic polymers

Generally, synthetic polymers are interesting for medical devices and tissue engineering thanks to their processability and low cost. Besides, many synthetic polymers are biocompatible. Polymer science allows to link the physical properties of the final material to the molecular structure. It is thus possible to tailor the final material by tuning the molecular properties of the polymer[40].

Polyesters are intensively studied due to their capacity to degrade in aqueous environment, which is often desired in tissue engineering[41]. Since polymer degradability does not depend only on the presence of the ester group (R-COO-R'), but also on the crystallinity and the molecular weight[42], the large panel of polyesters available allows to find one with appropriated features. Examples are poly(methyl methacrylate) PMMA, polylactic acid PLA, poly(lactic-co-glycolic) PLGA, poly(ε-caprolactone) PCL, poly(propylene fumarate) PPF or poly(ethylene terephthalate) PET. Other polymers are also widely employed in medicine such as polyurethanes PU (Section 1.3.1.2), polytetrafluoroethylene PTFE or poly(ethylene) glycol PEG etc. Polyethers or polymers without ester groups are less subject to hydrolysis so that they can be used for long-term implantation. This is the case for vascular grafts for which PTFE (commercial name Teflon®) is commonly used. Its fluorocarbon backbone is not biodegradable and its surface is highly electronegative which is known to be antithrombotic[43]. Polyamides or nylons are promising as well due to their mechanical strength and flexibility, and due to their amide bond which results in a molecular structure close to that of natural peptides[44]. Furthermore, surface functionality and activity are often improved by chemical and physical treatment.[45–47]. Polymers are also very good candidates for 3D printing (Section 1.4.2), which is rapidly developing in tissue engineering[48]. Here again, the physical properties of the polymers have to match well the requirements of 3D printing regarding their melt viscosity, their solid-to-melt transition or their solubility in solvents[49].

1.3.1.2 Example of a synthetic polymer: Polyurethanes (PU)

A more detailed description of the polyurethane chemistry is given since it is this class of polymer that we chose for the purpose of this Thesis. PU synthesis involves a reaction of *polyaddition* between a polyol (mainly a diol or a triol) and a di(tri)isocyanate, which leads to the urethane formation (Figure 1-3-a). Therefore, the PU is a copolymer with an alternation of polyols mono(oligo)mers and isocyanate mono(oligo)mers connected by the urethane linkage. Polyols have a high chain mobility and generally relatively high molecular weight which provides elasticity to the PU. Polyols are mostly aliphatic poly(ethers) (R-O-R') or poly(esters) (R-COO-R'). They can be liquid-like or waxy at room temperature according to their molecular weight which usually ranges from a few hundreds to few thousands. These are usually named "soft segments". A vast variety of soft segments exists for polyurethane. For example polyalkyl[50], polydimethylsiloxane[51], (PDMS) or polycarbonate[52].

The main isocyanates found in industry are shown in Figure 1-3-b. These are 4,4'-diphenylmethane diisocyanate (MDI) or its hydrogenized form, (HMDI). Toluene methyl diisocyanate, (TDI) is also widely used in industry. As part of this thesis, polymethylene polyphenylisocyanate (polyMDI) was used (Figure 1-3-b). The term "hard segments" is commonly employed to describe isocyanates. Basically, hard segments confer the stiffness to the polymer[53].

Another compound is also commonly added to the PU formulation which is called chain extender[54,55].

It can be either amine terminated as shown in Figure 1-3-c for the case of ethylene diamine (ED) or hydroxyl terminated as it is the case for 1,4 butane diol (BD). Chain extenders can increase average polymer chains between two cross link points, which, in turn, affects the mechanical properties of the final polymer. If the chain extender is an amine, the reaction between the amine groups and isocyanate forms urea, that will be incorporated in the chains to form poly(urethane urea). On the other hand, if a diol is used, then the further reaction with isocyanate leads to the formation of an urethane linkage (Figure 1-3-a).

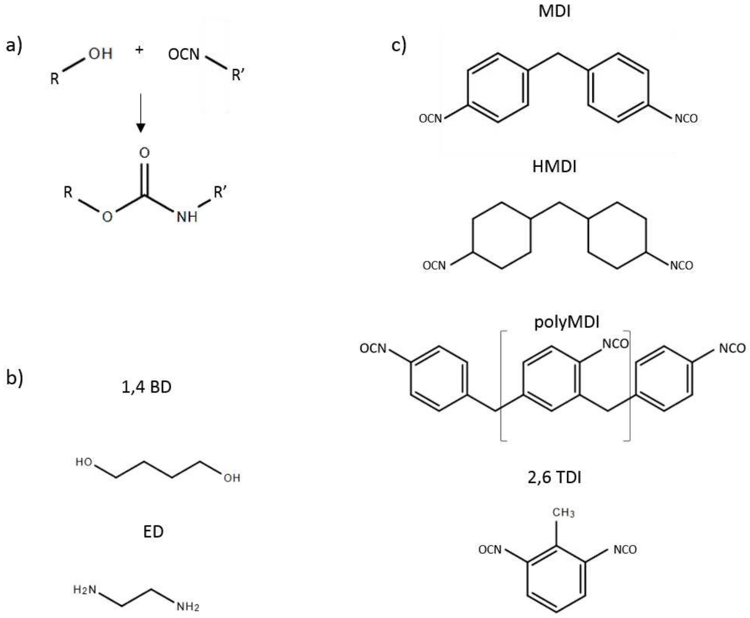

Figure 1-3 : a) Basic reaction of an isocyanate and a hydroxyl group leading to urethane linkage. b) Main isocyanates used in polyurethane chemistry. c) Main chain extenders used in industry.

It is well accepted that urea enhances the hydrogen bonding within the hard segment and plays a role in the phase separation that occurs within the PU[56]. Hence, the PU microstructure often consists of two distinct phases, one rich in soft segments and the other rich in hard segments[57]. The latter can be crystallized[58]. This phase separation provides unique mechanical and adhesive properties to the polymer[59]. This phase separation will be investigated more deeply in Section 4.2 .

Catalysts are also required in PU synthesis, especially when a polyurethane scaffold is prepared by foaming methods (see Section 1.4.4), which implies that the stability of the foam has to be ensured[60]. Since the solidification time is larger than the characteristic lifetime of the foam, catalysts are added to accelerate the solidification process. Two main classes of catalysts are usually employed, tin catalysts and tertiary amine catalysts. Tin catalysts promote the reaction between the hydroxyl and isocyanate groups and are considered as “gelling catalysts”, whereas, tertiary amine catalysts are known to catalyze the water/isocyanate reaction which, in turn, promotes the formation of carbon dioxide (CO_2 is used to generate the pores of the foam upon chemical foaming) and are called “blowing catalysts”. A detailed list of commonly used catalysts is given in the book of Ashida[61].

PUs show good outcomes in vivo, and are already used as catheters[62], vascular grafts[63] or stents[64]. But some work still need to be done to improve their degradation resistance against hydrolysis and oxidation[65,66] and to diminish their potential for acute inflammation[67].

1.3.2 Natural polymers

Naturally-derived polymers, especially those originating from the extracellular matrix (ECM), are gaining a lot of interest since their organization is closer to the native ECM. They can contain binding sites to support cellular adhesion and function or cleavable sites for enzymatic degradation[68]. Moreover, natural polymers are also biocompatible and can promote cell differentiation without the need to functionalize them, unlike it is the case for synthetic polymers. Collagen and gelatin (which is derived from collagen), or fibrin are commonly employed. They show good degradability and mechanical properties[69,70]. We can also find peptides or polypeptides which can be functionalized through their amine and carboxylic groups to graft molecules of interest. Naturally-derived polymers are often turned into hydrogels due to their high capacity to absorb water and biological fluids[71]. Some examples are alginate, hyaluronic acid, collagen, and chitosan-derived hydrogels[72,73]. However, natural polymers have varying chemical and mechanical properties and are difficult to process which is an important drawback[74].

Finally, we may say a few words on supramolecular assemblies which is a growing field. Those polymers are constructed on the basis of the supramolecular chemistry[75] that exploits the fact that bonds are non-covalent, reversible, directional and tunable to build materials with unique properties[76]. For instance, peptides can self-organize in water through hydrogen bonding or π-π interactions to form self-assembled polypeptides (SAP) which were found to be suitable for cell culture and tissue engineering[77,78]. SAP will be used in Chapter 5 as a cell carrier to be further injected into our scaffold.

1.3.3 Ceramics

Ceramics are inorganic and non-metallic composites. They are usually hard and brittle materials with applications mainly in hard tissues repair[79]. They can be divided into three sub classes, which are bioinert, bioactive and bioresorbable ceramics.

Bioinert ceramics are widely used for orthopedic repair. They possess high load-bearing features and lubricity which is interesting for gliding functions in articulations. These materials are biocompatible and their physical properties are maintained for long periods of time post-implantation[80]. Some examples are ceramic based on aluminum oxide, pyrolytic carbon or zirconium oxide. Bioactive ceramics form a biologically active surface in physiological environment and can form bonds with hard tissues[81]. Those ceramics are commonly used as coatings to enhanced implants integration[82]. We can cite for example Bioglass®[83]. Bioresorbable ceramics can be chemically dissolved by either the physiological medium, by cells such as osteoclasts, or even by macrophages[84]. The residual fragments are known to be harmless for the surrounding tissues. Hydroxyapatites, main composite of bones and teeth and β-tricalcium phosphate (TCP) are commonly used in this field[85]. Those materials resorb at an equivalent rate that the neo-tissue grows[86].

1.3.4 Metals

Metals and alloys offer outstanding structure-property relationship to be used as medical implants. Most metals used in medicine are stainless steel, titanium and titanium alloys and NITINOL. Their biocompatibility lies mostly in the fact that an inert oxide layer forms spontaneously on their surface. This prevents ion release and minimizes corrosion, which, in turn, avoids an adverse response from the host body even if small fibrous capsules are sometimes formed[87]. Atoms in metals are organized in crystalline structures and some heteroatoms can lodge in the interstitial space to form alloys. The composition of alloys is well standardized by the American Society for Testing and Materials (ASTM). According to their treatment (generally, thermal treatment) metals can undergo allotropic changes (i.e. switch from one lattice structure to another) and these changes in lattice structure lead to different mechanical properties. Heteroatoms can stabilize specific structures[88]. Besides, specific alloys can give "shape memory" properties (i.e. they can be deformed at low temperatures but return to their initial shape upon heating). This is, for instance, the case for NITINOL where "NI" stands for Nickel, TI for titanium and "NOL" for Naval Ordinance Laboratory, the lab in which the alloy was discovered[89].

We would like to emphasize that metal implants are often surface modified, and especially for joint replacements where abrasion or fatigue may deteriorate the material[90,91]. Besides, Mg-based alloys are interesting for their degradation properties: Degradation products form Mg salts, are biocompatible and slowly dissolve before being evacuated out of the body[92]. In this case, corrosion helps to trigger the degradation process of metal[93]. Complex structure of metal implants can be created by additive manufacturing technology[94], mainly via electron beam melting (EBM) or laser beam melting (SLM)[95]. For instance, Kolken *et al.*[96] processed titanium alloys using SLM technology to obtain an auxetic material (i.e. a material with a negative Poisson ratio) for hips implants.

1.4 Technics for the development of porous scaffolds

Scaffold design must provide control over porosity and the pore interconnectivity to allow nutrients and oxygen to diffuse across the scaffold. Besides, scaffold morphology is linked to the mechanical properties of the material. A wide literature is available on the different technologies that are used for scaffold design. We describe here the most frequently used techniques of scaffold preparation and in particular of "sphere templating" (see Section 1.4.3.1) approach which is employed in this Thesis.

1.4.1 Electrospinning

An electric field is applied between a grounded or oppositely charged surface (collector) and a tip. The tip is filled with a charged polymer solution which is ejected from the tip. When the electric field is strong enough, the polymer droplets that are ejected overcome the surface tension turning them into a jet that is propelled to the collector[105] . Electrospinning (Figure 1-4) allows to form three dimensional fibrous scaffolds with high surface to volume ratios. It also allows for an organization and porosity that can mimic the native environment of the cells. Electrospinning offers a large number of possibilities to play on the morphology and the assembly of the fibers. The collector-needle tip distance, the polymer concentration and thus, the viscosity of the solution and the conductivity are all parameters which ca affect the fiber morphology[106]. Agarwal *et al.*[107] reviewed the overall panel of polymers that can be used for electrospinning. It comes out that several functionalities can be incorporated in the scaffold such as biodegradability or the release of bioactive molecules[108–110]. Furthermore, the mechanical strength of electrospun scaffolds can also be tuned[111,112]. Even if electrospinning can provide an interconnected three dimensional architecture, some studies report that cell migration throughout the entire volume of the scaffold can be limited if the pores are too small or if the fibers are aligned[113]. Tight packing of the fibers can prevent nutrient and oxygen transport towards the center of the material[114]. This remains the major drawback of this approach. Recently, Kuo *et al.* [115] used two solutions to perform co-electrospinning, the resulting fiber network being composed of interpenetrated fibers of two types. This allowed to selectively dissolve one of them, and therefore, to reduce the packing of the fibers which enhanced cell growth.

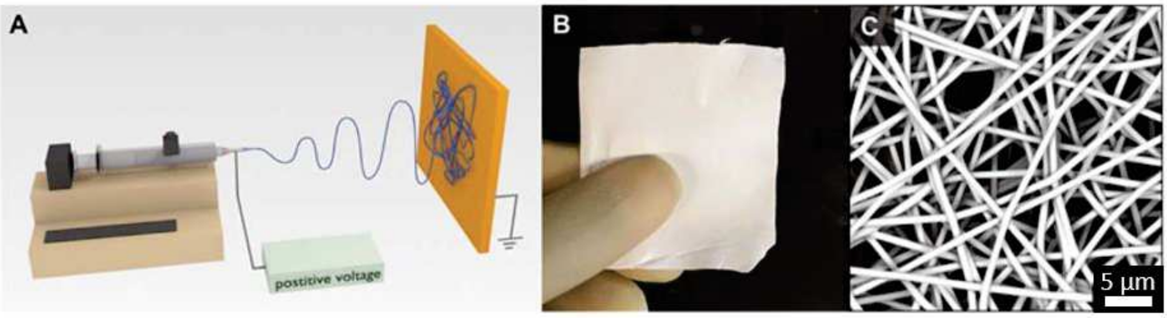

Figure 1-4 : A) General set up of electrospinning. B) Image of the obtained material. C) SEM image of the electrospun meshes from Kutz et al.[79]

1.4.2 Additive manufacturing

Additive manufacturing concerns the overall set of techniques that lies on the conception of pieces by adding material through a layer-by-layer process. Additive manufacturing is opposed to techniques such as etching where some material is removed during the process. Additive manufacturing is properly described by the ASTM F2792 standard and gains increasing attention due to the possibility to fabricate materials with an independent control over the pore shapes, the interconnections and the porosity, all being the cornerstones in scaffolds engineering. Typically, the construct is firstly modeled with a 3D software prior to be transferred to a slicer software which allows the printer to build the final material in a layer-by-layer fashion. At the end, some post proceeding steps such as curing and polymerisation may be needed[116]. Figure 1-5 gives an idea of all variants of this technology which can be applied to almost all types of materials from metals to ceramics, polymers and even composites. Thanks to the vast versatility of additive manufacturing, scaffolds defined for muscles[117], bone[118,119], tendon[120] or cartilage[121] can be prepared. Cells can even be printed at the same time as the scaffold[122,123]. This allowed to guarantee a homogenous colonization throughout the whole structure. Nevertheless, additive manufacturing fails in spanning the control at both the nano scale-up to the macro scale of the final material[124].

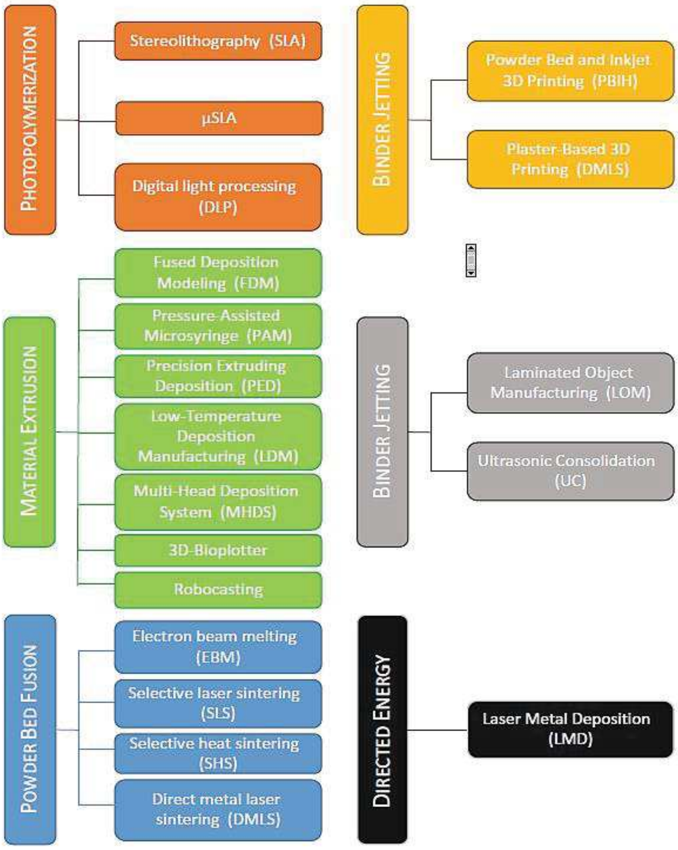

Figure 1-5 Summary of additive manufacturing technologies (from Ovsianikov et al.[116]).

1.4.3 Particle leaching

As shown in Figure 1-6, particle leaching requires that the material is in the liquid state prior to solidification. This liquid is cast on an assembly of sacrificial particles which act as a negative template for the final structure. Once the liquid (generally a monomer, a polymer melt or solution) is solidified and the solvent is evaporated, the sacrificial particles are selectively dissolved in an appropriate solvent to obtain a porous network (Figure 1-6-a). The morphology of the porous scaffold is controlled via the shape and organization/compaction of the initial template.

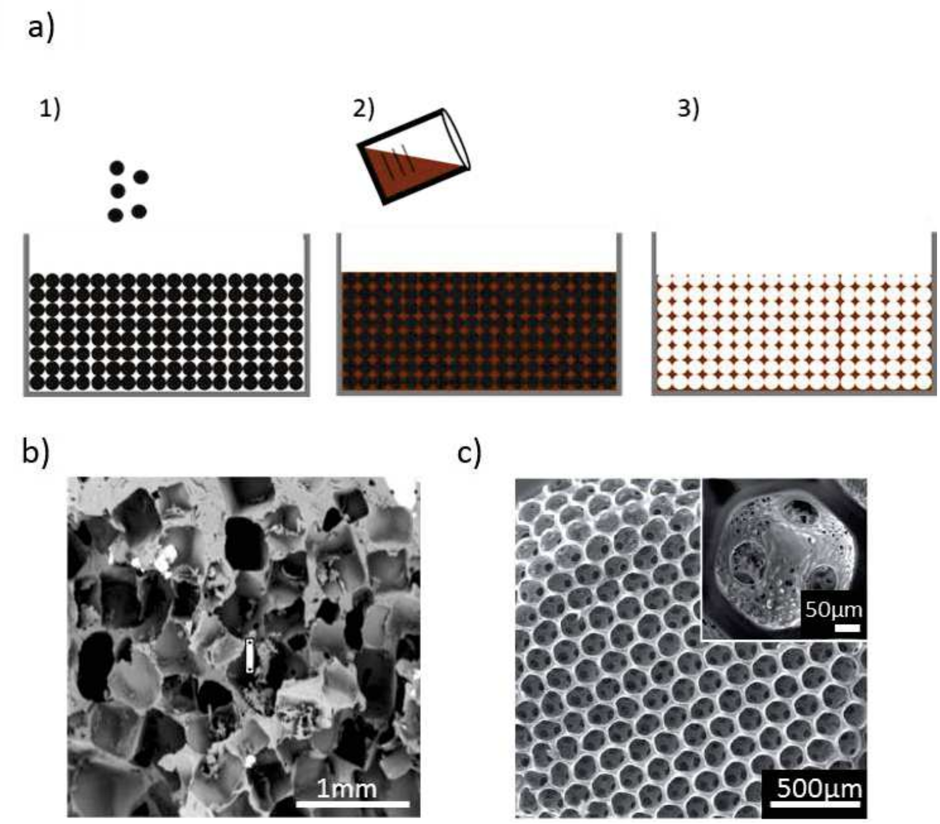

Figure 1-6 : a) Illustration of the process of sphere templating. 1) Particles are packed in a mold and 2) the polymer solution is cast onto the template. Once cured, the particles are (3) selectively dissolved leaving a three dimensional interconnected network. b) SEM image of a scaffold generated via salt leaching (from Janik et al.[125]) and c) via sphere templating (from Choi et al.[126]).

To form the template, the particle assembly must be "compact" to ensure the structural integrity of the template and thus the accuracy of the resulting porous structure. The sacrificial porogen is often salt[127] (Figure 1-6b), since it can be easily dissolved in water, avoiding the use of organic solvents. However, the use of other sacrificial agents such as paraffin or polymers are also reported in the literature. Despite its simplicity, this approach allows to control the pore size (from tens to hundreds of microns) and guarantees that the resulting porous material will be well interconnected. Furthermore, the structure depends only on the initial template regardless of the chosen polymer.

1.4.3.1 Sphere templating

Prior to present this approach, we present here the main vocabulary that will be followed along this thesis.

"Sphere templating" is the particular case where the sacrificial agent is composed of spheres (Figure 1-6-c). It is frequently used to produce tissue engineered scaffolds[37,130,131] . The spherical shape of the pores (Figure 1-7) renders the structure more homogeneous and reproducible than in the case of salt particles which lead to more random shapes (Figure 1-6-b). Monodisperse spheres can organize in densely packed structures which allows to get highly crystalline systems (Figure 1-6-c). In addition to providing a repetitive pattern in space, crystallized structures have an optimized number of neighboring spheres namely 12, and thus the number of interconnections per pore is optimized. However, due to the friction between the hard particles, one generally obtains "random loose packing", in which each sphere has on average 4 neighbors[132].

The contact area (or the neck) between spheres can also be varied, which, in turn, allows manipulating independently the pore size from the interconnection size as it is schematically shown in Figure 1-7 for paraffin spheres that were sintered at different levels. Depending on the chemical nature of the porogen agent, spheres can be partially fused by sintering[133], by chemical dissolution[131], or by the addition of an adhesive[134]. The ease of process of these approaches combined with the overall control on the morphology of the scaffold makes sphere templating a good candidate for applications in tissue engineering.

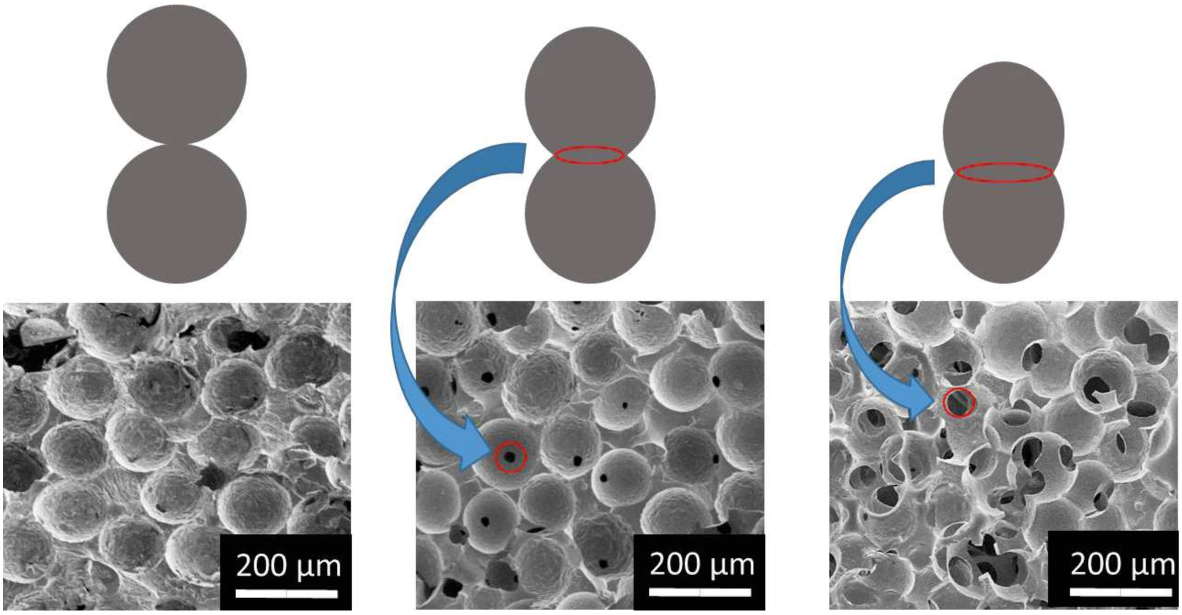

Figure 1-7 : Illustration of several stages of paraffin beads sintering, and the resulting scaffolds with various interconnection sizes (from this thesis).

A schematic representation of a porous scaffold with spherical pores is shown in Figure 1-8. We define the *pore diameter/radius* as *D*/*R*. The *interconnection* is the aperture that connects two adjacent pores. The diameter of the interconnection is defined as *d* and its respective radius *r*. The *interconnectivity* is also mentioned sometimes which is the degree of interconnection within a scaffold[128]. For instance, for a scaffold completely interconnected, a particle or a cell (sphere *A* in Figure 1-8) can diffuse or migrate across the entire scaffold and coming out through another output than the one by which it entered. On the other hand, a scaffold which is not fully interconnected blocks the propagations of cells/nutrients (particle B in Figure 1-8). The interconnectivity is not straightforward to establish; it can be estimated through algorithms by analyzing images taken by micro-CT[129].

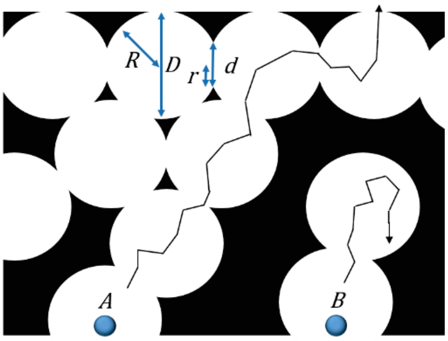

Figure 1-8 : Schematic representation of a porous scaffold seen in cross section. The pore diameter is defined as D and its corresponding radius as R. The diameter and the radius of the interconnections are defined as d and r respectively.

Another property of importance for this Thesis is the *porosity*. It is the ratio of the void volume of the scaffold divided by the total volume of the scaffold. The mathematical expression is given (Section 2.20).

1.4.4 Solid foams

Foams have been widely used as porous scaffold[135]. They can be created via chemical or physical foaming processes.

Chemical foaming is a process by which a gas releasing chemical reaction is triggered within an initially liquid/visco-elastic matrix. When the gas expands, it forms dispersed bubbles surrounded by the matrix. Once the matrix is solidified, it becomes a solid foam. Although chemical foaming has been employed to generate porous scaffolds[136,137], explicit control of structural parameters such as the pore size distribution, the interconnection size and the porosity is quite difficult.

Physical foaming allows to generate bubbles with well-controlled size distributions. Usually, in tissue engineering, scaffolds have pore sizes ranging from tens to hundreds of micrometers. Thus, microfluidic chips are adapted to obtain microbubbles[138]. As shown in Figure 1-9a, a continuous liquid phase and a non-miscible gas (the dispersed phase) are forced to flow through a constriction. At the passage of this constriction, the liquid which surrounds the gas creates a gas filament which breaks into bubbles[139,140].

Under the right flow conditions, this break-up is periodic and can therefore produce highly monodispersed bubbles. Generally, the bubbles have a diameter that is proportional to the diameter of the constriction, and the ratio of the gas flow rate to the liquid flow rate. Afterwards, the bubbles are collected in a container, and the liquid phase is let to solidify to end up with the solid foam. Since the bubble surfaces are liquid, the friction is low (compared to solid spheres in Section 1.4.3) and allows the relative motion of bubbles which can lead to an ordering of the bubbles into a highly crystalline system with hexagonally close-packed structure[60,141] (Figure 1-9b). This is relevant, since in an ordered foam, bubbles have 12 neighbors (compared to disordered systems having 6 neighbors), which implies maximized interconnectivity. This may influence mass transport properties as well as cell migration[142].

To our knowledge, only few studies have been conducted on the use of microfluidic foaming to produce tissue engineering (TE) scaffolds. One recent example was provided by Costantini *et al.* [143,144], who generated alginate scaffolds.

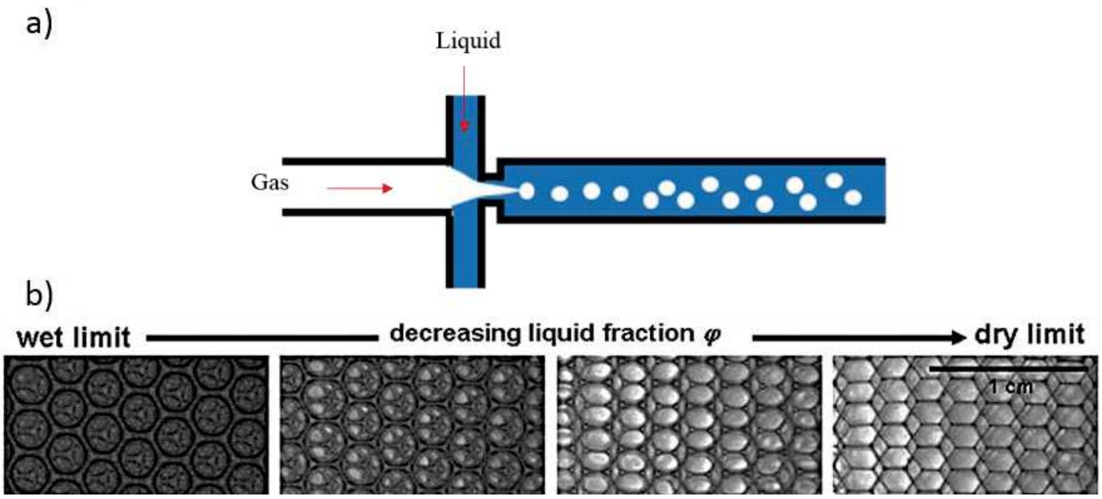

Figure 1-9 : a) Schematic description of bubbling through a microfluidic chip, b), evolution of a monodispersed foam with the liquid fraction (from Drenckhan et al. (2010).

They showed that a monodispersed scaffold has a much more homogeneous, interconnected structure with a higher hydraulic permeability (Section 2.19) compared to a polydisperse scaffold obtained via gas foaming. Cell migration was shown to be improved. Despite the promising possibilities that microfluidic foaming offers, we must emphasize that the generation process can remain "tricky" since the stability of the liquid template must by guaranteed. This implies to find an appropriated stabilizing agent, the adjustment of the solidification time must be finely tuned to obtain an open cell foam, and finally, the control on the size of the interconnections remains challenging, since the mechanism of the interconnection opening is still under debate[145,146].

1.5 Overview of clinical trials and future challenges

Transfering new concepts of tissue-engineered scaffolds toward clinics is the main achievement that researchers in this field can expect. Despite the fact that several studies were performed, only few examples were reported in which scaffolds were successfully implanted in humans. Many reasons can explain this fact: cost associated with the development of a tissue-engineered product and numerous regulatory constraints. Trials on animal models are mandatory for preclinical tests, but animals do not mimic perfectly human conditions[97]. Scaffolds are often filled with allogenic or xenogenic cells to enhance the integration by the host tissue upon implantation. To avoid biopsy on the patient, one needs to expand cells *ex-vivo*. However, the associated risks of teratoma formation or immunogenicity are serious issues to obtain the approval from regulatory organisms[98].

Cell free scaffolds are gaining attention since they can be considered as medical device by the U.S Food and Drug Administration FDA which can speed up their marketing[99]. Nonetheless, some tissue engineered scaffolds are already commercialised. For example, Organogenesis Incorporation fabricate three dimensional scaffolds made from polyglactin (Dermagraft®) or collagen (Apligraf®) within either neonatal fibroblasts or neonatal keratinocytes were allowed to proliferate and secrete ECM components which helped to further recruit endogenous cells in vivo. Those scaffolds were employed for foot ulcer treatment in diabetic patients[100,101].

Integra® (Integra Lifesciences) is a three dimensional matrix composed of chondroitin-6-sulphate and tendon collagen fixed on a polymer layer of silicone as skin substitute[102]. Some clinical or pre-clinical studies were performed with encouraging results. Debry *et al.* [103] conceived an artificial larynx composed of a permanent and porous titanium part which improved tissue integration. After 16-month implantation in a patient who underwent total laryngectomy, the patient could breathe through the artificial airway, swallow, and even speak again.

Actifit® is a polyurethane scaffold designed for meniscus replacement[104]. A study on several patients was conducted for a minimum of 5 years. Functional scores and cartilage were stable even if MRI images showed that the cartilage was immature. Moreover, the failure rate was high since the visual analogue scale for pain (VAS) (a score between 0 to 10 given by the patient to estimate his pain) was too high for some patients.

1.6 Review of the interactions between cells and materials

We introduce here the main processes that arise at the cell/scaffold interface and we show how a biomaterial can act as an extra-cellular matrix (ECM) of “substitution” and interacts with the cells.

1.6.1 The extracellular matrix (ECM)

Within tissues, cells are embedded within a three dimensional network composed of water, polysaccharides and proteins[147]. This network is also called the *extracellular matrix* (ECM). It provides adhesion sites with some specific peptide sequences such as RGD (arginine-glycine-aspartate acid)[148] which is present on some proteins such as fibronectin or vitronectin[149]. The ECM provides the structural integrity to the tissues. For example, collagen brings the stiffness while elastin provides the elasticity[150,151]. Glycosaminoglycans (GAGs) are sulphated disaccharides[152] (except hyaluronic acid) that act as water reservoir in the ECM due to their high capacity of retention of water. GAGs and proteins can bind together to form proteoglycans. These can also retain water, but they are also known to regulate signaling molecules and growth factors[153], which regulate cell proliferation and differentiation. The ECM composition, the cell density and their respective organization within the ECM vary depending on the tissue type. (Figure 1-10). Epithelial cells are contiguous cells that are linked together through tight junctions to form a monolayer. These cells are lying on an ECM called basement membrane, which acts as a support[154,155]. Fibroblasts and chondrocytes are the cells of the connective tissues such as cartilage. These cells are more scattered across the ECM[156]. Thereby, the ECM regulates the functions and the fate of the cells *in vivo*.

1.6.2 Interaction between cells and adsorbed proteins

Whether it is *in vivo* or *in vitro,* proteins are the first elements that adsorb onto the material surface, since they reach the surface before the cells[157]. Thus, the adhesion of the cells on a biomaterial is often mediated by the proteins. During the adsorption process, rearrangements occur. For example, fibrinogen (or molecules that diffuse faster at the surface) is often replaced by other proteins with a higher affinity toward the surface such as high molecular weight kininogen (smaller diffusion coefficient). This is called the Vroman effect[158]. As shown in Figure 1-10, cells usually bind to the proteins through transmembrane proteins called integrins[159].

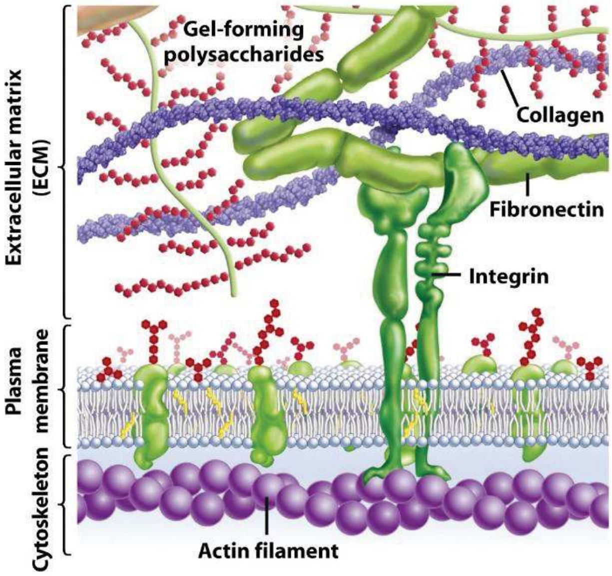

Figure 1-10 : Representation of the cell interaction with the ECM through integrins (From Freeman[159]).

Integrins are heterodimers composed of α and β subunits, which can recognize several types of adhesion sites that are present on some proteins[160]. Integrins bind to extracellular components and form a supramolecular complex called "focal contact" which links the inner part of the cells to its outer part[161] (Figure 1-10). We may note that cells reorganize their environment, according to their adhesion strength; they can make more or less stable focal contacts[162]. Cells may then, migrate by degrading the ECM through some enzymes such as matrix metalloproteinase (MMP). They can also secrete their own matrix. It has been demonstrated that even when no binding sites are present, cells produce their own ECM proteins and subsequently bind to them which allows the cells to "compatibilize" the surface of the biomaterial[163,164]. Proteins in an aqueous medium are usually arranged in quaternary structures[165]. This folding is explained by the fact that proteins possess hydrophobic and hydrophilic domains[166]. Thus, the substrate wettability can tremendously influence the structure of the proteins on the surface and their ability to expose the proper site to the cells. It is generally accepted that highly hydrophobic surfaces can denature the proteins (i.e. they are unfolded on the surface and expose their hydrophobic part) while highly hydrophilic surfaces prevent protein adsorption[32]. Indeed, hydrophilic surfaces are hydrated, implying that proteins "feel" like they are still in the blood (*in vivo*) or in the culture media (*in vitro*)[167]. Several authors coated or functionalized the surface of their biomaterial with poly(ethylene glycol) or with zwitterions which render the surface highly hydrophilic in order to prevent the adsorption of proteins (also known as anti-fouling surfaces)[168]. Thereby, a realistic view of the material/cells interface may be a protein-coated material, in which cells can subsequently adhere to. With this in mind, many studies have reported the use of coatings that can either increase the adsorption of proteins on the surface (and then, increase the adhesion of the cells)[169,170], or grafted some RGD containing peptides directly on the surface of the polymer [171,172] which mimic the presence of adsorbed proteins.

1.6.3 Surface topography

In addition to protein folding, cells are sensitive to nano cues such as surface roughness. Cells are indeed sensitive to surface topography. They can feel changes in the surface roughness of the order of a few nanometers, which may correspond to the roughness caused by an adsorbed protein[173]. For instance, the ordered or disordered organisation of nano pits modulates the adhesion of mesenchymal stem cells (MSCs)[174]. In a sense, cells scan the surface as an AFM tip. Tiny changes in surface topography induce significant changes in cellular response[175]. Furthermore, surfaces patterned with nano grooves also direct cell alignment[176]. Even if the mechanism by which cells respond to nano cues has still to be elucidated, the influence of such features is obvious.

Interestingly, cells are also sensitive to the microscale (from tens to hundreds of microns) topography and, for example, microgrooves also showed their ability to direct cell alignment[177] and more generally, micro patterns with various shapes have shown their impact on cell attachment and shape.[178]

1.6.4 Surface stiffness

It was demonstrated by Engler *et al.*[179] that mesenchymal stem cells (MSCs) can also feel the local elasticity of the substrate and this can subsequently direct the differentiation process toward different cell lineages. Engler *et al.* coated polyacrylamide hydrogels (with Young modulus ranging from 0.1 to 40 kPa) with type I collagen. They could demonstrate that mesenchymal stem cells were positive to neurogenic markers for substrates with $E = 0.1 - 1$ kPa (the range corresponding to brain tissues), to myogenic markers for substrates with Young Modulus $E = 8$ to 17 kPa (muscles) and cells were differentiating into preosteoblasts on substrates with modulus of 25 – 40 kPa. These findings underline the fact that cells are highly influenced by their physical environment, and that stem cell differentiation can be induced without the use of biochemical cues such as hormones or soluble growth factors that are normally used for this purpose solely by the Young modulus of the substrate. Several authors modified the Young modulus to control the differentiation pathway of mesenchymal stem cells[180,181].

As mentioned in Section 1.6.2, cells attach to proteins that coat the surface of biomaterials. In that sense, it was proposed that the substrate influences the way how collagen fibers are anchored. For instance, on a PDMS substrate, the evolution of the elastic properties did not affect stem cell fate (Trappmann *et al.*[182]), whereas stem cells underwent differentiation in response to variation in substrate modulus on the polyacrylamide hydrogels aforementioned. It was proposed that collagen could not penetrate the highly cross-linked PDMS matrix and thereby the fiber organization on the surface was not affected by changes of the modulus of the substrate (Figure 1-11-a). As shown in Figure 1-11-b, collagen could partially penetrate the soft (less cross-linked) polyacrylamide hydrogels. Therefore, the number and the distance of anchoring points of the collagen fibers is affected by the underlining substrate. This modifies the mechanical feedback felt by the cells when they pull on the collagen fibers and which is transmitted in the cell through integrins and actin filaments (Figure 1-10) and subsequently converted to biochemical cues that can guide the cell shape (Figure 1-12) and fate [182,183].

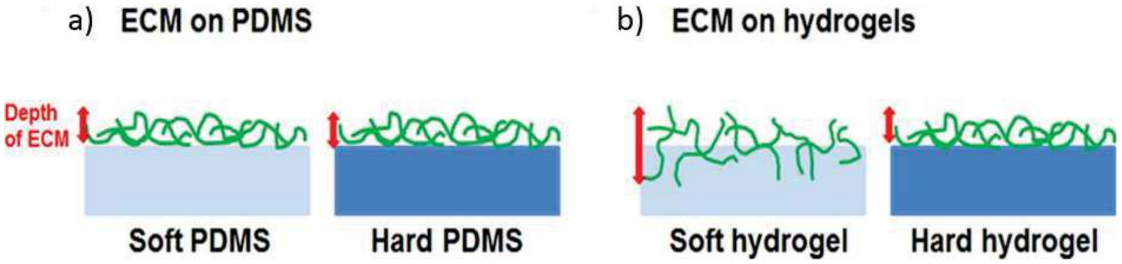

Figure 1-11 : Illustration of the organisation of ECM component on a) PDMS substrates with different stiffness b) a hydrogel with different stiffness (from Higuchi et al.[183]*).*

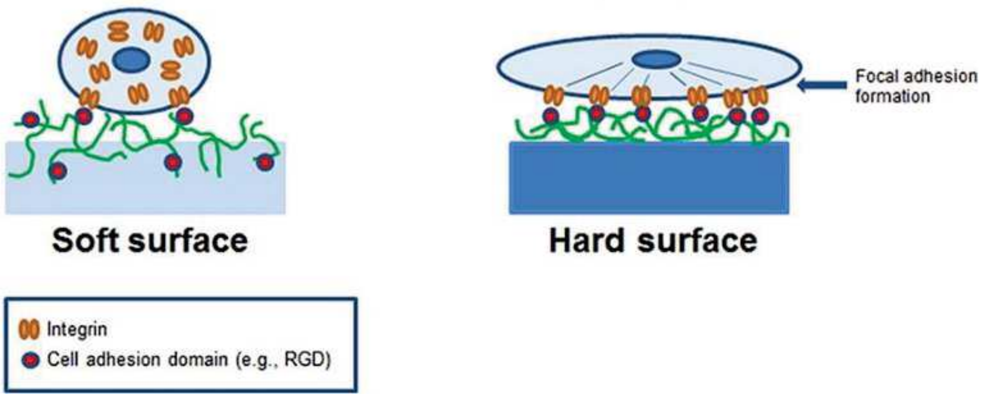

Figure 1-12 : Organization of focal contacts of stem cells on hydrogels with varying stiffness coated with collagen (from Higuchi et al.[183]*).*

More recently, it was also demonstrated by Chaudhuri *et al*[184], that stress-relaxation of alginate hydrogels can direct stem cell differentiation independently of the elastic modulus. Together these findings demonstrate that cells can feel their local environment by first adhering on it (mostly via ECM binding sites) and then, exert traction or tension on it. Nevertheless, even if the idea of controlling the fate of stem cells only by physical cues is cheering, it was demonstrated via 3D microarrays platforms that soluble growth factors are still predominant in the control of stem cell fate[185].

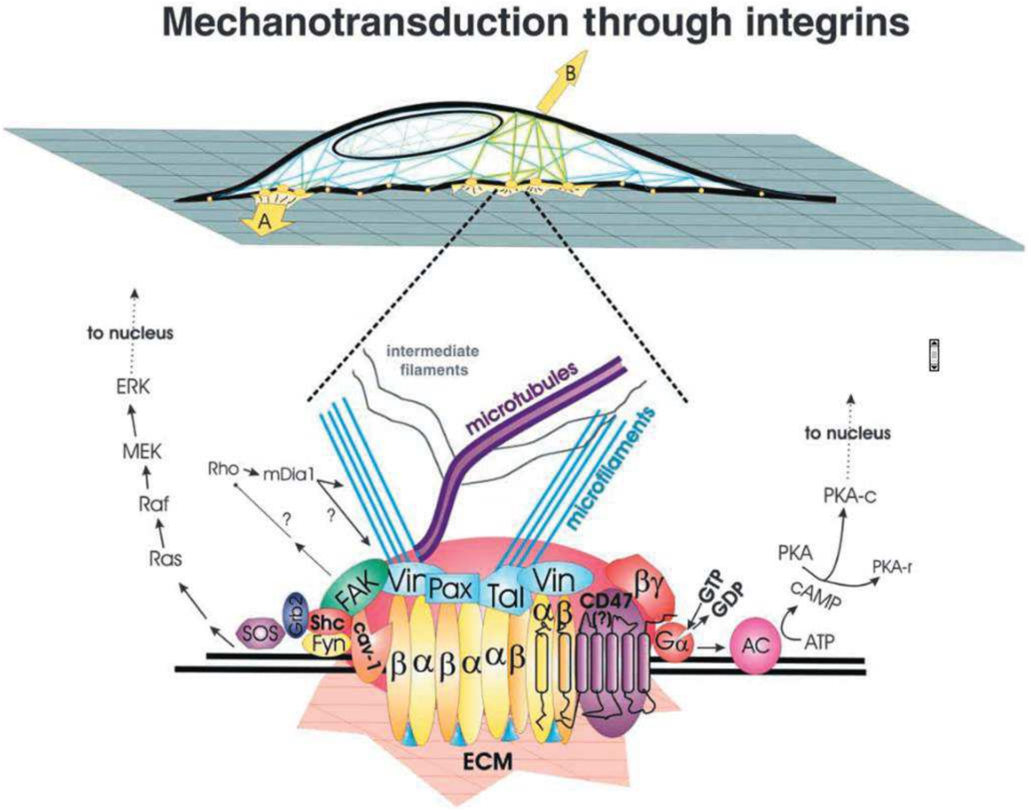

Figure 1-13 : Schematic representation of the complexes involved in the mechanotransduction (from Ingber et al.[186]).

The whole dynamic by which a mechanical signal is converted into a biochemical signal that induces a specific cell response is called mechanotransduction. In short, integrins are bound to the ECM outside the cell, and coupled to the cytoskeleton[186] (actin filaments, microtubules and intermediate filaments) in the cytoplasm as shown in Figure 1-13 where cells exert traction on the external environment by polymerization/depolymerization of actin filaments. These forces exerted on the cytoskeleton are translated into biochemical factors that contribute to modulate the cell response (i.e proliferation, migration, differentiation)[187].

1.6.5 Relationship between scaffold morphology and cell behavior

The interactions between cells and substrates described in Section 1.6 were focused on cells seeded on flat surfaces. However, it has been demonstrated that when cells are cultured on flat surfaces, they are forced to be organized in monolayers which is different of cell growth at the tissue level. Indeed, as previously mentioned, cells in vivo are spatially distributed in a three-dimensional way creating cell-cell contacts and cell-ECM contacts. Moreover, oxygen or nutrient gradients can drive cell migration and proliferation, which is hindered on flat surfaces[188]. Consequently, the gene expression is drastically different between cells cultured in 2D or 3D, which emphasizes the need to implement cell culture in three-dimensional environments. We discuss here the main parameters (i.e. pore size, porosity, pore shape, interconnection size) as defined in Section 1.4, which can be controlled by the manufacturing processes of tissue engineering scaffolds and that were found to affect the behavior of the cells.

1.6.6 Effect of pore size and shape

We gave an overview in Section 1.4 over the main techniques that are used to generate porous scaffolds with various morphologies which can be tuned to modulate the cellular response. In this section, we describe the influence of pore size (i.e. their diameter) and pore shape on cell growth. The cellular response to these parameters in our system will be presented in Chapter 4.

Polyurethane foams prepared by salt leaching by Van Tienen *et al.*[189] having pore diameters of 150 – 300 µm separated by micropores of 15-20 µm or at least 30 µm were implanted subcutaneously in rats. The authors reported that tissue ingrowth was higher in foams with micropores of at least 30 µm compared to 15-20 µm. The porosity was affected by the micropore size (73 % and 86 % for micropores of 15-20 µm and 30 µm, respectively) while the interconnection diameter was not specified (Figure 1-14-a).

Meniscus implant consisting of a polyurethane scaffold was also generated by particle leaching with pore diameters ranging between 150 and 355 µm[190]. The scaffold was highly interconnected, with interconnection diameters < 50 µm. It was implanted in a dog meniscus. After 6 months, the implants were filled by fibrovascular tissues. Despite the fact that particle leaching results in pores with irregular shapes and size distribution, the magnitude of the average diameter of the pores and the interconnections allowed cells to migrate in the whole implant. The authors noticed a slight foreign body response (FBR) characterized by the presence of giant cells which was attributed to the interaction of the polyurethane surface with macrophages. The level of cartilage degeneration was highly variable from one dog to another.

A collagen-hyaluronic acid scaffold was generated by Matsiko *et al.*[191] via freeze drying having average pore sizes of 94 ± 8, 130 ± 7 and 300 ± 8 µm and seeded with MSCs. While the cells were able to proliferate in all scaffolds, the authors investigated whether the MSCs were able to differentiate into chondrocytes preferably in one of these scaffolds. They quantified both type II collagen (COL2) and sulphated glycoaminoglycans (s-GAGs) which are known to account for chondrogenesis. They noticed that MSCs showed a significantly higher COL2 and s-GAGs expression level in scaffolds with 300 µm pore diameters compared to 94 and 130 µm after 28 days. The authors attributed these differences to the transport properties of nutrients (even if they did not quantify them) and they also noticed that cells adopted different morphologies. Cells were rounded on in scaffolds with 300 µm pore diameters while cells were flattened in the other scaffolds with smaller pore size. We may notice again that the pores had random shapes and neither the porosity nor the interconnection diameters were specified. Conversely, in another study[192], human skin fibroblasts showed better viability after one week on poly(L-lactic acid)

PLLA and poly(lactic-*co*-glycolic acid) PLGA scaffolds having pore sizes of 74 and 160 µm on average compared to other scaffolds with an average pore size ranging from 194 to 381 µm. Scaffolds had a porosity of 91,4 % and were generated by salt leaching. Again the interconnection diameter was not specified. Wang *et al*[193] found that scaffolds with a pore size (interconnection size) of 200 ± 85 µm (160 ± 56 µm) showed a higher tissue formation and colonization compared to those with 170 ± 80 µm (142 ± 50 µm) and 243 ± 95 µm (191 ± 63 µm) pore size (interconnection size). The porosity was ranging between 75 and 82 % for all scaffolds. They also changed the thickness of their samples from 1.5 mm to 4 mm and demonstrated that thickness of 4 mm restricted cells mainly on the outer edges of the scaffold while it was fully colonized in the case of 1.5 mm.

From that, we can conclude that the interaction between cells and scaffolds depends on the cell type, on the shape, porosity and on the pore size. This multicomponent dependency renders difficult to draw conclusions on the optimum scaffold morphology that would work universally.

The examples cited above were centered on the use of scaffolds for cartilage tissue regeneration since connective tissue regeneration and specially cartilage are under the scope of this Thesis. However, the influence of pore size for bone tissue engineering or cardiovascular tissues was also deeply investigated[194].

In contrast to salt leaching, the sphere templating (Section 1.4.3) approach allows to obtain scaffolds in which one can control accurately and simultaneously the size of the pores and of the interconnections within a fairly homogeneous structure. This can provide more relevant information even if the resulting scaffolds described in the literature were not generated from the same material from one study to another. For example, beta-tricalcium phosphate scaffolds were prepared by *Feng et al.*[195] and implanted in rabbits for 4 weeks. They generated porous structures with pore size of 300-400, 400-500, 500-600 and 600-700 µm while keeping the interconnection diameter constant at 120 µm (Figure 1-14-b). In all cases, the porosity was around 70 %. After 4 weeks, they showed that the percentage of fibrovascular tissue in the scaffold decreased when the pore size increased. They argued that the higher rate of tissue growth can be linked with the higher curvature in smaller pores.

Madden *et al.*[196] demonstrated that sphere-templated scaffolds made by poly(hydroxyethyl methacrylate-co-methacrylic acid) pHEMA-co-MAA having pore sizes of 40 µm compared to 80 and 20 µm (where interconnection sizes were about 40-50% of the pore size) promote a higher vascularization in rats after 4 weeks and promote a switch in macrophage polarization, favoring the M2 type which is known to be pro-healing. This important discovery implies that the pore size of a porous scaffold influences the inflammatory response in vivo. This finding also sets a pore size threshold around 80 µm that permits to control the host immune response. Above this value, more fibrous capsule formation is found and less vascularization occurs [37,197] .

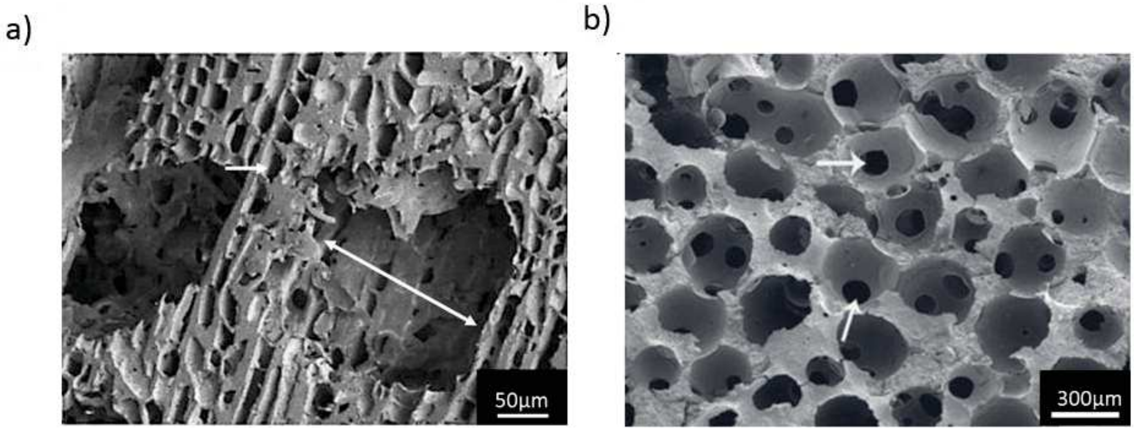

Figure 1-14 : a) SEM images of scaffolds with a bimodal pore size distribution (Van Tienen et al.[189]). The double arrow shows the pores with diameter of 150-300 µm, and the simple arrow points to a micropore with a diameter comprised between 15 and 20 µm. b) Scaffold generated by sphere templating (Feng et al.[195]) with arrows showing the interconnections.

Despite the fact that in the cited examples (the list being not exhaustive), the optimal pore size was ranging between 100 and 700 µm. These order of magnitude may be suitable to overcome the mass transport limitation in vitro (due to the absence of blood stream that continuously supplies either nutrients and oxygen in vivo) and thus, seem more suitable to the cells. Nevertheless, in vivo results demonstrate that when one needs to deal with the host response, pore sizes above 80 µm induce a detrimental inflammatory response which prevents a good healing[196]. One question which arises from that: is it possible to conduct in vitro studies in which we draw conclusions about the most effective pore size (i.e. that is the most suitable for the cells) that could be translated in vivo while keeping the same cell response?

1.6.7 Effect of pore interconnectivity

The influence of the interconnection size on cells is much less investigated in the literature than that of the pore size and porosity[198]. This can be explained by the fact that an independent control of the pore and interconnection size is not possible with the mentioned manufacturing techniques. Most of the time, when the pore size is increased, it comes with an increase in the interconnection size rendering difficult to identify which parameter is predominant. We review here some relevant studies from the literature, in which predominantly the sphere templating approach was used to study independently the effect of pore size from the interconnection size[199,200].

Beta-tricalcium phosphate scaffolds with pore sizes ranging from 300 to 400 µm were generated by Xiao *et al.*[201] via sphere templating. Interconnections were created by superficial dissolution of the porogen. Interconnections measured 104 ± 13, 117 ± 13, 149 ± 12 µm respectively. Human umbilical vein endothelial cells (HUVECs) were seeded onto these scaffolds. Results demonstrated that cells show a higher viability and were able to proliferate much more after 7 days of culture when the interconnection size was highest (150 µm). Additionally, cells exhibited a higher expression of PECAM-1 (a glycoprotein associated with angiogenesis) when cultured in the scaffold with interconnection diameters of 150 µm. Moreover, the authors conducted an in vivo study (in rabbits) for 12 weeks, and observed that the volume of blood vessels that formed inside the scaffold was much higher in the scaffold with the larger interconnection (150 µm).

Somo *et al.*[130] generated scaffolds having 130 - 150 µm in pore diameter and they compared structures with two interconnection diameters, 33 and 50 µm respectively. Their porosity was 63 % and 77 % respectively. They implanted the scaffold in rodents and demonstrated that tissue ingrowth and penetration depth as well a blood vessel density was significantly higher for the scaffold with larger interconnections after 3 weeks. However, the differences were not found statistically significant anymore after 6 weeks. This shows nonetheless that interconnections play a role in the kinetic of tissue growth (and cell migration) in porous scaffolds.

Choi *et al.*[202] showed that the uniformity of the whole structure impacts on the cell migration when sphere-templated scaffolds results in crystalline structure (i.e. obtained from monodispersed spheres with a diameter of 204 µm). The size distribution of the interconnections of crystalline structure being much sharper than when polydisperse microspheres (202 ± 94 µm, 36± 22 µm and 66± 7 µm) are used. Indeed, in the polydisperse systems, the average diameter of interconnections is lower than for the monodisperse system (with the same sphere diameter in average) because the aperture of the interconnection is limited by the smaller sphere in the case of two adjacent sphere. *Choi et al*[202] demonstrated that the cell distribution is much more homogeneous in monodisperse system. They argued that larger interconnections allow cells to migrate more easily, and that they have better access to nutrients and oxygen. This was consistent since they measured the "hydraulic permeability" which was found to increase by one order of magnitude between the scaffolds obtained from polydisperse and monodisperse spheres.

The *Hydraulic permeability* defines how easily a fluid can flow across a structure of a defined section (Section 2.19). The interconnection size was already shown to affect the hydraulic permeability in scaffolds. This, subsequently, affects the distribution of the cells within the structure and the transport of nutrients. Costantini e*t al.*[143] showed that the liquid path was much narrower in scaffolds prepared by gas foaming compared with a scaffold generated by microfluidics (Figure 1-15) with more homogenous distribution of the pore and interconnection sizes. Thereby, the nutrient and oxygen supply within porous structures can be limited when the interconnection size is small. Nonetheless, this can have beneficial effects on cells for which reduced oxygen partial pressure can induce an upregulation of matrix production or even induce differentiation. In cartilage, chondrocytes are naturally in an environment with a reduced oxygen partial pressure. This was demonstrated by Kemppainen *et al.*[203] , who showed that in scaffolds having smaller interconnection sizes (lower permeability), chondrocytes increased their production of cartilaginous matrix while bone marrow mesenchymal stem cells (BMSCs) showed an upregulation of both COL2 and aggrecan (which are associated to chondrogenic differentiation) in scaffold with large interconnections. However, we note that their results were not found to be statistically significant. This can be explained by the fact that the pore size were quite large (1 mm) and the respective interconnections (0.31, 0.46, 0.55 mm). The authors argued that the differences of the associated hydraulic permeability were quite small and therefore, the cells may not feel such small differences.

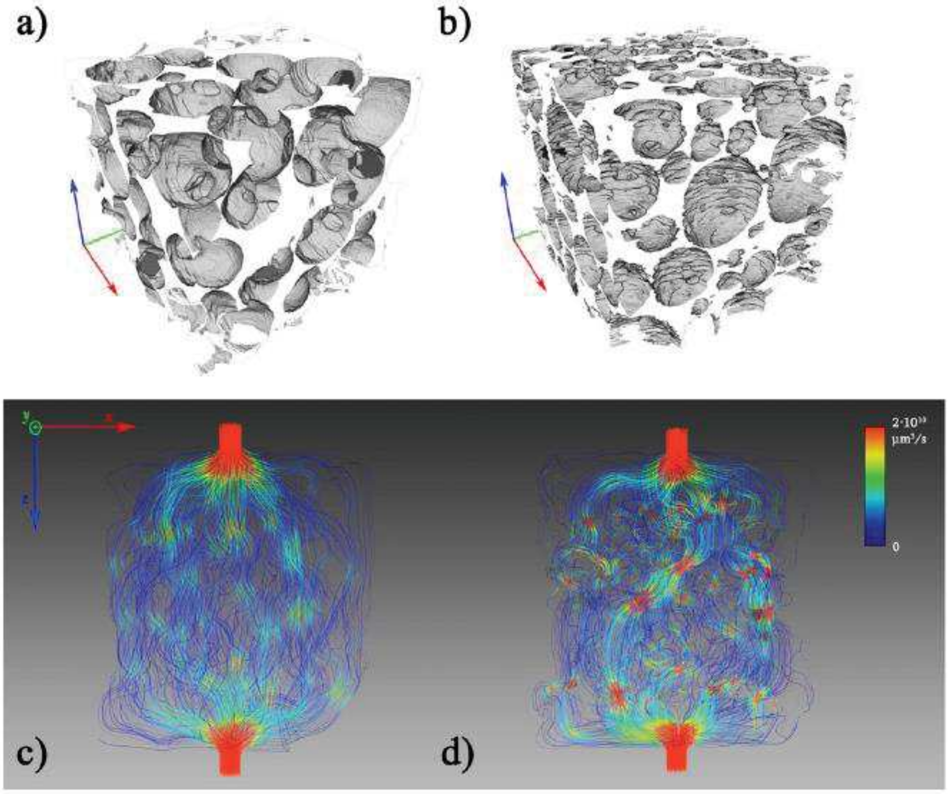

Figure 1-15 : 3D presentation of alginate scaffold generated by a) microfluidic (<D> = 143± 47 µm, <d>= 49 ± 14 µm)) and b) by gas foaming (<D> = 107± 21 µm, <d>= 38 ± 13 µm).c) and d), Flow fields obtained by simulation of samples shown in (a) and (b), respectively (from Costantini et al.[204]). The color scale indicates flow rates between 0 and 2.10^{10} µm^3/s.

In conclusion we can state that the importance of controlling the interconnection size as well as the pore size in porous scaffolds is obvious. But looking at the literature, disparities between different studies render difficult to compare the different results. We can nonetheless conclude from the examples cited above that interconnection size influences the migration capacity of cells and the hydraulic permeability which is likely related to the transport of nutrients and oxygen throughout the whole structure. This change in permeability may influence the local environment of the cells and promote some gradients that subsequently influence the biological response in terms of matrix production, differentiation etc. We can also conclude that the cell distribution within the scaffold is tightly related to the homogeneity of the structure. Hence, systems with monodisperse pore size and interconnection may also contribute to increase the integration of tissue engineering scaffold in the body. The goal of this Thesis is therefore to generate and to investigate porous scaffolds in which pore size and pore interconnections are precisely controlled.

1.6.8 The effect of the curvature

The morphology of a porous scaffold can be translated into a spatial arrangement of local curvature. For example, a pore radius of "*R*" of a spherical pore leads to a curvature of 1/*R*.

As mentioned in the preamble of this section, the genetic expression of cells in a curved environment is different to that found on flat surfaces. Porous scaffolds provide a surface curvature that could drive tissue growth. Indeed, Rumpler *et al.*[205] generated hydroxyapatite (HA) plates with four channel geometries (Figure 1-16-a), and they seeded pre-osteoblasts within the structure. They could demonstrate that tissue growth is higher in areas of high surface curvature. Once those areas were filled, the growth rate became linearly dependent on time. This curvature-driven tissue growth resembles to behavior of fluids which tend to decrease surface area. They also noticed that the organization of the F-actin filaments was different in areas of high curvature compared with areas with smaller curvature (Figure 1-16-b).

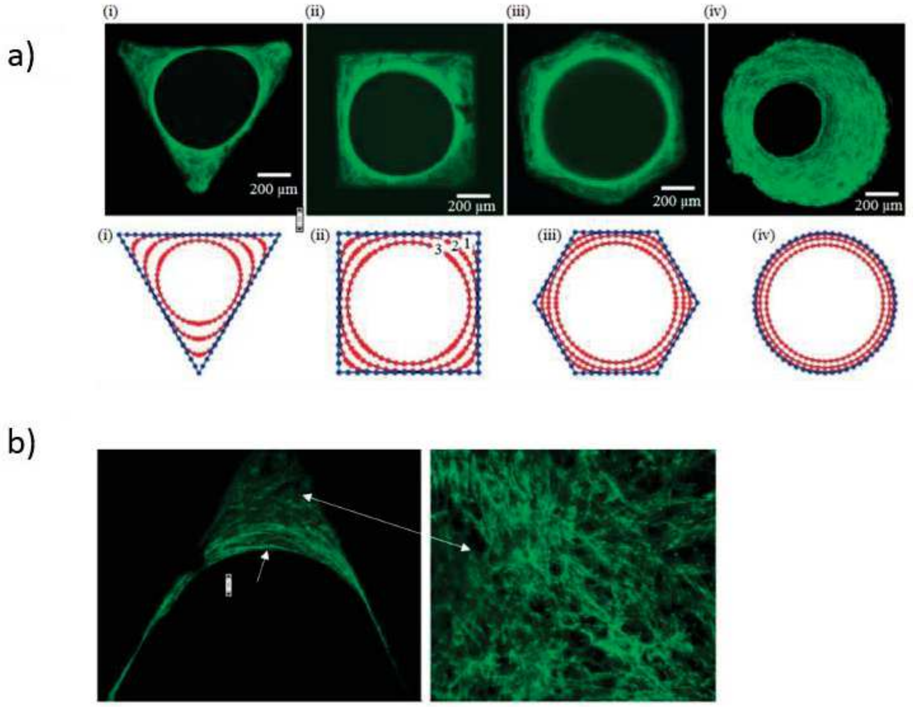

Figure 1-16: a) Tissue growth in HA channel with four different geometries: triangle, square, hexagon, and circle (i-iii) correspond to images taken after 21 days of culture and (iv) at 30 days, top images were taken under a confocal microscope and images at the bottom correspond to numerical simulations. b) Organization of F-actin filaments (green) in the region of high curvature (higher magnification on the right image) and in the region of the tissue/fluid interface (all images from Rumpler et al.[205]*).*

They proposed that the mechanical forces exerted onto or by the cytoskeleton may increase with the local curvature which, in turns, accelerates tissue growth. Thus, the channel geometry influences tissue growth rates through areas having locally high curvature. Guyot *et al.*[206] confirmed these findings by numerical simulations performed on systems seeded under dynamic flow perfusion. Bidan *et al*[207] generated more complex geometries and concluded that concave surfaces increased the rate of tissue growth whereas convex or flat surfaces were the last areas in which cells started to grow. This curvature-driven growth is a milestone in tissue engineering, since this elegant model allows to conceive scaffolds in which the tissue growth rate could be predicted by the geometry. 3D printing could perfectly design such complex geometries.

1.6.9 Mechanical properties of porous scaffolds

The Young modulus E_s of porous solids depends to a good approximation on the modulus of the bulk material E_b, and on the square of the relative density ρ_s / ρ_b [208].

$$E_s = E_b \left(\frac{\rho_s}{\rho_b}\right)^2, \qquad (2)$$

where ρ_s and ρ_b are the respective densities of the porous scaffold and the bulk material. The porosity of the porous structure is therefore defined as

$$P = 100 \times (1 - \frac{\rho_s}{\rho_b}). \qquad (3)$$

Hence from Equations (2) and (3), we can see that when the porosity increases, the Young modulus decreases in a predictable manner[209,210]. While researchers commonly generate scaffolds with porosities between 70 and 90 % to increase the void volume and thus the available space for neo tissue, the associated decrease of the Young modulus should be estimated to maintain the mechanical strength of the implanted scaffold. Moreover, in the case of biodegradable scaffolds, the loss in modulus will be even more pronounced due to the loss of material upon the process of degradation. When tissue grows progressively inside a scaffold, the compressive modulus of the scaffold/cells construct can also increase, since cells secrete extracellular components which can reinforce the mechanical strength of the system. This has been reported, for instance, for bone regeneration[211].

1.7 Conclusion and goal of this thesis

To conclude, the use of three-dimensional scaffolds for tissue engineering will surely become a solution to replace traditional grafts and implants. The research in this field is continuously gaining momentum. The joint efforts in disciplines related to tissue engineering have permitted to improve our understanding of the cell/scaffold relationship. However, to obtain a deeper insight into the relashionship of the cell behavior on the scaffold, we need to find ways to standardize the experiments in order to be able to compare them correctly and to be able to isolate the influence of individual parameters which influence cell fate. We identified here the following parameters:

1. The scaffold material
2. The surface properties of the scaffold
3. The pore size distribution and their shape

4. The interconnection size distribution

The goal of this Thesis is therefore to decouple carefully these parameters and to establish their influence on cell fate as schematically shown in Figure 1-17.

The patient-to-patient variability is also a big issue that may direct the research toward personalized scaffolds. Indeed, cells are highly complex systems that receive various cues and respond in many ways. Due to the complexity of the subject, researchers take the risk to "find what they are looking for", for instance by staining specific proteins, but this does not mean that other elements of interest are not secreted or do not play a central role. Besides, physical models that could predict cell response are lacking. The current platforms such as High Throughput screening[212] provide a unique approach to combine thousands of conditions. This is a promising way to find tailor made biomaterials with the highest efficiency.

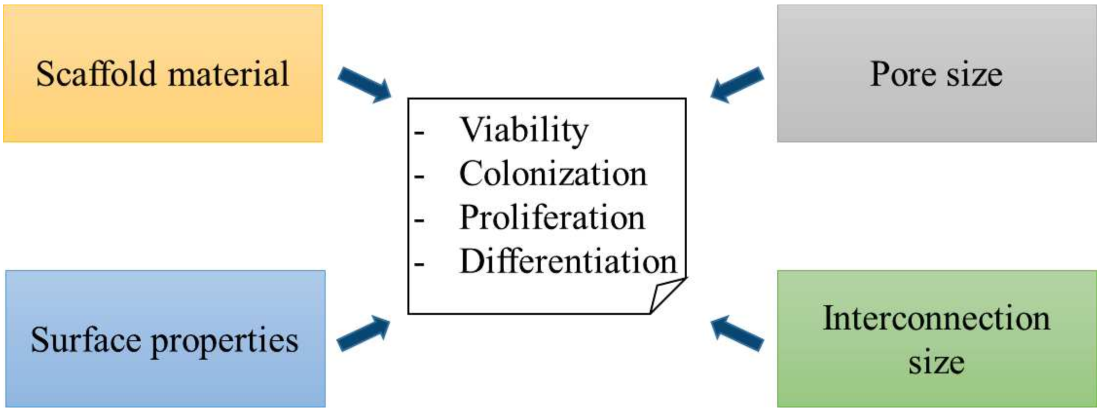

Figure 1-17 : Summary of the parameters investigated in this Thesis and their influence on cell fate.

References

1. Implants and Prosthetics. *08/28/2018* Available at: https://www.fda.gov/medical-devices/products-and-medical-procedures/implants-and-prosthetics.
2. Hildebrand, F. Biomaterials – a history of 7000 years . *BioNanoMaterials* **14,** 119 (2013).
3. A, Cotterell. *A dictionary of world mythology*. (Oxford University Press, 1986).
4. Irish, J. D. A 5,500-Year-Old Artificial Human Tooth from Egypt: A Historical Note. *Int. J. Oral Maxillofac. Implants* **19,** 645–647 (2004).
5. London Times (February 20, 2007)."5,000-Year-Old Artificial Eye Found on Iran-Afghan Border". foxnews. Retrieved December 14,2
6. D. F. Williams. Definitions in biomaterials, Ed., Elsevier, Amsterdam, 1987, 72 pp . *J. Polym. Sci. Part C Polym. Lett.* **26,** 414 (1988).
7. Ratner, B. D. & Bryant, S. J. Biomaterials: Where We Have Been and Where We Are Going. *Annu. Rev. Biomed. Eng.* **6,** 41–75 (2004).
8. Alwall, N. Historical Perspective on the Development of the Artificial Kidney. *Artif. Organs* **10,** 86–99 (1986).
9. Mellon, S. J., Liddle, A. D. & Pandit, H. Hip replacement: Landmark surgery in modern medical history. *Maturitas* **75,** 221–226 (2013).
10. Engh Jr, C. A., Young, A. M., Engh Sr, C. A. & Hopper Jr, R. H. Clinical consequences of stress shielding after porous-coated total hip arthroplasty. *Clin. Orthop. Relat. Res.* **417,** 157–163 (2003).
11. Ridzwan, M., Shuib, S., A.Y, H., Ahmed Shokri, A. & Ibrahim, M. Problem of Stress Shielding and Improvement to the Hip Implant Designs: A Review. *Journal of Medical Sciences* **7,** (2007).
12. Nerem, R. M. Tissue engineering in the USA. *Med. Biol. Eng. Comput.* **30,** CE8--CE12 (1992).
13. Langer, R. & Vacanti, J. P. Tissue engineering. *Science (80-.).* **260,** 920 LP-926 (1993).
14. Port, F. OPTN/SRTS annual report. *Sci. Regist. Transpl. Recip. Organ Procure. Transplant. Network, Washington, DC* (2002).
15. Grand view Research. Tissue Engineering Market Size, Share & Trends Report Tissue Engineering Market Size, Share & Trends Analysis Report By Application *(Cord Blood & Cell Banking, Cancer, GI & Gynecology, Dental, Skin/Integumentary, Orthopedics), And Segment Forecasts, 2018* . (2018).
16. Hastings, G. W. Definitions in biomaterials: progress in biomedical engineering 4, Editor: DF Williams. Elsevier, Amsterdam, 1987, pp viii+ 72, US $63.50. (1989).
17. Auffarth, G. U., Golescu, A., Becker, K. A. & Völcker, H. E. Quantification of posterior capsule opacification with round and sharp edge intraocular lenses. *Ophthalmology* **110,** 772–780 (2003).
18. Williams, D. F. On the mechanisms of biocompatibility. *Biomaterials* **29,** 2941–2953 (2008).
19. Williams, D. F. Biocompatibility Pathways: Biomaterials-Induced Sterile Inflammation, Mechanotransduction, and Principles of Biocompatibility Control. *ACS Biomater. Sci. Eng.* **3,** 2–35 (2017).

20. Ratner, B. D. A pore way to heal and regenerate: 21st century thinking on biocompatibility. *Regen. Biomater.* **3,** 107–110 (2016).

21. Lv, S. *et al.* Designed biomaterials to mimic the mechanical properties of muscles. *Nature* **465,** 69 (2010).

22. Ratner, B. D., Hoffman, A. S., Schoen, F. J. & Lemons, J. E. *Biomaterials science: an introduction to materials in medicine*. (Elsevier, 2004).

23. E, Baumgart. Stiffness — an unknown world of mechanical science ? *Injury* **31,** 14–84 (2000).

24. Kim, W. H. & Laird, C. Crack nucleation and stage I propagation in high strain fatigue—II. Mechanism. *Acta Metall.* **26,** 789–799 (1978).

25. Goulet, R. W. *et al.* The relationship between the structural and orthogonal compressive properties of trabecular bone. *J. Biomech.* **27,** 375–389 (1994).

26. Lin, C. Y., Kikuchi, N. & Hollister, S. J. A novel method for biomaterial scaffold internal architecture design to match bone elastic properties with desired porosity. *J. Biomech.* **37,** 623–636 (2004).

27. Teng, Z. *et al.* Nonlinear mechanical property of tracheal cartilage: A theoretical and experimental study. *J. Biomech.* **41,** 1995–2002 (2008).

28. Mattei, L., Di Puccio, F., Piccigallo, B. & Ciulli, E. Lubrication and wear modelling of artificial hip joints: A review. *Tribol. Int.* **44,** 532–549 (2011).

29. Locatelli, F. *et al.* Effect of Membrane Permeability on Survival of Hemodialysis Patients. *J. Am. Soc. Nephrol.* **20,** 645 LP-654 (2009).

30. Mariani, E., Lisignoli, G., Borzì, R. M. & Pulsatelli, L. Biomaterials: Foreign Bodies or Tuners for the Immune Response? *Int. J. Mol. Sci.* **20,** 636 (2019).

31. Velnar, T., Bailey, T. & Smrkolj, V. The Wound Healing Process: An Overview of the Cellular and Molecular Mechanisms. *J. Int. Med. Res.* **37,** 1528–1542 (2009).

32. Roach, P., Farrar, D. & Perry, C. C. Interpretation of Protein Adsorption: Surface-Induced Conformational Changes. *J. Am. Chem. Soc.* **127,** 8168–8173 (2005).

33. Stevens, M. M. & George, J. H. Exploring and engineering the cell surface interface. *Science* **310,** 1135–1138 (2005).

34. Schmidt, D. R., Waldeck, H. & Kao, W. J. in *Biological interactions on materials surfaces* 1–18 (Springer, 2009).

35. Anderson, J. M., Rodriguez, A. & Chang, D. T. Foreign body reaction to biomaterials. *Semin. Immunol.* **20,** 86–100 (2008).

36. Julier, Z., Park, A. J., Briquez, P. S. & Martino, M. M. Promoting tissue regeneration by modulating the immune system. *Acta Biomater.* **53,** 13–28 (2017).

37. Sussman, E. M., Halpin, M. C., Muster, J., Moon, R. T. & Ratner, B. D. Porous Implants Modulate Healing and Induce Shifts in Local Macrophage Polarization in the Foreign Body Reaction. *Ann. Biomed. Eng.* **42,** 1508–1516 (2014).

38. Tian, H., Tang, Z., Zhuang, X., Chen, X. & Jing, X. Biodegradable synthetic polymers: Preparation, functionalization and biomedical application. *Prog. Polym. Sci.* **37,** 237–280 (2012).

39. Nair, L. S. & Laurencin, C. T. Biodegradable polymers as biomaterials. *Prog. Polym. Sci.* **32,** 762–

798 (2007).

40. Rubinstein, M. & Colby, R. H. *Polymer physics*. **23,** (Oxford University Press New York, 2003).

41. Manavitehrani, I. *et al.* Biomedical Applications of Biodegradable Polyesters. *Polymers* **8,** (2016).

42. Castilla-Cortázar, I. *et al.* Hydrolytic and enzymatic degradation of a poly(ε-caprolactone) network. *Polym. Degrad. Stab.* **97,** 1241–1248 (2012).

43. Kannan, R. Y., Salacinski, H. J., Butler, P. E., Hamilton, G. & Seifalian, A. M. Current status of prosthetic bypass grafts: A review. *J. Biomed. Mater. Res. Part B Appl. Biomater.* **74B,** 570–581 (2005).

44. Winnacker, M. Polyamides and their functionalization: recent concepts for their applications as biomaterials. *Biomater. Sci.* **5,** 1230–1235 (2017).

45. Adipurnama, I., Yang, M.-C., Ciach, T. & Butruk-Raszeja, B. Surface modification and endothelialization of polyurethane for vascular tissue engineering applications: a review. *Biomater. Sci.* **5,** 22–37 (2017).

46. Ma, Z., Mao, Z. & Gao, C. Surface modification and property analysis of biomedical polymers used for tissue engineering. *Colloids Surfaces B Biointerfaces* **60,** 137–157 (2007).

47. Williams, R. *Surface modification of biomaterials: Methods analysis and applications*. (Elsevier, 2010).

48. Hollister, S. J. Porous scaffold design for tissue engineering. *Nat. Mater.* **4,** 518–24 (2005).

49. Guvendiren, M., Molde, J., Soares, R. M. D. & Kohn, J. Designing Biomaterials for 3D Printing. *ACS Biomater. Sci. Eng.* **2,** 1679–1693 (2016).

50. Brunette, C. M., Hsu, S. L., Macknight, W. J. & Schneider, N. S. Structural and mechanical properties of polybutadiene-containing polyurethanes. *Polym. Eng. Sci.* **21,** 163–171 (1981).

51. Grasel, T. G. & Cooper, S. L. Surface properties and blood compatibility of polyurethaneureas. *Biomaterials* **7,** 315–328 (1986).

52. Harris, R. F., Joseph, M. D., Davidson, C., Deporter, C. D. & Dais, V. A. Polyurethane elastomers based on molecular weight advanced poly (ethylene ether carbonate) diols. I. Comparison to commercial diols. *J. Appl. Polym. Sci.* **41,** 487–507 (1990).

53. Ionescu, M. *Chemistry and technology of polyols for polyurethanes. . Polymer International* **56,** (2007).

54. Blackwell, J., Nagarajan, M. R. & Hoitink, T. B. Structure of polyurethane elastomers: effect of chain extender length on the structure of MDI/diol hard segments. *Polymer (Guildf).* **23,** 950–956 (1982).

55. Skarja, G. A. & Woodhouse, K. A. Synthesis and characterization of degradable polyurethane elastomers containing an amino acid-based chain extender. *J. Biomater. Sci. Polym. Ed.* **9,** 271–295 (1998).

56. Delpech, M. C. & Coutinho, F. M. B. Waterborne anionic polyurethanes and poly (urethane-urea) s: influence of the chain extender on mechanical and adhesive properties. *Polym. Test.* **19,** 939–952 (2000).

57. Lee, H. S., Wang, Y. K. & Hsu, S. L. Spectroscopic analysis of phase separation behavior of model polyurethanes. *Macromolecules* **20,** 2089–2095 (1987).

58. Nalluri, S. M. *et al.* Hydrophilic polyurethane matrix promotes chondrogenesis of mesenchymal stem cells. *Mater. Sci. Eng. C* **54,** 182–195 (2015).

59. Kojio, K., Kugumiya, S., Uchiba, Y., Nishino, Y. & Furukawa, M. The microphase-separated structure of polyurethane bulk and thin films. *Polym. J.* **41,** 118 (2009).

60. Testouri, A. *et al.* Generation of Crystalline Polyurethane Foams Using Millifluidic Lab-on-a-Chip Technologies. *Adv. Eng. Mater.* **15,** 1086–1098 (2013).

61. Ashida, K. *Polyurethane and related foams: chemistry and technology*. (CRC press, 2006).

62. Inoue, H., Fujimoto, K., Uyama, Y. & Ikada, Y. Ex vivo and in vivo evaluation of the blood compatibility of surface-modified polyurethane catheters. *J. Biomed. Mater. Res. An Off. J. Soc. Biomater. Japanese Soc. Biomater.* **35,** 255–264 (1997).

63. der Giessen, W. J. *et al.* Marked inflammatory sequelae to implantation of biodegradable and nonbiodegradable polymers in porcine coronary arteries. *Circulation* **94,** 1690–1697 (1996).

64. Marois, Y. *et al.* In vivo evaluation of hydrophobic and fibrillar microporous polyetherurethane urea graft. *Biomaterials* **10,** 521–531 (1989).

65. Fabris, H. J. Thermal and oxidative stability of urethanes. *Adv. urethane Sci. Technol.* **6,** 173–196 (1978).

66. Zhao, Q. H. *et al.* Human plasma $α$2-macroglobulin promotes in vitro oxidative stress cracking of Pellethane 2363-80A: In vivo and in vitro correlations. *J. Biomed. Mater. Res.* **27,** 379–388 (1993).

67. Hunt, J. A., Flanagan, B. F., McLaughlin, P. J., Strickland, I. & Williams, D. F. Effect of biomaterial surface charge on the inflammatory reponse: Evaluation of cellular infiltration and TNF$α$ production. *J. Biomed. Mater. Res. An Off. J. Soc. Biomater. Japanese Soc. Biomater.* **31,** 139–144 (1996).

68. Neves, S. C., Pereira, R. F., Araújo, M. & Barrias, C. C. in (eds. Barbosa, M. A. & Martins, M. C. L. B. T.-P. and P. as B. for T. R. and R.) 101–125 (Woodhead Publishing, 2018). doi:https://doi.org/10.1016/B978-0-08-100803-4.00004-8

69. Malafaya, P. B., Silva, G. A. & Reis, R. L. Natural–origin polymers as carriers and scaffolds for biomolecules and cell delivery in tissue engineering applications. *Adv. Drug Deliv. Rev.* **59,** 207–233 (2007).

70. Lee, C. H., Singla, A. & Lee, Y. Biomedical applications of collagen. *Int. J. Pharm.* **221,** 1–22 (2001).

71. Caló, E. & Khutoryanskiy, V. V. Biomedical applications of hydrogels: A review of patents and commercial products. *Eur. Polym. J.* **65,** 252–267 (2015).

72. Gerecht, S. *et al.* Hyaluronic acid hydrogel for controlled self-renewal and differentiation of human embryonic stem cells. *Proc. Natl. Acad. Sci.* **104,** 11298 LP-11303 (2007).

73. Elisseeff, J., Ferran, A., Hwang, S., Varghese, S. & Zhang, Z. The Role of Biomaterials in Stem Cell Differentiation: Applications in the Musculoskeletal System. *Stem Cells Dev.* **15,** 295–303 (2006).

74. Sabir, M. I., Xu, X. & Li, L. A review on biodegradable polymeric materials for bone tissue engineering applications. *J. Mater. Sci.* **44,** 5713–5724 (2009).

75. Lehn, J.-M. Supramolecular Chemistry—Scope and Perspectives Molecules, Supermolecules, and Molecular Devices (Nobel Lecture). *Angew. Chemie Int. Ed. English* **27,** 89–112 (1988).

76. Webber, M. J., Appel, E. A., Meijer, E. W. & Langer, R. Supramolecular biomaterials. *Nat. Mater.* **15,** 13 (2015).

77. Kisiday, J. *et al.* Self-assembling peptide hydrogel fosters chondrocyte extracellular matrix production and cell division: Implications for cartilage tissue repair. *Proc. Natl. Acad. Sci.* **99,** 9996 LP-10001 (2002).

78. Ellis-Behnke, R. G. *et al.* Nano neuro knitting: Peptide nanofiber scaffold for brain repair and axon regeneration with functional return of vision. *Proc. Natl. Acad. Sci. U. S. A.* **103,** 5054 LP-5059 (2006).

79. Kutz, M. & others. *Standard handbook of biomedical engineering and design*. (McGraw-Hill New York, 2003).

80. Thomas, S., Balakrishnan, P. & Sreekala, M. S. *Fundamental Biomaterials: Ceramics*. (Woodhead Publishing, 2018).

81. Rezwan, K., Chen, Q. Z., Blaker, J. J. & Boccaccini, A. R. Biodegradable and bioactive porous polymer/inorganic composite scaffolds for bone tissue engineering. *Biomaterials* **27,** 3413–3431 (2006).

82. Ducheyne, P., Mauck, R. L. & Smith, D. H. Biomaterials in the repair of sports injuries. *Nat. Mater.* **11,** 652 (2012).

83. Hench, L. L. The story of Bioglass®. *J. Mater. Sci. Mater. Med.* **17,** 967–978 (2006).

84. de Bruijn, J. D., Bovell, Y. P., Davies, J. E. & van Blitterswijk, C. A. Osteoclastic resorption of calcium phosphates is potentiated in postosteogenic culture conditions. *J. Biomed. Mater. Res.* **28,** 105–112 (1994).

85.: Paramsothy, Muralidharan; Ramakrishna, S. Biodegradable Materials for Clinical Applications: A Review. *Rev. Adv. Sci. Eng.* **4,** (2015).

86. Doi, Y., Shibutani, T., Moriwaki, Y., Kajimoto, T. & Iwayama, Y. Sintered carbonate apatites as bioresorbable bone substitutes. *J. Biomed. Mater. Res.* **39,** 603–610 (1998).

87. Gotman, I. Characteristics of metals used in implants. *J. Endourol.* **11,** 383–389 (1997).

88. Welsch, G., Boyer, R. & Collings, E. W. *Materials properties handbook: titanium alloys*. (ASM international, 1993).

89. Duerig, T., Pelton, A. & Stöckel, D. An overview of nitinol medical applications. *Mater. Sci. Eng. A* **273–275,** 149–160 (1999).

90. Kunčická, L., Kocich, R. & Lowe, T. C. Advances in metals and alloys for joint replacement. *Prog. Mater. Sci.* **88,** 232–280 (2017).

91. Liu, X., Chu, P. K. & Ding, C. Surface modification of titanium, titanium alloys, and related materials for biomedical applications. *Mater. Sci. Eng. R Reports* **47,** 49–121 (2004).

92. Zheng, Y. F., Gu, X. N. & Witte, F. Biodegradable metals. *Mater. Sci. Eng. R Reports* **77,** 1–34 (2014).

93. Yang, K. *et al.* Bio-Functional Design, Application and Trends in Metallic Biomaterials. *International Journal of Molecular Sciences* **19,** (2018).

94. Brandt, M. *Laser Additive Manufacturing: Materials, Design, Technologies, and Applications*. (Woodhead Publishing, 2016).

95. Murr, L. E. *et al.* Metal fabrication by additive manufacturing using laser and electron beam melting technologies. *J. Mater. Sci. Technol.* **28,** 1–14 (2012).

96. Kolken, H. M. A. *et al.* Rationally designed meta-implants: A combination of auxetic and conventional meta-biomaterials. *Mater. Horizons* **5,** 28–35 (2018).

97. Madry, H. *et al.* Barriers and strategies for the clinical translation of advanced orthopaedic tissue engineering protocols. *Eur Cell Mater* **27,** 17–21 (2014).

98. Webber, M. J., Khan, O. F., Sydlik, S. A., Tang, B. C. & Langer, R. A Perspective on the Clinical Translation of Scaffolds for Tissue Engineering. *Ann. Biomed. Eng.* **43,** 641–656 (2015).

99. Kon, E., Roffi, A., Filardo, G., Tesei, G. & Marcacci, M. Scaffold-based cartilage treatments: with or without cells? A systematic review of preclinical and clinical evidence. *Arthrosc. J. Arthrosc. Relat. Surg.* **31,** 767–775 (2015).

100. Naughton, G., Mansbridge, J. & Gentzkow, G. A Metabolically Active Human Dermal Replacement for the Treatment of Diabetic Foot Ulcers. *Artif. Organs* **21,** 1203–1210 (1997).

101. Falanga, V. & Sabolinski, M. A bilayered living skin construct (APLIGRAF®) accelerates complete closure of hard-to-heal venous ulcers. *Wound Repair Regen.* **7,** 201–207 (1999).

102. Machens, H.-G., Berger, A. C. & Mailaender, P. Bioartificial skin. *Cells Tissues Organs* **167,** 88–94 (2000).

103. Debry, C., Vrana, N. E. & Dupret-Bories, A. Implantation of an Artificial Larynx after Total Laryngectomy. *N. Engl. J. Med.* **376,** 97–98 (2017).

104. Leroy, A. *et al.* Actifit® polyurethane meniscal scaffold: MRI and functional outcomes after a minimum follow-up of 5 years. *Orthop. Traumatol. Surg. Res.* **103,** 609–614 (2017).

105. Kishan, A. P. & Cosgriff-Hernandez, E. M. Recent advancements in electrospinning design for tissue engineering applications: A review. *J. Biomed. Mater. Res. Part A* **105,** 2892–2905 (2017).

106. Haider, A., Haider, S. & Kang, I.-K. A comprehensive review summarizing the effect of electrospinning parameters and potential applications of nanofibers in biomedical and biotechnology. *Arab. J. Chem.* **11,** 1165–1188 (2018).

107. Agarwal, S., Wendorff, J. H. & Greiner, A. Use of electrospinning technique for biomedical applications. *Polymer (Guildf).* **49,** 5603–5621 (2008).

108. Müller, K. *et al.* Polyelectrolyte functionalization of electrospun fibers. *Chem. Mater.* **18,** 2397–2403 (2006).

109. Kenawy, E.-R. *et al.* Release of tetracycline hydrochloride from electrospun poly (ethylene-co-vinylacetate), poly (lactic acid), and a blend. *J. Control. release* **81,** 57–64 (2002).

110. Yu, D.-G. *et al.* Oral fast-dissolving drug delivery membranes prepared from electrospun polyvinylpyrrolidone ultrafine fibers. *Nanotechnology* **20,** 55104 (2009).

111. Powell, H. M. & Boyce, S. T. Engineered Human Skin Fabricated Using Electrospun Collagen–PCL Blends: Morphogenesis and Mechanical Properties. *Tissue Eng. Part A* **15,** 2177–2187 (2009).

112. Shields, K. J., Beckman, M. J., Bowlin, G. L. & Wayne, J. S. Mechanical Properties and Cellular Proliferation of Electrospun Collagen Type II. *Tissue Eng.* **10,** 1510–1517 (2004).

113. Stachewicz, U., Szewczyk, P. K., Kruk, A., Barber, A. H. & Czyrska-Filemonowicz, A. Pore shape and size dependence on cell growth into electrospun fiber scaffolds for tissue engineering: 2D and 3D analyses using SEM and FIB-SEM tomography. *Mater. Sci. Eng. C* **95,** 397–408 (2019).

114. Gizaw, M., Faglie, A., Pieper, M., Poudel, S. & Chou, S.-F. The Role of Electrospun Fiber Scaffolds in Stem Cell Therapy for Skin Tissue Regeneration. *Med One* **4,** (2019).

115. Kuo, T.-Y. *et al.* Incorporation and selective removal of space-forming nanofibers to enhance the permeability of cytocompatible nanofiber membranes for better cell growth. *J. Taiwan Inst. Chem. Eng.* **91,** 146–154 (2018).

116. Ovsianikov, A., Yoo, J. & Mironov, V. *3D Printing and Biofabrication*. (Springer, 2018).

117. Yeo, M., Lee, H. & Kim, G. H. Combining a micro/nano-hierarchical scaffold with cell-printing of myoblasts induces cell alignment and differentiation favorable to skeletal muscle tissue regeneration. *Biofabrication* **8,** 35021 (2016).

118. Castilho, M. *et al.* Fabrication of computationally designed scaffolds by low temperature 3D printing. *Biofabrication* **5,** 35012 (2013).

119. Bose, S., Vahabzadeh, S. & Bandyopadhyay, A. Bone tissue engineering using 3D printing. *Mater. today* **16,** 496–504 (2013).

120. Liu, A. *et al.* 3D printing surgical implants at the clinic: a experimental study on anterior cruciate ligament reconstruction. *Sci. Rep.* **6,** 21704 (2016).

121. Sun, A. X., Lin, H., Beck, A. M., Kilroy, E. J. & Tuan, R. S. Projection stereolithographic fabrication of human adipose stem cell-incorporated biodegradable scaffolds for cartilage tissue engineering. *Front. Bioeng. Biotechnol.* **3,** 115 (2015).

122. Cui, X., Boland, T., DD'Lima, D. & K Lotz, M. Thermal inkjet printing in tissue engineering and regenerative medicine. *Recent Pat. Drug Deliv. Formul.* **6,** 149–155 (2012).

123. Di Bella, C., Fosang, A., Donati, D. M., Wallace, G. G. & Choong, P. F. M. 3D bioprinting of cartilage for orthopedic surgeons: reading between the lines. *Front. Surg.* **2,** 39 (2015).

124. Mosadegh, B., Xiong, G., Dunham, S. & Min, J. K. Current progress in 3D printing for cardiovascular tissue engineering. *Biomed. Mater.* **10,** 34002 (2015).

125. Janik, H. & Marzec, M. A review: Fabrication of porous polyurethane scaffolds. *Mater. Sci. Eng. C* **48,** 586–591 (2015).

126. Choi, S.-W., Zhang, Y., MacEwan, M. R. & Xia, Y. Neovascularization in Biodegradable Inverse Opal Scaffolds with Uniform and Precisely Controlled Pore Sizes. *Adv. Healthc. Mater.* **2,** 145–154 (2012).

127. Shahriari, D., Koffler, J. Y., Tuszynski, M. H., Campana, W. M. & Sakamoto, J. S. Hierarchically ordered porous and high-volume polycaprolactone microchannel scaffolds enhanced axon growth in transected spinal cords. *Tissue Eng. Part A* **23,** 415–425 (2017).

128. Murphy, W. L., Dennis, R. G., Kileny, J. L. & Mooney, D. J. Salt fusion: an approach to improve pore interconnectivity within tissue engineering scaffolds. *Tissue Eng.* **8,** 43–52 (2002).

129. Otsuki, B. *et al.* Pore throat size and connectivity determine bone and tissue ingrowth into porous implants: Three-dimensional micro-CT based structural analyses of porous bioactive titanium implants. *Biomaterials* **27,** 5892–5900 (2006).

130. Somo, S. I. *et al.* Pore Interconnectivity Influences Growth Factor-Mediated Vascularization in Sphere-Templated Hydrogels. *Tissue Eng. Part C Methods* **21,** 773–85 (2015).

131. Descamps, M. *et al.* Manufacture of macroporous β-tricalcium phosphate bioceramics. *J. Eur. Ceram. Soc.* **28,** 149–157 (2008).

132. Silbert, L. E. Jamming of frictional spheres and random loose packing. *Soft Matter* **6,** 2918–2924 (2010).

133. Linnes, M. P., Ratner, B. D. & Giachelli, C. M. A fibrinogen-based precision microporous scaffold for tissue engineering. *Biomaterials* **28,** 5298–5306 (2007).

134. Zhao, K., Tang, Y. F., Qin, Y. S. & Luo, D. F. Polymer template fabrication of porous hydroxyapatite scaffolds with interconnected spherical pores. *J. Eur. Ceram. Soc.* **31,** 225–229 (2011).

135. Jacobs, L. J. M., Kemmere, M. F. & Keurentjes, J. T. F. Sustainable polymer foaming using high pressure carbon dioxide: a review on fundamentals, processes and applications. *Green Chem.* **10,** 731–738 (2008).

136. Costantini, M. & Barbetta, A. in (eds. Deng, Y. & Kuiper, J. B. T.-F. 3D T. E. S.) 127–149 (Woodhead Publishing, 2018). doi:https://doi.org/10.1016/B978-0-08-100979-6.00006-9

137. Deb, P., Deoghare, A. B., Borah, A., Barua, E. & Lala, S. Das. Scaffold Development Using Biomaterials: A Review. (2017).

138. Dehli, F., Rebers, L., Stubenrauch, C. & Southan, A. Highly ordered gelatin methacryloyl hydrogel foams with tunable pore size. *Biomacromolecules* (2019).

139. Drenckhan, W. & Saint-Jalmes, A. The science of foaming. *Adv. Colloid Interface Sci.* **222,** 228–259 (2015).

140. Isabelle Cantat, Sylvie Cohen-Addad, Florence Elias, Francois Graner, Reinhard Hohler, Olivier Pitois, Florence Rouyer, Arnaud Saint-Jalmes, Ruth Flatman, S. C. *Foams: Structure and Dynamics*. (Oxford University Press, 2013).

141. Andrieux, S., Drenckhan, W. & Stubenrauch, C. Highly ordered biobased scaffolds: From liquid to solid foams. *Polymer (Guildf).* **126,** 425–431 (2017).

142. Andrieux, S., Quell, A., Stubenrauch, C. & Drenckhan, W. Liquid foam templating--A route to tailor-made polymer foams. *Adv. Colloid Interface Sci.* (2018).

143. Costantini, M. *et al.* Correlation between porous texture and cell seeding efficiency of gas foaming and microfluidic foaming scaffolds. *Mater. Sci. Eng. C* **62,** 668–677 (2016).

144. Costantini, M. *et al.* Microfluidic Foaming: A Powerful Tool for Tailoring the Morphological and Permeability Properties of Sponge-like Biopolymeric Scaffolds. *ACS Appl. Mater. Interfaces* **7,** 23660–23671 (2015).

145. Rossmy, G. R., Kollmeier, H. J., Lidy, W., Schator, H. & Wiemann, M. Cell-opening in one-shot flexible polyether based polyurethane foams. The Role of Silicone Surfactant and its Foundation in the Chemistry of Foam Formation. *J. Cell. Plast.* **13,** 26–35 (1977).

146. Yasunaga, K., Neff, R. A., Zhang, X. D. & Macosko, C. W. Study of Cell Opening in Flexible Polyurethane Foam. *J. Cell. Plast.* **32,** 427–448 (1996).

147. Hay, E. D. *Cell biology of extracellular matrix*. (Springer Science & Business Media, 2013).

148. Bellis, S. L. Advantages of RGD peptides for directing cell association with biomaterials. *Biomaterials* **32,** 4205–4210 (2011).

149. Underwood, P. A. & Bennett, F. A. A comparison of the biological activities of the cell-adhesive proteins vitronectin and fibronectin. *J. Cell Sci.* **93,** 641–649 (1989).

150. Urry, D. W. *et al.* Elastin: a representative ideal protein elastomer. *Philos. Trans. R. Soc. B Biol.*

Sci. **357,** 169 (2002).

151. Parry, D. A. D. The molecular fibrillar structure of collagen and its relationship to the mechanical properties of connective tissue. *Biophys. Chem.* **29,** 195–209 (1988).

152. Höök, M., Kjellén, L., Johansson, S. & Robinson, J. Cell-surface glycosaminoglycans. *Annu. Rev. Biochem.* **53,** 847–869 (1984).

153. Bi, Y. *et al.* Extracellular matrix proteoglycans control the fate of bone marrow stromal cells. *J. Biol. Chem.* **280,** 30481–30489 (2005).

154. Kalluri, R. Basement membranes: structure, assembly and role in tumour angiogenesis. *Nat. Rev. Cancer* **3,** 422 (2003).

155. Timpl, R. Structure and biological activity of basement membrane proteins. *Eur. J. Biochem.* **180,** 487–502 (1989).

156. Guilak, F. *et al.* Control of Stem Cell Fate by Physical Interactions with the Extracellular Matrix. *Cell Stem Cell* **5,** 17–26 (2009).

157. Wilson, C. J., Clegg, R. E., Leavesley, D. I. & Pearcy, M. J. Mediation of Biomaterial–Cell Interactions by Adsorbed Proteins: A Review. *Tissue Eng.* **11,** 1–18 (2005).

158. Wojciechowski, P., Ten Hove, P. & Brash, J. L. Phenomenology and mechanism of the transient adsorption of fibrinogen from plasma (Vroman effect). *J. Colloid Interface Sci.* **111,** 455–465 (1986).

159. Freeman, S. *Biological Science, 2nd*. (Pearson Prentice Hall, 2005).

160. Huettner, N., Dargaville, T. R. & Forget, A. Discovering Cell-Adhesion Peptides in Tissue Engineering: Beyond RGD. *Trends Biotechnol.* **36,** 372–383 (2018).

161. Zamir, E. & Geiger, B. Molecular complexity and dynamics of cell-matrix adhesions. *J. Cell Sci.* **114,** 3583 LP-3590 (2001).

162. Galbraith, C. G., Yamada, K. M. & Sheetz, M. P. The relationship between force and focal complex development. *J. Cell Biol.* **159,** 695 LP-705 (2002).

163. Ferreira, S. A. *et al.* Bi-directional cell-pericellular matrix interactions direct stem cell fate. *Nat. Commun.* **9,** 4049 (2018).

164. Vining, K. H. *et al.* Synthetic Light-Curable Polymeric Materials Provide a Supportive Niche for Dental Pulp Stem Cells. *Adv. Mater.* **30,** 1704486 (2017).

165. Agashe, M., Raut, V., Stuart, S. J. & Latour, R. A. Molecular simulation to characterize the adsorption behavior of a fibrinogen \$γ\$-chain fragment. *Langmuir* **21,** 1103–1117 (2005).

166. Privalov, P. L. & Gill, S. J. in *Advances in protein chemistry* **39,** 191–234 (Elsevier, 1988).

167. Chen, S., Li, L., Zhao, C. & Zheng, J. Surface hydration: Principles and applications toward low-fouling/nonfouling biomaterials. *Polymer (Guildf).* **51,** 5283–5293 (2010).

168. Krishnan, S., Weinman, C. J. & Ober, C. K. Advances in polymers for anti-biofouling surfaces. *J. Mater. Chem.* **18,** 3405–3413 (2008).

169. Maheshwari, G., Brown, G., Lauffenburger, D. A., Wells, A. & Griffith, L. G. Cell adhesion and motility depend on nanoscale RGD clustering. *J Cell Sci* **113,** 1677–1686 (2000).

170. Tsai, W.-B., Chen, W.-T., Chien, H.-W., Kuo, W.-H. & Wang, M.-J. Poly(dopamine) coating of scaffolds for articular cartilage tissue engineering. *Acta Biomater.* **7,** 4187–4194 (2011).

171. Ying, L. *et al.* Immobilization of galactose ligands on acrylic acid graft-copolymerized poly (ethylene terephthalate) film and its application to hepatocyte culture. *Biomacromolecules* **4,** 157–165 (2003).

172. Zhu, H. *et al.* Surface engineering of poly (DL-lactic acid) by entrapment of alginate-amino acid derivatives for promotion of chondrogenesis. *Biomaterials* **23,** 3141–3148 (2002).

173. Washburn, N. R., Yamada, K. M., Simon Jr, C. G., Kennedy, S. B. & Amis, E. J. High-throughput investigation of osteoblast response to polymer crystallinity: influence of nanometer-scale roughness on proliferation. *Biomaterials* **25,** 1215–1224 (2004).

174. Dalby, M. J. *et al.* The control of human mesenchymal cell differentiation using nanoscale symmetry and disorder. *Nat. Mater.* **6,** 997 (2007).

175. Dalby, M. J., Riehle, M. O., Johnstone, H. J. H., Affrossman, S. & Curtis, A. S. G. Polymer-Demixed Nanotopography: Control of Fibroblast Spreading and Proliferation. *Tissue Eng.* **8,** 1099–1108 (2002).

176. Teixeira, A. I., Abrams, G. A., Bertics, P. J., Murphy, C. J. & Nealey, P. F. Epithelial contact guidance on well-defined micro-and nanostructured substrates. *J. Cell Sci.* **116,** 1881–1892 (2003).

177. Karuri, N. W., Nealey, P. F., Murphy, C. J. & Albrecht, R. M. Structural organization of the cytoskeleton in SV40 human corneal epithelial cells cultured on nano-and microscale grooves. *Scanning* **30,** 405–413 (2008).

178. Nikkhah, M., Edalat, F., Manoucheri, S. & Khademhosseini, A. Engineering microscale topographies to control the cell-substrate interface. *Biomaterials* **33,** 5230–5246 (2012).

179. Engler, A. J., Sen, S., Sweeney, H. L. & Discher, D. E. Matrix Elasticity Directs Stem Cell Lineage Specification. *Cell* **126,** 677–689 (2006).

180. Pek, Y. S., Wan, A. C. A. & Ying, J. Y. The effect of matrix stiffness on mesenchymal stem cell differentiation in a 3D thixotropic gel. *Biomaterials* **31,** 385–391 (2010).

181. Lozoya, O. A. *et al.* Regulation of hepatic stem/progenitor phenotype by microenvironment stiffness in hydrogel models of the human liver stem cell niche. *Biomaterials* **32,** 7389–7402 (2011).

182. Trappmann, B. *et al.* Extracellular-matrix tethering regulates stem-cell fate. *Nat. Mater.* **11,** 642 (2012).

183. Higuchi, A., Ling, Q.-D., Chang, Y., Hsu, S.-T. & Umezawa, A. Physical Cues of Biomaterials Guide Stem Cell Differentiation Fate. *Chem. Rev.* **113,** 3297–3328 (2013).

184. Chaudhuri, O. *et al.* Hydrogels with tunable stress relaxation regulate stem cell fate and activity. *Nat. Mater.* **15,** 326 (2015).

185. Ranga, A. *et al.* 3D niche microarrays for systems-level analyses of cell fate. *Nat. Commun.* **5,** 4324 (2014).

186. Ingber, D. E. Tensegrity II. How structural networks influence cellular information processing networks. *J. Cell Sci.* **116,** 1397 LP-1408 (2003).

187. Ingber, D. E. Tensegrity: the architectural basis of cellular mechanotransduction. *Annu. Rev. Physiol.* **59,** 575–599 (1997).

188. Antoni, D., Burckel, H., Josset, E. & Noel, G. Three-dimensional cell culture: a breakthrough in vivo. *Int. J. Mol. Sci.* **16,** 5517–5527 (2015).

189. Van Tienen, T. G. *et al.* Tissue ingrowth and degradation of two biodegradable porous polymers with different porosities and pore sizes. *Biomaterials* **23,** 1731–1738 (2002).

190. Tienen, T. G. *et al.* Replacement of the knee meniscus by a porous polymer implant: a study in dogs. *Am. J. Sports Med.* **34,** 64–71 (2006).

191. Matsiko, A., Gleeson, J. P. & O'Brien, F. J. Scaffold Mean Pore Size Influences Mesenchymal Stem Cell Chondrogenic Differentiation and Matrix Deposition. *Tissue Eng. Part A* **21,** 486–497 (2014).

192. Yang, J. *et al.* Fabrication and surface modification of macroporous poly (L-lactic acid) and poly (L-lactic-co-glycolic acid)(70/30) cell scaffolds for human skin fibroblast cell culture. *J. Biomed. Mater. Res. An Off. J. Soc. Biomater. Japanese Soc. Biomater. Aust. Soc. Biomater. Korean Soc. Biomater.* **62,** 438–446 (2002).

193. Wang, H., Pieper, J., Péters, F., van Blitterswijk, C. A. & Lamme, E. N. Synthetic scaffold morphology controls human dermal connective tissue formation. *J. Biomed. Mater. Res. Part A* **74A,** 523–532 (2005).

194. Bružauskaitė, I., Bironaitė, D., Bagdonas, E. & Bernotienė, E. Scaffolds and cells for tissue regeneration: different scaffold pore sizes—different cell effects. *Cytotechnology* **68,** 355–369 (2016).

195. Feng, B. *et al.* The effect of pore size on tissue ingrowth and neovascularization in porous bioceramics of controlled architecture in vivo. *Biomed. Mater.* **6,** 15007 (2011).

196. Madden, L. R. *et al.* Proangiogenic scaffolds as functional templates for cardiac tissue engineering. *Proc. Natl. Acad. Sci. U. S. A.* **107,** 15211–6 (2010).

197. Marshall, A. J. Biomaterials with tightly controlled pore size that promote vascular in-growth. *Polym. Prepr.* **45,** 100–101 (2004).

198. Karande, T. S., Ong, J. L. & Agrawal, C. M. Diffusion in musculoskeletal tissue engineering scaffolds: design issues related to porosity, permeability, architecture, and nutrient mixing. *Ann. Biomed. Eng.* **32,** 1728–1743 (2004).

199. Descamps, M. *et al.* Manufacture of macroporous ??-tricalcium phosphate bioceramics. *J. Eur. Ceram. Soc.* **28,** 149–157 (2008).

200. Lutzweiler, G. *et al.* Modulation of Cellular Colonization of Porous Polyurethane scaffolds via the control of pore interconnection size and nanoscale surface modifications. *ACS Appl. Mater. Interfaces* (2019).

201. Xiao, X. *et al.* The promotion of angiogenesis induced by three-dimensional porous beta-tricalcium phosphate scaffold with different interconnection sizes via activation of PI3K/Akt pathways. *Sci. Rep.* **5,** 9409 (2015).

202. Choi, S.-W., Zhang, Y. & Xia, Y. Three-dimensional scaffolds for tissue engineering: the importance of uniformity in pore size and structure. *Langmuir* **26,** 19001–19006 (2010).

203. Kemppainen, J. M. & Hollister, S. J. Differential effects of designed scaffold permeability on chondrogenesis by chondrocytes and bone marrow stromal cells. *Biomaterials* **31,** 279–287 (2010).

204. Costantini, M. *et al.* Correlation between porous texture and cell seeding efficiency of gas foaming and micro fluidic foaming scaffolds. **62,** 668–677 (2016).

205. Rumpler, M., Woesz, A., Dunlop, J. W. C., van Dongen, J. T. & Fratzl, P. The effect of geometry

on three-dimensional tissue growth. *J. R. Soc. Interface* **5,** 1173–1180 (2008).

206. Guyot, Y. *et al.* A computational model for cell/ECM growth on 3D surfaces using the level set method: a bone tissue engineering case study. *Biomech. Model. Mechanobiol.* **13,** 1361–1371 (2014).

207. Bidan, C. M. *et al.* Geometry as a Factor for Tissue Growth: Towards Shape Optimization of Tissue Engineering Scaffolds. *Adv. Healthc. Mater.* **2,** 186–194 (2013).

208. Gibson, L. J. & Ashby, M. F. *Cellular solids: structure and properties*. (Cambridge university press, 1999).

209. Haiying, Y., Howard, W. M., Paul, H. W. & Shang-you, Y. Effect of Porosity and Pore Size on Microstructures and Mechanical Properties of Poly-e-Caprolactone-Hydroxyapatite Composites. *J. Biomed. Mater. Res. Part B Appl. Biomater.* **86,** 541–547 (2008).

210. Sobral, J. M., Caridade, S. G., Sousa, R. A., Mano, J. F. & Reis, R. L. Three-dimensional plotted scaffolds with controlled pore size gradients: effect of scaffold geometry on mechanical performance and cell seeding efficiency. *Acta Biomater.* **7,** 1009–1018 (2011).

211. Murphy, W. L., Kohn, D. H. & Mooney, D. J. Growth of continuous bonelike mineral within porous poly (lactide-co-glycolide) scaffolds in vitro. *J. Biomed. Mater. Res. An Off. J. Soc. Biomater. Japanese Soc. Biomater.* **50,** 50–58 (2000).

212. Hook, A. L. *et al.* High throughput methods applied in biomaterial development and discovery. *Biomaterials* **31,** 187–198 (2010).

Chapter 2. Materials and methods

2.1 *Introduction*

We provide here the main experimental techniques which were used in this Thesis. We describe the « sphere templating » approach (Chapter 3) and the associated characterization techniques. We present also the cell seeding methods that were developed to allow the cell to penetrate inside the porous scaffold (Section 2.7.1). Finally, we expose the formulation used to synthesize polyurethane that was used along the whole thesis as well as the relevant parameters that were varied to modulate the PU properties (Section 2.7).

2.2 *Generation of paraffin spheres*

We generated the paraffin spheres by a dispersion method inspired by Ma *et al.*[1]. We used paraffin with a molecular weight of 341.451 g/mol from Fischer Scientific (CAS 8002-74-2). Its melting point is given at 58-62°C, which is confirmed by our DSC measurements shown in Figure 2-1. The endothermic peak at 55-67 °C corresponds to the melting point which is in accordance with the range given by the supplier. However, one can also see a slight shoulder in the curve around 40°C which indicates that some paraffin chains may have started to melt already before the melting point. All our experiments were typically conducted between 35 and 42°C, thus, even if our working temperatures were below the melting transition, due to the polydisperse nature of paraffin, we expected that some hydrocarbon chains may have melted at these temperatures.

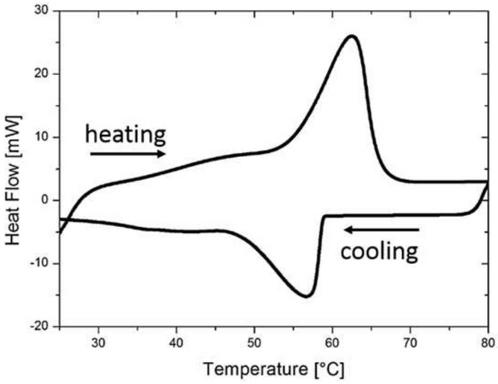

Figure 2-1: DSC curve of the paraffin wax used for the sphere templating.

To generate the spheres, we added 10 g of paraffin to a 400 mL solution of 70 °C osmosed water with 3 g of Polyvinyl alcohol (PVA) (Sigma, CAS 9002-89-5 , MW 31 000- 50 000 89% hydrolysate). The mixture was kept in an 800 mL beaker as sketched Figure 2-2, and was vigorously stirred with a magnet (35 mm length) for 10 min at different rotation velocities (400, 700, 950 and 1200 rpm). Higher rotation speeds of 3200 and 4200 rpm are obtained using an ultra-Turrax (IKA ®T25). Since the paraffin is liquid at the chosen temperature, the vigorous stirring creates a paraffin-in-oil emulsion whose drops are stabilised against coalescence by the PVA. With increasing rotation speed, the paraffin is broken into increasingly smaller drops, leading to smaller spheres after solidification.

We quenched the emulsion by the addition of 400 mL of 4 °C osmosed water, leading to nearly instantaneous solidification of the liquid drops into spherical beads as schematically shown in Figure 2-3a. We noticed that with decreasing bead size, the surface of the spheres roughens. This may be due to the increasing surface-to-volume ratio and potentially associated shrinkage phenomena.

Using numerical microscopy combined with image analysis (Section 2.12.4) we determined the size distributions of the obtained paraffin spheres. Figure 2-3d shows examples of size distributions obtained for two different rotation speeds (400, 950 rpm), putting clearly in evidence the systematic decrease of the sphere radius R with rotation speed. Since the distributions were quite polydisperse, we reduced the polydispersity using stainless steel sieves with different mesh sizes (32, 50, 80, 125, 200, 300 µm) to select the desired size ranges. The sieving was applied directly to the liquid sphere dispersion by sieving progressively from the largest to the smallest mesh size. Figure 2-3e and f show examples of the narrow distributions obtained after sieving together with the resulting average sphere radii $\langle R \rangle$. We mostly used paraffin beads obtained at 400 and 950 rpm. For the interested reader we provide the size distributions of paraffin spheres for higher stirring rates in Figure 3-11.

After sieving, the paraffin spheres were left to dry under a fume hood for 24 hours.

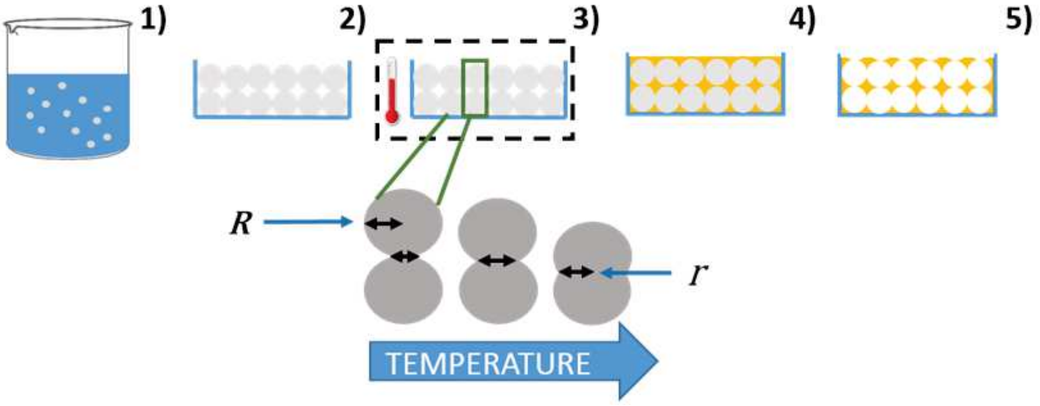

Figure 2-2: Scheme of the sphere templating approach to generate PU scaffolds. Paraffin spheres are first generated by quenching a paraffin emulsion 1), the obtained paraffin spheres are then sieved, dried and packed in a mould 2), the mould is subsequently placed in an oven to promote the sintering of the spheres and to obtain the negative template 3), the PU is then poured on the top of the template and left to infiltrate between the spheres and to solidify 4). Finally, the paraffin spheres are selectively dissolved to leave an interconnected porous network.

2.3 Determination of the sphere size distribution

We used the numerical microscope Keyence VHX-5000 (Section 2.12.4) to obtain the sphere size distributions. For the imaging, we dispersed about 1 mg of dried paraffin spheres on a microscope slide and placed it on the transparent tray of the microscope. Images were recorded with the transmitted lighting mode. For the image analysis, we used the software supplied with the microscope. First we applied the "brightness" mode to select the desired image area and chose the most appropriate threshold level which allows to identify (Figure 2-3a) and to isolate spheres which are stuck together (Figure 2-3b). We further applied the "separation tool" to separate spheres contained in clusters, as shown in Figure 2-3c. After detecting at least 800 spheres, the size distributions are expressed as the probability density function defined by

$$\mathrm{PDF} = \frac{n(R < R_b < R + \Delta R)}{N \Delta R}. \tag{4}$$

Here, R_b is the measured sphere radius and $n(R < R_b < R + \Delta R)$ is the number of spheres having a radius between R and $R + \Delta R$, where ΔR is the bin width of the frequency count histogram. N stands for the total number of particles. We use OriginPro 8 software for the data treatment. The obtained PDFs are then fitted to Gaussian distributions, as shown in Figure 2-3d-f.

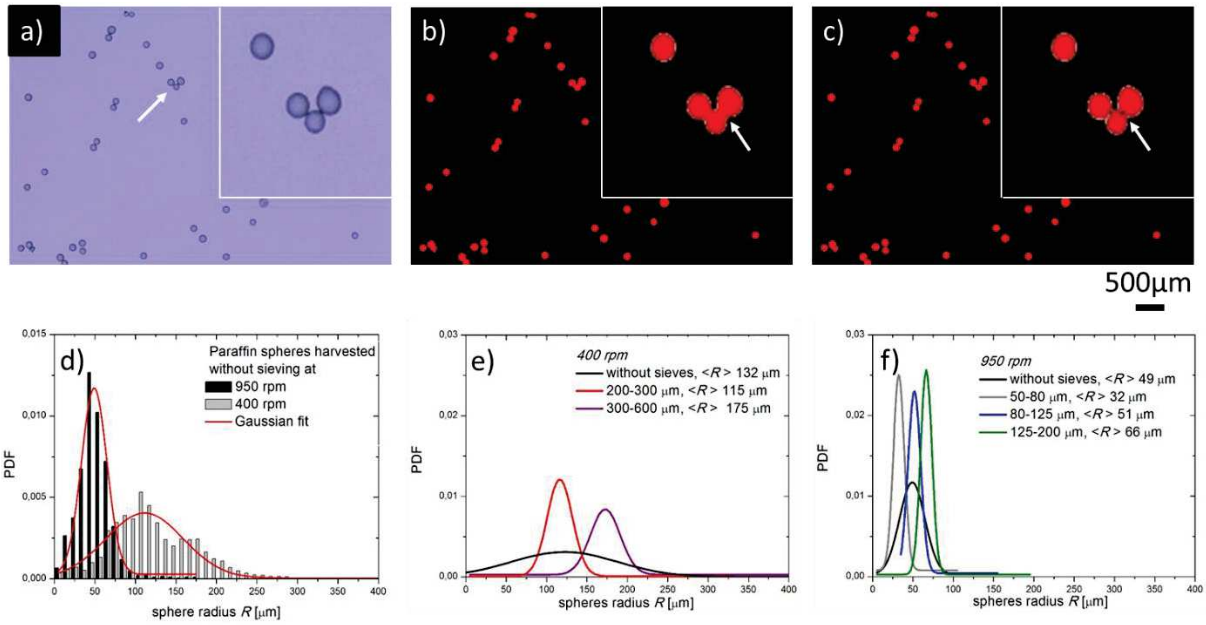

Figure 2-3: a) Photograph of paraffin spheres taken under a microscope. b) Image thresholded with selected spheres in red. c) Same image after using the separation tool provided with the Keyence Software. The inset shows a zoom on the selected group of spheres. d) Probability density function (PDF) of the radii of the paraffin spheres and the corresponding Gaussian fits for two different rotation speeds. e-f) PDF of selected sphere ranges after sieving for different rotation speeds and sieve dimensions.

2.4 Sintering procedure

We added 3 g of paraffin spheres with given average radius $<R>$ (Section 2.2) to a petri dish (34 mm in diameter, VWR) and pack them manually by tapping (Figure 2-2-2). The height of the entire template was roughly 7 mm. Small holes were drilled into the bottom and on the sides of the Petri dish beforehand to help air removal upon polymer filling. We initially close the holes from the outside with parafilm to prevent the loss of paraffin spheres. The Petri dishes containing the paraffin spheres were then put in an oven (Memmert) at temperatures ranging from 35°C to 42°C for sintering times up to 18 hours (Figure 2-2-3). We pre-heated the oven for 24 hours to ensure stable temperatures. Once the required sintering time was reached, the mold was cooled down at room temperature and we removed the parafilm.

Using a microprocessor thermometer (HANNA instruments, HI 8757), we characterised the evolution of the temperature in the oven and at the center of the sphere template. As shown in Figure 2-4, the fluctuations of the oven temperature were of the order of 0.5 °C, and the effective temperature measurement was always 2 °C below the temperature indicated by the oven. All the temperatures given in this thesis are the ones actually measured in the oven. One noticed that it took about 60 min for the sphere packing to reach the temperature of the oven. This was expected since the template contains a lot of air which is a good insulator. In order to avoid misinterpretation of the data due to this initial equilibration time, we characterised the template morphology for samples which spent at least 2 hours in the oven.

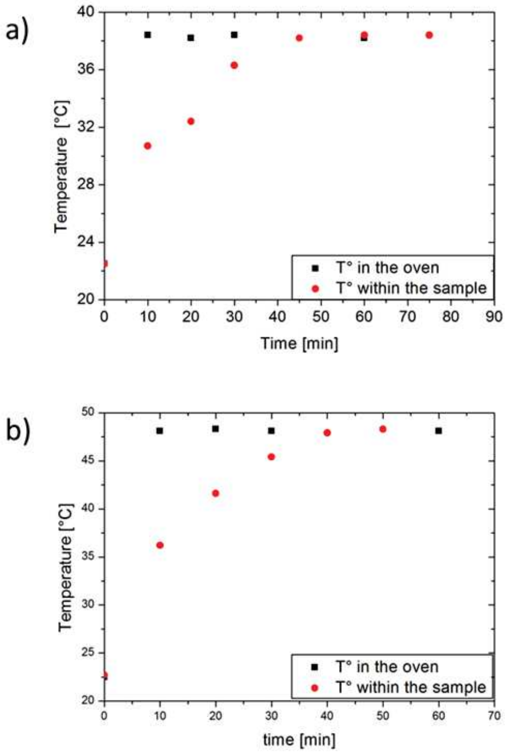

Figure 2-4: Evolution of the temperature in the oven (black dots) and within the sphere template (red dots) with time. Temperature of the oven was fixed at a) 40°C and at 50°C b).

2.5 Generation of macroporous polyurethane

All polyurethane precursors were kindly supplied by FoamPartner (Gontenschwil, Swiss). We used the polyether-based triol Voranol 6150 and poly(methylene diphenyleneisocyanate) (polyMDI) M220 (both from DOW chemical) at various weight ratios depending on the desired isocyanate index (Section 2.7). The polyurethane was obtained by simply mixing both components using an Ultra Turax, IKA ®T25 at 20K rpm, for 2 minutes except for PU scaffolds shown in Section 4.1 we mixed manually polyol and isocyanate. No catalyst was added to let enough time for the liquid mixture to infiltrate the sphere packing before solidification and to maintain a low reaction temperature to avoid additional sphere deformation. The mixture was then poured directly onto the sintered sphere packing where it spontaneously fills the interstitial spaces between the beads (see Figure 2-2-4). This filling process took about 1 h. The sample was then left at room temperature for 72 h to ensure full solidification of the polyurethane.

Finally, we used Soxhlet extraction by n-hexane for 6 h, at 100°C in order to remove the paraffin spheres. The resulting porous polyurethanes were left to dry overnight under a fume hood at room temperature.

SEM images of the paraffin spheres and the corresponding porous material can be seen in Chapter 3, in Figure 3-1.

2.6 Determination of the distribution of the interconnection sizes

We imaged the sphere templates and the porous polyurethanes with an SEM (see Section 2.12.1) to investigate the pore and interconnection morphologies. Before observation of the paraffin sphere templates, they were quenched in liquid nitrogen at -196 °C and then directly broken. This helped to conserve the template structure and, in particular, the geometry of the necks. The PU sponges were cut at room temperature using a cutter knife and imaged directly (Figure 2-5*a*).

The obtained images were treated with ImageJ software. In the case of the sphere templates, the pore radius R and interconnection radius r were measured by hand, taking into account at least 130 pores and interconnections for each data point to ensure good statistic.

In the case of the PU sponges, the interconnection sizes were calculated semi-automatically by employing the « particle analysis » tool (*Figure 2-5*c) after proper thresholding (*Figure 2-5*b) of the initial image (*Figure 2-5*a). In order to exclude zones which are not interconnections, only objects with a circularity higher than 0.5 were selected. We also only considered “particles” whose area is between 60 and 6000 µm². Since the circular interconnections were imaged at different angles, they commonly appeared as ellipses. We used the measurement of half of the major axis of the ellipse (Frenet diameter), which corresponds to the real radius r of the interconnections. For each data point we measured at least 200 interconnections to ensure good statistics.

The average values of the sphere radii $\langle R \rangle$ and the interconnection radii $\langle r \rangle$ were obtained by the arithmetic mean of the distributions, while we used the standard deviation as the error of one sample.

The error bars given in the unscaled graphs of (Chapter 3, Figure 3-5a and Figure 3-6a) are obtained by repeating each experiment three times. The error bar corresponds to the standard deviation calculated for the overall set of values.

The error bars in scaled graphs (such as Chapter 3 in Figure 3-5b,c and Figure 3-6b,c) are obtained by linear error propagation. If we plot the function $F = r/R^{1-\alpha}$ its relative error is given by

$$\frac{\Delta F}{F} = \frac{\Delta r}{r} + (1-\alpha)\frac{\Delta R}{R} \ , \qquad (5)$$

where Δr and ΔR are the errors of r and R, respectively.

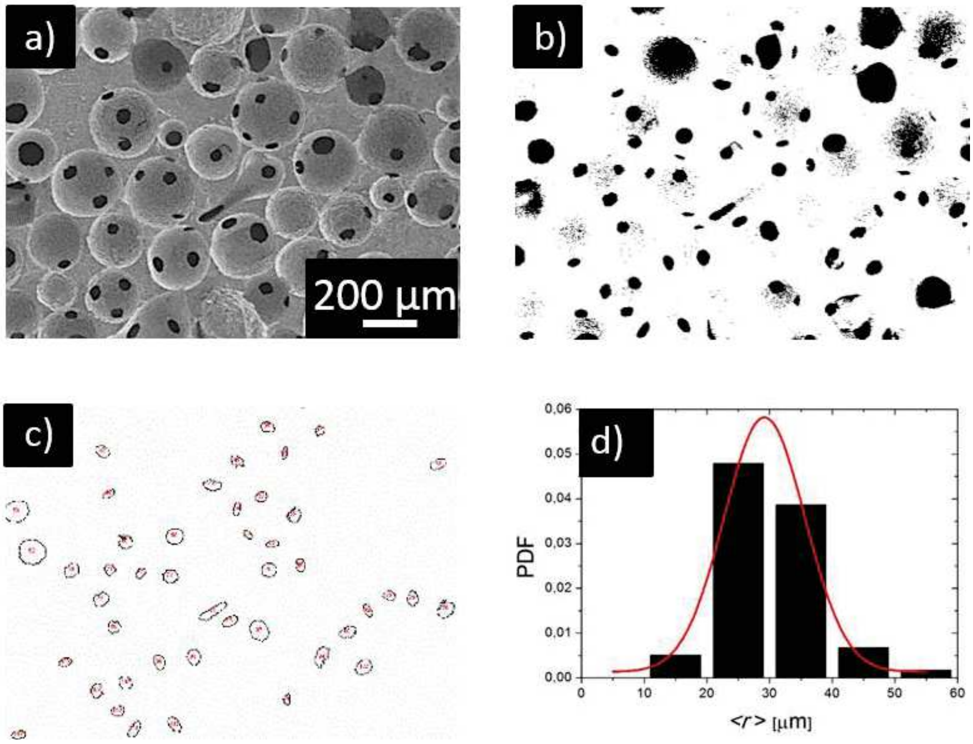

Figure 2-5: a) SEM image of a porous polyurethane sample. b) Thresholded image of (a) to bring out the interconnections. c) Objects with circularity above 0.5 are selected as interconnections. d) Probability Density Function (PDF) of the interconnection radii r *corresponding to the image (a) and the corresponding Gaussian fit (red curve).*

2.7 Formulation of the polyurethane

As described in Section 1.3.1.2 polyurethane formation involves the reaction between polyols and isocyanates in the simplest cases. The ratio of isocyanate to polyol plays an important role in the final properties of the PU matrix. However, we may note that often, other compounds such as water, chain extenders or catalysts may be introduced. They need to be taken into account for the calculation of the amount of each compound to obtain the desired formulation. Beside, due to the hygroscopic nature of polyols, water is retained and further reacts with isocyanate forming CO_2 resulting in foaming. To avoid it, polyol is degassed before reaction. To produce a polyurethane with stoichiometric ratio between isocyanate and hydroxyl functions, one needs to know the molecular weight of each species which is not always straightforward with industrial-grade chemicals. Indeed, polyols have an average molecular weight, and isocyanate are often not pure, but mixed with additives for instance. Hence, some analytic terms were developed and this specific nomenclature for polyurethanes will be described here. More detailed explanations are given in the book of Hepburn[2].

The equivalent weight (EW) is the first notion that we need to introduce. It is the molecular weight (MW) of a molecule divided by its functionality f (i.e. the number of active functions) per molecule. For example, a diol has $f = 2$ and for a triol $f = 3$.

$$EW = \frac{MW}{f}. \tag{6}$$

For isocyanates, suppliers often give what is called the free percentage of isocyanate (%freeNCO) which takes into account the effect of impurities and adhesives in the isocyanate solution. It quantifies the overall amount of isocyanate functions that are available to react. One can then obtain the equivalent weight of the isocyanate *EW(NCO)* from the following formula

$$EW(NCO) = \frac{42}{\% freeNCO}, \tag{7}$$

where 42 is the molecular weight of the NCO group.

For polyols, the number of free hydroxyl groups that can react is usually obtained by the “hydroxyl number” OH_{Numb}, which is the equivalent of milligrams of potassium hydroxide used to neutralize acetic acid (i.e. equivalent to the number of active functions (OH)) for one gram of the polyol. For this purpose, the polyol is first acetylated usually by reacting with acetic anhydride in the presence of a catalyst such as pyridine. Acetic acid which results from the aforementioned reaction is quantified by titration with potassium hydroxide[3]. From this, the equivalent weight of polyols *EW(OH)* is given by,

$$EW(OH) = \frac{56100}{OH_{Numb}}, \tag{8}$$

where 56100 is the molecular weight (in milligrams) of potassium hydroxide.

The isocyanate index (NCO index) is by convention 100 times the ratio of free isocyanate functions to free hydroxyl functions that are introduced in the initial batch before the reaction[4]. One needs to calculate the equivalent weight of both the polyol and isocyanate by which one can obtain the relative amount (in weight) of each compound to achieve the stoichiometric formulation. For example, for the polyol Voranol 6150, *EW(OH)* = 1934,48 and for the reacting isocyanate Voranate M220, *EW(NCO)* = 136. This means that for 1934,48g of polyol, 136g of isocyanate is the weight needed to ensure that each

NCO index	isocyanate/polyol (%wt ratio)
75	0.055
100	0.08
200	0.14
300	0.21
400	0.28

Table 2-1 : Weight ratios between isocyanate (Voranate M220) and polyol (Voranol 6150) to obtain PU with different NCO indexes.

hydroxyl function reacts with one isocyanate function. Thereafter, one can adjust the isocyanate index by increasing or decreasing the amount of isocyanate. In Table 2-1 are summarized some weight ratios between isocyanate and polyol that were used in Section 4.2 to obtain PU films with different NCO indexes.

Summaries of the polyether triols and isocyanate used for this thesis are given in Table 2-2 and Table 2-3.

Name	OH_{numb} (mg KOH/g)	MW (g/mol)	composition
Voranol 6150	29	6000	15% EO + 85% PO
Voranol CP1421	36	5000	75% EO + 25 % PO
Lupranol 2074	48	3500	10-15% EO + 85-90 % PO

Table 2-2: Summary of the compositions, molecular weight (MW) and hydroxyl number for polyether triols used for polyurethane synthesis. EO corresponds to ethylene oxyde while PO stands for propylene oxide.

Name	% free NCO	MW (g/mol)	composition
Voranate M220	30.9	340-380	polymethylene polyphenylisocyanate (MDI)

Table 2-3: Isocyanate used for the synthesis of polyurethane with the percentage of free isocyanate group (% free NCO), the molecular weight (MW) and the composition

In this Thesis, we use different NCO indexes especially in Section 4.2 the corresponding formulation are given in . Moreover, the majority of our experiments were done by using the polyol Voranol 6150 with the isocyanate Voranate M220. Their respective molecular structure is represented in Section 4.2. We tested which polyol among the ones cited in Table 2-2 was the best to support cell adhesion/survival. We seeded 3T3 fibroblasts as model cells on PU scaffolds where the polyol used in the formulation was varied. The scaffolds were pre-incubated for 2 days in FBS to allow proteins to adsorb onto the surface and cells were then injected on the top of each scaffold. In Figure 2-6, one can see that regardless of the polyol that was chosen, cells were more likely to sink at the bottom of each well. Moreover, the choice of the polyol was not a relevant parameter since the fluorescent intensity which depends on the number of cells alive was not drastically affected be the polyol. This can be explained by the very similar molecular structure of each polyol. Indeed, all polyols are based on PEO and PPO and its just their relative ratio that is changed. The Voranol 6150-based PU a slightly better viability of cells compared to the Lupranol 2074 and Voranol CP1421-based PU. Therefore, we chose to conduct experiments almost exclusively with Voranol 6150.

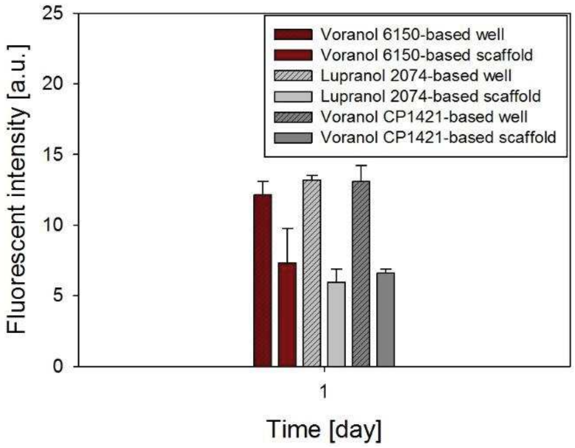

Figure 2-6: Evaluation of the viability of 3T3 Fibroblasts in response to the chemistry of the scaffolds. Viability was assessed by resazurin 24 h after seeding.

2.7.1 Cell seeding protocol

PU scaffolds were cut into cylinders of 1 mm height and 13 mm in diameter. Samples were sterilized in 70% ethanol overnight, then let dry under a fume hood for 24 h and placed under UV radiation 15 min for each face for sterilization just before seeding. The samples were then placed in a 24 well-plate. The PU scaffolds treated with plasma were taken out of the well plate to be placed under the plasma cleaner (Harrick Plasma PDC-002) for 3 min and put back in the wells.

Murine fibroblasts NIH 3T3 (ATCC) were firstly cultured in T175 flasks in DMEM (Dulbecco's modified Eagle's Media) supplemented with 10% (v/v) of decomplemented Fetal Bovine serum (FBS) and 1% (v/v) penicillin/streptomycin in a humidified incubator (5% CO_2, 37°C). Wharton's Jelly derived mesenchymal stem cells (WJMSCs) were harvested from four consenting patients with a procedure described elsewhere[5] (Authorization body: Inserm, ITMO Santé Publique Pôle Recherche Clinique PRC)), Authorization number: DC-2015-2364) and cultured in T175 flasks, in α-MEM Eagle (Gibco) supplemented with 20 % of decomplemented Fetal Bovine Serum (FBS), 1 % (v/v) penicillin/streptomycin/amphotericin and 1 % of L-glutamine. Once cells reached about 70-80 %

confluence, cells were washed with PBS and passaged with trypsin-EDTA solution. WJMSCs were seeded at passage 4 to 6, while fibroblasts were seeded at passages between 8 and 16.

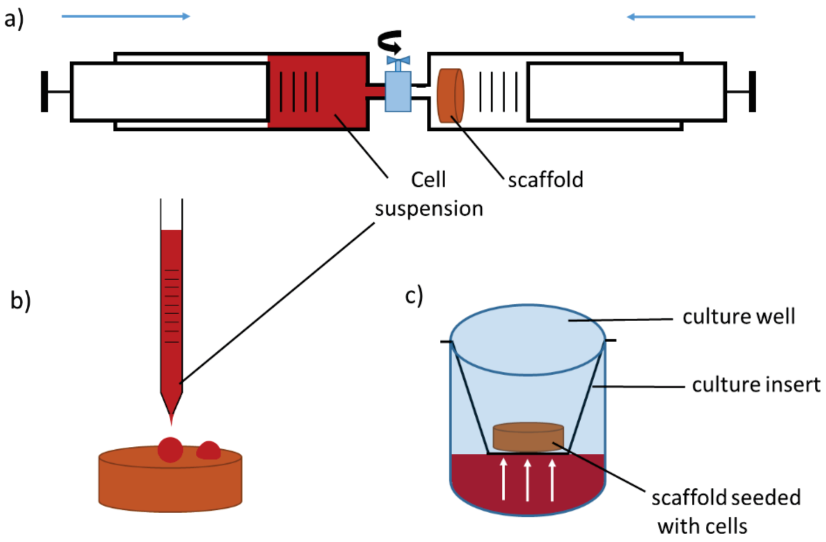

Figure 2-7 : Different seeding protocols, a) two syringes connected with a valve; b) the cell suspension is directly added dropwise on the top of the scaffold and c) the scaffold which is seeded dropwisely before being placed in a culture insert. The media is then added in the well and the media penetrates into the scaffold slowly from the membrane at the bottom of the insert.

Cell seeding in PU scaffolds was achieved by different ways that are schematically shown in Figure 2-7. In the first case (Figure 2-7-a), cells suspended in 2 mL of media were forced to flow through the porous scaffold by moving back and forth by hand the piston of two syringes (50 ml, BD Plastipak™) connected through a valve (Discofix® 1-Way, D100, B. Braun) via their Luer Lok™ mouthpiece. After approximately 20 cycles, the scaffold was removed from the syringe and placed in a 24 well plate. The cell suspension liquid was directly added into the well.

Another way of seeding cells in shown in Figure 2-7-b. It was used in three cases, namely for scaffolds that were previously treated with plasma cleaner, or untreated, or preincubated for 2 days in culture medium to allow proteins to be deposited on the PU surface. Scaffolds were just placed in the bottom of a 24 well plate and the cell suspension (from 20 to 150 µL) was added dropwise with a micropipette and 2 mL of culture media was added in the well. Some ways of seeding cells were tested for 24h to see if significant differences could have emerged at early times. As shown in Figure 2-8, when cells are directly seeded on the bare PU scaffold, less cells remained within the porous material after 24h, and almost the same amount of cells drawn at the bottom of the wells. When cells are seeded on plasma-treated PU, we can see more cells are located inside the porous scaffold which is comparable to the case where cell suspension was forced inside the scaffold via the syringes. One can clearly see that the seeding efficiency is still not optimized since many cells are sinking to the bottom of the wells.

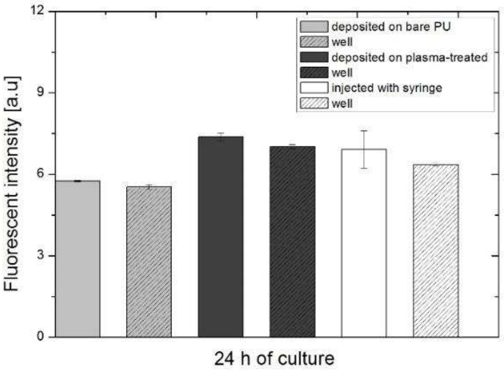

Figure 2-8: Evaluation of cell amount in scaffolds seeded by depositing the cell suspension on the bare scaffold (grey), by injecting the cell suspension onto a scaffold pre-treated by plasma (dark grey) and by forcing the cell suspension through a syringe (white). Cell number was also recorded at the bottom of each well to account for the cell loss. The cell viability was assessed by resazurin after 24 h of culture.

The last procedure to seed the cells is shown in Figure 2-7-c. In this case (for scaffold treated with plasma treatment or preincubated in culture medium), the scaffold seeded with cells is placed in the bottom of a culture insert (3.0 µm pore size, Corning Inc, reference 353292) in a 12 well plate. Then, 3 mL of culture medium is added into the well next to the culture insert. Hence, the medium penetrate slowly by the bottom of the insert across the porous membrane. This allows the medium to penetrate inside the scaffold with a lower flow rate compared to the case where the media is poured directly on the scaffold as shown Figure 2-7-b. This allows to minimize the cell loss since cells only weakly adhered to the substrates. The cell seeding density was varied from 0.5 to 10×10^6 cells per scaffold depending on the experiment performed. All the experiments were conducted in hydrophobic coated well plates. Hydrophobic 12 well plates were prepared as follows: 350 µL of poly(2-hydroxyethyl methacrylate) (pHEMA) (Sigma Aldrich, P3932) solution at 0.5% (w/v) in ethanol was incubated in each well plate and put in an incubator at 39°C for 24 hours until complete evaporation of ethanol. Then, culture plates were sterilized for 15 minutes under UV before use.

2.7.1.1 Cells embedded in peptide hydrogels

In Chapter 5, we encapsulate cells within a hydrogel and injected it inside the porous scaffold, we describe here the experimental part of this Chapter.

Self-assembled peptide (SAP) hydrogels were obtained from Biogelx™, and the product was Biogelx-S (cat# A0X-0000). A pre gel solution was prepared by adding 68 mg of the supplied powder into 5 ml of sterilized water. Then, the solution was vortexed and mixed by pipetting. Air bubbles were removed by sonication. Aside, cells (WJMSCs) were centrifuged at 1200 rpm for 5 min, and the media was then removed without disturbing the cell pellet at the bottom of the tube. Then, the pre gel solution was added on the cells and homogenized by pipetting carefully, without adding air bubbles in the gel. 500 µl of cells embedded in pre gel solution was added into a 24 well plate and 600 µl of culture media was added dropwise on the top of the pre gel. When the culture media is added, the gelation start to occur. Samples were then placed in an incubator at 37°C, 5% CO_2 for 2h. Fresh medium was then added by carefully avoiding that the pipette touches the gel. Media was changed each day for two days, and each two day until the end of the experiment.

2.7.2 Flow perfusion system

As described in Section 4.1, our PU scaffold did not promote very well proliferation. As all our cell culture experiments were conducted statically, an efficient removal of cellular waste and the supply of nutrients could be limited by diffusion due to the tortuosity in the scaffold. Dynamic perfusion is often used to overcome these diffusional limitations since the culture medium is continuously circulating across the scaffold.

We developed a homemade bioreactor to see if we could improve cell proliferation or viability in the scaffold when the medium is flowing across the scaffold. Scaffold was seeded with cells and let in a well plate statically for 24h to let enough time to the cells to adhere. This scaffold was then inserted in a home-made bioreactor shown in Figure 2-9. As shown in Figure 2-9b, a 50 mL syringe (BD Plastipak™) was used and the piston was drilled along the long axis to obtain 4 holes having 1.5 mm diameter to allow the liquid to pass. Silicone tubes with 1.6 mm internal diameter (Fischer Scientific) were inserted into the holes. The culture media was contained in a glass bottle with 3 entries, one for the liquid output, and one for the liquid to come back. The last entry was connected to a filter (Filtropur S, diameter 0.45 µm, Sarstedt) to allow gas exchanges while keeping the whole set up sterile. The medium was pumped with a peristaltic pump (MINIPULS 3, Gilson) to pass through the syringe and thereby across the scaffold which was squeezed between the piston and the bottom of the syringe and went then back into the bottle. Silicone tubes were 2 m long, since the bottle and the bioreactor were placed in an incubator at 37°C and 5 % CO_2. The pump was kept outside of the incubator. The liquid was perfused at a flow rate of 0.1 mL/h.

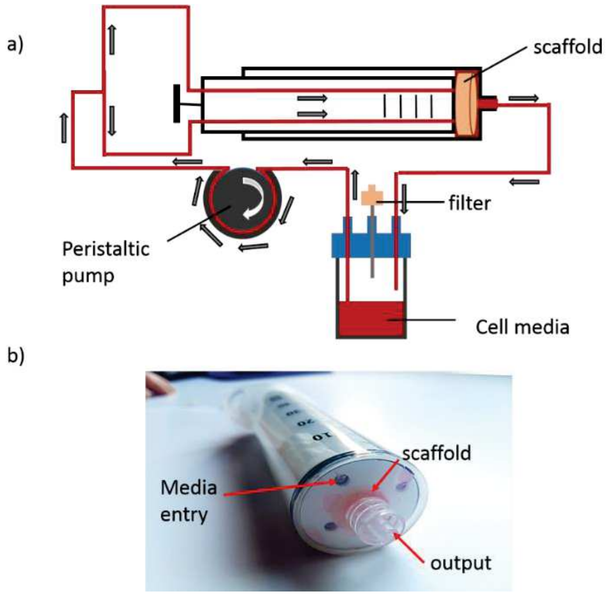

Figure 2-9 : a) Scheme of the flow perfusion system and b) photo of the syringe that serves as bioreactor.

We made some experiments with the bioreactor described in Figure 2-9. The amount of cells remaining within the PU scaffold was observed under confocal microscope (Figure 2-10a). One can clearly see that for dynamic conditions, no cell remained inside the scaffold after 7 days compared to static condition. WJMSCSs viability was assessed by resazurin, and the results shown in Figure 2-10b are in accordance with confocal images, where no more cells are present in the scaffold after seven days. Even if the flow rate selected was in the order of what can be found in the literature, the poor adhesion of cells shown in Section 4.1 may have contributed to take away the cells out of the scaffold.

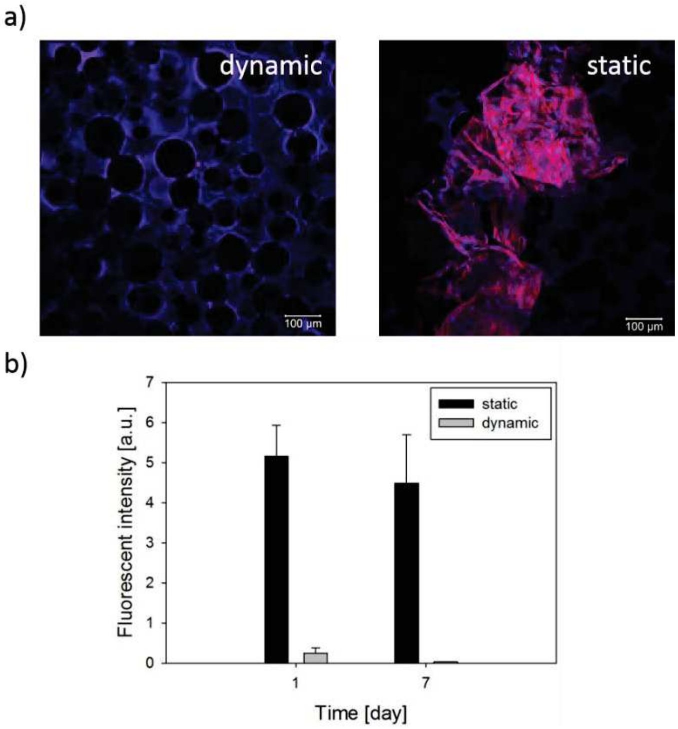

Figure 2-10: Comparison between static and dynamic conditions of culture for Wharton's Jelly Mesenchymal Stem cells (WJMSCs). Images of WJMSCs taken with a confocal microscope where cells were stained with DAPI/Phalloidin to visualize the nuclei (blue) and F-actin filament (red) in a) after 7 days of culture. Evaluation of the viability by resazurin of WJMSCs in the PU scaffold at day 1 and day 7 after being placed in the bioreactor in b).

We also tried a 3D printed bioreactor supplied by Protip Medical (France). We used the same peristatic pump, and connectors. Only the bioreactor was replaced by the one shown in Figure 2-11. However, the seal was not efficient to prevent leakages of medium. Since PU scaffolds were hydrophobic (Section 4.1.3.1), it may have been difficult for the liquid to pass through the sample and the pressure induced by the accumulation of liquid could have promote some leaks.

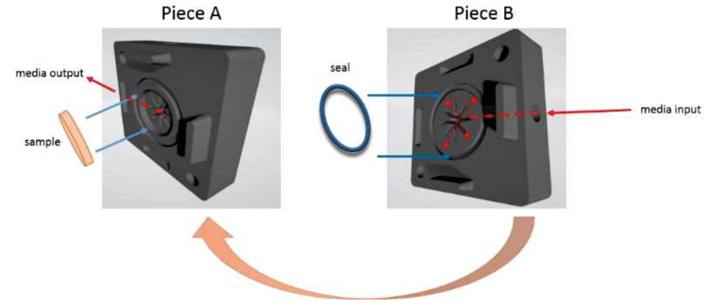

Figure 2-11: Schematic representation of the 3D-printed bioreactor used for dynamic cell culture experiments. The sample is placed at the centre of the piece A and surrounded by a silicone seal which is placed in the grooves shown on piece B. Piece A and B were clamped together and screwed. Finally, fresh media is perfused through the input of the piece B, and cross the sample before leaving the reactor through the output in piece A.

2.8 Assessment of cell viability

2.8.1 Resazurin reduction

AlamarBlue™ (ThermoFisher) assay was used to measure the metabolic activity of the cells and thus to estimate their proliferation and survival. Rezazurin, the active agent, is reduced within the mitochondria into rezorufin which is fluorescent. A solution of AlamarBlue of 10 % (v/v) in culture medium is prepared and protected from light. Then, the culture medium is removed from the wells and cells or scaffolds seeded with cells are rinsed with PBS. Afterward, 1 mL (per 24 well plate) or 2 mL (12 well plate) per well is added and the samples are let to incubate for 2 h within at 37°C, 5 % CO_2. After incubation, 100 µL of solution (3 per sample) is poured in a 96 well plate. The fluorescent intensity was then recorded with a photospectrometer SAFAS (Section 2.14) with excitation/emission ($\lambda_{exc}/\lambda_{em}$) wavelengths at 560/590 nm.

2.8.2 Phenol Chloroform method for DNA extraction

Scaffolds with cells were crushed and immersed in a lysis extraction buffer, (10 mM tris-HCl, 1mM of ethylene diamine tetraacetic acid (EDTA) (Sigma), and 0.1 % v/v of Triton® X-100 (Euromedex, France) in sterilized water adjusted at pH 8. The solution was placed in a 10 mL falcon tube in a freezer at -80°C overnight. DNA purification was performed by the Phenol/Chloroform method. 200 µL of the lysed cells solution were poured in a 2 mL tube and an equal volume of Phenol/Chloroform/Isoamyl alcohol 25:24:1 (Sigma Aldrich) solution was added to the solution. The mixture was vortexed for 20 s 10 times, and centrifuged at 13 000 rpm at 4°C for 5 min. The aqueous phase (containing the solubilized DNA) was extracted by carefully pipetting, and placed in a new 2 mL tube. Again, an equal volume of Phenol/Chloroform/isoamyl alcohol 25:24:1 solution was added and the operation was repeated. After centrifugation, the supernatant was pipetted and poured into a new tube, in which an equal volume of pure chloroform (Sigma) was added. The mixture was vortexed again 20s 10 times and centrifuged 5 min at 13000 rpm for 5 min. DNA was precipitated by adding 150 µL of sodium acetate 5.5 M and two times the volume of sodium acetate solution (i.e. 300 µL) of 100% ethanol was added. The tubes were placed at -20°C overnight. Samples were vortexed for 20 min at 4°C at 13 000 rpm, and supernatant was removed, leaving the pellets at the bottom of the tubes. Samples were washed in 80% ethanol, vortexed 3 times and centrifuged at 13000 rpm. Ethanol was removed and tubes were let under a fume hood for the complete evaporation of ethanol for 20 min. 200 µL of buffer solution (10 mM tris-HCl, 1 mM of EDTA (Sigma) pH 8 was added to solubilized DNA pellets and the DNA concentration (µg/mL) was read on a Nanodrop device. The value was divided by the scaffold weight to get a DNA concentration relative to the material amount to account for the differences between samples.

2.9 Cytotoxicity assessment

Cytotoxicity of the different PU samples was tested towards NIH 3T3 fibroblasts via indirect contact method according to ISO STANDARD 10993-5. This experiment was performed on extraction vehicle. PU samples were immersed in 1mL of cell culture medium (DMEM supplemented) for 24 hours at 37°C in order to extract all potential harmful monomers (extraction vehicle). In the same time, NIH 3T3 cells were seeded in a 24 well plate at a density of 60 000 cells/well to obtain a cell layer of 80% confluency after 24 hours. Then after 24 hours, the extraction vehicle is transferred on the cell layer and let in contact for 24 hours. MTT test (bromure 3-(4,5-dimethyltiazol-2-yl)-2-5 diphenyl tetrazolium) is then performed to assess the metabolic activity of cells and determine the percentage of viability. Viability is normalized with a control which is a cell layer cultured for 48 hours without exposition with the extraction vehicle. Using ISO STANDARD 10993-5, a sample is considered cytotoxic if the viability normalized with control is less than 70%.

2.10 Protein adsorption tests

Two tests were conducted to ensure that the results were accurate and reliable. The first method was the Bradford method. Polyurethane samples were cut into discs having 13 mm in diameter and 5 mm height. PU samples with NCO indexes from 75 to 400 were first immersed in 2 mL FBS for 24h. After that, samples were rinsed with PBS, and placed in a 24 well plate. The adsorbed proteins were then detached by using a detergent solution (3M urea (Aldrich), and sodium dodecyl sulfate, SDS 5% (Sigma-Aldrich) in PBS) overnight. Aside, a calibration curve was generated by using bovine serum albumin BSA (Sigma) diluted at 1% as the standard protein since the serum in culture medium is mainly composed of BSA. The second method consisted on immersing PU samples with different NCO indexes in 1 mL of a solution of 0,25mg/mL of FITC-BSA in PBS for 30min in the dark. Samples were then washed with PBS and let into PBS à 4°C until observation.

2.11 Cell staining with fluorescent markers

2.11.1 Cell staining with DAPI/ Phalloidin

For staining the cells, cells in the scaffolds were fixed in a 4% paraformaldehyde solution in PBS, for 30 min at ambient temperature. Thereafter, the samples were washed with PBS, and the cell membrane was permeabilized with a solution of 0.1 % Triton® X-100 in PBS for 10 min, followed by two washing steps with PBS, and incubated with a solution of 1% v/v of Bovine Serum Albumin (BSA) for 20 min. The actin filaments of cells in scaffolds were then stained with a fluorescent molecule: Phalloidin (Alexa Fluor™ 568) at 1/40 v/v in PBS for 1 h. Afterwards, samples were washed two times with PBS for 5 min, and subsequently incubated in a DAPI (4',6 diamidino-2-phenylindole, PromoKine) solution (concentration of 1/100 in PBS) for 5 min. At the end, samples were washed two times in PBS for 5 min and kept in PBS at 4°C prior to the microscope observation.

2.11.2 Staining with Green calcein

Cells were stained for green calcein just before being seeded. Cells were suspended in serum free medium, and 5µl of calcein (Vybrant Cell Adhesion Assay kit V-13181), ThermoFisher, per million of cells and thoroughly placed in an incubator at 37°C for 30 min and protected from light. Afterward, cells were centrifuged and re-suspended in classical culture medium prior to be seeded. This method allows to stain the cells alive and therefore, to observe them under microscope.

2.11.3 Immunostaining for Vinculin

Cells in scaffolds were firstly attached to the PU substrate with a solution of paraformaldehyde 4% (v/v) in PBS for 30 min at RT. Samples were then washed two times with PBS, and stored in PBS at 4°C. To detect vinculin, the samples were incubated with the primary antibody anti-mouse vinculin (US Biological life sciences, V2122-63) at a concentration of 1/50 in PBS for 1h30. Afterward, samples were washed two times in PBS for 5 min. Samples were then incubated with secondary antibody anti – goat conjugated with fluorescein (Goat, Pab, IgG, Alexa Fluor® 488) at a concentration of 1/500 in PBS for 30 min. Samples were finally rinsed.

2.11.4 FITC-bovine serum albumin

Samples that were loaded or not with gel (in Chapter 5) were incubated at a concentration of 0.25mg/ml of albumin fluorescein isothiocyanate conjugated protein (Sigma Aldrich, A9771-250MG) for 30 min in an incubator. Samples were then rinsed with PBS two times, stored at 4°C and protected from light prior to be analyzed by confocal microscopy. Since FITC-BSA can adsorbed on many cytoplasmic components, we use BSA to see whether it can adsorb on the hydrogel fibers.

2.11.5 Type II collagen

Cells were first rinsed in PBS, and fixed in 4% paraformaldehyde in PBS for 30 minutes at ambient temperature. Cells were then immersed in PBS and stored at 4°C until staining. Cells were permeabilized with 0,1% Triton X-100 in PBS for 10 min and then washed 2 times in PBS for 5mins. Afterward, samples were incubated in BSA (Sigma, A9647-100G) 1% in PBS for 20 minutes at room temperature. Samples were subsequently incubated in Collagen II monoclonal primary antibody (MA5-12789 thermofisher) diluted at 1/200 in PBS for 30 minutes at room temperature, and then washed in PBS for 10 minutes. Samples were incubated in goat anti-mouse secondary antibody Oregon Green® 488 (011033) at a dilution of 1/200 for 1h and protected from light.

2.12 Microscopes

2.12.1 Scanning electron microscope (SEM)

Samples were observed with an SEM Hitachi SU8010 under 1KeV voltage acceleration to investigate the structural properties of the samples in general (paraffin spheres packing, PU scaffolds etc.) and the dimensions of the pores and interconnections in particular.

2.12.2 Confocal microscope

Confocal images were taken after the staining of the cells using an inverted Zeiss LSM 710 microscope. Objectives x10 and x20 or x40 were used to visualize the cells on the films (Section 4.2) or within the scaffolds (Sections 4.2 and Chapter 5). Excitation/emission wavelengths were 489/556 nm, 578/600 nm and 360/460 nm for green calcein, Alexa Fluor™ 568 Phalloidin and DAPI respectively.

2.12.3 Optical microscope

Images of cells on flat surfaces were taken with an optical inverted microscope (Eclipse, TS100, Nikon) mounted with a digital camera (DS-Fi2-L3, Nikon).

2.12.4 Numerical microscope

Keyence VHX-5000 numerical microscope was used to determine the size distribution of paraffin spheres (Chapter 3)

2.12.5 Atomic Force Microscope (AFM)

Polyurethane films were cast in a petri dish until reaching a height of approximately 1 mm. Once dried, samples were cut into disc having 13 mm in diameter and 1 mm height. Samples were placed under the microscope in air.

AFM experiments were carried out with a multimode AFM 8 mounted with a controller Nanoscope LVIII 64 bits from Bruker. Experiments were conducted in peakforce tapping mode by using a Probe Scan Asyst fluid (0.7 Nm) probe from Bruker. Surface roughness was expressed as root mean square value (RMS) by using the software Nanoscope Analysis 1.5.

2.13 Quantification of cell secretions

2.13.1 Quantification of collagenous and non-collagenous content

Collagen and non-collagenous proteins secreted by cells were quantified using the Sirius Red/Fast Green Collagen Staining kit (Chondrex, Inc). Scaffolds seeded with cells were first rinsed in PBS two times. Then samples were immersed in the dye solution for 30 min. Sirius Red binds to the helical structure of fibrillary collagen regardless of their type while Fast Green binds to non-collagenous proteins according to the supplier. Afterwards, the samples were rinsed with distilled water several times until the water became clear. Porous scaffolds were then immersed in 1 mL of Dye extraction buffer for 15 min. 100 µL of the solution were collected in a 96-well plate and absorbance values at 540 and 605 nm were recorded with a spectrophotometer. The collagenous and non-collagenous parts were calculated with the equation given in the kit protocol:

$$\text{Collagenous part (µg of protein/ mg of material)} \quad \frac{(\mathrm{OD\ 540\ nm} - (\mathrm{OD\ 605\ nm} * \ 0{,}291)}{0{,}0378 * scaffold\ weight}, \tag{9}$$

$$\text{Non-collagenous part (µg of protein/ mg of material)} \quad \frac{\mathrm{OD\ 605\ nm}}{0{,}00204 * scaffold\ weight}, \tag{10}$$

OD 540 nm and OD 605 nm are the optical densities at 540 and 605 nm respectively. Scaffolds were weighted before seeding to quantify the amount of proteins relative to the amount of material. Optical densities were recorded with a spectrofluorimeter.

2.13.2 Sulphated Glycoaminoglycan quantification sGAGs

1,9-dimethylmethylene blue is the dye that is specifically used to bind to the sGAGs. It is provided by Glycoaminoglycan Assay, Blyscan™, (Tebu-Bio). First, samples (cells + scaffolds) are rinsed with PBS, and digested in a buffer solution containing 50 mL of a Na_2HPO_4 (Sigma Aldrich) at 0.2 M and pH 6.4 with 200 mg of EDTA (Alfa Aesar GmbH) and 400 mg of sodium acetate (Sigma Aldrich), with 40 mg of L-cystein in 50 mL of demineralized water. Foams seeded with cells are immersed in 1 mL of buffer solution described above and supplemented with 25 µL of papain (Sigma Aldrich) per mL of buffer. Samples are put in bain-Marie at 65°C overnight. After being removed, 50 µL of sample solution are added to 50 µL of buffer to make a 100 µL solution. In parallel, a calibration curve is prepared by using the reference GAGs solution supplied in the kit. Calibration samples are prepared by adding 0, 1, 2 ,3, 4, 5 µg of GAGs in 100 µL demineralized water as solvent. Subsequently, 1mL of dye reagent is poured in each tube, and let for 30 min to precipitate GAGs while being regularly shaken. Tubes are then centrifuged at 12000 rpm for 10 min, and the supernatant is removed to let only the precipitate in the bottom of each tube. Afterward, 500 µL of dissociation reagent is added to dissolve the precipitate for 10 min, and protected from light. Tubes are centrifuged again to remove the foam layer, and finally, 200 µL of each tube are pipetted in 96 well plates and absorbance is read at 656 nm at the spectrofluorimeter.

2.14 Spectrofluorimeter SAFAS

The spectrofluorimeter SAFAS, (FLX-Xenius®) was employed to measure either the absorbance or the fluorescent intensity. Solutions were poured in a 96 well plate and placed under the spectrofluorimeter. The selected emission wavelengths and filters at which the absorbance was read are given in each section with their respective protocol.

2.15 X-Ray Photoelectron spectroscopy (XPS)

The X-ray photoelectron spectroscopy (XPS) measurements were carried out in an ultrahigh vacuum (UHV) spectrometer equipped with a CLAM4 (MCD) hemispherical electron analyzer. A dual anode Al Kα X-ray source (1486.6 eV) was used as incident radiation. Survey and high resolution spectra were recorded in constant pass energy mode (100 and 20 eV respectively).

2.16 Fourier Transform Infrared Spectroscopy (FTIR)

FTIR was carried out for the solid PU films with a Bruker Vertex 70 instrument equipped with an attenuated total reflectance (ATR) module. Scans were performed from 400 to 4000 cm^{-1} with a spectral resolution of 2 cm^{-1}. Spectra were treated with the software Opus 7.5.

2.17 Rheology

Experiments were conducted with a rheometer MRC 702 MultiDrive® from Anton Paar at various temperatures (30, 32, 34, 36, 38, 40, 42). The cone plate configuration with an angle of 5° was used. Before the tests, platelets of paraffin wax were deposited onto a peltier plate and heated up to 60°C to melt paraffin. The rheometer cone was then approached until making a full contact with the wax and down to the desired gap. The paraffin was then cooled down to 20 °C/min until 25°C to obtain a solid between the plateaux. Afterwards, the solidified sample was heated up at 5°C/min until the desired temperature was reached to simulate the conditions of the oven. The rheological measurements were started once the sample reached a thermal equilibrium. The dynamic viscosity of paraffin was obtained through a frequency sweep from 0.01 to 10 Hz (50 points log spaced) at a constant strain of 0.1 %.

2.18 Mechanical tests

PU films (15 mm thick) were shaped into dumbbells (90 mm long) and typical stress-strain curves were obtained according to the NF EN ISO 527-1 and NF EN ISO 527-2 standards. Traction tests were performed using a machine of universal assays (Zwick) mounted with a sensor of 200 N. A preload of 1 N was applied and the stretching was performed at a rate of 50 mm/min.

Typical stress-strain curves in Section 4.1 were obtained with a standard rheometer (Kinexus ultra +, Malvern). Samples were cut into discs (26 mm in diameter, 5 mm height) and preloaded with 0,5N which was considered as the force when the plate was in contact with the surface of samples. Samples were compressed until 20% strain. Young modulus was calculated from the slope of the obtained stress-strain curves.

2.19 Measurement of the hydraulic permeability

The hydraulic permeability of porous samples to water was measured using a gravimetric method described in detail elsewhere[6]. Briefly, the porous sample cut into a disc shape of thickness H (mainly between 2 and 4 mm) was placed to fill the entire passage of a U-shaped apparatus (Figure 2-12). A valve allows to generate a water height difference Δh (i.e a pressure gradient $\Delta P = \rho g \Delta h$, where ρ is the density of water and g the gravitational acceleration) which, when opened, gives the driving force for the water to flow across the sample. We made a movie of the process and we recorded how much time water needed to rise a certain height (Δh = 5cm). Since the polyurethane was hydrophobic, we added 1

% wt of silicone surfactant (Tegostab® 8002, Evonik) to the water to ensure that the scaffold was completely wetted.

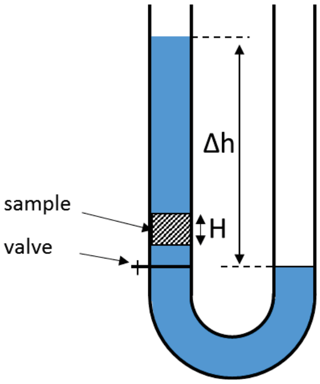

Figure 2-12 : Principle of the U-shaped apparatus used for water hydraulic permeability measurement.

The surfactant does not influence the flow properties. We measured the velocity V_D ("Darcy velocity") at which the water passes through the sample over the entire range of Δh (i.e. ΔP). Both are related by Darcys' law

$$V_D = \frac{\partial(\Delta h)}{\partial t} = k\frac{\rho g \Delta h}{\eta H}, \qquad (11)$$

where η is the dynamic viscosity of the water (taken as 10^{-3} Pa.s) and k the hydraulic permeability (in cm^2). We thus obtain k by taking the slope of the V_D (Δh) curve and multiplying it by ($H\eta/\rho$g).

2.20 Porosity

The porosity was assessed by the formula

$$P(\%) = 100 * [1 - \frac{\rho_p}{\rho_b}], \qquad (12)$$

where ρ_p and ρ_b are the densities of the porous and the bulk polymer respectively. The densities were obtained by preparing a pure polymer solid and the scaffolds having the same volume and by weighting them using a balance in order to obtain the density ratio.

2.21 Contact angle measurement

Surface wetting properties of the PUs were obtained by static contact angle measurements with purified water (Milli-Q). The sessile drop technique (Attension theta, Biolin Scientific) was used and the values of the contact angles were obtained by image treatment using the software Oneattension. Each experiment was repeated three times to ensure the reproducibility.

2.22 Differential Scanning Calorimetry (DSC)

We place 8.2 mg of the paraffin in a stainless steel capsule and put the capsule inside the instrument (PerkinElmer DSC 8500). Experiments were done under nitrogen atmosphere. Curves were obtained by heating/cooling between 25 °C and 80°C with a ramp of 10 °C/min. A first cycle has also been performed to erase the thermal history of the paraffin.

2.23 Small Angle X-ray Scattering (SAXS) and Wide Angle X-ray Scattering (WAXS)

SAXS experiments were performed with a diffractometer developed by Molecular Metrology (Elexience in France) that uses a Rigaku Micromax 007HF generator with a copper-rotating anode. The wavelength of the incident X-ray beam is λ =1.54 Å. This diffractometer operates with a pinhole collimation of the X-ray beam focused by a multilayer optic designed by Osmic and a two-dimensional gas-filled multiwire detector. The sample-detector distance was set at 0.7 m, leading to a range of scattering vectors covered by the experiment $0.01 < q < 0.32$ Å^{-1}, or $0.1 < q < 3.2$ nm^{-1}. The scattering vector q is defined by $q = (4\pi/\lambda)\sin(\theta/2)$, where λ is the wavelength of the incident beam and θ, the scattering angle. The q-resolution related to the beam size on the sample and the beam divergence was close to 0.005 Å^{-1}, or 0.05 nm^{-1}. PU films of thicknesses close to 1 mm were studied. Measurements were performed at room temperature.

WAXS experiments were carried out from the same diffractometer by using Phosphor imaging plates from Molecular dynamics as detectors. These plates were set at 0.06 m from the samples, allowing to explore scattering vectors ranging from $q = 0.05$ Å^{-1} to 3.5 Å^{-1}. The same films of thicknesses close to 1 mm were used in the same positions with respect to the incident X-ray beam than for the SAXS experiments. Measurements were also performed at room temperature.

2.23.1 Data treatment

For SAXS, all data were treated according to standard procedures for isotropic small angle X-ray scattering. After radial averaging, the spectra were corrected from electronic noise of the detector, empty cell, absorption and sample thickness. A 55Fe source was used for the corrections of geometrical factors and detector cells efficiency as well as a Silver Behenate sample, for the q-calibration. The normalization to the unit incident flux was then obtained by using water or Lupolen (polyethylene) as standard samples. Nevertheless, such measurements on an absolute scale, scattered intensities I(q) expressed in cm^{-1}, were not perfectly achieved for the WAXS experiments. The spectra were then locked onto the related SAXS ones. After all these data treatments, the scattered intensities at low q-values only associated with the concentration fluctuations, should still be corrected from the scattering related to the density fluctuations. This last correction was done through the subtraction of an additional constant that allows observing a q^{-4} scattering behavior characteristic of the existence of sharp interfaces for some samples. Indeed, the "far-away point" method[7], which assumes that the density fluctuations are almost identical for the background and the film, could not be used here as the density fluctuations were already taking place in a q-range in which the concentration fluctuations are not still negligible ($q \approx 0.3$ Å^{-1}). According to such a procedure, the scattered intensity I(q) at low q-values, containing all the structural information, is obtained for each film.

The WAXS scattered intensities, which are related to density fluctuations, present a broad maximum ranging from 1 and 2 Å^{-1}, without any Bragg peak. They are quite identical for all the studied samples and indicate an amorphous state, or a disordered local order, in both phases resulting from the separation of incompatible hard and soft segments. Actually there is none crystallinity, or paracrystalline order, in all the studied samples.

We must emphasize that the density fluctuations present independently in both phases yield contributions to the scattered intensities that already play a role in the usual SAXS q-range ($q < 0.6$ Å^{-1}). Actually, they cannot be neglected as soon as $q > 0.3$ Å^{-1}. For each sample, the scattered intensity can therefore be written as:

$$\mathrm{I}(q) = \mathrm{I}_{coh}(q) + \mathrm{I}_s(q) + \mathrm{I}_h(q) \qquad (13)$$

$\mathrm{I}_{coh}(q)$ is the scattering due to the concentration fluctuations, i.e. that would be achieved if both phases had a constant density (ideal two-phase model). $\mathrm{I}_s(q)$ *(soft segments)* and $\mathrm{I}_h(q)$ *(hard segments)* result from the density fluctuations in both phases. The cross correlation term $\mathrm{I}_{sh}(q)$ can be neglected, specifically in a two-phase model with sharp interfaces. Thus, for obtaining $\mathrm{I}_{coh}(q)$, which contains all the information about the large-scale structure associated with the microphase separation, we still need subtracting $\mathrm{I}_h(q) + \mathrm{I}_s(q)$, which is not a simple constant in the whole explored q-range by SAXS, a priori. This background correction could be carried out by extrapolating the scattering curve beyond the small q-range through an empirical equation as $A+Bq^2$ (fitted from the end of the SAXS regime toward the beginning of the amorphous halo see Figure 4-16). However, we first replaced $\mathrm{I}_s(q) + \mathrm{I}_h(q)$ by a constant ΔB for $q < 0.3$ Å^{-1}. Assuming a two-phase model, a characteristic q^{-4} scattering behavior is naturally expected at high q-values. So, restricting the scattered intensity of each copolymer film to its SAXS contribution, we can write:

$$I_{SAXS}(q) = \frac{A}{q^4} + \Delta B \qquad (14)$$

And a plot of $q^4 I_{SAXS}(q)$ versus q^4 allows evaluating ΔB via the slope of the observed straight line. Such a plot is presented in Figure 2-13 for the sample having an NCO index of 400.

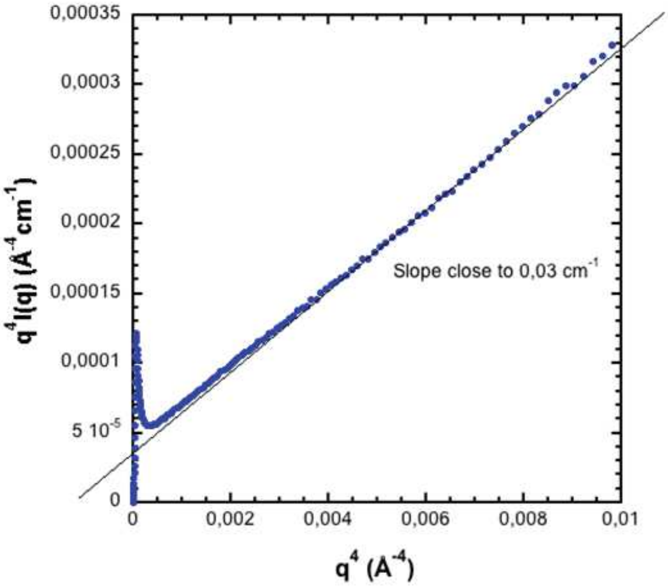

Figure 2-13: SAXS scattered intensity of the copolymer film with NCO index of 400. The plot of $q^4 I(q)$ vs. q^4 is used for evaluating an approximate background associated with density fluctuations (Equ. 14).

ΔB is then close to 0.0307 cm^{-1}. In the same way, we obtain: ΔB= 0.0301 cm^{-1}, for the sample NCO index 300; 0.0314 cm^{-1}, for the sample with an NCO index 200; 0.0310 cm^{-1}, for the NCO index 100; 0.0317 cm^{-1}, for the sample 75. The background correction is therefore almost identical whatever the copolymer film in agreement with the observation of their similar scattered intensity in the WAXS q-range. The background subtraction can finally be improved using the Porod representation (q^4I(q) vs. q) of the SAXS data, as shown in Figure S 8. The final ΔB values are:

Table 2-4: Values of the offset obtained from the slope of the curved $q^4 I(q)$ vs.q for samples with different NCO indexes

	Sample 400	Sample 300	Sample 200	Sample 100	Sample 75
ΔB (cm^{-1})	0.0294	0.0286	0.0310	0.0300	0.0304

The corrected scattered intensities $I_{coh}(q)$ are used in the following analyses according to the non-particulate two-phase structural model. For simplicity, $I_{coh}(q)$ will be simply written I(q).

The characteristics of the elementary scatterers involved in the SAXS experiments are listed in Table 2-5. Z is the number of electrons of the elementary scatterer (E.S.). The coherent X-ray scattering length of the E.S. is proportional to Z and defined by the relation:

$$a\ (cm) = 0.282\ 10^{-12}\ Z. \qquad (15)$$

The coherent X-ray scattering length density, ρ_{sl} (cm) is then obtained through the equation:

$$\rho_{sl} = \frac{a}{v} N_A \tag{16}$$

a (cm) is the scattering length of the E.S, *v* (cm^{3}mol^{-1}), its molar volume and N_A (mol^{-1}) the Avogadro number.

The molar volumes of most of the various E.S. involved in the studied copolymers are listed in the book of Van Krevelen *et al.*[8], and for some others, the additivity law of the partial molar volumes can be used.

Table 2-5 : Characteristics of the various elementary scatterers involved in this study Z is the number of electrons; a, the coherent X-ray scattering length (see Equ.15); v, the molar volumes (amorphous state in black; crystalline state in red), ϕ stands for an aromatic cycle especially those present in the polyMDI shown in Figure 4-9.

E.S.	Z	*v* (cm^{3}mol^{-1})	a (fm=10^{-13} cm)	ρ_{sl} (10^{10} cm^{-2})
-CH$_2$-CH$_2$-O-	24	36.74 / 33.36	67.68	11.09 / 12.22
-CH$_2$-CH(CH$_3$)-O-	32	53.09 / 48.03	90.24	10.24 / 11.31
- ϕ-CH2- ϕ-	88	147.37 / 132.68	248.16	10.14 / 11.26
-CONH-	22	21	62.04	17.79
-OCONH-	30	29	84.60	17.57
-CONH-ϕ-CH2-ϕ-NHOCO-	140	197.37 / 177.38	394.80	12.05 / 13.40

The contrast between the hard and soft segments (-CONH-ϕ-CH2- ϕ -NHOCO- and -CH$_2$-CH(CH$_3$)-O) is then $\Delta\rho^2 = (\rho_s - \rho_h)^2 = 3.2761\ 10^{20}$ cm^{-4}, assuming an amorphous state for both segments. It becomes $\Delta\rho^2 = (\rho_s - \rho_h)^2 = 9.9856\ 10^{20}$ cm^{-4}, when the hard segments are considered in their crystalline state.

2.24 Statistical analysis

All the statistical analyses were performed using SigmaPlot 11.0. Statistical treatments were carried out on at least sets of 3 samples (n=3). Depending on the number of variables, Two-ways or Three Ways analysis of variance (ANOVA) were used with the Holm-Sidak method for pairwise multiple comparisons.

2.25 References

1. Ma, P. X. & Choi, J.-W. Biodegradable Polymer Scaffolds with Well-Defined Interconnected Spherical Pore Network. *Tissue Eng.* **7**, 23–33 (2001).

2. Hepburn, C. *Polyurethane elastomers*. (Springer Science & Business Media, 2012).

3. Briones, R., Serrano, L., Llano-Ponte, R. & Labidi, J. Polyols obtained from solvolysis liquefaction of biodiesel production solid residues. *Chem. Eng. J.* **175**, 169–175 (2011).

4. Modesti, M. & Lorenzetti, A. An experimental method for evaluating isocyanate conversion and trimer formation in polyisocyanate--polyurethane foams. *Eur. Polym. J.* **37**, 949–954 (2001).

5. Aubert, L. *et al.* Collagen-based medical device as a stem cell carrier for regenerative medicine. *Int. J. Mol. Sci.* **18**, (2017).

6. Marshall, A. J. & Ratner, B. D. Quantitative characterization of sphere-templated porous biomaterials. *AIChE J.* **51**, 1221–1232 (2005).

7. Lindner, P. & Zemb, T. Neutron, X-ray and light scattering: introduction to an investigative tool for colloidal and polymeric systems. (1991).

8. Van Krevelen, D. W. & Te Nijenhuis, K. *Properties of polymers: their correlation with chemical structure; their numerical estimation and prediction from additive group contributions*. (Elsevier, 2009).

Chapter 3. Generation and characterization of PU scaffold via "sphere templating"

3.1 Résumé

Comme expliqué dans la Section 1.4, les méthodes d'élaboration de matériaux poreux pour l'ingénierie tissulaire sont nombreuses (moussage chimique, electrospinning, impression 3D etc..). De nombreuses études ont été conduites afin d'établir une corrélation entre les propriétés architecturales du matériau comme par exemple le diamètre des pores, le diamètre des interconnexions ou la porosité, et le comportement induit sur les cellules. Il faut néanmoins rappeler qu'à la vue de la grande diversité de matériaux (et donc de propriétés chimiques) les conclusions s'avèrent parfois contradictoires et difficilement comparables entre elles. Afin de contrôler ces paramètres de manière indépendante, la méthode dite de « sphere-templating » est particulièrement adaptée puisqu'elle permet de générer des matériaux avec un diamètre de pore contrôlé, ainsi qu'un diamètre d'interconnexion contrôlé ce qui rend possible l'étude d'un seul de ces paramètres individuellement.

Dans le chapitre ci-après, nous nous proposons de décrire le développement de matériaux poreux à base de polyuréthane, ainsi que leur caractérisation. Le procédé de « sphere-templating » sera décrit en détails. Celui-ci se base sur l'utilisation d'un agent sacrificiel (dans notre étude, il s'agit de microbilles de paraffine). Nous générons des microbilles à l'aide d'une émulsion dans laquelle la paraffine fondue est mélangée sous agitation à de l'eau avec du tensioactif qui stabilise les gouttes formées. Cette approche nous permet de contrôler la distribution en taille des billes ainsi obtenues selon que la vitesse de rotation est plus ou moins élevée. Une fois les billes formées, celles-ci sont tamisées puis tassées dans un moule et finalement placées dans une enceinte chauffante.

Le chauffage permet de provoquer la coalescence partielle ou frittage des microbilles, ce qui crée un cou entre les billes en contact. La croissance de ce « cou » est dépendante de la température, du temps ainsi que de la taille des billes. Le frittage fut d'abord décrit par Frenkel et est couramment utilisé au cours de procédés industriels. Dans ce chapitre, nous démontrons que le modèle donné par Frenkel ne parvient pas à décrire efficacement la croissance du cou mais qu'un autre modèle, bien que non publié, écrit par Scott Milner, semble mieux rendre compte de nos résultats expérimentaux. Nous montrerons également qu'il est possible d'améliorer encore la description de la cinétique de croissance du cou via un ajustement d'un des paramètres du modèle de Milner. Nous tenterons de fournir des arguments physiques qui permettent de justifier les écarts entre les modèles de Frenkel et de Milner avec nos données expérimentales.

Une fois le chauffage terminé, le polyuréthane liquide est versé sur l'ensemble cohésif de microbilles frittées. Le polymère s'infiltre dans l'espace interstitiel entre les microbilles, puis se solidifie. Une fois le polyuréthane polymérisé, les microbilles de paraffine sont sélectivement dissoutes, laissant ainsi un matériau poreux ayant des pores sphériques dont le rayon est donné par le rayon des microbilles et le rayon des interconnexions est fixé lors du frittage.

Nous démontrerons que le procédé de « sphere templating » est une méthode simple et peu onéreuse qui permet de répondre aux prérequis de l'ingénierie tissulaire. A travers le frittage des microbilles, il est possible de contrôler de manière prédictible, la taille des interconnexions du poreux. Par ailleurs, il est également possible de contrôler la taille des pores via la vitesse de rotation (et donc le cisaillement) durant l'émulsion ainsi que par du tamisage a posteriori. Nous avons choisi d'étudier 3 distributions en taille de billes ayant respectivement des rayons moyens de 33, 62 et 125 µm car ce sont les ordres de grandeurs qui correspondent aux tailles généralement intéressantes en ingénierie tissulaire. Cependant, nous montrerons que nous pouvons produire des billes de rayons < 32 µm jusqu'à des rayons compris entre 300 et 600 µm donnant ainsi la possibilité de confectionner sur-mesure un matériau tridimensionnel.

3.2 Abstract

Sacrificial sphere templating is frequently used to generate macroporous materials with well-defined, interconnected pores. For this purpose, the interstices of a sphere packing are filled with a solidifying matrix, from which the spheres are subsequently removed to obtain interconnected voids. Different types of sintering techniques are used to create bridges between the spheres of the template which lead to interconnections between the pores in the final material. While the science of sintering has been explored in depth in the past, its fine and predictive control is not yet systematically exploited for the generation of macroporous polymers with well-defined morphologies. Using the example of paraffin beads for the initial sphere template and polyurethane for the final porous material, we show here how protocols of bead generation and sintering can be combined to obtain predictive control over the pore and interconnection sizes of the porous material. We show that the dependence of the dimensions of the interconnections on bead size, sintering time and temperature, can be quantitatively predicted by a theory of early-stage, visco-elastic sintering developed by S. Milner [arXiv:1907.05862]. This theory makes more refined approximations than the commonly used Frenkel model, leading to slightly different scalings that describe sintering. The general applicability of the predictive scaling makes it transferable to a wide range of formulations and therefore provides a powerful toolbox to create porous materials with finely controlled morphologies.

3.3 Introduction

Macro-porous materials with pore sizes larger than 10 µm are employed in many fields[1–4], ranging from catalysis, absorption, acoustics, heat transfer to tissue engineering applications. This widespread use is motivated by the broad variety of macroporous materials which can be manufactured in terms of their *porous structure* (open- vs closed-cell, low- vs high density, etc.)[5,6] and their *base materials* (metals, ceramics, synthetic or natural polymers, etc.)[7–9].

Key parameters of the *porous structure* are the dimensions of the pores and of their interconnections. Their impact on the material properties has been put in evidence in different fields. For example, in acoustics, Trinh et al.[10] and Jahani *et al.*[11] showed how the number and size of the interconnections relates to the sound absorption coefficient. Ke *et al.*[12] put in evidence that a graded pore size can improve the sound absorption capacity compared to uniform pore size. In catalysis, a high degree of interconnectivity helps to reduce the pressure drop in reactors[13]. Langlois *et al.*[14] demonstrated how the number and the size of the interconnections are related to the flow resistivity. And for tissue engineering, it has been shown that pore and interconnection sizes impact significantly the behaviour of cells[15,16], fibrotic encapsulation and vascularisation within the body[17–19].

Of particular interest to this Chapter are macro-porous *polymers*. The explicit control of their pore and interconnection sizes remains an important challenge. *Liquid foams or emulsions* may be used as templates for this purpose[20–23]. The pore dimensions can then be controlled via the choice of the foaming/emulsification methods[24] and/or via the formulation[25]. In particular, microfluidic techniques allow to generate porous materials with highly monodisperse and even periodic pores [26,27]. However, since the pore opening mechanisms are badly understood[28,29], it remains a major challenge to control the stability of the initially liquid template and to tune the presence and size of the interconnections. Moreover, the necessity to stabilise the initially liquid template of two immiscible fluids puts important constraints on possible formulations.

One way to overcome these challenges is the so-called *sphere templating* approach[30–32], which is sketched in Figure 3-1. The principle is based on the use of solid spherical particles which are tightly packed in a mould. The interstices between the spheres are infiltrated by an initially liquid matrix (monomers, polymer solutions or melts, etc.), which is then solidified through polymerisation and/or cross-linking. Once the matrix is solidified, the spheres are selectively dissolved in order to leave an interconnected network of pores. In this process, the final pore diameter is given by the diameter of the sacrificial spheres, while the interconnections are obtained by *sintering* of the original sphere template. The latter is obtained by heating the sphere template to temperatures which allow for a material transport from the spheres to the interconnections[33], without melting the entire structure. This material transport is driven by the surface energy of the spheres, which is reduced by a progressive filling of the interconnections creating a growing “neck” between the spheres. The material transport can arise via different phenomena[33]. Of interest here are those which result from viscous flow.

Such sphere templating approaches have been successfully employed in the past for the generation of macro-porous polymers. For example, Somo *et al.* [34] and Chen *et al.*[35] used Poly (methyl methacrylate) *PMMA spheres* to produce scaffolds with micrometric pore size (20 - 110 μm) for tissue engineering purposes. The spheres were sintered for variable times (0 – 30 h) and temperatures (110 - 175°C) to tune the interconnections sizes. *Paraffin* is also regularly used as a porogen, since spherical paraffin beads can be easily produced via quenching of an emulsion[36,37]. For example, Grenier *et al.*[38] produced a polyurethane scaffold using paraffin as sacrificial template, but without sintering. Ma *et al.*[31] sintered paraffin spheres at 37°C for 20 min to generate a porous scaffold. Takagi *et al.* [39] sintered *polyethylene spheres* to form the template of a porous bio-ceramic.

Alternative approaches to sintering for the control of the interconnections may be used. For example, Zhao *et al.*[40] used poly(styrene-co-divinylbenzene) spheres as porogens, creating the neck (i.e interconnections) by addition of an adhesive which accumulated in the contact zone of the spheres. In another case, Descamps *et al.* [41] created the neck between PMMA spheres using acetone which slightly dissolved the spheres creating a neck at their contact.

Even if sphere templating via *sintering* is regularly used to obtain macro-porous polymers, the detailed mechanism of the formation of the interconnections has not been studied in a sufficiently systematic manner to profit from the predictive power of an accompanying model. As discussed in more detail in Section 3.4, for systems where the relaxation dynamics can be described by a viscous flow, the first theoretical description of the phenomenon dates back to a theory proposed by Frenkel[42]. His model has been used quite successfully to account for a wide range of experimental results[37,43,44]. Some modifications of Frenkel’s theory were made by Bellehumeur *et al.*[45] to take into account the viscoelastic properties of polymeric spheres. More recently, Frenkel’s model has been challenged by Milner[46,47] who established an analogy between elastic Hertzian contacts and the early stages of viscous sintering. Milner showed that the characteristic size of the flow in the neck region is incorrectly estimated in Frenkel’s model and that the resulting correction leads to a slightly different scaling for the neck evolution (Section 3.4). This improved model was shown to describe successfully the flattening polystyrene latex microsphere on glass surfaces[47]. Moreover, Milner’s analysis provides predictions of the scaling for *visco-elastic* spheres, for which the flow cannot be considered as purely viscous.

Goal of this Chapter is to evaluate the proposed scalings describing the growth of the necks (interconnections) during sintering by providing a quantitative investigation of the sphere templating approach to generate porous polymeric structures with explicitly controlled pore and interconnection diameters. As template system we use spheres of paraffin with radii R in the range of 50 - 300 μm (top row Figure 3-1) which we generate via an emulsification process (Section 2.2). We propose a systematic approach to control simultaneously the bead size distribution (i.e. the resulting pore size distribution) and the neck formation between the beads (i.e. the distribution of the interconnection sizes) (middle row of Figure 3-1). We show that for the entire range of the used control parameters, the associated mechanisms are better captured by Milner's model (Section 3.4) than by Frenkel's. We also show that the best description is obtained by taking into account the visco-elastic nature of the paraffin. By replicating the sintered sphere templates, we obtain macroporous polyurethanes (bottom row of Figure 3-1) with finely controlled pore and interconnection sizes. Since this approach can be transferred to a wide range of polymers, it will provide the reader with a powerful tool for the design of macro-porous polymers.

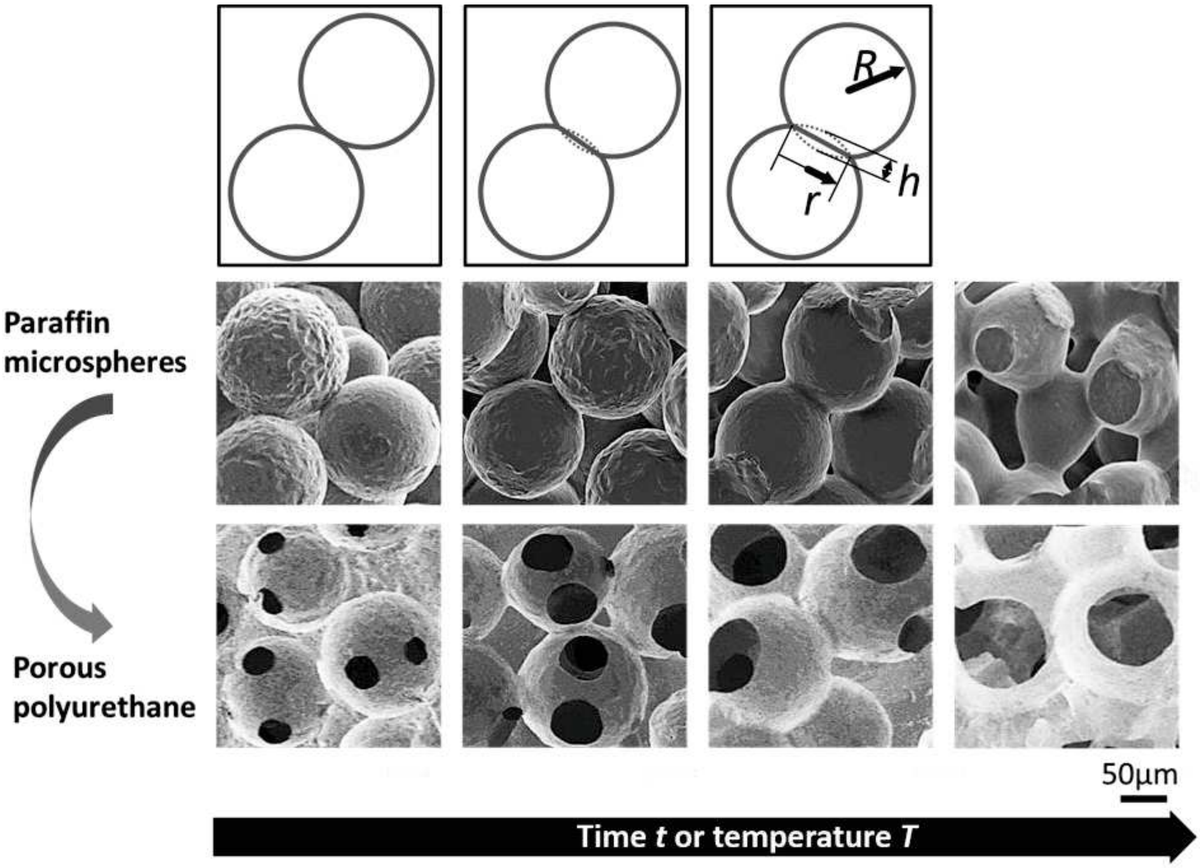

Figure 3-1: Examples of SEM images of paraffin beads (central row) showing the increase of interconnection radius r *with increasing sintering time t or temperature T. The bottom row shows the macroporous polyurethanes obtained from moulding the sphere template. The top row sketches the deformation of two contacting spheres together with the variables used in this article.*

3.4 Theory

The sintering process of spheres in contact is driven by the high surface energy of the sphere packing which is proportional to its surface area. An important reduction of this surface area is achieved by progressively filling the contact zones between the spheres. This filling process can arise in many different ways[33], ranging from solid-state diffusion of the sphere surface to viscous flow of the contact zone. Which type of mechanism is dominant depends on the type of material used and on the sintering conditions (temperature in particular).

Paraffin wax is a mixture of alkanes, iso-alkanes or cyclo-alkanes[48] and the sintering process at work in our experiments is well described by a viscous flow in the vicinity of the contact area of the spheres induced by surface forces. A comprehensive theoretical treatment of the complete dynamics is highly complex due to the non-trivial intermediate states of the system. A thorough and illuminating treatment of the early stages of sintering has been given recently by Milner[46,47]. Here we shall only provide a short summary of the main arguments.

An initial dimensional analysis of the problem shows that for a Newtonian fluid of viscosity η, the evolution of the radius $r(t)$ of the circular, symmetric contact between two spheres of radius R (see Figure 3-2) must fulfil the general scaling

$$r(t) = f\left(\frac{\gamma t}{R\eta}\right) R. \qquad (17)$$

Here, t is the time and γ the surface tension of the spheres. The mass density does not enter since the sintering processes are sufficiently slow to neglect inertial effects. Additionally, the considered sample heights are sufficiently small so that the pressure force induced by gravitation can be neglected with respect to surface forces.

Note that

$$\tau = \frac{R\eta}{\gamma} \qquad (18)$$

provides a characteristic sintering time which highlights the important influence of the sphere radius: the smaller the spheres, the faster the sintering process.

In the regime of small deformations ($r(t)/R \ll 1$), Equ. (17) is expected to be well approximated by a power law[46]

$$r(t) = \left(C_\alpha \frac{\gamma}{\eta}\right)^{\alpha} t^{\alpha} R^{1-\alpha}, \qquad (19)$$

where C_α is a numerical constant. First quantitative expressions for Equ. (19) were provided by Frenkel in 1945[42]. Using a scaling argument, he predicted that $\alpha = 1/2$ with $C_\alpha = 4$. The resulting expression has been used quite successfully in the past to describe experimental observations[37,43,44]. However, as Milner pointed out, such a scaling does not capture properly the underlying mechanism.

The dynamics is controlled by the balance between the rate of change of the surface energy, $\dot{E}_{\mathrm{surf}} = -2\pi\gamma(\mathrm{d}r^2/\mathrm{d}t)$, and the dissipation rate $\dot{E}_{\mathrm{kin}} = -(\eta/2)\int[\partial_{\mathrm{rk}} v_i + \partial_{\mathrm{ri}} v_k]^2\, d^3\tau$, where v is the velocity field of the sphere with the indices i,k,r indicating the Cartesian coordinates x,y,z[49]. Milner noticed that the typical strain rate $\dot{\varepsilon} \approx \partial_r v$ scales as $\dot{h}/r$, where $[2R - h(t)]$ is the distance between the centres of the spheres at time t. Note that in the early stage of sintering, one can approximate the geometry by overlapping spheres, as sketched in Figure 3-1. This gives simply $h \approx r^2/R$. The key difference between Milner's and Frenkel's approach is to realise that the flow extends along the symmetry axis only up to a characteristic length r (and not R), since at early times, the only relevant length scale of the flow (whose equation is $\nabla^2(\vec{\nabla} \times \vec{v}) = \vec{0}$) is given by the boundary extension, namely by r. The typical volume in which the flow develops is therefore proportional to r^3, as in the Hertz contact problem[50], and not proportional to R^3, as assumed by Frenkel. Since the curvature imposed by the spherical geometry is negligible, one can therefore write the scaling $\dot{E}_{\mathrm{kin}} \approx -\eta r^3 \left[\frac{\dot{h}}{r}\right]^2 \approx -\eta r^3 \left[\frac{\dot{r}}{R}\right]^2$, and the balance $\gamma r \dot{r} = \frac{\eta r^3 \dot{r}^2}{R^2}$, giving

$$\left(\frac{r}{R}\right)^3 \propto \frac{t}{\tau}. \qquad (20)$$

This leads to the dimensional form provided in Equ. (19) with $\alpha = 1/3$. Thanks to a refined argument which exploits quantitatively the geometry of the Hertz contact, Milner also obtains the prefactor[46] $C_\alpha = 3\pi/32$. Equ. (19) therefore becomes

$$r(t) = \left(\frac{3\pi t}{32\tau}\right)^{1/3} R = \left(\frac{3\pi}{32}\right)^{1/3} \left(\frac{\gamma}{\eta}\right)^{1/3} t^{1/3} R^{2/3}. \qquad (21)$$

It is important to keep in mind that this initial growth regime, which we may call the "crushing flow", is expected to dominate only for small deformations. For larger deformations, a secondary "smoothing flow" takes over. Both types of flow are sketched in Figure 3-2. The smoothing flow is driven by the fact that the contact zone between the two spheres is cusp-like, with very small radii of curvature. As a result, the surface tension also drives a radial flow in the neck region. This flow becomes dominant for larger deformations, for which the growth of the neck radius r is predicted (see Annexe 3.8.2) to become linearly dependent on time t and independent of R, i.e.

$$r \approx \frac{\pi\gamma}{\eta} t. \qquad (22)$$

Comparison of Equ.s (21) and (22) shows that the *crushing flow* with $r \propto t^{1/3}$ dominates at short times because $\left(\frac{t}{\tau}\right)^{1/3} \gg (t/\tau)$ for $t \to 0$. Quantitatively, it yields also the criterion $\frac{r(t)}{R} \approx 0.18$ beyond which the *smoothing flow* should start to play a role. However, different experimental investigations[47], including our own, show that experimentally this onset seems to arise much later than theoretically predicted. See Section 3.6 for a more in-depth discussion of this question.

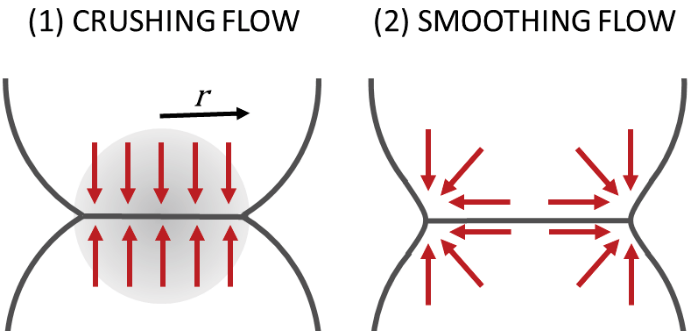

Figure 3-2: Schematic presentation of the crushing flow and the smoothing flow. Both take place simultaneously, with the crushing flow dominating at early times due to its larger growth rate

3.5 *General description of the results*

Figure 3-3 shows a series of SEM images for different sphere sizes and sintering temperatures after 18 hours of sintering time. Images after shorter sintering times show the same overall pattern but with less pronounced evolutions of the interconnections. Following the indications of Figure 3-1, we denote in the following $\langle R \rangle$ the average radius of the spheres and $\langle r \rangle$ the average radius of their interconnections.

From Figure 3-3 we can see very clearly the influence of the sphere radius R and the sintering temperature T on the kinetics of formation of the interconnections. Globally, one observes that the radius r of the interconnections increases with temperature. For example, at the lowest temperature and for the largest sphere sizes, the interconnections are almost singularities as it is the case for two hard spheres in contact. With increasing temperature or decreasing sphere size, the deformation is accelerated and the spheres start to flatten earlier, forming a neck which can be observed from the side or through its footprint left after breaking the contact (i.e. the flat circles visible on the spheres). This flattening is a consequence of the "crushing flow" (Figure 3-2 and Section 3.4) as described by Milner. It is clearly seen at 40°C for the largest spheres ($<R>$ = 125 µm). For smaller spheres at higher temperatures, one observes that the radius of curvature in the cusp of the interconnection increases, i.e. the interconnection does not only grow in area but its boundaries also becomes increasingly rounded. This is a signature of the onset of the so-called “smoothing flow”, also described by Milner (Figure 3-2, Sections 3.4 and 3.8.2), which arises during the later stages of sintering, when the viscous flow becomes radial within the interconnections to decrease the high curvatures of the cusp.

For the smallest spheres (<*R*> = 33 µm), the spheres coalesce completely at the highest temperature. This is why the item is represented by a cross in Figure 3-3.

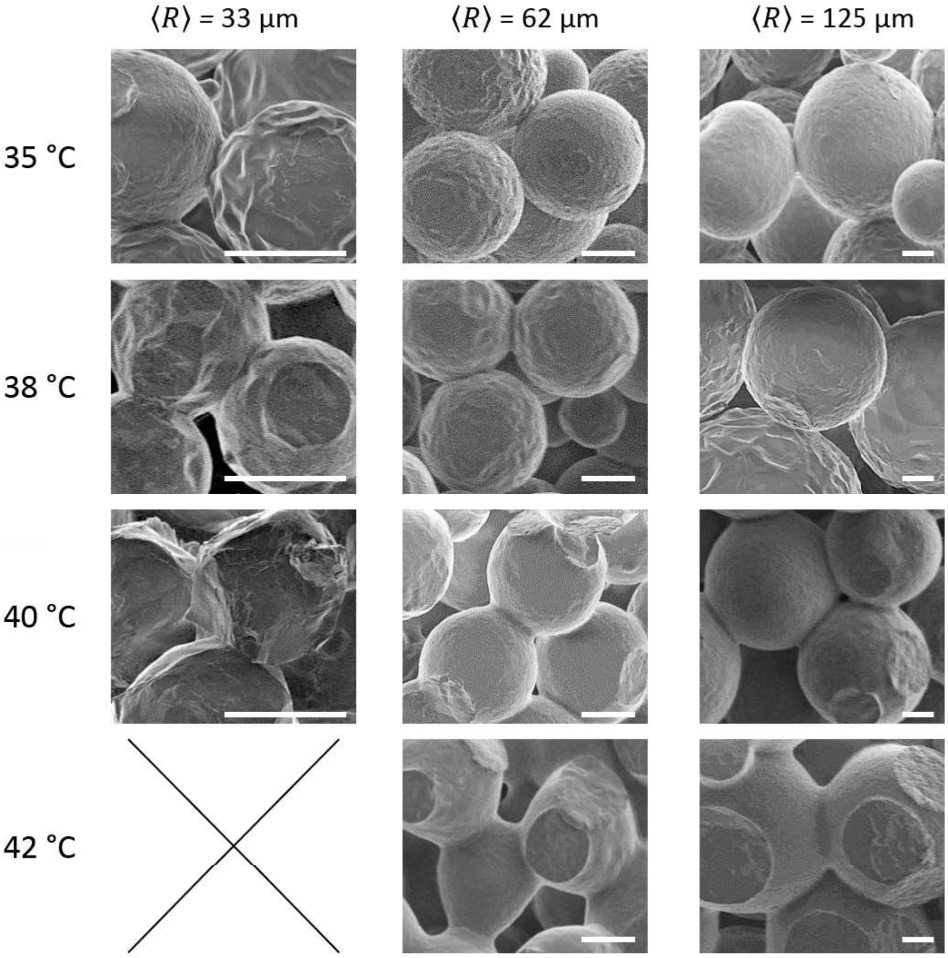

Figure 3-3:SEM images of paraffin sphere templates having an average radius of <R> = 33 µm (left column), <R> = 62 µm (column in the middle) and <R> = 125 µm (right column) for several sintering temperatures. All templates were sintered for 18 hours. The scale bars are 50 µm.

Figure 3-4 shows the macroporous polyurethanes obtained from the sphere templates shown in Figure 3-3. One notices that these are accurate negative copies of the initial template, containing spherical pores with circular interconnections. Accordingly, the radii of the interconnections increase in the same manner with increasing temperature and decreasing sphere radius. For the structures with the smallest pore radii, the interstices between the spheres are too small to allow for the polymer to spread homogeneously through the template. This is why these structures are represented by a cross in Figure 3-4. One notices that when the radius of the interconnections becomes of the order of the sphere radius, the structure loses its spherical morphology and evolves into a very open “bicontinous like” shape, which may be interesting for applications looking to optimise permeability while maintaining a characteristic pore size and a certain mechanical stability of the material. This transition happens between 35 and 38°C for the smallest pore radius ($\langle R \rangle$ = 33 µm) and between 40 and 42°C for the structure with the intermediate pore radius ($\langle R \rangle$ = 62 µm). For the largest pore diameters, the transition happens above 42°C.

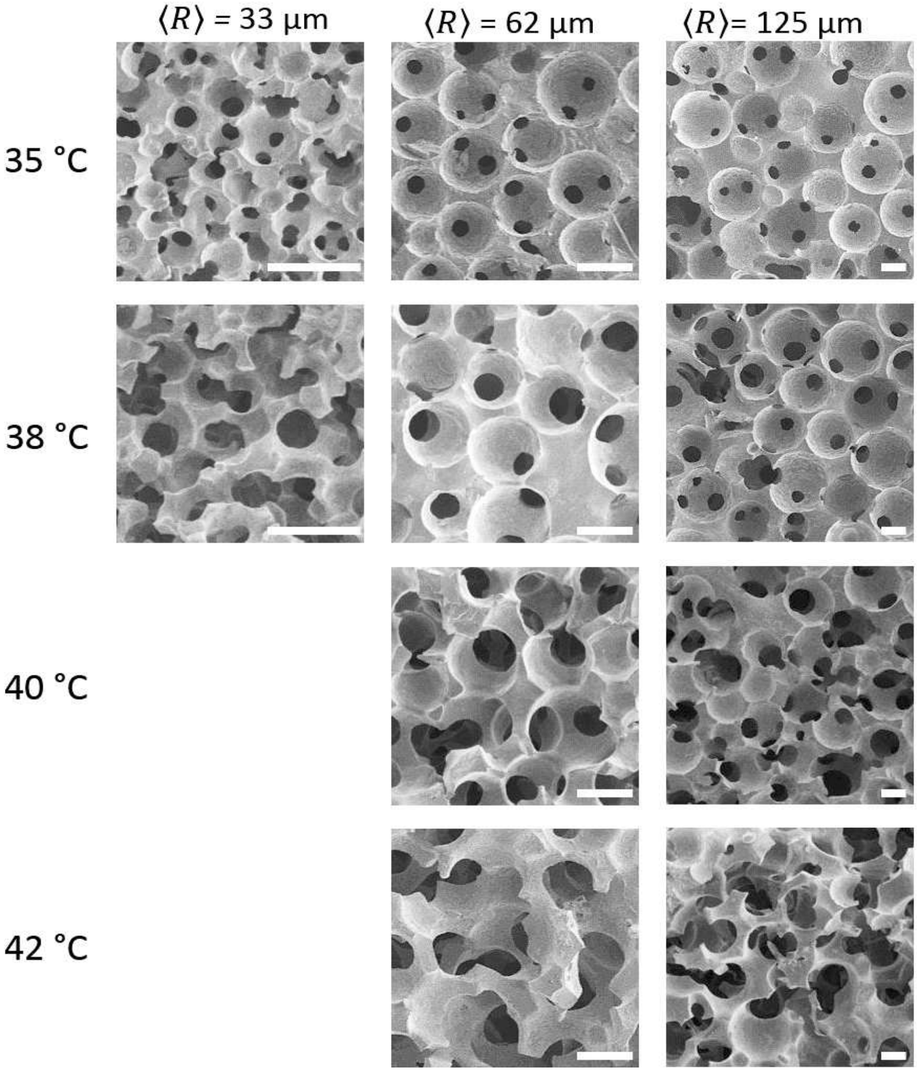

Figure 3-4: Macroporous polyurethanes generated from the sphere templates shown in Figure 3-3. Scale bars: 100 µm.

3.6 Quantitative analysis and interpretation

Figure 3-5a shows an example of the evolution of the mean radius <*r*> of the interconnections with time for the same sphere sizes shown in Figure 3-3 ($\langle R \rangle$ = 33, 62 and 125 µm) at 38°C. The error bars are obtained by the procedure described in Section 2.6. Despite some scatter, all curves follow a clear trend: a rapid increase of $\langle r \rangle$ over a few hours is followed by a much slower evolution. Moreover, the evolution of $\langle r\rangle$ depends clearly on the radius $\langle R\rangle$ of the spheres. A natural temptation would be to normalise the data by $\langle R\rangle$. However, as Figure 3-5b shows, this scaling does not collapse the data since it does not capture properly the underlying mechanisms: viscous flow driven by surface tension forces. A more appropriate scaling is provided by Milner[46] and given in Equ. (2) in Section 3.4: $\langle r\rangle/\langle R\rangle^{2/3}$ should be plotted as a function of $t^{1/3}$. Equ. (21) predicts that this should collapse the data on straight lines of slope $\left(\frac{3\pi}{32}\right)^{1/3}\left(\frac{\gamma}{\eta}\right)^{1/3}$. Since neither γ nor η depend on the sphere radius R or on the sintering time t, all curves are expected to fall onto the same master curve. Figure 3-5c shows that this is indeed the case within the experimental scatter of the data.

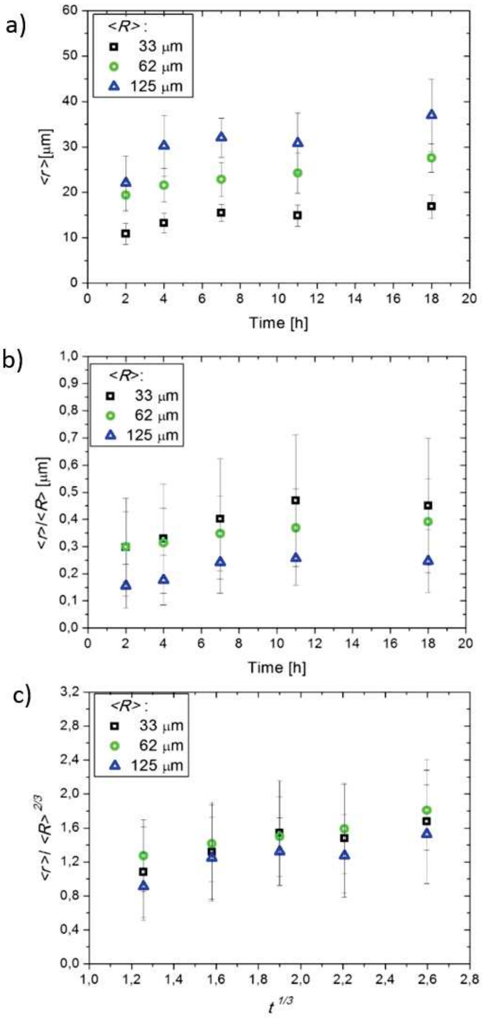

Figure 3-5 : Evolution of the average interconnection radius ⟨r⟩ as a function of the sintering time t for three different sphere radii at a sintering temperature of 38°C. (a) Unscaled results. (b) Trivial Scaling. (c) Milner's scaling. Error bars are calculated according to Section 2.6.

We further investigated the influence of the sintering temperature T on the formation of the interconnections. A set of examples of obtained results is shown in Figure 3-6 for the same sphere radii as in in Figure 3-3 ($\langle R\rangle$ = 33, 62, 125 μm) after 18 hours of sintering for a temperature range of 35-

42°C. As expected, $\langle r \rangle$ increases significantly with the sintering temperature. As in Figure 3-5a, $\langle r \rangle$ depends strongly on the sphere radii $\langle R \rangle$, a dependence which a trivial scaling $\langle r \rangle / \langle R \rangle$ (Figure 3-6b) cannot remove for the same reasons as for Figure 3-5a. Figure 3-6c therefore applies Milner's scaling of Equ. (21) by plotting $\langle r \rangle / \langle R \rangle^{2/3}$ as a function of temperature T. This collapses the data onto a single master curve within the experimental scatter. The existence of this master curve shows that Milner's scaling captures well the underlying physical phenomena. It also confirms that the ratio (γ / η) evolves with temperature in the same manner for all sphere sizes, implying the absence of finite size effects. The interpretation of the overall shape of the master curve depends on how exactly (γ / η) depends on temperature, which is discussed in more detail at the end of this section.

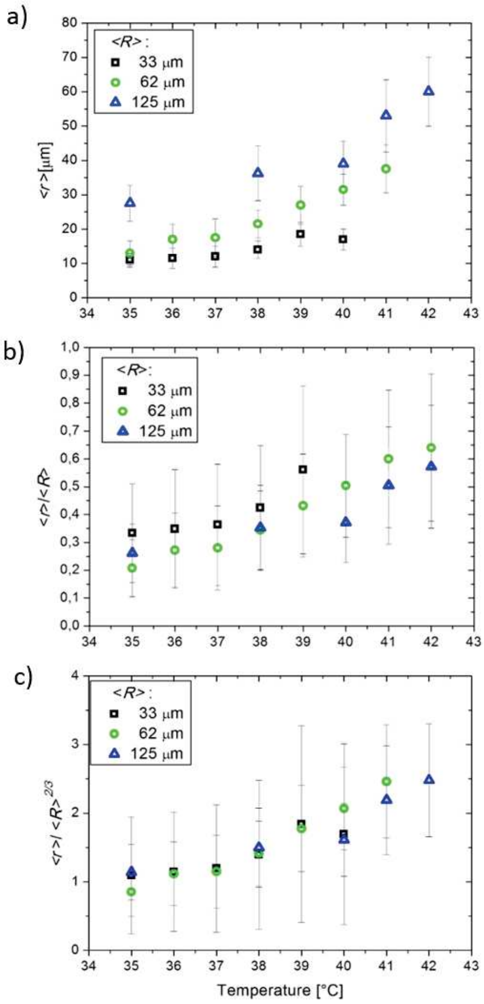

Figure 3-6: a) Evolution of the mean interconnection radius $\langle r \rangle$ as a function of the temperature T for three different sphere radii after 18 hours of sintering. (a) Unscaled results. (b) Trivial Scaling. (c) Milner's scaling. Error bars are calculated according to Section 2.6.

For illustrative purposes, Figure 3-5 and Figure 3-6 contained only a subset of the full data set, which is shown in Figure 3-7a for different sphere sizes ($\langle R \rangle$ = 33, 62, 125 μm), sintering temperatures (T = 35 – 42°C) and sintering times (2-18 hours). As in the examples of Figure 3-5 and Figure 3-6, the trivial scaling $\langle r \rangle / \langle R \rangle$ shown in Figure 3-7b cannot capture the main trends. We therefore scale all data by the scaling provided by Equ. (19) in Section 3.4

$$\left[\frac{\langle r(t)\rangle}{t^{\alpha}\langle R\rangle^{1-\alpha}}\right]^{1/\alpha} = C_{\alpha}\frac{\gamma}{\eta}. \qquad (23)$$

$\alpha = 1/2$ gives Frenkel's scaling while $\alpha = 1/3$ gives Milner's scaling. We chose to use the exponent 1/α to ensure that the units on the y-axis are homogenous, rendering the three curves comparable.

A first observation is that while the data remain fairly scattered after application of Frenkel's scaling, Milner's scaling collapses the data more convincingly, especially for the lower temperatures. To quantify the quality of the scaling, we fit the scaled data to a second order polynomial

$$\left[\frac{\langle r(t)\rangle}{t^{\alpha}\langle R\rangle^{1-\alpha}}\right]^{1/\alpha} = a(T-35°C)^{2} + b(T-35°C) + c \equiv B_{\alpha}(T), \qquad (24)$$

with a,b and c being the fitting parameters. This captures in particular the temperature variation of the viscosity η of the paraffin, which is quite important since the experiments are done in the first endothermic shoulder in the DSC curve (Section 2.22) close to the melting transition. The temperature variation of γ can be assumed negligible in comparison to that of η in our temperature range. The resulting fits are shown in Figure 3-7c and d, while the resulting fit parameters are given in Table 3-1.

Table 3-1: Summary of exponents and fit parameters obtained for the different scaling by fitting Equ (24).

Name	α	a	b	c	Err
Frenkel's scaling	1/2	2.10^{-2}	-2.10^{-6}	33.10^{-2}	3617
Milner's scaling	1/3	9.10^{-3}	-1.10^{-2}	5.10^{-2}	1235
Free scaling	1/5	1.10^{-3}	-2.10^{-3}	1.10^{-3}	586

To obtain a quantitative assessment of the difference between these models and our experimental results, we generate an error function

$$E_{rr} = \sum_{i,j}\left[r_{exp_{i,j}} - t_{exp_{i,j}}^{\alpha} R_{exp_{i,j}}^{1-\alpha}\left(a(T-35)^{2} + b(T-35) + c\right)^{\alpha}\right]^{2} \qquad (25)$$

where i represents the set of sintering temperatures and j the different sintering times. In case of a perfect fit to the data one would find Err = 0. The obtained errors are shown in Figure 3-7 and in the last column of Table 3-1.

This procedure confirms the visual impression that Milner's scaling (Figure 3-7d), $\alpha = 1/3$, Err = 1235) describes better the data than Frenkel's scaling (Figure 3-7c), $\alpha = 1/2$, Err = 3618).

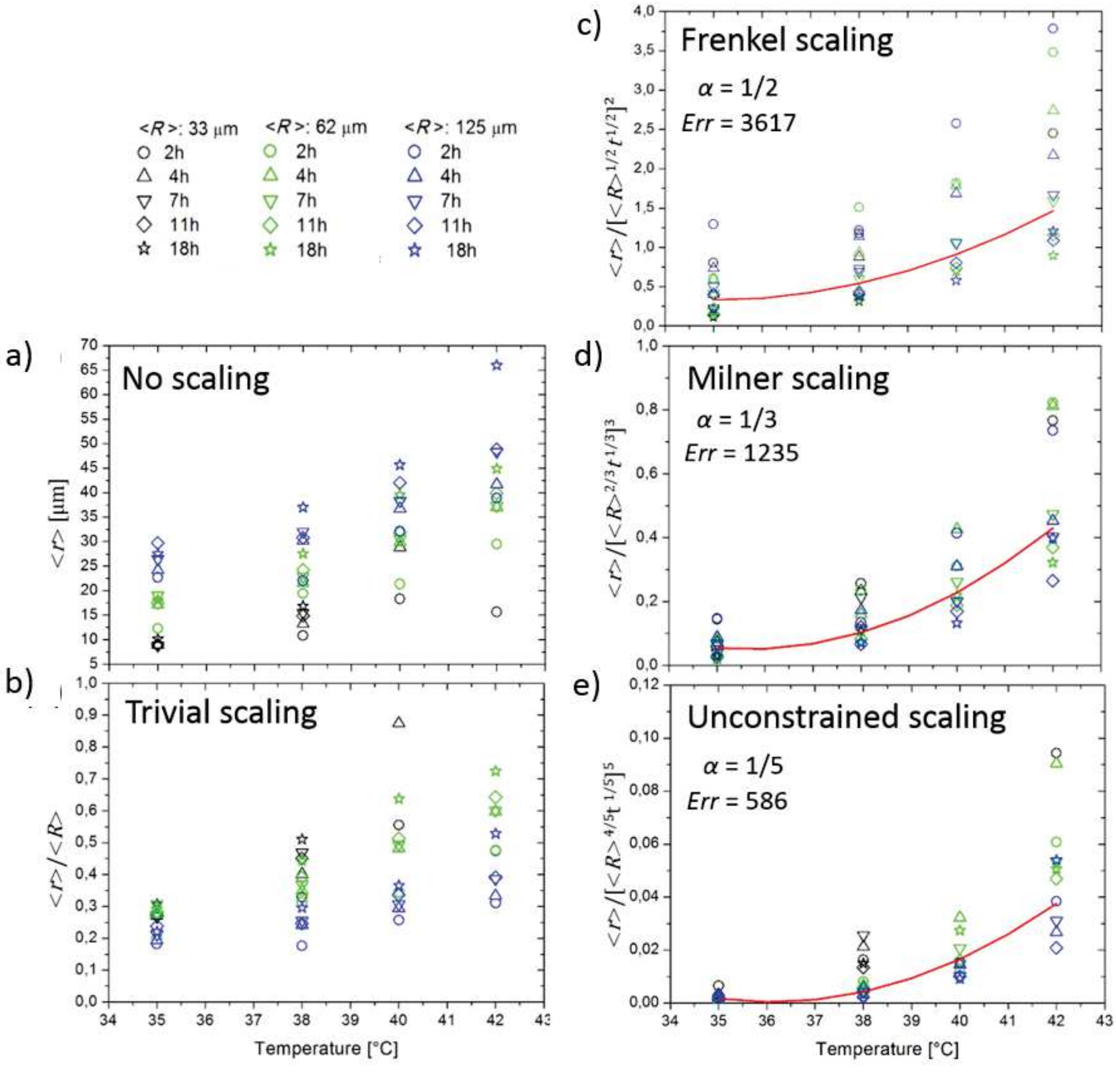

Figure 3-7: a) Summary of all data. b-e) Scaled data using $[r/R^{1-\alpha}t^{\alpha}]^{1/\alpha}$ as a function of temperature for α-values following b) the trivial scaling (α = 0), (c) Frenkel's model (α = ½), d) Milner's model (α = 1/3) using an unconstrained fit (α ≈ 0,2). The red curve indicates the best fits obtained by Equ.(24). The associated fitting parameters are summarised in Table 3-1.

An important question arises as to the ideal exponent α to collapse the data on a mastercurve. We therefore provide in Figure 3-7d a fit which also uses α as fitting parameter. This fit shows that the data are, in fact, more accurately described (*Err* = 586) by an exponent of $\alpha \approx 0.2$, which is even lower than the one proposed by Milner's model. This lower value is hardly surprising when taking into consideration that all scalings considered up to now only use a temperature-dependent, but Newtonian shear viscosity.

However, taking a closer look at Figure 3-8 shows that the shear viscosity η of the paraffin (obtained through shear rheology, Section 2.17) does not only depend on the temperature T, but also on the shear frequency ω. In fact, the $\eta\,(\omega)$ curves are well fitted by a simple power law

$$\eta(\omega) = \xi(T)\omega^{\nu(T)}, \tag{26}$$

with$|\nu| \epsilon]0,1[$. The resulting fits are shown in Figure 3-8 together with the obtained fit parameters in Table 3-2.

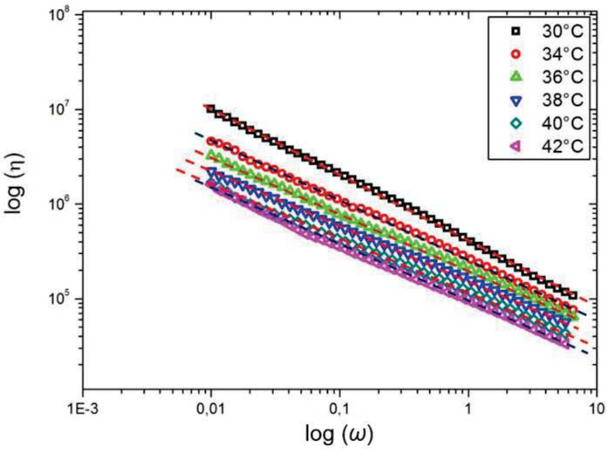

Figure 3-8: Frequency-dependent shear viscosity of paraffin for different temperatures obtained by shear rheology (Section 2.17). Dashed lines indicate the fit obtained using the power law of Equ.(26). The fit parameters are given in Table 3-2.

Table 3-2: Fit parameters obtained after fitting Equ. (26) to the viscosity data obtained from rheology (Section 2.17).

Temperature (°C)	ξ (Pa.s)	ν
30	449 148	-0.66
34	272 835	-0.61
36	206 597	-0.59
38	158 684	-0.57
40	117 897	-0.56
42	93 655	-0.59

In theory, for ω probing timescales slower than the longest natural relaxation time ω_{paraff} of the paraffin, $\eta(\omega)$ should reach a plateau $\eta(\omega) \approx \eta$, characteristic of Newtonian behaviour. The lowest frequency we could measure reliably is $\omega = 0.01\ \text{s}^{-1}$, which corresponds to a characteristic experimental time of $\tau_{\text{rh}} \approx$ 600 s, which is still much shorter than the 18 h of our experiments. However, for paraffin below the melting temperature, ω_{paraff} is likely to be extremely small, and addresses timescales larger than the 18 hours of our experiments. This assumption is backed by noticing that curves of Figure 3-8 do not show any bending at low frequencies which would be the precursor of a crossover of the Newtonian regime. In the following, we therefore make the bold assumption that the powerlaw behaviour of Figure 3-8 and therefore Equ. (26) can be extended to the whole frequency range relevant to our sintering experiments (i.e. down to frequencies of $\omega \approx 2\pi/(18\ \mathrm{h})$.

In his paper[46], Milner extended the scaling of Equ. (21) to the sintering of *viscoelastic* liquids, leading to the prediction

$$r(t) = \left(\frac{3\pi\gamma R^2 J(t)}{32}\right)^{1/3}. \qquad (27)$$

Here *J(t)* is the creep compliance of the viscoelastic spheres[51]. Note that the asymptotic regime of *J(t)* for very long times is t/η. Therefore, Equ. (27) is in full accordance with its Newtonian analogue given in Equ. (21) in the appropriate time regime.

J(t) can be obtained from $\eta(\omega)$ via some mathematical manipulation. As shown in the Appendix 3.8.3, using the power law relation of Equ. (26), we obtain that

$$J(t) = \frac{\sin(\pi\nu/2)}{\xi(1\ \ \nu)\Gamma(1\ \ \nu)} t^{\ \nu+1}. \qquad (28)$$

The non-Newtonian scaling of Equ. (27) therefore becomes

$$r(t) = \left(\frac{3\pi R^2 \sin(\frac{\pi\nu}{2})}{32\xi(1-\nu)\Gamma(1-\nu)}\right)^{1/3} t^{(1-\nu)/3} \qquad (29)$$

One notices that the viscoelastic model accounts naturally for the trend towards an exponent α smaller than 1/3 expressed in the unconstrained fit in Figure 3-7e .

In Equ. (29), the only unknown (temperature-dependent) parameter is the surface tension γ of the paraffin, while ν and ξ are known from fitting the rheological measurements of data of Figure 3-8. Therefore, we performed a fit of $\gamma(T)$ by assuming a second order polynomial expansion around the lowest temperature 35°C: $\gamma(T) = \gamma_0(T) + (T-35)\gamma_1(T) + (T-35)^2\gamma_2(T)$.

In Figure 3-9 are shown the results for the best fits for all the data. It is performed with the function "*fminsearch*" of Matlab© which looks for a minimum for

$$F(a_0,a_1,a_2) = \sum_j \left[\langle r_j\rangle - C_j^{1/3} t_j^{(1-\nu_j)/3} \langle R_j\rangle^{2/3} \left(\gamma_0(T) + (T_j-35)\gamma_1 + (T_j-35)^2\gamma_2\right)^{1/3}\right]^2, \qquad (30)$$

where

$$C_j \equiv \frac{3\pi\sin(\pi\nu_j/2)}{32\xi_j(1-\nu_j)\Gamma(1-\nu_j)}. \qquad (31)$$

Here j represents a measure, namely a set of time t_j or temperature T_j (determining the viscoelastic parameters $\xi_j = \xi(T_j)$ and $\nu_j = \nu(T_j)$, average radii of the spheres $\langle R_j \rangle$ and the corresponding average radii of the interconnections $\langle r_j \rangle$). The function of the fitting curve of Figure 3-9 is $\gamma(T_j) = \left\{ r_j / \left[C_j^{1/3} t_j^{(1-\nu_j)/3} R_j^{2/3} \right] \right\}^3$ as a function of temperature, together with the result of the best fit obtained for the values of $(\gamma_0, \gamma_1, \gamma_2)$ shown in the text box of the figure.

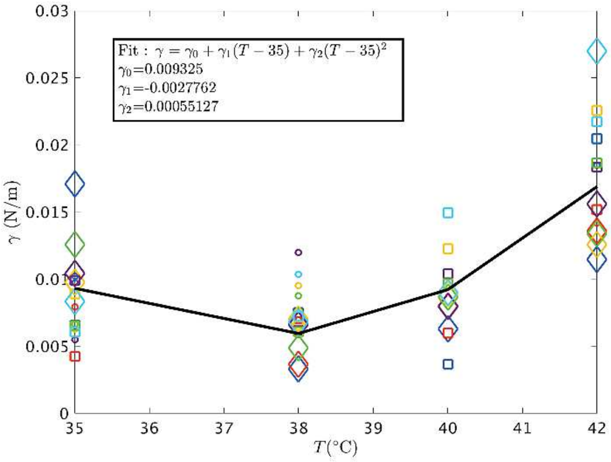

Figure 3-9: Best fit results for the surface tension γ(T) with all the data available. The different sizes are represented by circles (<R> = 33 μm), squares (<R> = 62 μm), and diamonds (<R> = 125 μm) respectively. The different times: t = 1,2, 4, 7, 11, 18 hours are represented by the colour marine blue, red, yellow, purple, green, and cyan, respectively.

The characteristic values obtained for $\gamma \approx 0.01$ N/m are very satisfactory, since they are compatible with the values for the wax surface tension measured in the literature (see www.accudynet.com/polymer_surface_data/paraffin.pdf), where it is found that $\gamma \approx 0.02$ N/m . On the other hand, the temperature dependence of $\gamma(T)$ we found is not correct, because $\gamma(T)$ is always a decreasing function of temperature, which is against the temperature dependence of Figure 3-9. However, a significant increase in temperature is observed only for the highest temperature T= 42 °C. For the loweest temperatures, γ is essentially independent of temperature. At the highest temperature, the problem may presumably arise from a failure of our assumption according to which the viscoelastic behaviour of $\eta(\omega) = \xi\omega^{-\nu}$ could be extended to the extremely low frequency range appropriated for our experiment. At this temperature, the longest relaxation time of the paraffin may be shorter than the 18 hours of our longest experiment. Another possible cause of discrepancy could be sought in the fact that for the highest temperature, the sintering dynamics is the fastest, and therefore, the largest values of $\langle r \rangle / \langle R \rangle$ are measured. As a result, some quantitative discrepancies with the theory which is intended to describe the $\langle r \rangle / \langle R \rangle << 1$ regime only, might show up here. In particular, the secondary flow described in the annex 3.8.2 could be no longer negligible here. And last but not least, as Figure 3-8 shows, even though the viscosity remains well described by a power law in the measured range, the slope of the curve is inconsistent with the results for the other temperatures. This may be due to a change in regime in the response of the paraffin.

3.7 Conclusions

In this article we present the results of thoroughly conducted sintering experiments with paraffin spheres. All results were compared to four different scaling (Table 3-3) of the general form of Equ. (21), which result from slightly different physical assumptions. All scalings assume viscous flow as response to the driving force of surface minimisation. The historic scaling by Frenkel assumes that the extension of the associated flow field is of the order of the sphere radius R, while Milner's scaling assumes that it has a reduced extension of the order of the interconnection radius r. Using the same scaling, we also provide a fit to the experimental data with an unconstrained exponent, which we find to be even lower than the one predicted by Frenkel and Milner. While all these scalings assume a unique Newtonian viscosity of the paraffin for each temperature, we provide a final scaling (also inspired by Milner), which takes into account the visco-elastic nature of paraffin.

Table 3-3: Summary of scalings used for the different fitting procedures in this article. In these formula, the temperature-dependent prefactors $B_{1/2,fit}$, $B_{1/3,fit}$, $B_{\alpha,fit}$ and γ_{fit} are the results of the best fits appropriate to each case given in Equ. (24). Notice that for the unconstrained fit, the exponent α is also an adjusted parameter.

Model	Frenkel	Newtonian Milner	Unconstrained exponent	Viscoelastic Milner
Formula for $\frac{r(t)}{R}$	$\left(\frac{B_{1/2,fit}t}{R}\right)^{1/2}$	$\left(\frac{B_{1/3,fit}t}{R}\right)^{1/3}$	$\left(\frac{B_{\alpha,fit}t}{R}\right)^{\alpha}$	$\left(\frac{3\pi\gamma_{fit}\sin(\pi\gamma/2)}{32R\xi(1-\nu)\Gamma(1-\nu)}\right)^{1/3} t^{(1-\nu)/3}$

In order to compare how well these four scalings capture the experimental data, we plot in Figure 3-10 the experimental results of the scaled interconnection radii $[r(t)/R]_{\mathrm{exp}}$ on the X-axis together with the values of $[r(t)/R]_{\mathrm{theo}}$ predicted by each of the scalings (Table 3-3) on the Y-axis. The latter include the different fit parameters obtained in Section 3.6. Figure 3-10 shows convincingly that the viscoelastic model gives the best results in collapsing fairly neatly the data on the line $X = Y$, being even superior to the unconstrained fit! The data treated by the viscoelastic fit are slightly above the line $Y = X$ for values of $X > 0.25$. However, this deviation can be explained by two arguments. On the one hand it is coherent with the onset of the smoothing flow, which is expected to start playing a role for for $r/R > 0.18$ and which follows a different scaling, as discussed in Section 3.4 and in the Annexe 3.8.2. The smoothing flow would lead to larger X-values, as observed. On the other hand, at these large $r(t)/R$ values, interconnections start to interact on the surfaces of the spheres, leading to a shift away from the scalings which are derived for isolated interconnections. In summary we can therefore state that both of Milner's scalings capture our experiments better than Frenkel's scaling, while the quality of the visco-elastic scaling clearly indicates the importance of taking into account the visco-elastic nature of the paraffin spheres.

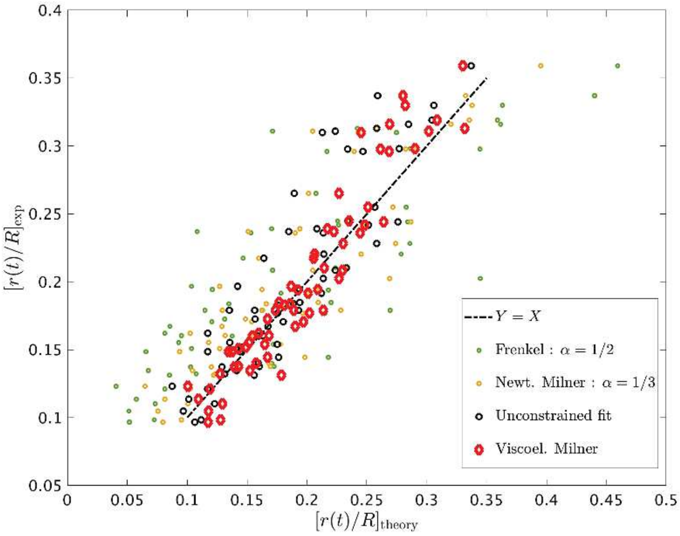

Figure 3-10: Experimental values of r(t)/R as a function of the values predicted by the different theories, where the best fit of the unknown parameter have been chosen, see Table 3-1 . A theory describing perfectly data devoid of any measurement errors would match on the black dash-dotted line X=Y

In order to fully validate this conclusion, it will be important to conduct future experiments with model-spheres in which both, visco-elasticity and surface energy are known and controlled in a precise manner. It would be important to validate not only the visco-elastic model, but to access also the transition to the regime in which the smoothing flow becomes dominant. Last but not least, it would be interesting to analyse the influence of the multiple contacts on each sphere[52].

3.8 Appendix

3.8.1 Sphere sizes for higher shear rates

In Figure 3-11 we show for the interested reader the size distributions of paraffin spheres obtained by a wider range of shear rates than the ones used for this article.

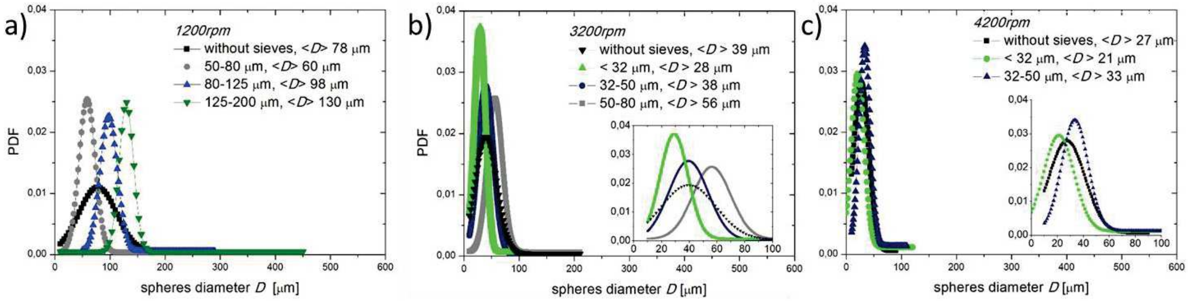

Figure 3-11: Size distributions of paraffin spheres generated by an emulsion under stirring at 1200 rpm a), 3200 rpm b), and 4200 rpm c).

3.8.2 Transition between crushing and smoothing flow

In this appendix, we follow closely the arguments presented by Milner in his recently published paper titled “Early stages of spreading and sintering”[46]. In this paper, Milner shows that the initial stage of spreading of a droplet on a flat surface corresponds to a “crushing flow” where the velocity field is purely normal to the contact surface between the sphere and the solid, as sketched in Figure 3-2a. This is imposed by the no-slip boundary condition which inhibits any tangential flow component of the velocity vector. This restriction is, in principle, removed if one considers the sintering of two identical drops. Milner identifies the driving force of this secondary “smoothing flow” (Figure 3-2b) by noting that the boundary of the contact surface is cusp-like and tends to smoothen due to an imbalanced Laplace pressure drop. In practice, the sintering between two spheres is initially dominated by the crushing flow, which is then overtaken by the smoothing flow. Since both are described by different scalings (Section 3.4) it is important to know at what point of the sintering process the change of regime arises.

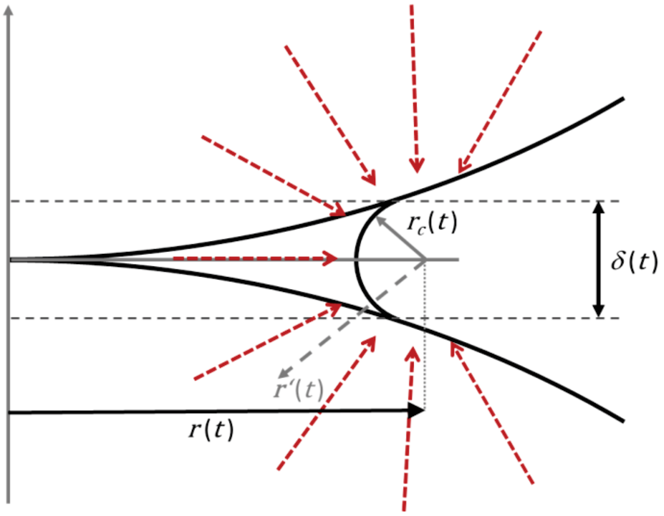

Figure 3-12: Sketch of the geometry and variables used in the derivation of the smoothing flow

For the derivation, let us consider the geometry sketched in Figure 3-12. Two spheres of radius R, are in contact, with a cusp of radius r_c centered around r. Let us assume early stages of sintering so that $r_c << r$. Then, the external boundary of the contact area between two sintering spheres is a circle of approximately radius $r(t) + r_c(t) \approx r(t)$. In the smoothing flow regime, the fluid is flowing radially, with a component tangential to the contact line. In the cross section, this flow is approximately a two-dimentional sink flow (red dashed arrows in Figure 3-12), with material being conveyed to fill the gap between the spheres. This approximation is justified in the early times when the angle between the two spheres at the boundary is small. The two-dimensional incompressible flow has a well-known velocity field $\boldsymbol{v}(\boldsymbol{r}') = -\frac{v_0(t)\delta(t)}{2}\frac{\boldsymbol{r}'}{(\boldsymbol{r}')^2}$, where $v_0(t)$ is the velocity of the smoothed cusp and r is taken from the sink centre. Notice in his formula, the radius r_c of the smoothed cusp has been approximated by $\delta(t)/2$ where $\delta(t)$ is defined in Figure 3-12. This parameter is geometrically related to $r(t)$ and provided that $r(t)/R << 1$, one has $\delta(t) \sim r(t)^2/R$.

This velocity field is responsible for a flow rate $\dot{V} = 2\pi r(t) \int\limits_{cusp} v(r)dl = 2\pi^2 r(t)\delta(t)v_0(t)$, where dl is the line element along the cusp in the cross-section. Notice that (i) the integral has been performed on a complete circle assuming that the cusp is sufficiently small so that all flow direction contributes to the sink flow; and (ii) the term $2\pi r(t)$ accounts for the summation along the boundary circle which shows that possible effects due to the curvature of the boundary circle are neglected. This is justified because the characteristic length of the flow is $\delta(t) \sim r(t)^2/R$ which is $<< r(t)$ in the early time of sintering.

Another expression for $\dot{V}$ is obtained as one realises that $\dot{V}$ is the time derivative of the volume already filled by the flow. This leads to the expression $V(t) = \int_0^{r(t)} 2\pi r(r^2/R)dr = \pi r(t)^4/(2R)$ and $\dot{V} = 2\pi \dot{r}(t) r^3(t)/R$. Bringing together the two expressions for $\dot{V}$ yields the kinematic relation

$\dot{r}(t) = \pi v_0(t)$. A second dynamical relation is obtained by equating the rate of change in surface energy – the driving of the flow with the dissipation rate. The liquid/air interface disappears during the sintering with a rate $\dot{E}_{surf} = -\gamma\partial_t(2\pi r(t)^2) = -4\pi\gamma r(t)\dot{r}(t)$. As for the dissipation rate, one relies on the well-known equation[49]

$$\dot{E}_{diss} = -\frac{\eta}{2}\int\sum\nolimits_{i,k\in\{x,y,z\}}(\partial v_i/\partial r_k + \partial v_k/\partial r_i)^2 dV, \qquad (32)$$

which for the radial flow near the circular contour line gives

$$\dot{E}_{diss} = -\eta\pi r(t)\int_{\delta(t)/2}^{\infty} r'dr'd\theta(\partial v_x/\partial y + \partial v_y/\partial x)^2 = -4\pi^2\eta v_0(t)^2 r(t) = -4\dot{r}^2(t)r(t). \qquad (33)$$

By equating $-E_{diss}$ and $\dot{E}_{surf}$, one obtains

$$\dot{r} = \frac{\pi\gamma}{\eta}. \qquad (34)$$

We can use Equ. (34) to predict the transition between the crushing and the smoothing flow (Figure 3-2). For early times, the "crushing flow" and its growth law $r(t) \propto t^{1/3}$ must dominate until the "smoothing flow" $\propto t$ takes over. To obtain a quantitative estimation of the crossover time t_{cr} between the two regimes, Milner proposes the criterion of *equality of rate of growth* between the two mechanisms. This calculation yields

$$t_{cr} = \left(\frac{\eta R}{\gamma}\right)\frac{1}{(12\pi)\sqrt{2}}. \qquad (35)$$

At this time, the crushing flow has grown the contact surface to a radius

$$\frac{r_{cr}}{R} = 2^{-\frac{5}{2}} = 0.1768. \qquad (36)$$

It is interesting to note that at the crossover time t_{cr}, the normalised radius $r(t)/R$ predicted by the crushing flow of Equ. (21) is only ~ 0,06. This means that the effective validity of the approximation where only the crushing flow is taken into account, goes probably farther than the value given in Equ. (36). This is effectively what we seem to see in the experiments, which are well described by the crushing scaling up to $r(t)/R \sim 0.25$. One additional reason may be that the sphere surfaces have properties which do not give full-slip flow condition, as required for the smoothing flow scaling to be valid. An indication may be given the fact that when we break the samples, the interconnections break neatly at the contact area between neighbouring spheres, indicating that the paraffin properties must be different in this contact area.

3.8.3 Creep compliance in terms of frequency-dependent viscosity

In this appendix we explain how to obtain the creep compliance *J(t)* in term of frequency-dependent viscosity. The frequency-dependent viscosity $\eta(\omega)$ is related to the stress relaxation modulus $G(t)$ via[51]

$$\eta(\omega) = \int_0^\infty dt G(t)\cos(\omega t) , \qquad (37)$$

Defining the Laplace transform of *G(t)* as

$$\hat{G}(s) = \int_0^\infty G(t) e^{-ts} , \qquad (38)$$

one notices that $\eta(\omega) = \Re\left\lfloor \hat{G} \right\rfloor (s = -i\omega)$.

As discussed in Section 3.6, in the experimentally accessible frequency range, $\eta(\omega)$ of the paraffin is convincingly described by a powerlaw (Figure 3-8), namely $\eta(\omega) \approx \xi\omega^{-\nu}$ with ν and ξ being temperature-dependent phenomenological coefficients. It is worth stressing that $\nu \in \left]0,1\right[$.

G(t) is then obtained directly , because the inverse cosine-Fourier transform of $\xi\omega^{-\nu}$ is exactly known[53] to be

$$G(t) = \frac{2\xi\Gamma(1-\nu)\cos(\pi\nu/2)}{\pi} t^{\nu-1}. \qquad (39)$$

$J(t)$ then follows from the fact that *J(t)* and *G(t)* are exactly related via

$$\hat{G}(s)\hat{J}(s) = 1/s^2 . \qquad (40)$$

One therefore finds $\hat{J}(s) = \sin(\pi\nu/2)/\left(\xi s^{2-\nu}\right)$, whose inverse Laplace transform is known[53]

$$J(t) = \frac{\sin(\pi\nu/2)}{\xi(1-\nu)\Gamma(1-\nu)} t^{-\nu+1} . \qquad (41)$$

Hence we have a direct expression for the creep compliance $J(t)$ from the rheology measurements of the parrafin. This formula is neither valid at very short times nor at very long times (because the formula $\eta(\omega) = \xi\omega^{-\nu}$ is not valid outside a certain frequency window). The viscoelastic approach of the sintering in this article is based on the assumption that Equ.(41) can be used to analyse all experiments, namely that the rheological measurement of $\eta(\omega)$ extend down to low frequencies $\omega \approx 2\pi/(1 \text{ day})$, substantially lower than those accessible experimentally.

3.9 References

1. Betke, U. & Lieb, A. Micro-Macroporous Composite Materials – Preparation Techniques and

Selected Applications: A Review. *Adv. Eng. Mater.* **20**, 1800252 (2018).

2. Evans, A. G., Hutchinson, J. W. & Ashby, M. F. Multifunctionality of cellular metal systems. *Prog. Mater. Sci.* **43**, 171–221 (1998).
3. Inagaki, M., Qiu, J. & Guo, Q. Carbon foam: Preparation and application. *Carbon N. Y.* **87**, 128–152 (2015).
4. Glicksman, L., Schuetz, M. & Sinofsky, M. Radiation heat transfer in foam insulation. *Int. J. Heat Mass Transf.* **30**, 187–197 (1987).
5. Isabelle Cantat, Sylvie Cohen-Addad, Florence Elias, Francois Graner, Reinhard Hohler, Olivier Pitois, Florence Rouyer, Arnaud Saint-Jalmes, Ruth Flatman, S. C. *Foams: Structure and Dynamics*. (Oxford University Press, 2013).
6. Janik, H. & Marzec, M. A review: Fabrication of porous polyurethane scaffolds. *Mater. Sci. Eng. C* **48**, 586–591 (2015).
7. Hammel, E. C., Ighodaro, O. L.-R. & Okoli, O. I. Processing and properties of advanced porous ceramics: An application based review. *Ceram. Int.* **40**, 15351–15370 (2014).
8. Michael S. Silverstein, Neil R. Cameron, M. A. H. *Porous Polymers*. (Wiley, 2011).
9. Banhart, J. Manufacture, characterisation and application of cellular metals and metal foams. *Prog. Mater. Sci.* **46**, 559–632 (2001).
10. Trinh, V. H. *et al.* Tuning membrane content of sound absorbing cellular foams: Fabrication, experimental evidence and multiscale numerical simulations. *Mater. Des.* **162**, 345–361 (2019).
11. Jahani, D. *et al.* Open-cell cavity-integrated injection-molded acoustic polypropylene foams. *Mater. Des.* **53**, 20–28 (2014).
12. Ke, H., Donghui, Y., Siyuan, H. & Deping, H. Acoustic absorption properties of open-cell Al alloy foams with graded pore size. *J. Phys. D. Appl. Phys.* **44**, 365405 (2011).
13. Richardson, J. ., Peng, Y. & Remue, D. Properties of ceramic foam catalyst supports: pressure drop. *Appl. Catal. A Gen.* **204**, 19–32 (2000).
14. Langlois, V. *et al.* Permeability of solid foam: Effect of pore connections. *Phys. Rev. E* **97**, 53111 (2018).
15. Lutzweiler, G. *et al.* Modulation of Cellular Colonization of Porous Polyurethane scaffolds via the control of pore interconnection size and nanoscale surface modifications. *ACS Appl. Mater. Interfaces* (2019).
16. Costantini, M. *et al.* Correlation between porous texture and cell seeding efficiency of gas foaming and microfluidic foaming scaffolds. **62**, 668–677 (2016).
17. Madden, L. R. *et al.* Proangiogenic scaffolds as functional templates for cardiac tissue engineering. *Proc. Natl. Acad. Sci. U. S. A.* **107**, 15211–6 (2010).
18. Choi, S. W., Zhang, Y., Macewan, M. R. & Xia, Y. Neovascularization in Biodegradable Inverse Opal Scaffolds with Uniform and Precisely Controlled Pore Sizes. *Adv. Healthc. Mater.* **2**, 145–154 (2013).
19. Ussman, E. R. I. C. M. S., Alpin, M. I. C. H., Uster, J. E. M., Oon, R. A. T. M. & Atner, B. U. D. R. Porous Implants Modulate Healing and Induce Shifts in Local Macrophage Polarization in the Foreign Body Reaction. **42**, 1508–1516 (2014).

20. Andrieux, S., Drenckhan, W. & Stubenrauch, C. Generation of Solid Foams with Controlled Polydispersity Using Microfluidics. *Langmuir* **34**, 1581–1590 (2018).

21. Stubenrauch, C., Menner, A., Bismarck, A. & Drenckhan, W. Emulsions- und Schaumtemplatierung – vielversprechende Methoden zur Herstellung maßgeschneiderter poröser Polymere. *Angew. Chemie* **130**, 10176–10186 (2018).

22. Silverstein, M. S. PolyHIPEs: Recent advances in emulsion-templated porous polymers. *Prog. Polym. Sci.* **39**, 199–234 (2014).

23. Kimmins, S. D. & Cameron, N. R. Functional Porous Polymers by Emulsion Templating: Recent Advances. *Adv. Funct. Mater.* **21**, 211–225 (2011).

24. Drenckhan, W. & Saint-Jalmes, A. The science of foaming. *Adv. Colloid Interface Sci.* **222**, 228–259 (2015).

25. Kim, H., Lee, S., Han, Y. & Park, J. Control of pore size in ceramic foams: Influence of surfactant concentration. *Mater. Chem. Phys.* **113**, 441–444 (2009).

26. Testouri, A. *et al.* Generation of Crystalline Polyurethane Foams Using Millifluidic Lab-on-a-Chip Technologies. *Adv. Eng. Mater.* **15**, 1086–1098 (2013).

27. Costantini, M. *et al.* Highly ordered and tunable polyHIPEs by using microfluidics. *J. Mater. Chem. B* **2**, 2290 (2014).

28. Yasunaga, K., Neff, R. A., Zhang, X. D. & Macosko, C. W. Study of Cell Opening in Flexible Polyurethane Foam. *J. Cell. Plast.* **32**, 427–448 (1996).

29. Tammaro, D. *et al.* Validated modeling of bubble growth, impingement and retraction to predict cell-opening in thermoplastic foaming. *Chem. Eng. J.* **287**, 492–502 (2016).

30. Stein, A. Sphere templating methods for periodic porous solids. *Microporous Mesoporous Mater.* **44**–**45**, 227–239 (2001).

31. Ma, P. X. & Choi, J.-W. Biodegradable Polymer Scaffolds with Well-Defined Interconnected Spherical Pore Network. *Tissue Eng.* **7**, 23–33 (2001).

32. Marshall, A. J. & Ratner, B. D. Quantitative characterization of sphere-templated porous biomaterials. *AIChE J.* **51**, 1221–1232 (2005).

33. K, S.-J. L. K. *SINTERING, densification, grain growth & microstructure*. (2005).

34. Somo, S. I. *et al.* Pore Interconnectivity Influences Growth Factor-Mediated Vascularization in Sphere-Templated Hydrogels. *Tissue Eng. Part C Methods* **21**, 773–85 (2015).

35. Chen, R., Ma, H., Zhang, L. & Bryers, J. D. Precision-porous templated scaffolds of varying pore size drive dendritic cell activation. *Biotechnol. Bioeng.* **115**, 1086–1095 (2018).

36. Chen, V. J. & Ma, P. X. Nano-fibrous poly(l-lactic acid) scaffolds with interconnected spherical macropores. *Biomaterials* **25**, 2065–2073 (2004).

37. Zhang, J., Zhang, H., Wu, L. & Ding, J. Fabrication of three dimensional polymeric scaffolds with spherical pores. *J. Mater. Sci.* **41**, 1725–1731 (2006).

38. Grenier, S., Sandig, M. & Mequanint, K. Polyurethane biomaterials for fabricating 3D porous scaffolds and supporting vascular cells. *J. Biomed. Mater. Res. A* **82**, 802–9 (2007).

39. Takagi, K., Takahashi, T., Kikuchi, K. & Kawasaki, A. Fabrication of bioceramic scaffolds with ordered pore structure by inverse replication of assembled particles. *J. Eur. Ceram. Soc.* **30**,

2049–2055 (2010).

40. Zhao, K., Tang, Y. F., Qin, Y. S. & Luo, D. F. Polymer template fabrication of porous hydroxyapatite scaffolds with interconnected spherical pores. *J. Eur. Ceram. Soc.* **31**, 225–229 (2011).

41. Descamps, M. *et al.* Manufacture of macroporous β-tricalcium phosphate bioceramics. *J. Eur. Ceram. Soc.* **28**, 149–157 (2008).

42. FRENKEL & J., J. Viscous flow of crystalline bodies under the action of surface tension. *J. Phys.* **9**, 385 (1945).

43. Verbelen, L. *et al.* Characterization of polyamide powders for determination of laser sintering processability. *Eur. Polym. J.* **75**, 163–174 (2016).

44. Pokluda, O., Bellehumeur, C. T. & Vlachopoulos, J. Modification of Frenkel's model for sintering. *AIChE J.* **43**, 3253–3256 (1997).

45. Bellehumeur, C. T., Kontopoulou, M. & Vlachopoulos, J. The role of viscoelasticity in polymer sintering. *Rheol. Acta* **37**, 270–278 (1998).

46. Milner, S. T. Early stages of spreading and sintering. ArXiv 1907.05862 (2019).

47. Ramírez, L. M., Milner, S. T., Snyder, C. E., Colby, R. H. & Velegol, D. Controlled Flats on Spherical Polymer Colloids. *Langmuir* **26**, 7644–7649 (2010).

48. Himran, S., Suwono, A. & Mansoori, G. A. Characterization of alkanes and paraffin waxes for application as phase change energy storage medium. *Energy Sources* **16**, 117–128 (1994).

49. L. D. Landau, E. M. L. *Fluid Mechanics*. (Elsevier, 1987).

50. Spence, D. A. The Hertz contact problem with finite friction. *J. Elast.* **5**, 297–319 (1975).

51. Rubinstein, M. *Polymer Physics*. (2003).

52. Ginot, G., Höhler, R., Mariot, S., Kraynik, A. & Drenckhan, W. Juggling bubbles in square capillaries: an experimental proof of non-pairwise bubble interactions. *Soft Matter* **15**, 4570–4582 (2019).

53. Gradshteyn, I. S. & Ryzhik, I. M. *Table of integrals, series, and products*. (Academic press, 2014).

Chapter 4. Cellular response to architectural features of PU scaffolds, to surface treatment and to the formulation of the PU

Résumé

L'importance de l'architecture des matériaux poreux utilisés pour la régénération tissulaire est un fait largement discuté dans la littérature. L'intérêt est de fournir aux cellules un environnement dans lequel elles puissent adhérer, puis proliférer afin d'y former un réseau tridimensionnel proche de leur configuration dans les tissus. De nombreuses études ont montré que le diamètre des pores influe sur la capacité de migration des cellules, sur la diffusion des nutriments et de l'oxygène et sur l'évacuation des déchets cellulaires. La taille des interconnexions joue elle aussi un rôle sur la diffusion et la capacité des cellules à envahir le matériau. La chimie du matériau semble prédominante pour favoriser ou non l'ancrage des cellules au substrat. La prolifération et l'éventuelle différenciation des cellules dépendent aussi de l'adhésion et des gradients éventuels de nutriments. Enfin, comme décrit dans le chapitre bibliographique (Section 1.6.8), la géométrie et notamment la courbure des pores peuvent aussi induire des tensions au niveau du cytosquelette et par conséquence, peuvent moduler l'activité cellulaire.

Dans ce contexte, nous proposons dans ce chapitre de rechercher un optimum en matière de morphologie du matériau, à savoir, le diamètre des pores et le diamètre des interconnexions. Un diamètre des pores (de 133 µm en moyenne) est choisi en nous appuyant sur la littérature ainsi que sur une approche itérative (Figure C 1), alors que le diamètre des interconnexions sera varié pour y trouver un optimum au regard du comportement des cellules.

Le chapitre suivant se décompose en deux parties. Dans la première, on analyse le comportement de deux types de cellules (fibroblastes (NIH 3T3) et cellules mésenchymateuses issues de la gelée de Wharton (WJMSCs)) ensemencées dans des matériaux poreux en polyuréthane. Ces matériaux poreux ont été conçu par la méthode de « sphere templating » décrite dans le Chapitre 3. Nous avons choisi de générer un matériau avec un diamètre moyen de pores de 133 µm que nous avons gardé constant pour l'ensemble de l'étude, ainsi que la formulation du polyuréthane (avec un indice d'isocyanate de 400 voir Section 2.7). Le diamètre des interconnexions a, en revanche, été modulé. Deux structures ont ainsi été générées, l'une ayant un diamètre d'interconnexions moyen de 27 µm et l'autre de 52 µm.

Pour différencier l'influence de la structure du poreux de l'interaction des cellules avec la surface du matériau cette partie décriera aussi le comportement des cellules en réponse à des traitements de surface. En effet, il sera démontré que le matériau en lui-même étant très hydrophobe, le recours à des traitements de surface permet une meilleure colonisation des cellules. Deux traitements de surface seront utilisés : le traitement aux plasma, ainsi qu'un revêtement à base de polydopamine.

Nous caractériserons les matériaux en termes de porosité et de perméabilité hydraulique notamment pour établir un lien entre la morphologie et les changements induits sur les propriétés du matériau. L'impact des traitements de surface sur les propriétés de mouillage sera également étudié. Enfin, nous tenterons de relier les différentes réponses cellulaires, à savoir leur survie, leur organisation et leur

niveau de sécrétion de matrice, aux paramètres architecturaux et chimiques des matériaux. Cette première partie reprend une publication :

Lutzweiler, G.; Barthès, J.; Koenig, G.; Kerdjoudj, H.; Mayingi, J.; Boulmedais, F.; Schaaf, P.; Drenckhan, W.; Vrana, N. E. *Modulation of Cellular Colonization of Porous Polyurethane Scaffolds via the Control of Pore Interconnection Size and Nanoscale Surface Modifications.* ***ACS Appl. Mater. Interfaces*** **2019.**

Dans cet article, nous démontrons que les modifications de surface permettent aux cellules de pénétrer dans les pores du matériau en le rendant plus hydrophile. Ces revêtements déclenchent aussi des réponses spécifiques suivant le type de cellule. En effet, nous montrons que les fibroblastes peuvent adhérer au matériau recouvert de polydopamine alors que les WJMSCs n'y adhèrent pas. A l'inverse le traitement plasma permet aux WJMSCs d'envahir le matériau et d'y adhérer par la suite, alors que les fibroblastes montrent moins d'affinité avec le substrat. Il convient de préciser que le traitement au plasma étant réversible, il permet dans un premier temps aux cellules en suspension dans leur milieu de culture de pénétrer le poreux. Cependant, après un laps de temps relativement court, les cellules interagissent avec le polyuréthane d'origine. Alors que la réponse des cellules est spécifique selon le traitement de surface, l'effet de la taille des interconnexions, prépondérante sur la survie et l'organisation des cellules à long terme, est indépendante du matériau et du type de cellule étudié. Les grandes interconnexions favorisent la propagation des cellules et donc leur colonisation et les contacts cellules-cellules sont favorisés. Les propriétés de transport des poreux avec de grandes interconnexions (i.e. la perméabilité hydraulique) sont largement augmentées par rapport aux matériaux ayant de petites interconnexions. Nous émettons l'hypothèse que la diffusion y est également limitée lorsque les interconnexions sont petites et la communication cellulaire via des messagers solubles amoindrie.

Dans une deuxième partie (Section 4.2), nous avons modifié la formulation du polyuréthane en lui-même. Cela permet de moduler les capacités d'adhésion des cellules sur le matériau sans avoir recours à des modifications de surface ultérieures. Pour ce faire, le ratio d'isocyanate ajouté dans la synthèse du polyuréthane a été varié. Ceci a permis de montrer la présence d'un seuil critique au-delà duquel les deux types de cellules peuvent adhérer au matériau. Nous tenterons d'établir un lien entre les propriétés physico-chimiques du matériau et l'adhésion cellulaire. L'étude systématique sera essentiellement conduite sur des films de polyuréthane et non pas sur des matériaux poreux. Néanmoins, une expérience de comparaison avec les systèmes tridimensionnels montre les mêmes effets dans les poreux.

4.1 Modulation of Cellular Colonization of Porous Polyurethane scaffold via pore interconnection size control and nanoscale surface modifications

G. Lutzweiler[1,2,3], J. Barthes[4], G. Koenig[1,2], H. Kerdjoudj[6], J. Mayingi[5], F. Boulmedais[3], P. Schaaf[1,2]*, W. Drenckhan[3], N.E. Vrana[4]**

[1] Institut National de la Santé et de la Recherche Medicale, UMR_S 1121, 11 rue Humann 67085 Strasbourg Cedex, France.

[2] Université de Strasbourg, Faculté de Chirurgie Dentaire, 8 rue Sainte Elisabeth, 67000 Strasbourg, France.

[3] Université de Strasbourg, CNRS, Institut Charles Sadron, 23 rue de Loess, 67034 Strasbourg, France.

[4] Protip Medical SAS, 8 Place de l'Hôpital, 67000 Strasbourg, France.

[5] CETIM, 24a Rue d'Alsace, 67400, Illkirch-Graffenstaden, France.

[6] EA 4691, Biomateŕiaux et Inflammation en Site Osseux (BIOS), SFR-CAP Santé (FED4231), Université de Reims Champagne Ardenne, 51100 Reims, France UFR d'Odontologie, Université de Reims Champagne Ardenne, 51100 Reims, France

KEYWORDS: Polyurethane scaffold, Wharton jelly mesenchymal stem cells, fibroblasts, interconnected pores, surface modification, Dopamine

4.1.1 Abstract

Full-scale cell penetration within porous scaffolds is required to obtain functional connective tissue components in tissue engineering applications. For this aim, we produced porous polyurethane (PU) structures with well-controlled pore and interconnection sizes. While the influence of the pore size on cellular behavior is widely studied, we focused on the impact of the size of the interconnections on the colonization by NIH 3T3 fibroblasts and Wharton's jelly derived mesenchymal stem cells (WJMSCs). To render the material hydrophilic and allow good material wettability, we treated the material either by plasma or by polydopamine (PDA) coating. We show that cells weakly adhere on these surfaces. Keeping the average pore diameter constant at 133 µm, we compare two structures, one with LARGE (52 µm) and one with SMALL (27 µm) interconnection diameters. DNA quantification as well as extracellular matrix (ECM) production reveal that larger interconnections are more suitable for cells to move across the scaffold and form a three-dimensional cellular network. We argue that LARGE interconnections favor cell communication between the different pores which then favors the production of extracellular matrix. Moreover, PDA treatment shows a truly beneficial effect on fibroblast viability and on matrix production whereas plasma treatment shows the same effect for WJMSCs. We therefore

claim that both pore interconnection and surface treatment play a significant role to improve the quality of integration of tissue engineering scaffolds.

4.1.2 Introduction

As they are used for withstanding the mechanical constraints of a tissue or an organ to be replaced, a tissue engineering scaffold should allow cell migration and proliferation into its empty volumes, favor intercellular exchanges and production of extracellular matrix[1]. 3D porous scaffolds, which fulfill these requirements[2,3], are manufactured using different types of material, such as metals, ceramics, natural or synthetic polymers[4,5]. They need to be well interconnected to allow cell migration through the whole structure and to guarantee good oxygen and nutrient supply as well as removal of metabolic wastes[6,7]. Many techniques were employed to generate such structures as for example particle leaching[8], gas foaming[9], freeze drying[10] or 3D printing[11]. The influence of the pore size on cell behavior in porous structures has been widely studied[12–15]. However, the great diversity of manufacturing techniques, the cell type, material and culture conditions differ from one study to another rendering difficult to draw conclusions on what can be the optimal scaffold. Pamula *et al.* [16] generated PLGA scaffolds, having three different pore sizes: 40, 200 and 600 µm. They demonstrated that osteoblast-*like* MG63 migration was improved in scaffolds with pore size of 600 µm compared to 40 and 200 µm. Stenhamre *et al.* [17] showed that for human chondrocytes seeded on polyurethane (PU) scaffolds, chondrogenesis markers (i.e. Glycosaminoglycans, GAGs and type II collagen) were upregulated in scaffolds having the smallest pore size (i.e. (< 150 µm) compared to larger ones (300-500 µm). Conversely, rat mesenchymal stem cells seeded on collagen-hyaluronic scaffolds secreted more sulfated GAGs, type II collagen and showed a higher SOX9 expression in structures with pore diameter of 300 µm compared to 94 or 130 µm.[18] While information on the optimization of the pore size for a given cell type is available, the influence of interconnection size between two adjacent pores in porous structures on cell behavior has been more rarely investigated which is the focus of the current study.

For example, supercritical foamed scaffolds were generated using different molecular weight PLGA, giving structures with different distributions of pore and interconnection diameters.[19] However, the change in pore size was accompanied by a systematic change in the interconnections, making it impossible to draw solid conclusions about the specific influence of either of the parameters. In another study, bone marrow stromal cells (MSCs) were seeded on two hydroxyapatite scaffolds, with interconnection sizes of more than 200 µm for a first group and below 100 µm for a second group, and subsequently implanted subcutaneously in mice[20]. The authors reported that interconnection size has a significant effect on the diameter of blood vessels formed within the scaffold. Yet, the fabrication processes of the different scaffolds used were not the same and the resulting structures were different. Results may thus have been influenced by other factors than the interconnections only.

Separation and fine control of both interconnection and pore sizes cannot be achieved in all fabrication processes. "Sphere templating" gives an explicit control over the size of the pore interconnections while keeping the chemical nature of the material constant. The principle of this method is based on a sacrificial porogen agent packed in a container on which an initial liquid material is poured in order to fill the space between the porogen particles. Once the liquid phase is solidified, the porogen is dissolved and removed, leaving a porous structure whose architecture can be precisely controlled via the geometrical properties of the porogen (Figure 4-1a). Spherical particles of poly(methylmethacrylate)[21] or paraffin[22] are commonly used as porogens.

Polyurethane is known for its biocompatibility and is widely used for tissue engineering applications[23,24]. However, many authors reported the use of coatings or modifications in the formulation during the polyurethane synthesis in order to increase the affinity of cells for the surface. For example, Li *et al.* [25] seeded MSCs onto a fibrin-polyurethane hybrid scaffold to minimize cell loss during seeding and to obtain a homogenous distribution throughout the scaffold.

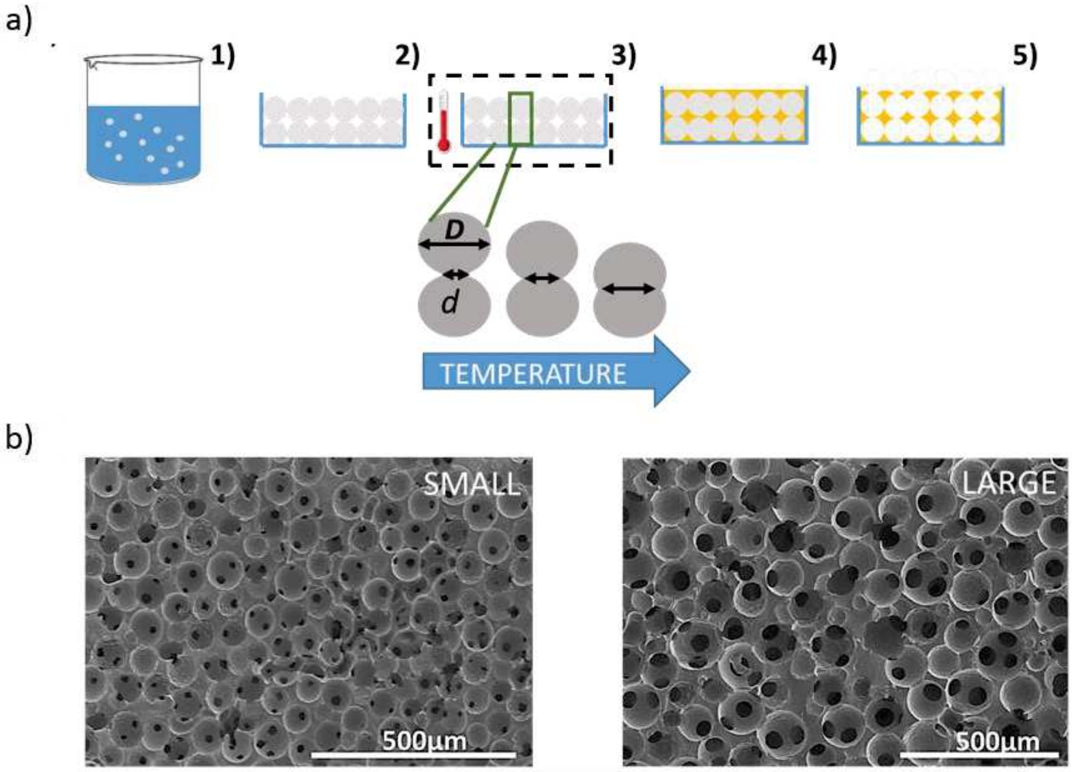

Figure 4-1 : a) 1) Paraffin sphere generation by an emulsion dispersion method. 2) Paraffin sphere packing in a petri dish followed by 3) sintering in a mould at various temperatures. 4) Polymer solution is poured on the top to infiltrate between beads. 5) Paraffin dissolution in solvent. b) SEM images of the resulting scaffold with SMALL and LARGE interconnections.

Li *et al.* [26] grafted type I collagen onto polyurethane surfaces to increase the hydrophilicity of the substrate as well as cell attachment. In another study, Lin *et al.*[27] grafted RGD peptide sequences onto a polyurethane backbone in order to improve endothelial cell adhesion.

Another promising coating is dopamine, a chemical close to the adhesive molecules found in mussels[28]. It can self-polymerize to form thin polydopamine (PDA) films which adhere on almost any type of surface. PDA films are easy to process since the coating is done by simply dipping the sample in a solution. PDA coating was already employed to improve cell adhesion and proliferation[29-30].

In this paper, we study the influence of the interconnection size of a porous polyurethane (PU) material supplemented with different surface functionalizations, on cell colonization. For this purpose, we first produced by sphere templating two structures with identical pore size but different interconnection diameters. Bare PU scaffolds appeared extremely hydrophobic preventing the penetration of the cell suspension. Hence, PU scaffolds were functionalized to render them more hydrophilic by both PDA and plasma treatments. The functionalized structures were seeded with two cell types: NIH 3T3 fibroblasts to study cell migration and distribution and Wharton's jelly derived mesenchymal stem cells (WJMSCs) as a potential cell source for chondrogenesis for cartilage tissue engineering. Therefore, we investigated the combination of surface chemistry with the architecture of the scaffold on cell colonization. While surface chemistry could promote or prevent cell survival and colonization regarding the cell type, the diameter of the interconnections appeared to be a key feature for supporting the organization of cells in a three-dimensional way, and to improve their viability.

4.1.3 Results and discussion

4.1.3.1 Morphology and permeability of PU scaffolds

Porous PU scaffolds were generated by a sphere templating method using spherical paraffin beads (Section 2.2) at the desired dimensions. After synthesis and sieving of 133 µm diameter paraffin beads, they were packed in a petri dish and were sintered at 43°C for two different times to create a neck of tunable cross-section between adjacent particles (Figure 4-2).

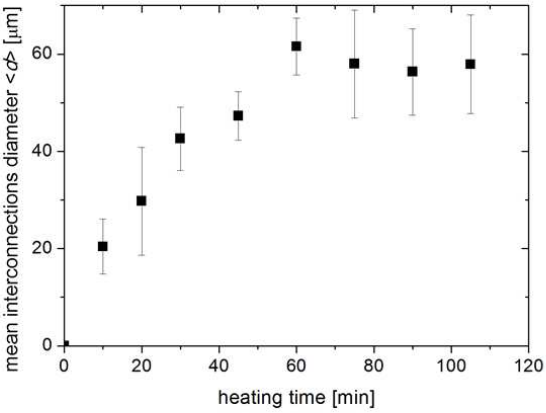

Figure 4-2 : Evolution of the interconnection diameter against heating time for paraffin beads having an average diameter of 133± 28 µm heated at 43°C.

After cooling, a mixture of polyol and isocyanate was casted on the petri-dish. After 48 h, the paraffin beads were dissolved with hexane.

Struture name	Mean pore diameter <*D*> [µm]	Mean interconnection diameter <*d*> [µm]	Porosity *P* [%]	Permeability *k* [cm²]
LARGE	133 ± 28	52 ± 12	81 ± 13	$5.\ 10^{-6}$
SMALL	133 ± 28	27 ± 10	60 ± 11	$4.5.\ 10^{-7}$

Table 4-1 : Summary of the properties of scaffolds used for cellular studies.

PU porous scaffolds were produced with an average pore size of 133 ± 28 µm and with two interconnection sizes depending on the sintering time of paraffin beads (Figure 4-1-b).

For a sintering time of paraffin beads of 20 min, the average diameter of the interconnection <*d*> of the resulted scaffold was 27 ± 10 µm, named SMALL scaffold (Figure 4-1-b, left). With a sintering time of 1 h, the average diameter <*d*> was 52 ± 12 µm, named LARGE scaffold (Figure 4-1-b, right). The spherical footprint of the paraffin template allows to keep a homogenous geometry across the entire both samples. The backbone of the polymer was polyether-based to reduce hydrolysis and therefore to maintain the integrity of the scaffold for the whole experiment. PU scaffold porosity increases with the interconnection sizes from 60% for SMALL to 81% for LARGE scaffolds. Young modulus was shown to be higher for scaffold having SMALL interconnections, we found $E = 284.4$ kPa for SMALL interconnections and $E = 239$ kPa for LARGE interconnections (Figure S 4). However, mechanical tests were performed by compressing the whole scaffold, thus, the mechanical response is a macroscopic response of the scaffold. At the cell level, cell may only sense the local modulus of the polyurethane which was the same for all samples. Since the sintering of the paraffin beads leads to larger neck formation (i.e. larger interconnections), there is less space available for PU penetration in the interstitial space and then more void space after paraffin beads dissolution leading to more porous structures. Aqueous permeability of PU scaffolds was also investigated by measuring the hydraulic permeability *k* (Section 2.19 in Material and Methods section). The values obtained for LARGE scaffolds are one order of magnitude larger than those for SMALL ones (Table 4-1). Similar values of the hydraulic permeability were found by Li *et al.*[37] for PVA scaffolds with nearly the same pore diameter (150 µm) as we found in the case of LARGE interconnections. The dependence of the hydraulic permeability on the interconnection diameters was reported by Marshall *et al.*[33] who provided a model where the hydraulic permeability increases with the square of the interconnection radius. Moreover, Kemppainen *et al.*[38] designed 3D printed poly(ε-caprolactone) (PCL) scaffolds with tailored interconnection diameter with different hydraulic permeability where they demonstrate that interconnection size is a key parameter for transport properties throughout the scaffold.

Aqueous solutions deposited on top of a bare PU material present a high contact angle and do not penetrate into the scaffold due to its hydrophobicity. We thus functionalized the material either by exposition to plasma or by bringing it in contact with a dopamine solution in order to create a thin polydopamine coating on the porous scaffold. The hydrophobic character of flat PU surfaces was confirmed by contact angle measurement (Figure 4-3-a) with a contact angle of 95°. It decreased continuously for 7 mins upon exposure to plasma before reaching an equilibrium value around 35°. It is known that plasma treatment induces cleavage of polymer chains, which promotes the formation of free radicals and highly reactive species that mostly react with oxygen or water vapor to form hydroxyl groups[39,40]. These polar groups increase the wettability of the PU as shown by a decrease of the contact angle values. Yet, a rapid hydrophobic recovery of the surface was observed after plasma treatment due to re-arrangement of polymer chains that expose the hydrophobic part toward air[41]. As seen on Figure 4-3-b, after only 5 mins, contact angle rises from 35° to 48° and stabilizes around 60° for longer times.

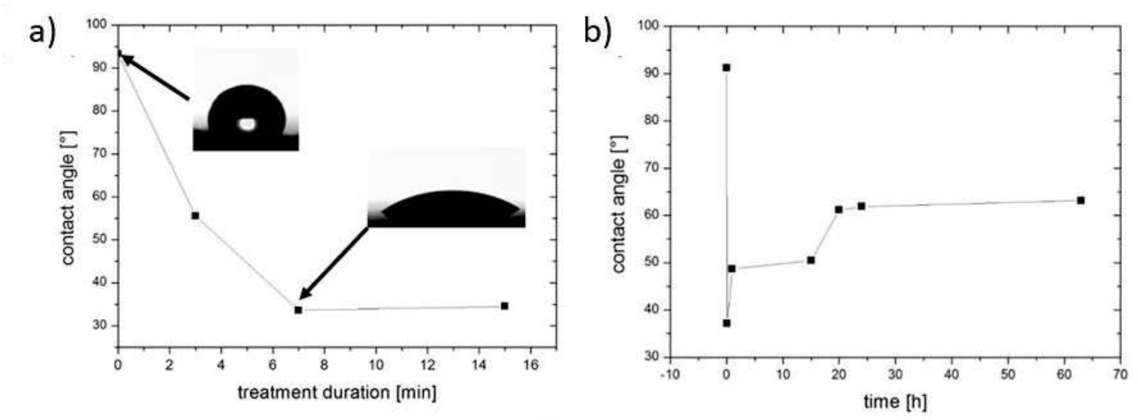

Figure 4-3: a) Water contact angle measurement on PU flat surface after various plasma treatment durations, b) water contact angle measurement as a function of the time after plasma treatment.

In order to achieve a permanent improvement of the scaffold wettability, polydopamine (PDA) coatings were deposited on PU.

Dopamine is known for its ability to stick on many types of surfaces and to self-polymerize to give thin film depositions. The surface modification is versatile and easy to process since the sample coverage is obtained by a simple dipping step, as explained in the Material and Method (see Section 2.7.1). After PDA deposition, aggregates were observed on PU scaffolds, as reported in other studies (Figure 4-4-a)[42]. Surface hydrophilicity of PDA-treated PU surfaces greatly increases after 3 h of dipping and continues to increase slightly for longer dipping durations (Figure 4-4-b). A change of color is observed proving PDA deposition on the whole surface (Figure 4-4-b inserts). Unlike the plasma treatment, PDA coating shows a much better stability with time regarding the wetting properties remaining stable for 48 h (Figure 4-4-c), instead of only 5 mins for plasma treatment (Figure 4-3-b).

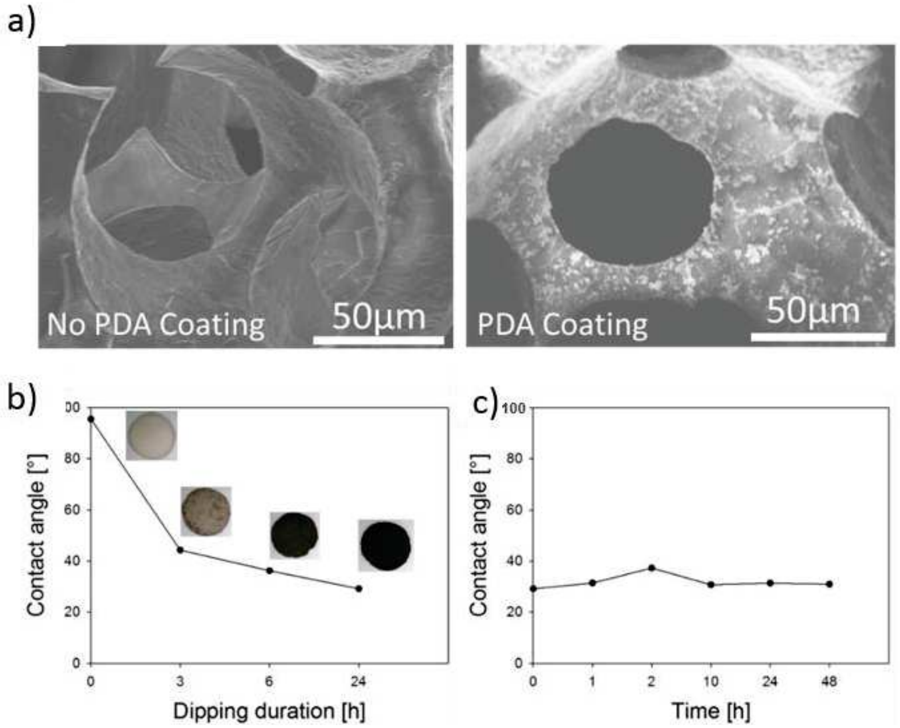

*Figure 4-4 **:** a) SEM images of PU scaffold with and without PDA coating for 24h, b) contact angle measurement of PDA-coated PU flat surfaces with various dipping times and c), contact angle evolution with time after PDA treatment on PU dipped in PDA solution for 24h.*

4.1.3.2 Cell growth in porous scaffold

Cells were brought in contact with PU scaffolds functionalized by plasma treatment and with PDA. In the case where we functionalized the PU scaffold by plasma treatment, since the hydrophilicity decreases with time, we seeded the cells immediately after plasma exposure for studying the effect of the interconnection diameter. We quantified the DNA by phenol/Chloroform extraction (see Section 2.8.2), the collagen and the non-collagenous using Chondrex kit (see Section 2.13.1) such as GAG contents after 14 and 21 days of culture. Because matrix production is a slow process, collagenous and non-collagenous secretions were not quantified before day 14, furthermore, it guarantees to be above the detection limit of the quantification kit. DNA content reflects the number of cells present in the scaffold. In order to avoid as much as possible, the presence of dead cells that will contribute to DNA content, we thoroughly rinsed the scaffold before each measurement. Collagen and non-collagen contents reflect the extracellular matrix (ECM) produced by the cells. The results are summarized on Figure 4-5 for NIH 3T3 cells and on Figure 4-6 for WJMSCs. One first observes that the two cell types respond differently to the functionalization method.

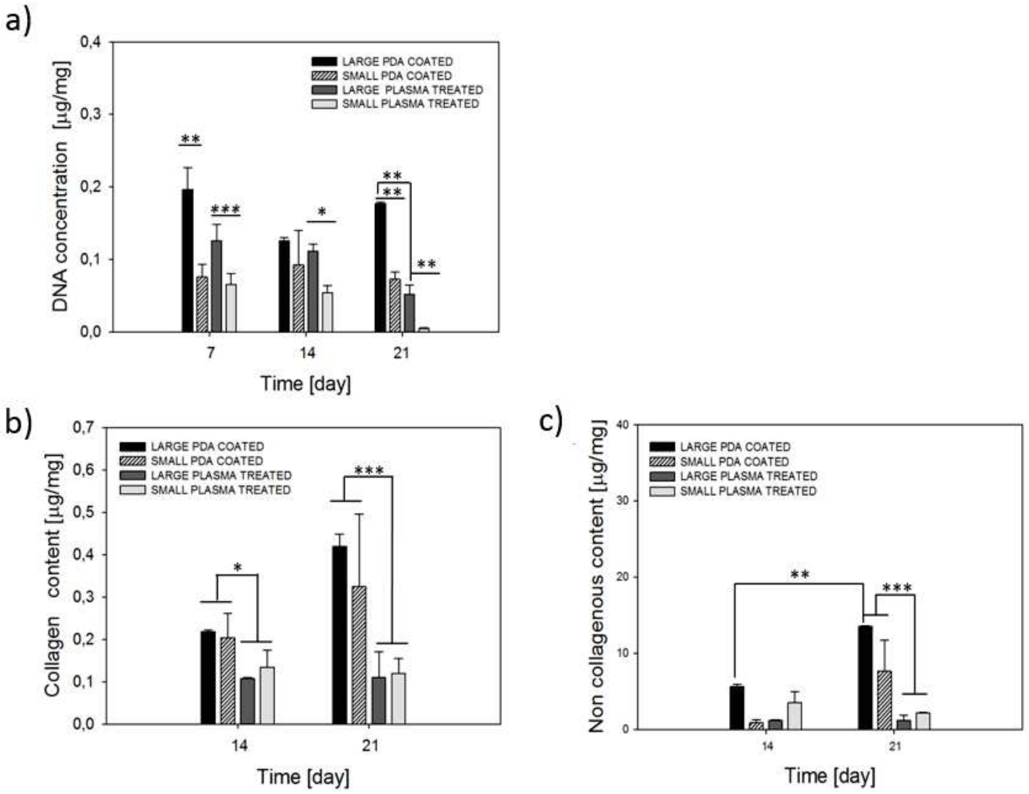

*Figure 4-5: a) DNA quantification of NIH 3T3 in PU scaffolds, either coated with PDA or just treated with plasma b) Collagen secreted quantification in PU scaffold and c), non-collagenous content secretion, values expressed as mean ± SD n = 3 * p < 0.05, ** p < 0.01, *** p < 0.001.*

The DNA quantification of fibroblasts, illustrated in Figure 4-5, did not show significant variation of measured values over the studied time for PDA treated scaffold but showed a significant decrease for plasma. Furthermore, collagen and non-collagenous contents are significantly higher on PDA coated samples after 14 and 21 days of culture, respectively compared to plasma treated samples for a given interconnection size Figure 4-5b and 5c.

In contrast to fibroblast, WJMSCs behavior is better on plasma treated PU scaffold compared to PDA. For fibroblasts, the ECM production is favored on PDA coated samples in comparison to plasma treated ones. As far as DNA content is concerned, it remains fairly constant over time for PDA treated samples (compare D7 to D21) and its decreases for plasma treated samples. This indicates that on PDA treated samples, the number of cells remains fairly constant overtime. For WJMSCs, DNA content decreases over time.

Collagen and non-collagenous content are always significantly higher on plasma treated samples compared to PDA coated samples for a given interconnection size. For WJMSCs, the ECM production is significantly higher on plasma treated samples compared to PDA coated ones. In the case of PDA coated samples, almost no ECM production was observed. As for as DNA content is concerned, it is significantly higher over time on plasma treated samples compared to PDA coated ones even if it is decreasing a bit over time. One does observe opposite behavior between fibroblasts and WJMSCs with respect to the surface treatment.

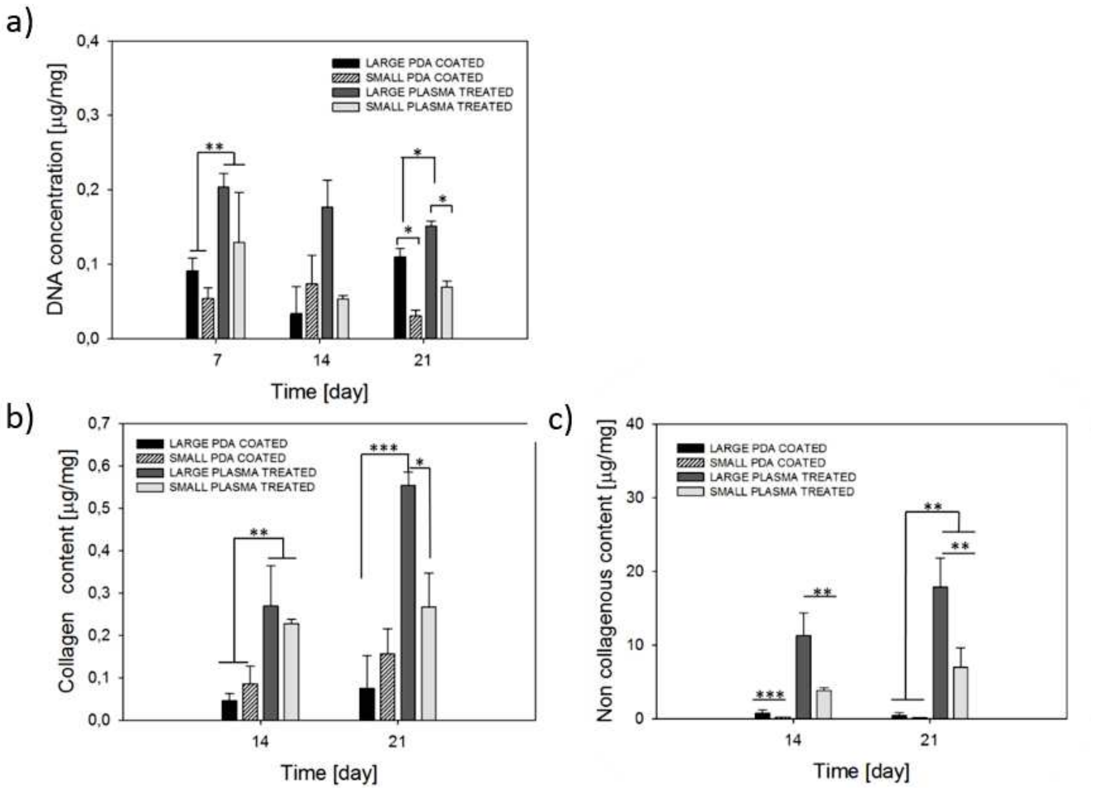

*Figure 4-6: a) DNA quantification of WJMSCs in PU scaffolds, either coated with PDA or treated with plasma b) Collagen secreted quantification in PU scaffold and c), non-collagenous content secretion, values expressed as mean ± SD n = 3 * $p < 0.05$, ** $p < 0.01$, *** $p < 0.001$.*

Hence, as demonstrated in Figure 4-3 and Figure 4-4, surface functionalization improves the wettability of the PU scaffolds. As a result, cell suspension could clearly penetrate within the pores. Therefore, surface treatments allowed cells to colonize the scaffold in a preliminary way. The further interaction between the cells and the surface dictated the long-term response of the cells toward the PU surface. This was demonstrated to be rather cell specific.

In their respective favorable conditions, matrix synthesis by NIH 3T3 and WJMSCs is significantly higher for LARGE interconnections compared to SMALL ones, indicating the strong influence of the interconnection size on cell behavior.

We also performed confocal imaging of the scaffolds after 21 days of cell culture where cells were stained with DAPI (blue) and phalloidin (red) to visualize the nuclei and the F-actin filaments, respectively (experimental details can be found in Section 2.11.1). Typical images are shown on Figure 4.7 for NIH 3T3 cells and on Figure 4.8 for WJMSCs.

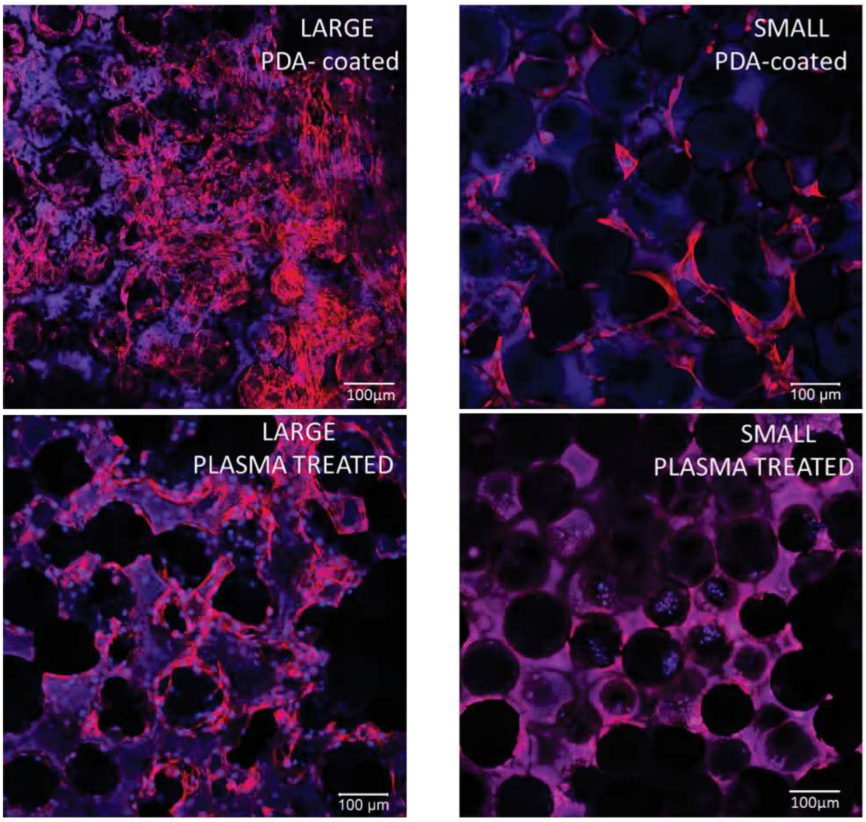

Figure 4-7: Confocal images of scaffolds seeded with NIH 3T3 Fibroblasts for 21 days of culture, cells were stained with DAPI (blue) for nucleus and phalloidin (red) for F-actin filament, images were taken in the center of the scaffold approximately.

For both cells seeded on the favorable coated PU, scaffolds with LARGE interconnections are always more colonized than scaffold with SMALL ones. As far as NIH 3T3 cells are concerned, one observes that for LARGE interconnections, the whole pores are colonized in the case of PDA treatment whereas cells essentially colonize the surface of the pores for plasma treated PU (Figure 4-7). After 24h of culture, more fibroblasts were observed in structures with SMALL interconnections compared to day 21, for LARGE interconnections, no significant differences were seen between day 1 and day 21 (

Figure S 3). In the case of WJMSCs, cells fully colonize the plasma treated PU with LARGE interconnections whereas for SMALL interconnections, the material appears sparsely colonized. No colonization is observed when the PU was functionalized with PDA. These results are in agreement with those found by the DNA and ECM content analysis.

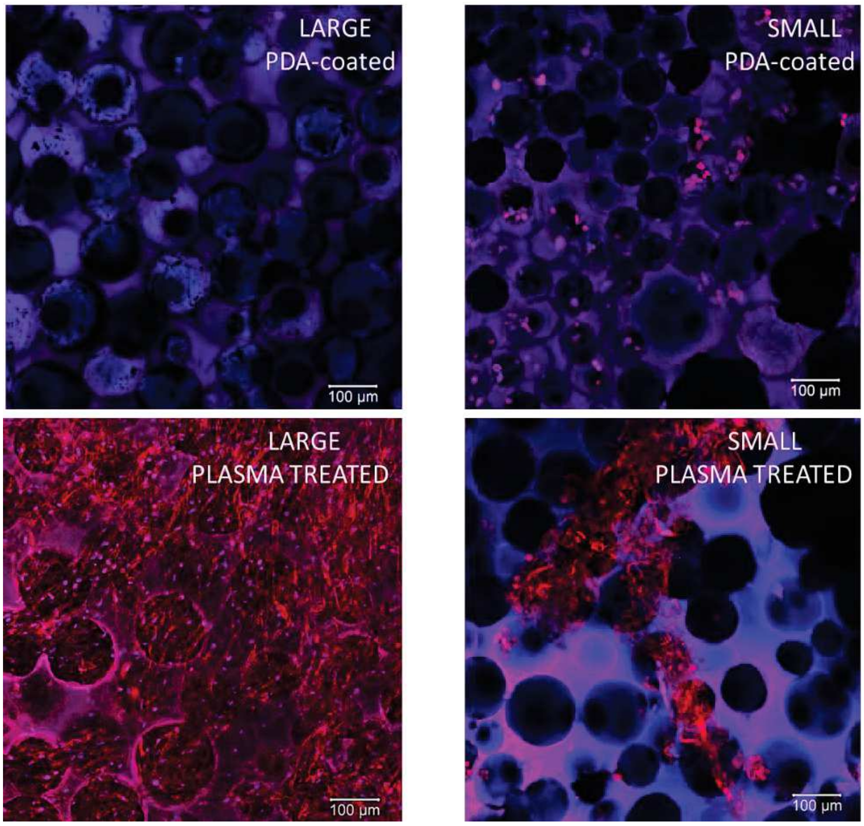

Figure 4-8: Confocal images of scaffolds seeded with WJMSCs for 21days of culture, cells were stained with DAPI (blue) for nucleus and phalloidin (red) for F-actin filaments, images were taken in the center of the scaffold approximately.

In order to obtain a better understanding of the colonization process, we also performed cell adhesion experiments on flat surfaces of PU (either raw PU or with surface functionalization) (Figure S 1 of Supplementary information, SI). Different behaviors occur regarding the cell type. On plasma treated PU, WJMSCs are spreading on the substrate after 1 day but cells become round shaped after 2 days of culture (Figure S 2 in SI). One the other hand, fibroblasts poorly adhere on this substrate and present a tendency to form cell aggregates on the surface. One can thus conclude that WJMSCs and NIH 3T3 cells interact differently on the two substrates but in any case, their adhesion appeared rather weak.

From our observations one can conclude that despite weak adhesion, cells can colonize porous materials, synthesize extracellular matrix and even totally fill the material. We find that interconnection size between the different pores is of great importance, LARGE interconnections (larger than 50 µm) being needed for cell colonization. Moreover, we find that surface treatment plays an important role for cell colonization but must be adapted to the cell type.

4.1.4 Discussion

Let us now discuss our results in the light of the literature. It has already been reported that when the cells have poor interactions with a biomaterial, they do secrete their own ECM on the surface of the material to create a more favorable environment. For instance, Ferreira *et al.*[43] produced a combination of sulfated-modified hyaluronic acid and polyethyleneglycol diacrylate hydrogel that did not contain any adhesion motifs and they showed that human bone marrow mesenchymal stem cells secreted their own local pericellular ECM to which cells subsequently attached. One can assume that cells are able to create a local environment when they do not adhere directly on the material. Cells could then either recruit proteins from the serum or synthesize their own ECM to adhere on the material surface. This was shown on trimethylpropane trimethacrylate where poorly adherent dental pulp stem cells showed an upregulation of collagen II, collagen IV and vitronectin genes in serum free conditions which was attributed to a mechanism allowing the cells to remain attached on the material by their own secreted proteins[44]. For fibroblasts, collagen secretion was 0.2 ± 0.003 µg/mg on PDA-coated samples versus 0.1± 0.003 µg/mg on plasma treated ones at day 14 in the case of LARGE interconnections (Figure 4-5-b) and non-collagenous content was 5.6± 0.3 µg/mg on PDA-coated samples and 1.2 ± 0.08 µg/mg on plasma treated samples at day 14 (Figure 4-5-c). For all samples coated with PDA, both collagenous and non-collagenous secretion increased from day 14 to day 21 indicating the production of ECM by fibroblasts whereas on plasma treated PU, these contents remained constant.

For WJMSCs, there were only small collagen secretion with no non-collagenous secretions on PDA treated PU whereas significant secretions were observed on plasma-treated PU. In this later case, an important increase in the secreted amounts of collagen (0.26± 0.09 to 0.56 ± 0.03 µg/mg) and non-collagen content (11.2 ± 3.12 to 18 ± 3.9 µg/mg) are observed between day 14 and day 21 for structures with LARGE interconnections (Figure 4-6b, c). This indicates a strong ECM production consistent with the entire pore colonization of NIH 3T3 cells on PDA coated PU with LARGE interconnections and WJMCSs on plasma treated PU with LARGE interconnections.

One can thus assume that in both cases the interactions of the cells with the surface favors ECM production onto which cells can further attach, this process going on until the whole pores are filled. These findings demonstrate that the surface treatment can influence cell behavior and that this influence is highly dependent on the cell type.

Our results also show that the size of the interconnections of the scaffolds has a significant influence on cell survival and on matrix production regardless of the surface modification. For both cell types, the DNA concentration is significantly higher in scaffolds with LARGE compared to SMALL interconnections (Figure 4-5a and Figure 4-6a).

For instance, in PDA-coated PU structures, DNA concentration of fibroblasts at day 21 was 0.17 ± 0.002 µg/mg for LARGE interconnections while it was only 0.07 ± 0.009 µg/mg for SMALL interconnections. Likewise, for WJMSCs, on plasma treated PU with LARGE interconnections at day 21, DNA concentration was 0.15 ± 0.006 µg/mg whereas it was 0.07 ±0.008 µg/mg for SMALL interconnections.

Cellular organization was also checked by confocal images. In Figure 4-7, observations by confocal microscopy show that fibroblasts do not colonize the samples with SMALL interconnections either plasma-treated or PDA coated. In the case of SMALL PDA-coated samples, only few cells after 21 days of culture are spread on the scaffold whereas for SMALL plasma treated samples, cells do not spread at all and have a rounded shape consisting with necrotic behavior. As previously explained, in samples with LARGE interconnections, fibroblasts react differently to surface treatments. In LARGE PDA-coated samples, cells fully colonized the pores after 21 days of culture with extensive spreading of their cytoplasm with elongated F-Actin filaments. One can even observe that cells have been able to spread throughout the structure and create cell-cell contacts between adjacent pores. In LARGE plasma treated samples, cells colonized the pores and remained generally on the outer part of the pores thus favoring cell-substrate contacts instead of cell-cell contacts.

The effects of surface treatment and interconnection size are even more pronounced for WJMSCs (Figure 4-8). In PDA-coated samples with SMALL or LARGE interconnections, almost no cells were observed after 21 days of culture, they did not colonize the scaffold. On plasma treated samples, the effect of interconnection size was more obvious since for LARGE interconnections, cells colonize the pores completely and spread throughout the entire structure creating also cell-cell contacts. On the contrary, with SMALL interconnections we can only observe few cells that spread across the scaffold but most of the scaffold remains acellular. These data corroborated our quantitative findings which showed that LARGE PDA-coated scaffolds appear as best substrates for 3T3 cells and LARGE plasma treated scaffolds appear as best substrates for WJMSCs.

The effect of interconnection size on cell behavior may be multifactorial and complex. LARGE interconnections may facilitate cell diffusion through the matrix. A typical cell size being of the order of a few to 10 µm, a pore interconnection size of 27 µm should allow for cell diffusion, but, when cells produce their matrix it may become more difficult for cells to cross the interconnection. Moreover, larger interconnections should favor cell-cell communication between cells of adjacent pores. As discussed previously, the extracellular matrix produced by cells seems to play an important role in cell attachment and further cell behavior. But the significant difference in cell behavior regarding the interconnection sizes can also be correlated to the transport properties as summarized in Table 4-1 where one observes that the hydraulic permeability is changing by one order of magnitude between scaffold with 27 and 52 µm interconnections. As discussed previously, the interconnection diameter is the key parameter regarding the hydraulic permeability that may affect the transport properties through the center of the scaffold. This may affect oxygen and nutrient supply in the center of the sample. This was reported by Kemppainen *et al.*[38] who generated PCL scaffolds in which permeability was controlled. Scaffold with lowest permeability value showed the higher cartilage matrix formation when seeded with chondrocytes compared with scaffolds having higher permeability values. These results were attributed to the lower oxygen tension that may promote cartilaginous matrix formation. Fan *et al.*[45] seeded MC-3T3-E1 cells on tricalcium phosphate scaffolds with varying permeability. Under static culture conditions, they found that cell survival was enhanced in the scaffold with the highest permeability even if the effect was more pronounced under flow perfusion. Again, the authors reported that permeability affects the transport properties regarding both the nutrients and oxygen supply to the center of the scaffold, and the waste removal which may drastically lower the local pH value. Moreover, cellular growth on porous scaffold is thought to be faster for cells on the outer surface than for cells in the deeper layers because on the outside, cells have a better access to nutrients. For instance, Galban *et al.*[46] gave a mathematical approach to describe cell growth in a porous polymer. They proposed that cells located on the outer surface will grow more rapidly than the cells located deeper in the scaffold due to a higher nutrient supply. They argued that cells on the outer surface will merge and finally cover the whole surface. At this point, nutrient supply inside the construct will be limited by diffusion through the cell layer prior to reach the cells inside the scaffold.

Let us finish by discussing the effect of polydopamine (PDA) on cell adhesion. We observe that PDA-treatment of the PU scaffold is favorable for NIH-3T3 proliferation inside the material while it does not allow WJMSCs to proliferate. Polydopamine structure on surfaces is still not well understood. Some authors are considering it as an assembly of supramolecular aggregates rather than a polymer[47]. This material derived from mussel foot protein can virtually bind to any kind of surface through its catecholamine groups such as dopamine. Over the last ten years, functionalization with polydopamine layer has been used to promote cell adhesion on different substrates such as PDMS[48], PCL[49], PLGA[49] or PU[50]. This PDA layer has been shown to promote serum protein adsorption and thus provide an adhesion motif for cells to attach and grow[48]. However, the adsorption of serum proteins alone could not explain cell proliferation and growth on such a substrate as many studies have demonstrated that the adhesion on PDA depends on cell type. It has been found that dopamine induces human adiposed derived stem cells (ADSCs) proliferation on poly (lactic-co-glycolic acid) (PLGA) coated substrate while it did not have any effect on polystyrene (PS). It was also shown that PDA coated PLGA did not promote proliferation of other cell types such as HUVECs or IPSCs[51] . These results are consistent with our study and highlight the complexity of cell adhesion processes on solid surfaces. WJMSCs were already seeded onto a polydopamine modified calcium silicate/poly-capro-lactone (PCL) composite scaffold [52]. No significant proliferation was found with respect to the control which was WJMSCs seeded on a 2D plate for 7 days. This indicates that polydopamine alone did not promote stem cells proliferation in other porous substrates. However, in another study, dopamine-coated calcium silicate surface was shown to increase WJMSCs adhesion for 7 days and beta-1 integrin expression was also higher on dopamine-coated surface.[53] These results clearly demonstrate that the mechanism through which a defined cell type can or cannot adhere and proliferate on PDA layer is yet to be understood.

4.1.5 Conclusion

The physicochemical properties of porous scaffolds significantly affect their ability to be integrated with the host tissue via in-growth of the connective tissue cells. Here, we have introduced a scaffold production protocol which can control the interconnections of the pores while keeping the pore size constant in polyurethane scaffolds. The interconnections significantly affect cell distribution, and ECM secretion when coupled with either plasma or PDA surface treatment in a cell type dependent manner. The extent and response to the surface treatments were different for WJMSCs, where plasma treatment enhanced cell colonization, and fibroblasts where it is the PDA treatment that favored cell colonization. The effect of interconnection size was equally important for both stem cells and fibroblasts where colonization and cell growth were promoted by LARGER interconnections mostly likely due to the significantly improved permeability and ease of cellular connections within 3D structures. Precise control of pore interconnectivity at microscale and surface properties at nanoscale could provide optimized 3D scaffolds for both cell migration and differentiation. Dynamic culture conditions are considered for further work to better harness the improved transport properties in scaffolds with LARGE interconnections.

4.1.6 *References*

1. Karp, J. M., Dalton, P. D. & Shoichet, M. S. Scaffolds for Tissue Engineering. *MRS Bull.* **28**, 301–306 (2003).

2. Karageorgiou, V. & Kaplan, D. Porosity of 3D biomaterial scaffolds and osteogenesis. *Biomaterials* **26**, 5474–5491 (2005).

3. Hutmacher, D. W. Scaffolds in tissue engineering bone and cartilage. *Biomaterials* **21**, 2529–2543 (2000).

4. Vrana, N. E., Liu, Y., McGuinness, G. B. & Cahill, P. A. Characterization of Poly(vinyl alcohol)/Chitosan Hydrogels as Vascular Tissue Engineering Scaffolds. *Macromol. Symp.* **269**, 106–110 (2008).

5. Vrana, N. E. *et al.* Hybrid titanium/biodegradable polymer implants with an hierarchical pore structure as a means to control selective cell movement. *PLoS One* **6**, (2011).

6. Jafari, M. *et al.* Polymeric scaffolds in tissue engineering: a literature review. *J. Biomed. Mater. Res. - Part B Appl. Biomater.* **105**, 431–459 (2017).

7. Laschke, M. W. *et al.* Angiogenesis in Tissue Engineering: Breathing Life into Constructed Tissue Substitutes. *Tissue Eng.* **12**, 2093–2104 (2006).

8. Bil, M., Ryszkowska, J. & Kurzydłowski, K. J. Effect of polyurethane composition and the fabrication process on scaffold properties. *J. Mater. Sci.* **44**, 1469–1476 (2009).

9. Hafeman, A. E. *et al.* Injectable Biodegradable Polyurethane Scaffolds with Release of Platelet-derived Growth Factor for Tissue Repair and Regeneration. *Pharm. Res.* **25**, 2387 (2008).

10. Lv, Q. & Feng, Q. Preparation of 3-D regenerated fibroin scaffolds with freeze drying method and freeze drying/foaming technique. *J. Mater. Sci. Mater. Med.* **17**, 1349–1356 (2006).

11. Hung, K.-C., Tseng, C.-S. & Hsu, S. Synthesis and 3D Printing of Biodegradable Polyurethane Elastomer by a Water-Based Process for Cartilage Tissue Engineering Applications. *Adv. Healthc. Mater.* **3**, 1578–1587 (2014).

12. Oh, S. H., Kim, T. H., Im, G. Il & Lee, J. H. Investigation of pore size effect on chondrogenic differentiation of adipose stem cells using a pore size gradient scaffold. *Biomacromolecules* **11**, 1948–1955 (2010).

13. O'Brien, F. J., Harley, B. a., Yannas, I. V. & Gibson, L. J. The effect of pore size on cell adhesion in collagen GAG scaffolds. *Biomaterials* **26**, 433–441 (2005).

14. Sobral, J. M., Caridade, S. G., Sousa, R. A., Mano, J. F. & Reis, R. L. Three-dimensional plotted scaffolds with controlled pore size gradients: Effect of scaffold geometry on mechanical performance and cell seeding efficiency. *Acta Biomater.* **7**, 1009–1018 (2011).

15. Costantini, M. *et al.* Microfluidic Foaming: A Powerful Tool for Tailoring the Morphological and

Permeability Properties of Sponge-like Biopolymeric Scaffolds. *ACS Appl. Mater. Interfaces* **7**, 23660–23671 (2015).

16. Pamula, E. *et al.* The influence of pore size on colonization of poly(l-lactide-glycolide) scaffolds with human osteoblast-like MG 63 cells in vitro. *J. Mater. Sci. Mater. Med.* **19**, 425–435 (2008).

17. Stenhamre, H., Nannmark, U., Lindahl, A., Gatenholm, P. & Brittberg, M. Influence of pore size on the redifferentiation potential of human articular chondrocytes in poly(urethane urea) scaffolds. *J. Tissue Eng. Regen. Med.* **5**, 578–588 (2010).

18. Matsiko, A., Gleeson, J. P. & O'Brien, F. J. Scaffold Mean Pore Size Influences Mesenchymal Stem Cell Chondrogenic Differentiation and Matrix Deposition. *Tissue Eng. Part A* **21**, 486–497 (2014).

19. Reinwald, Y. *et al.* Interconnectivity and permeability of supercritical fluid-foamed scaffolds and the effect of their structural properties on cell distribution. *Polymer (Guildf).* **55**, 435–444 (2014).

20. Mastrogiacomo, M. *et al.* Role of scaffold internal structure on in vivo bone formation in macroporous calcium phosphate bioceramics. *Biomaterials* **27**, 3230–3237 (2006).

21. Madden, L. R. *et al.* Proangiogenic scaffolds as functional templates for cardiac tissue engineering. *Proc. Natl. Acad. Sci. U. S. A.* **107**, 15211–6 (2010).

22. Ma, P. X. & Choi, J.-W. Biodegradable Polymer Scaffolds with Well-Defined Interconnected Spherical Pore Network. *Tissue Eng.* **7**, 23–33 (2001).

23. Oloffs, A. *et al.* Biocompatibility of silver-coated polyurethane catheters and silvercoated Dacron® material. *Biomaterials* **15**, 753–758 (1994).

24. Laschke, M. W. *et al.* In vivo biocompatibility and vascularization of biodegradable porous polyurethane scaffolds for tissue engineering. *Acta Biomater.* **5**, 1991–2001 (2009).

25. Li, Z., Yao, S.-J., Alini, M. & Stoddart, M. J. Chondrogenesis of Human Bone Marrow Mesenchymal Stem Cells in Fibrin–Polyurethane Composites Is Modulated by Frequency and Amplitude of Dynamic Compression and Shear Stress. *Tissue Eng. Part A* **16**, 575–584 (2009).

26. Li, Y.-H. & Huang, Y.-D. The study of collagen immobilization on polyurethane by oxygen plasma treatment to enhance cell adhesion and growth. *Surf. Coatings Technol.* **201**, 5124–5127 (2007).

27. Lin, H.-B. *et al.* Synthesis, surface, and cell-adhesion properties of polyurethanes containing covalently grafted RGD-peptides. *J. Biomed. Mater. Res.* **28**, 329–342 (2018).

28. B, M. P. Mussel-Inspired Surface chemistry for Multifunctionnal Coatings. *Science (80-.).* **318**, 426–431 (2007).

29. Ku, S. H. & Park, C. B. Human endothelial cell growth on mussel-inspired nanofiber scaffold for vascular tissue engineering. *Biomaterials* **31**, 9431–9437 (2010).

30. Tsai, W. B., Chen, W. T., Chien, H. W., Kuo, W. H. & Wang, M. J. Poly(dopamine) coating of scaffolds for articular cartilage tissue engineering. *Acta Biomater.* **7**, 4187–4194 (2011).

31. Grenier, S., Sandig, M. & Mequanint, K. Polyurethane biomaterials for fabricating 3D porous

scaffolds and supporting vascular cells. *J. Biomed. Mater. Res. A* **82**, 802–9 (2007).

32. Loh, Q. L. & Choong, C. Three-dimensional scaffolds for tissue engineering applications: role of porosity and pore size. *Tissue Eng. Part B Rev.* **19**, 485–502 (2013).

33. Marshall, A. J. & Ratner, B. D. Quantitative characterization of sphere-templated porous biomaterials. *AIChE J.* **51**, 1221–1232 (2005).

34. Pennella, F. *et al.* A Survey of Methods for the Evaluation of Tissue Engineering Scaffold Permeability. *Ann. Biomed. Eng.* **41**, 2027–2041 (2013).

35. Smith, J. R. *et al.* Standardizing Umbilical Cord Mesenchymal Stromal Cells for Translation to Clinical Use: Selection of GMP-Compliant Medium and a Simplified Isolation Method. *Stem Cells Int.* **2016**, 14 (2016).

36. Schneider, C. A., Rasband, W. S. & Eliceiri, K. W. NIH Image to ImageJ: 25 years of image analysis. *Nat. Methods* **9**, 671–675 (2012).

37. Li, M. V. C. and W. A permeability measurement system for tissue engineering scaffolds. *Meas. Sci. Technol.* **18**, 208 (2007).

38. Kemppainen, J. M. & Hollister, S. J. Differential effects of designed scaffold permeability on chondrogenesis by chondrocytes and bone marrow stromal cells. *Biomaterials* **31**, 279–287 (2010).

39. Myung, S.-W., Yeom, Y.-H., Jang, Y.-M., Choi, H.-S. & Cho, D. Preparation of a reticulated polyurethane foam grafted with poly(acrylic acid) through atmospheric pressure plasma treatment and its lysozyme immobilization. *J. Mater. Sci. Mater. Med.* **16**, 745–751 (2005).

40. Sanchis, M. R., Calvo, O., Fenollar, O., Garcia, D. & Balart, R. Characterization of the surface changes and the aging effects of low-pressure nitrogen plasma treatment in a polyurethane film. *Polym. Test.* **27**, 75–83 (2008).

41. Sanchis, M. R., Calvo, O., Fenollar, O., Garcia, D. & Balart, R. Surface modification of a polyurethane film by low pressure glow discharge oxygen plasma treatment. *J. Appl. Polym. Sci.* **105**, 1077–1085 (2007).

42. Della Vecchia, N. F. *et al.* Tris Buffer Modulates Polydopamine Growth, Aggregation, and Paramagnetic Properties. *Langmuir* **30**, 9811–9818 (2014).

43. Ferreira, S. A. *et al.* Bi-directional cell-pericellular matrix interactions direct stem cell fate. *Nat. Commun.* **9**, 4049 (2018).

44. Vining, K. H. *et al.* Synthetic Light-Curable Polymeric Materials Provide a Supportive Niche for Dental Pulp Stem Cells. *Adv. Mater.* **30**, 1704486 (2017).

45. Fan, J., Jia, X., Huang, Y., Fu, B. M. & Fan, Y. Greater scaffold permeability promotes growth of osteoblastic cells in a perfused bioreactor. *J. Tissue Eng. Regen. Med.* **9**, E210–E218 (2013).

46. Galban, C. J. & Locke, B. R. Analysis of cell growth in a polymer scaffold using a moving boundary approach. *Biotechnol. Bioeng.* **56**, 422–432 (2000).

47. Bernsmann, F. *et al.* Dopamine−Melanin Film Deposition Depends on the Used Oxidant and

Buffer Solution. *Langmuir* **27**, 2819–2825 (2011).

48. Ku, S. H., Lee, J. S. & Park, C. B. Spatial Control of Cell Adhesion and Patterning through Mussel-Inspired Surface Modification by Polydopamine. *Langmuir* **26**, 15104–15108 (2010).

49. Jo, S. *et al.* Enhanced Adhesion of Preosteoblasts inside 3D PCL Scaffolds by Polydopamine Coating and Mineralization. *Macromol. Biosci.* **13**, 1389–1395 (2013).

50. Davoudi, P. *et al.* Biomimetic modification of polyurethane-based nanofibrous vascular grafts: A promising approach towards stable endothelial lining. *Mater. Sci. Eng. C* **80**, 213–221 (2017).

51. Yang, K. *et al.* Polydopamine-mediated surface modification of scaffold materials for human neural stem cell engineering. *Biomaterials* **33**, 6952–6964 (2012).

52. Chen, Y.-W. *et al.* Osteogenic and angiogenic potentials of the cell-laden hydrogel/mussel-inspired calcium silicate complex hierarchical porous scaffold fabricated by 3D bioprinting. *Mater. Sci. Eng. C* **91**, 679–687 (2018).

53. Kao, C.-T. *et al.* Surface Modification of Calcium Silicate via Mussel-Inspired Polydopamine and Effective Adsorption of Extracellular Matrix to Promote Osteogenesis Differentiation for Bone Tissue Engineering. *Materials* **11**, (2018).

4.1.7 Annexes

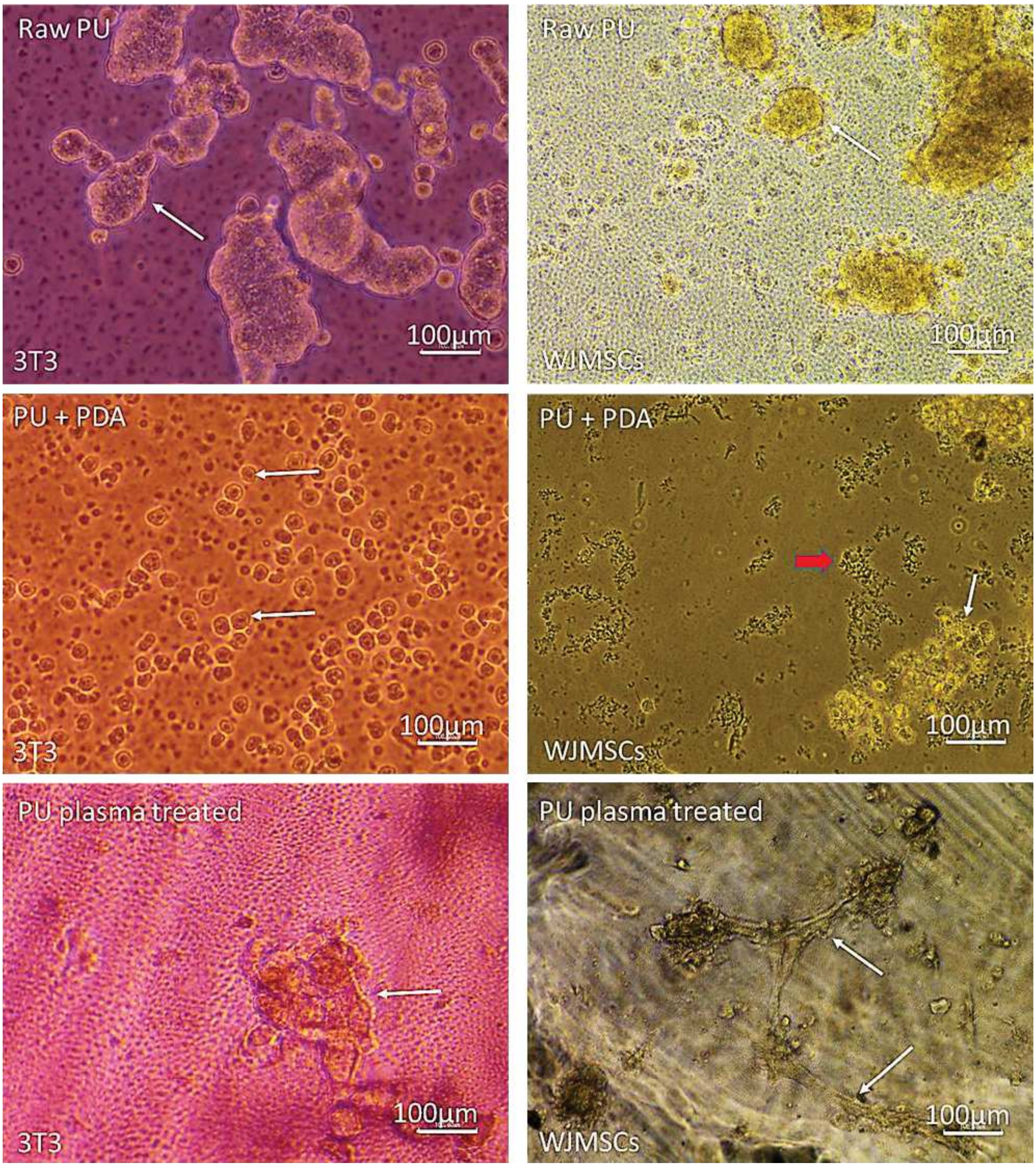

Figure S 1: Images taken with optical microscope of 3T3 Fibroblasts (left column) and WJMSCs (right column) on PU flat surfaces after 24h of culture. Cells were seeded on raw PU labelled as (Raw PU, top images), PDA-coated PU labelled as PU + PDA (images in the middle), and PU that underwent plasma treatment labelled PU plasma treated (images at the bottom).

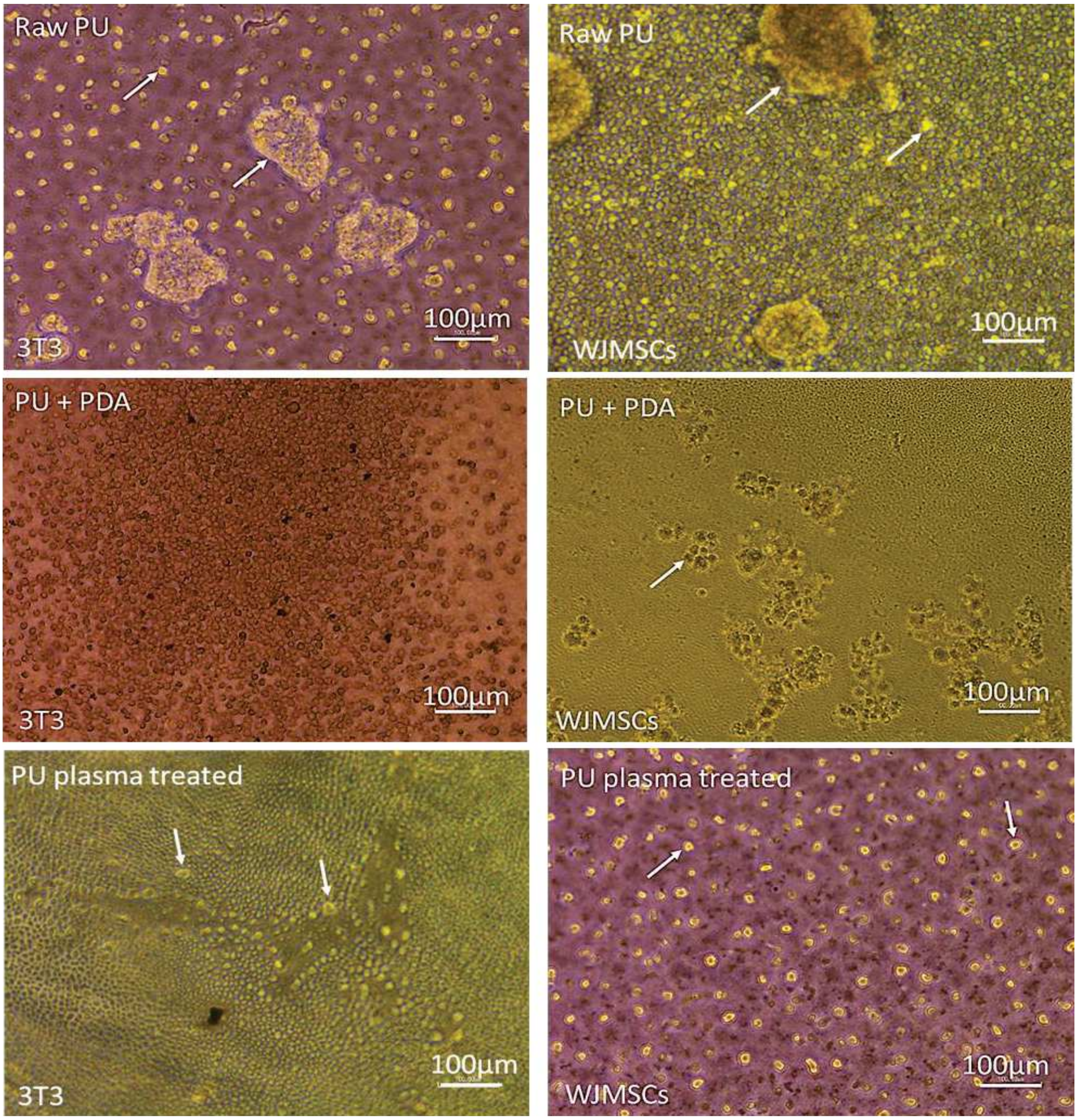

Figure S 2: Images taken with optical microscope of 3T3 Fibroblasts (left column) and WJMSCs (right column) on PU flat surfaces after 48h of culture. Cells were seeded on raw PU labelled as (Raw PU, top images), PDA-coated PU labelled as PU + PDA (images in the middle), and PU that underwent plasma treatment labelled PU plasma treated (images at the bottom).

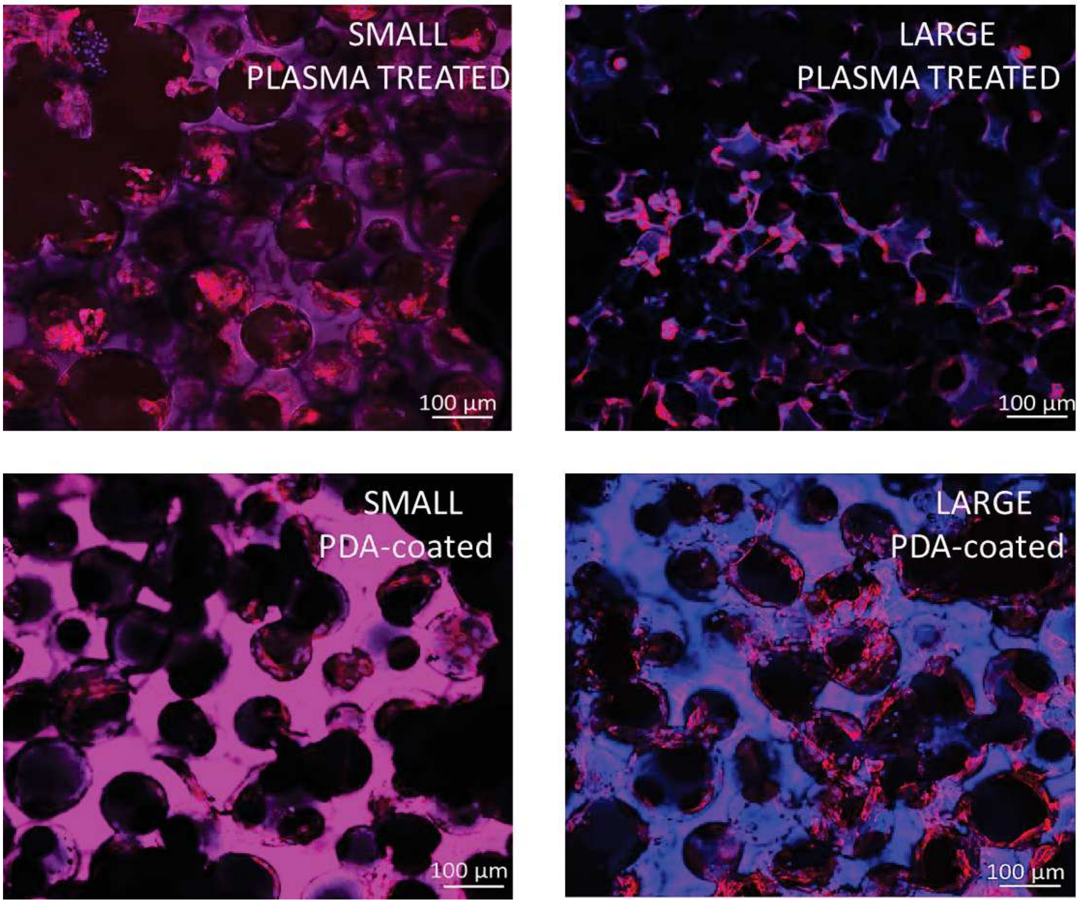

Figure S 3: Confocal images of NIH 3T3 fibroblast in PU scaffolds after 24h of culture. Left column corresponds to scaffold having SMALL interconnections while in the right column, scaffolds have LARGE interconnections. Images on the top represent scaffolds that were treated with plasma prior seeding the cells, while images at the bottom represent scaffolds that were coated with PDA. Cells were stained with DAPI/Phalloidin. Images were taken at the center of the scaffold approximately.

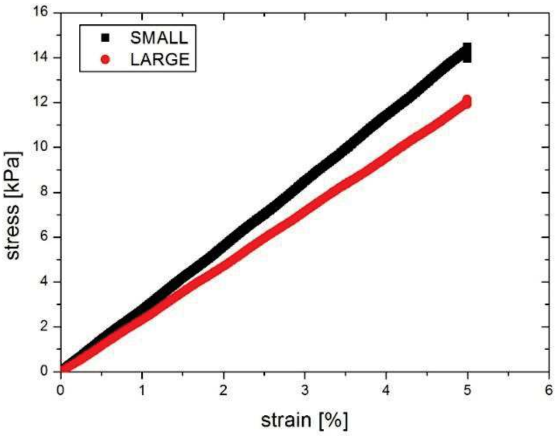

Figure S 4: Typical stress-strain curves of scaffolds with SMALL and LARGE interconnections.

4.1.8 Résultats complémentaires

4.1.8.1 *Approche itérative pour la détermination du diamètre optimal des pores et des interconnexions.*

Nous avons montré dans ce chapitre l'importance du diamètre des interconnexions sur la survie à long terme ainsi que sur l'organisation des cellules souches et des fibroblastes. Nous avons pu constater que le traitement de surface est spécifique au type de cellule employé (Section 4.1.3.2) . Nous avons choisi de conserver le diamètre des pores constant à 130 µm en nous appuyant sur les données disponibles dans la littérature. Néanmoins, nous avons testé d'autres combinaisons de diamètres de pores et d'interconnexions qui sont présentées ci-après.

Nous avons généré des matériaux poreux avec différents diamètres de pores ($<D>$ = 66±20 µm, 133 ±12 µm et 245±60 µm). Nous avons utilisé la méthode de « sphere templating » décrite Chapitre 3 pour contrôler la taille des interconnexions. Nous avons comparé des échantillons ayant les mêmes diamètres d'interconnexions mais différents diamètres de pores pour avoir la contribution de la taille des pores seule. Les interconnexions ont un diamètre $<d> \approx$ 30, 40, et 60 µm comme montrés dans la Figure C 1. On peut clairement s'apercevoir que le diamètre d'interconnexion le plus grand favorise la colonisation des cellules ainsi que leur capacité à se propager dans le matériau. Lorsque les pores sont petits (i.e. $<D>$ = 66 µm) les cellules restent agrégées dans les pores. Les pores plus grands ne favorisent pas d'avantage la colonisation si les interconnexions sont trop petites c-a-d < 50 µm. En suivant la prolifération sur 21 jours, on constate néanmoins une prolifération pendant les 14 premiers jours (Figure C 2). Les échantillons avec des interconnexions de petites tailles (< 30 µm) semblent d'ailleurs promouvoir d'avantage la prolifération. Les échantillons ont tous été traités avec la polydopamine qui présente un effet bénéfique pour les fibroblastes. Cependant, l'impact des interconnexions est un facteur commun, quel que soit le type de cellule. La prolifération visible sur les 14 premiers jours dans toutes les conditions montre que les cellules peuvent envahir le matériau et les pores. Lorsque les pores sont remplis, les cellules filles ne peuvent plus adhérer au matériau et se détachent expliquant ainsi la baisse d'intensité de fluorescence au jour 21 de la Figure C 1. Ceci peut être observé sur la Figure C 1 pour la condition $<D>$ = 66 µm, $<d>$ = 30 µm où des cellules sont toujours présentes dans les pores, leur densité semble élevée mais elles sont arrondies. L'autre explication pourrait être que les cellules qui « tapissent » la surface externe du poreux créent une barrière de diffusion aux cellules situées plus au centre du matériau. Cela peut provoquer leur apoptose par hypoxie ou par un abaissement local du pH. Les grandes interconnexions permettent aux cellules de se propager au sein du poreux. Une porosité et des interconnections plus grandes (cf Table 4-1) permettent ainsi une augmentation des propriétés de transport ainsi qu'un meilleur apport d'oxygène et de nutriments aux cellules. Ces résultats confirment qu'à long terme, le contrôle des interconnexions est essentiel. Nous avons choisi un diamètre moyen des pores de 130 µm pour nos expériences dans la Section 4.1.3.2 bien que les résultats pour des pores de 245 µm soient tout aussi concluants. Ce choix est motivé par le fait qu'il a été montré que des pores de tailles trop grandes jouent un rôle dans les réactions inflammatoires qui mènent à l'encapsulation fibreuse (Voir Section 1.2.3). Bien que nos expériences aient été conduites uniquement *in-vitro* nous avons décidé de générer des structures qui peuvent malgré tout, représenter des modèles « réalistes » en vue d'éventuels essais *in-vivo*.

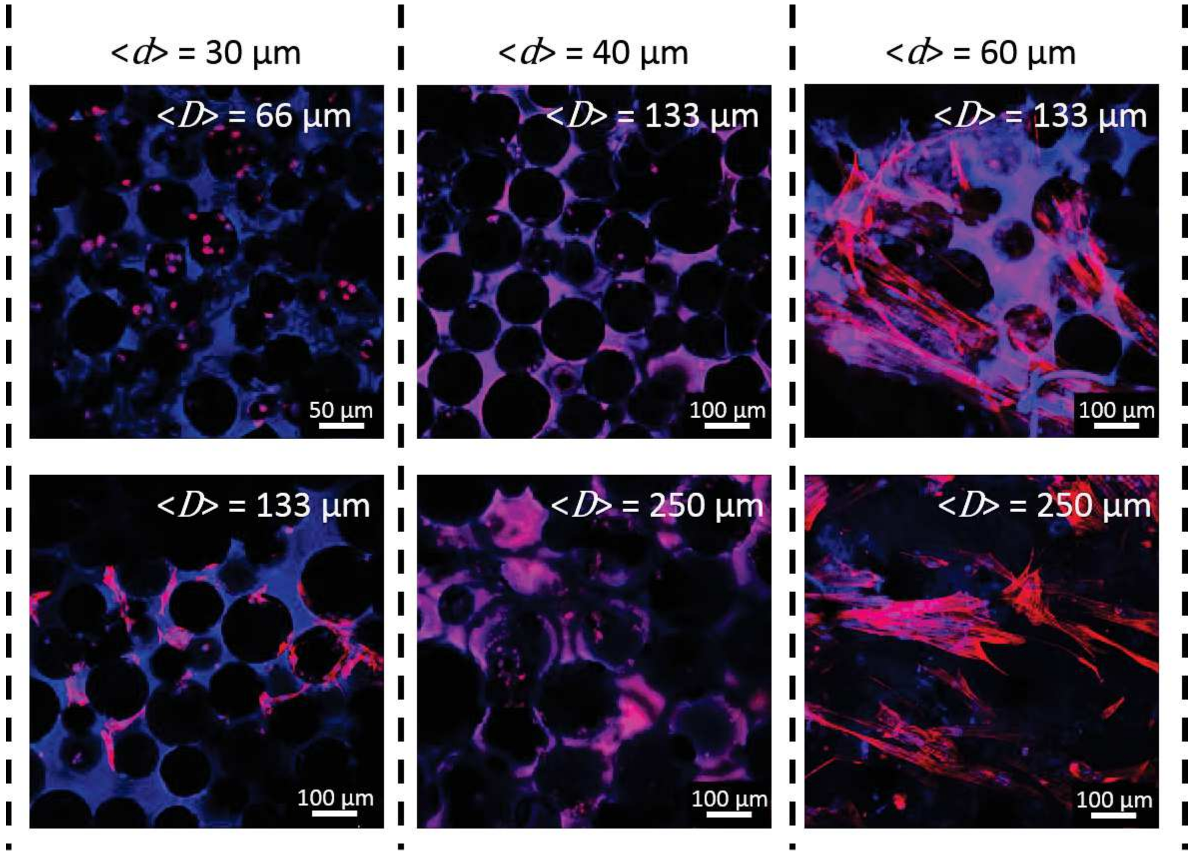

Figure C 1 : : Images prises par microscope confocale de fibroblastes (NIH 3T3) après 21 jours de culture. Les cellules sont marquées avec du DAPI/phalloidine pour visualiser les noyaux (bleu) et les filaments d'actine (rouge). Les cellules ont été ensemencées dans des matériaux avec différents diamètres de pore <D> et d'interconnexions <d>. Les images sont prises approximativement au centre du matériau.

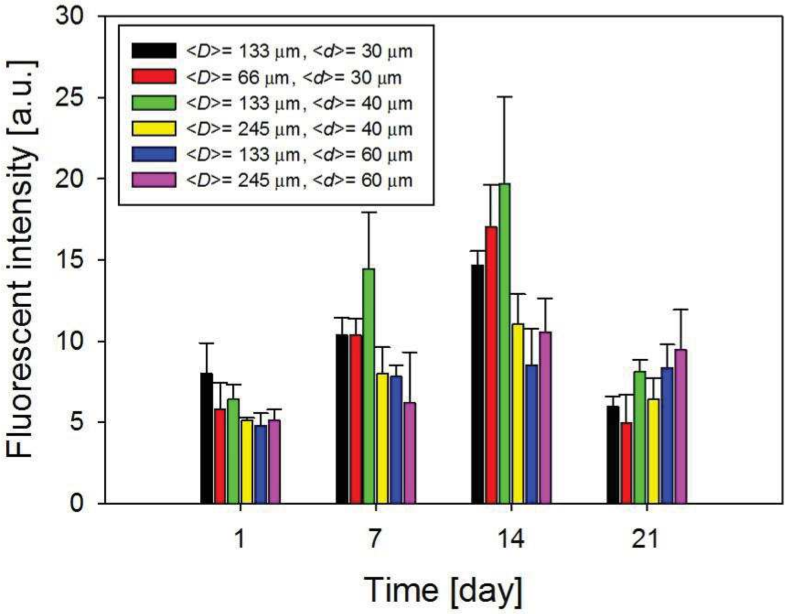

Figure C 2: Mesure de la viabilité/proliferation des fibroblastes par Alamar blue® pour des cellules ensemencées dans des matériaux avec différents diamètres de pores <D> et d'interconnexions <d>.

4.1.8.2 Etude de la formation des contacts focaux des cellules souches en réponse aux traitements de surface.

La formation de contacts focaux est un indicateur d'une adhésion stable entre une cellule et un substrat. Nous avons ainsi tenté de visualiser leur évolution sur les cellules souches uniquement. Nous pouvons constater sur la Figure C 3 que la fibronectine permet l'accumulation de vinculine aux extrémités des filaments d'actine. Nous ne voyons pas de fuseaux distincts car les cellules sont visualisées dans les poreux, Ainsi, des effets d'orientation peuvent jouer. Cette accumulation de vinculine est généralement considérée comme un indicateur dans la formation de contacts focaux. Lorsque le traitement plasma est appliqué, les cellules peuvent pénétrer dans la structure, mais celles-ci semblent privilégier les contacts entre cellules plutôt qu'avec le substrat après 2 jours de culture. Après 21 jours en revanche, on peut apercevoir la formation de points distincts qui impliquent que les cellules ont adhéré au matériau (probablement par l'intermédiaire de protéines sécrétées). Le traitement par la polydopamine, quant à lui, permet une adhésion des cellules rapidement, mais celles-ci deviennent arrondies après 21 jours. Cela semble confirmer l'effet cytotoxique de la polydopamine déjà souligné dans la Figure 4-6.

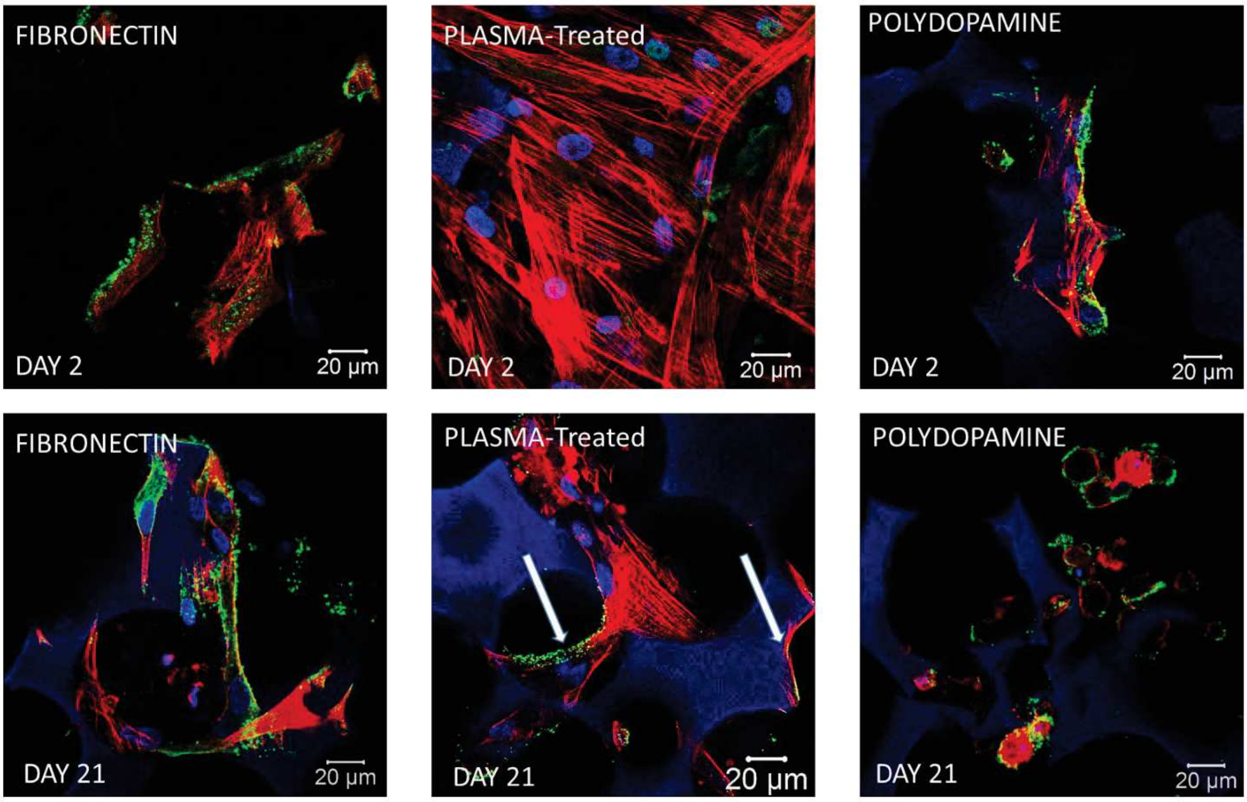

Figure C 3: Image prise par microscopie confocale après 2 jours (ligne du haut) et 21 jours (ligne du bas) de cellules souches de la gelée de Wharton ensemencée sur du PU avec des surfaces traitées avec de la fibronectine (colonne de gauche), le traitement plasma (colonne du milieu) et la polydopamine (colonne de droite). Les cellules ont été marquées avec du DAPI (bleu) pour visualiser les noyaux, de la phalloidine pour voir les filaments d'actine (rouge) et la vinculine a été marquée en vert indiqué par une flèche pour les échantillons traités au plasma à j21.

4.2 Adjustment of cell adhesion and elastic modulus of polyurethane structures with controlling hard/soft segments ratio

4.2.1 Abstract

Obtaining materials that either prevent or promote cell adhesion is still challenging. Currently available methods require surface post modifications or complex chemical synthesis. Herein, polyurethane (PU) films were synthesized by simply mixing hard and soft segments (i.e. a polyether triol and an isocyanate) at different ratios or "isocyanate indexes" to achieve structures with a wide range of mechanical properties and cell adhesiveness. As in most studies polyurethane was synthesized close to the stoichiometry which is by definition an isocyanate index of 100 (i.e. a ratio of isocyanate to hydroxyl function of 1). An increase of the hard segment content results in an increase the crosslink density and the resulting material becomes stiffer. Polyurethane with isocyanate indexes of 75, 100, 200, 300 and 400 corresponding to ratios of isocyanate to hydroxyl functions of 0.75:1, 1:1, 2:1, 3:1, 4:1 respectively. We demonstrated that the adhesion capacities of two cell types, NIH 3T3 fibroblasts (3T3) and Wharton's jelly mesenchymal stem cells (WJMSCs), depend on the isocyanate index (NCO index). For NCO indexes below 300, no cell adhesion was observed regardless of the cell type whereas NCO indexes of 300 and 400 allow cells to adhere on the PU surface. Using Wide Angle X-ray Scattering (WAXS) and Small Angle X-ray Scattering (SAXS) we could show that the control of NCO indexes allows to modulate the phase separation in PU films. Indeed, films with NCO indexes of 300 and 400 undergo a phase separation where hard segments form hard domains that are randomly distributed in the soft segment matrix. Using Porod's law, we could show that for samples with NCO indexes of 300 and 400, hard domains make more sharp interfaces with soft surrounding matrix. Conversely, samples with smaller NCO indexes present diffuse interfaces which implies that soft and hard segments are interpenetrated at the hard/soft segment interface. Based on the literature, hard segments favor cell attachment on PU substrates and group into nano domains that form topographical cues that guide cellular adhesion. While sharp interfaces allow the existence of distinct areas composed of hard segments only, diffuse interfaces form hard segment rich areas where soft segments are present. Hence, the degree of the phase separation in the PU matrix, which is the phase separation state of the system compared to a system with only sharp interfaces, appears to be a critical feature that correlates with the adhesion capacity of cells.

4.2.2 Introduction

Cell attachment is often considered as the first step needed to trigger the proliferation and afterwards the colonization of porous scaffolds. Cell adhesion is often mediated by integrins, which are transmembrane proteins composed of α and β subunits that combine and recognize specific sequences of peptides to which they can bind to[1]. The most studied adhesion peptide sequence is the RGD (Arg-Gly-Asp) sequence that is naturally present on some extracellular proteins[2]. Synthetic materials do not have such adhesive motifs. Hence, often biomaterial surfaces are coated or functionalized with proteins or peptides to enhance cellular adhesion[3–5]. Polyurethane (PU) is widely used in the medical field due to its biocompatibility as well as the advantageous mechanical properties than can be tailored to match the ones of a given tissue[6,7]. Polyurethanes are produced by the reaction between a polyol and an isocyanate (Figure 4-9a). Sometimes, a chain extender is used to increase the chain length of the final polymer[8]. Polyols have longer molecular weights than isocyanates, they have a high mobility and flexibility of their chains, they are also called **soft segments**. Isocyanate provide stiffness to the polymer and are often called **hard segments** (Figure 4-9b). Hard and soft segments can separate into two distinct phases (due to their incompatibility) within the polymer matrix where hard segments can self-arrange by π-stacking or hydrogen bonding forming distinct micro domains randomly distributed in the matrix of soft segments. Phase separation depends on several factors such as the thermal history of the polymer[9] or the molecular structure of the hard and the soft segments[10]. This phase separation has already been studied in the past by X-Ray photoelectron spectroscopy (XPS)[11], Fourier Transformed Infrared Spectroscopy (FTIR)[9] and Small Angle X-ray Scattering (SAXS)[12] and was shown to induce different responses regarding mechanical properties[13]. To our knowledge, only few examples are reported in the literature where the influence of this "biphasic" system on cell attachment and proliferation on the PU surface is investigated. Yuan *et al.*[14] produced poly(caprolactone)-based PU and modified the hard segment fraction in their formulation. They showed that endothelial cells form a well-organized network of cells on films having a microphase separation within the bulk compared to homogenous PU films (i.e. when the polymer do not exhibit two distinct phases). The authors argued that cells felt the phase segregation and especially hard segment domains with a higher local stiffness that could help cells to form stable focal contacts. The ability of the distinct domains containing hard segments to support cell adhesion was also demonstrated by Nalluri *et al.*[15]. They generated polyurethanes having poly(ethylene glycol) as soft segments (which prevent cell adhesion), and hard segments that were composed of either hexamethylene diisocyanate (HDI) or 4,4'-methylenebis (cyclohexyl isocyanate) (HMDI). While HDI-based PU exhibited a phase segregation, HMDI-based PU showed that hard and soft segments were more homogenously mixed. This was attributed to the fact that HMDI cannot self-organize due to steric hindrance. Mesenchymal Stem Cells (MSCs) were making stable focal contacts on PU having a microphase separation which was also attributed to the interaction between cells and the hard segment domains. Furthermore, Mi *et al.*[16] used two commercial polyurethanes with two hard segment fractions. They showed that the polymers become increasingly hydrophobic when the hard segment content increases, and that the protein adsorption is higher when the hard segments content decreases. They demonstrated that 3T3 fibroblasts showed better viability on PU having a higher hard segment fraction despite the fact that those films were more hydrophobic and that less proteins were adsorbed on their surface. Even if these authors did not investigate whether some phase separation is present within the polymer, these findings highlight the fact that cells respond differently regarding the microstructure of the PU underneath.

In the present study, we synthesized PU films with different isocyanate indexes, respectively 75-100-200-300 and 400 and we investigated how these changes in isocyanate content affect the microstructure of the PU. We further evaluated how the microstructure of the PU affects the ability of 3T3 fibroblasts and WJMSCs to attach to the PU surfaces. We characterized the obtained films in terms of wettability, protein adsorption, surface and bulk chemistry and phase separation of hard and soft segments within the matrix to establish a correlation between the cellular response to the material and its structural features. Finally, we extrapolated this flat model to a three-dimensional porous material to investigate if cell colonization can be improved by the modulation of the NCO index.

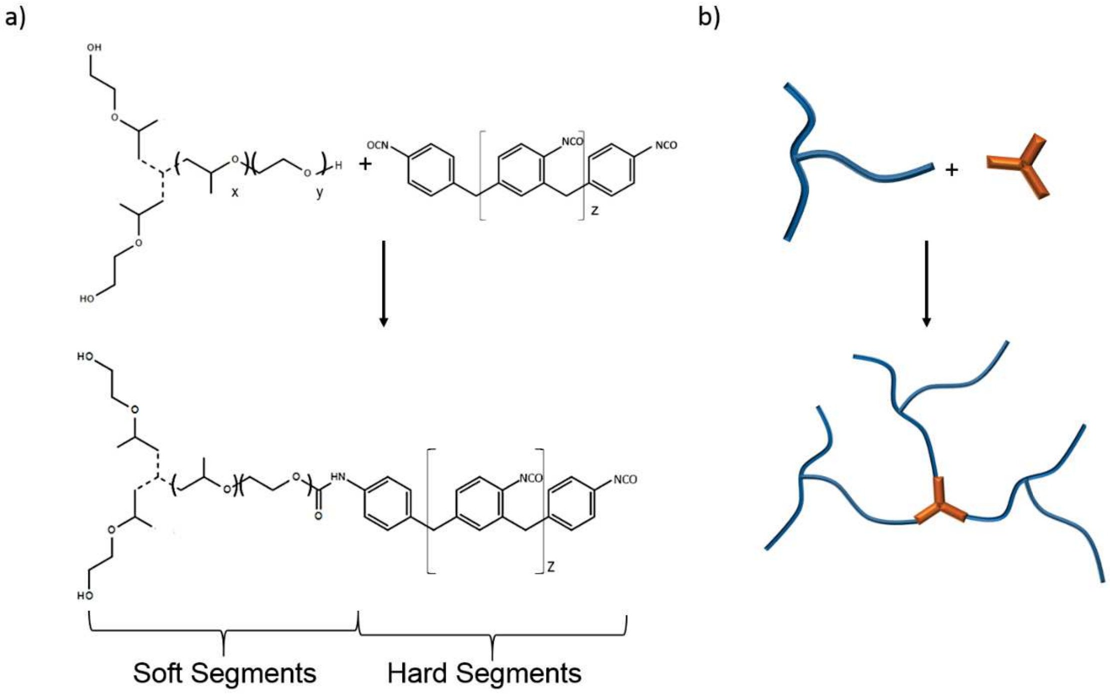

Figure 4-9 : Reaction scheme of the PU synthesis from the reaction of a polyether triol composed of a polypropylene oxide (PPO) backbone end capped with polyethylene oxide PEO and the polyMDI a). b) schematic representation of the PU with the main building blocks.

4.2.3 Results

We seeded WJMSCs and 3T3 fibroblasts on PU films having NCO indexes of 75, 100, 200, 300, and 400. As shown in Figure 4-10, both 3T3 fibroblasts and WJMSCs adhesion shows a dependence on the NCO index. A threshold value seems to appear between NCO_{200} and NCO_{300}. For PU films having NCO index < 200, cells have a round shape and aggregate. Starting from NCO_{300}, cells can clearly spread on the substrate which indicates that they are able to adhere on the material surface. From Figure 4-10, one can also notice that the threshold value in the NCO index seems to be the same for both cell types. Hence, cells adhesion on PU films was greatly affected by the NCO index.

Cells were also fixed in paraformaldehyde and stained for F-actin filaments and nucleus by using DAPI/Phalloidin. For NCO indexes below 200, no more cells were present after rinsing with PBS (see Section 2.11.1). This is due to the rinsing steps needed upon the staining procedure (Figure S 5). For PU films having an NCO index above 200, we can observe again that both cell types can spread on the surface.

In order to identify the origin of this difference in cell spreading, we first tested the cytotoxicity of the samples via indirect contact in order to verify if they release harmful compounds (see Section 2.9). For all the tested samples (i.e. NCO_{ind} of 75, 100 and 400) no cytotoxic effect appeared (Figure S 6) as viability rate remains above 80% for all samples.

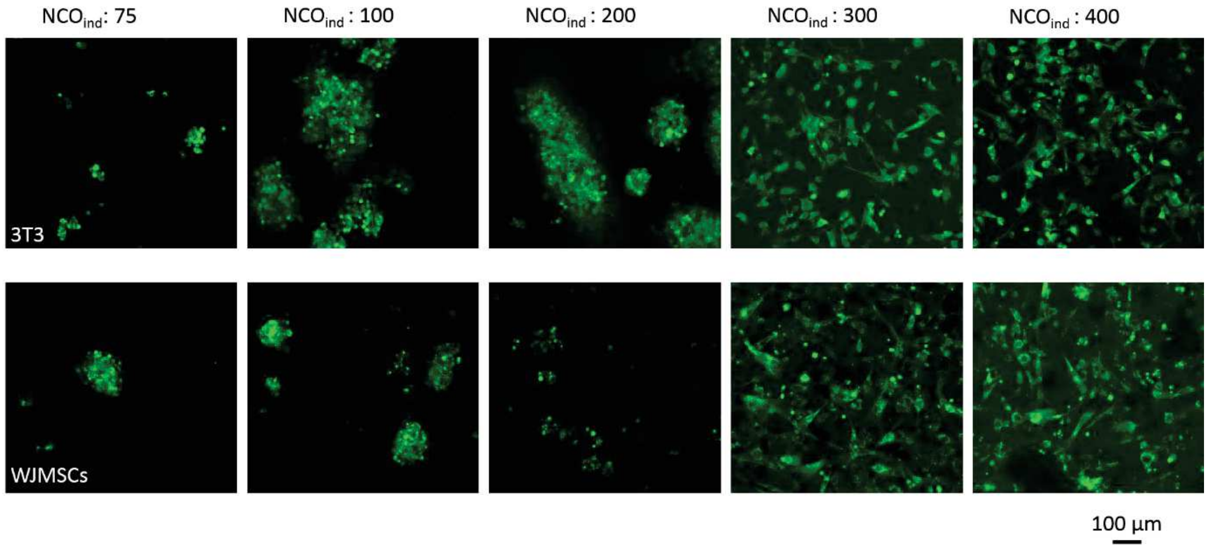

Figure 4-10: 3T3 fibroblasts (top row) and WJMSCs (bottom row) seeded on PU films with various isocyanate indexes after 24h, cells were stained with Grenn-calcein.

Since the attachment of cells to a surface is often mediated by protein adsorption, we examined if the amount of adsorbed proteins depends on the NCO index. We quantified the number of protein adsorbed onto PU surface by two methods (see Section 2.10) to ensure the reliability. We found that for samples having NCO indexes of 75 and 100, less proteins were adsorbed onto the PU surface compared to samples with NCO indexes higher than 200 (Figure S 7). But even if less proteins adsorbed onto the substrate, this cannot explain alone why cell adhesion seems prohibited on these films. Furthermore, even if the amount of adsorbed proteins on samples with NCO index 200 is at the same level as that of samples with NCO index of 300 and 400, cells were not able to adhere on the 200 index sample.

We further seeded WJMSCs into a porous scaffold made from the same polyurethanes in order to evaluate if the NCO index can influence the ability of cells to colonize a scaffold. Details on the scaffold production and the cell culture are published elsewhere[22]. We kept the same porous structure, using a PU that was synthesized with two different NCO indexes: 100 which prevents cell adhesion and 400 as a permissive substrate for cell attachment. We seeded only WJMSC cells because the cell response to the NCO index was the same for both 3T3 and WJMSCs. Figure 4-11 shows that no cell remain in the scaffold with an NCO index of 100 after 7 days whereas WJMSCs are able to colonize the scaffold having an NCO index of 400. As on the flat substrate, one observes that cell colonization is much more facilitated for scaffold made by PU with NCO index of 400 compared to 100.

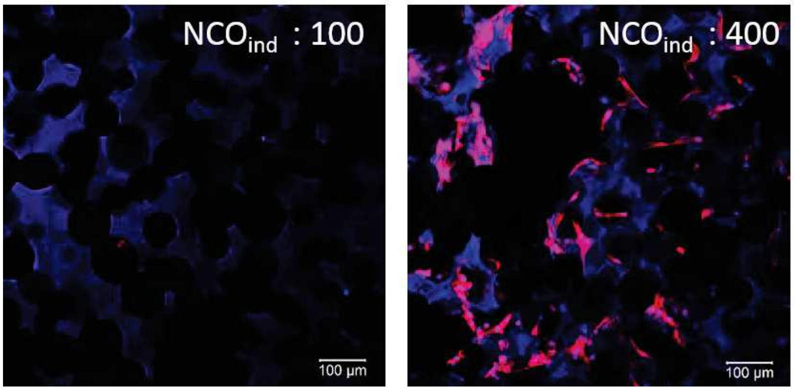

Figure 4-11 : Images of WJMSC cells after 7 days of cell culture in a PU scaffold having an NCO index of 100 (left) and 400 (right). Cells were stained with DAPI/Phalloidin for the visualization of F-actin filaments and nucleus respectively.

To understand how the changes in isocyanate content can affect PU properties, and accordingly the adhesion capacity of the cells, we investigated the mechanical properties of the samples. To this end, tensile tests were performed on 1-mm-thick PU films of variable NCO index and the corresponding experimental part can be found in Section 2.18. Typical stress-strain curves are shown in Figure 4-12a. Curves are shown until rupture of the PU film. For all NCO indexes, they show a nearly linear stress-strain dependence until rupture. As the isocyanate index increases, the initial slope of strain versus stress increases as well. Hence, the Young modulus, which is given by this slope, increases with the amount of isocyanate used in the formulation. This is a well-known effect, since hard segments contribute to make the polymer stiffer[23]. The obtained Young modulii and the elongation at break are shown in Figure 4-12b. For an isocyanate index of 75, the Young modulus was 0.2 MPa while it was 8 MPa for NCO index of 400. The Young's modulus increases significantly (nearly linearly) with isocyanate content until an NCO index of 300. Above this value the increase in modulus with NCO index is less pronounced but as we only have one data point above the NCO$_{ind}$: 300, we cannot conclude that this is a general trend. Therefore, cells start to adhere on PU films with Young moduli around 8 MPa. Nevertheless, care must be taken to not hurriedly correlate those values to the ability of cells to sense the substrate stiffness. Indeed, the range of Young moduli in substrate stiffness to which cells are sensitive is commonly between tens to hundreds of kPas[24]. Therefore, we hypothesize that for films having Young moduli above 0.7 MPa, cells do not feel the averaged modulus that is measured by the mechanical testing but rather to more local material properties. One can also remark that the elongation at break decreases with increasing isocyanate index (Figure 4-12b). For the lowest index (i.e. NCO$_{ind}$:75), the elongation at break is 73% compared to 24 % for NCO index of 400. These differences can be explained by the increasing crosslinking density NCO index. Therefore, variation of the NCO/OH functions in the formulation of polyurethane allows adjusting finely the mechanical properties[25].

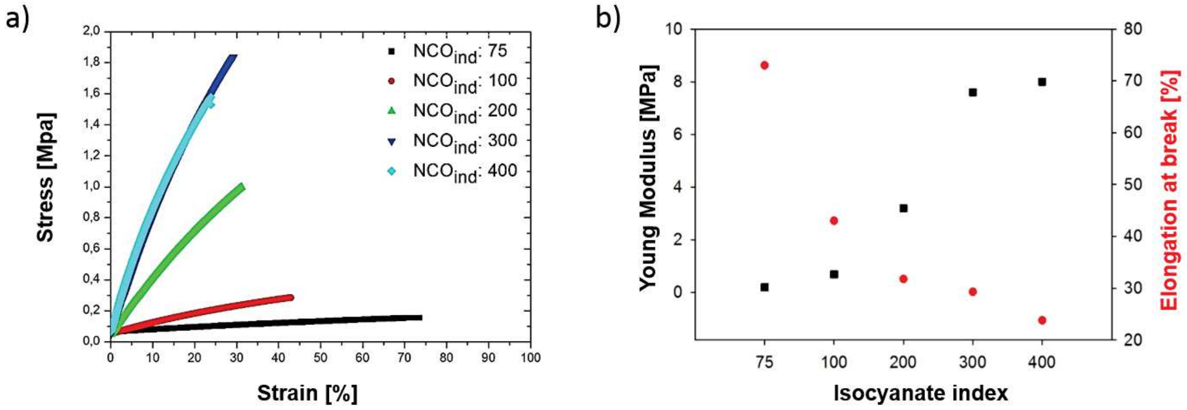

Figure 4-12: (a) Stress-strain curve of polyurethane films obtained upon stretching and their correspondingYoung modulus and elongation at break (red plots) (b).

Infrared spectroscopy was also employed to investigate the differences in chemical functions for the different samples. The FTIR spectra obtained for PUs with increasing NCO index are shown in Figure 4-13. An increase in the NCO content of the polymer shows an increase in the intensity of the band at 2274 cm^{-1} associated with free NCO groups[18] as well as an increase of the bands at 1597 and 1411 cm^{-1} which are attributed to aromatic and isocyanurate vibrations respectively. Peaks at 1510 and 1539 cm^{-1} correspond to amide I and II respectively[26]. On Figure 4-13, one can clearly see that peaks associated to free NCO groups increase with increasing NCO index. This is quite logical since unreacted isocyanate functions remain left for NCO indexes greater than 100. However, due to the highly reactive nature of isocyanate, free NCO groups tend to react with other free NCO groups to form isocyanurates which are indeed present by looking at the band at 2274 cm^{-1} (Figure 4-13b). Additionally, NCO groups are also known to be able to react with primary and secondary amines[27]. Urea, biuret or allophanates are common products of this reaction[27]. These side products are associated to the peaks at 1510 and 1539 cm^{-1} corresponding to amide I and II vibrations respectively. In Figure 4-13b, the curves for NCO indexes 75 and 100 show the same profile whereas, for higher indexes, all the peaks associated to species that result from the reaction of free isocyanates groups are increasing.

To gain more insight into the process by which cells can adhere to the PU surface, one needs to sense the outermost surface of the considered material. It is well known that the surface chemistry of polyurethanes tends to be different from the bulk composition[28]. Hence, X-Ray Photoelectron Spectroscopy (XPS) analyses were carried out to evaluate if the changes in isocyanate index induce changes in surface chemistry (see Section 2.15 of Materials and Methods).

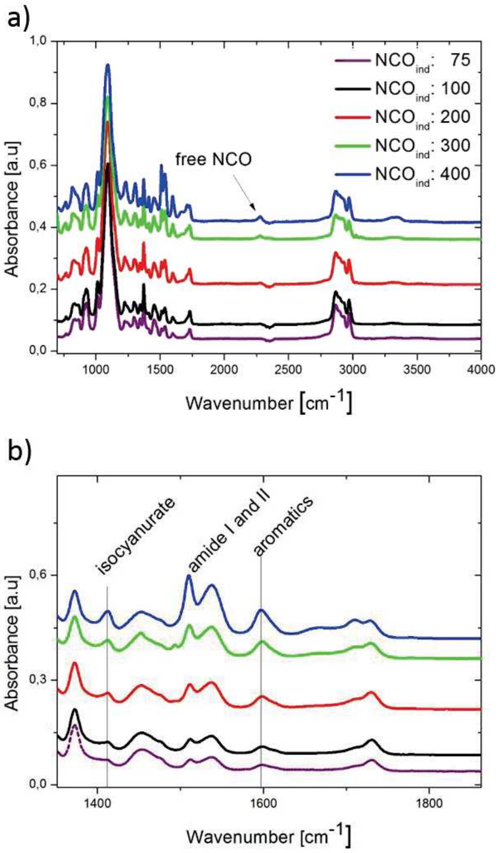

Figure 4-13: FTIR spectra of PU films with various isocyanate indexes in a) and a higher magnification of the region between 1350 and 1850 cm^{-1} in b).

The respective peaks of the O_{1S}, C_{1S} and N_{1S} orbitals are shown in Figure 4-14a,b and d. We were not able to obtain the spectra of the sample with an NCO index of 75 because the ultra-high vacuum could not be achieved. This could be due to unreacted monomers that leached out of the sample. Peaks at 284,6 and 286,5 eV on the C_{1S} spectra are attributed to aliphatic carbons and ether carbons respectively[29]. The peak at 400 eV on the N_{1S} nitrogen curve (Figure 4-14d) corresponds to nitrogen atoms in the urethane and/or urea bonds[11]. Interestingly, when the NCO index increases, the nitrogen percentage at the surface does almost not vary from NCO_{ind} of 100, 200 and 300 where values are comprised between 0.3 to 0.6 %. Nitrogen content increases more for NCO_{ind} 400 to reach 1.9 %. As nitrogen is only present on hard segments, one can use the nitrogen quantification as a reflect of the amount of hard segment on the outermost surface of the PU. These findings are in good agreement with other studies which demonstrated hard segments content at PU surface remains fairly constant[30,31]. One generally accepted explanation is that PU outermost surface is enriched in soft segments to lower the surface energy[32,33]. However, XPS analysis are performed under high vacuum, and these conditions are not necessarily accurate to describe the surface in aqueous media. Nevertheless, XPS measurements allow us to identify the chemical species formed in the PU. Of particular interest is the spectrum associated to nitrogen which is never shifted. This implies that the side products formed by the reaction of free isocyanate with other groups than hydroxyl are not present in the outermost surface of the samples.

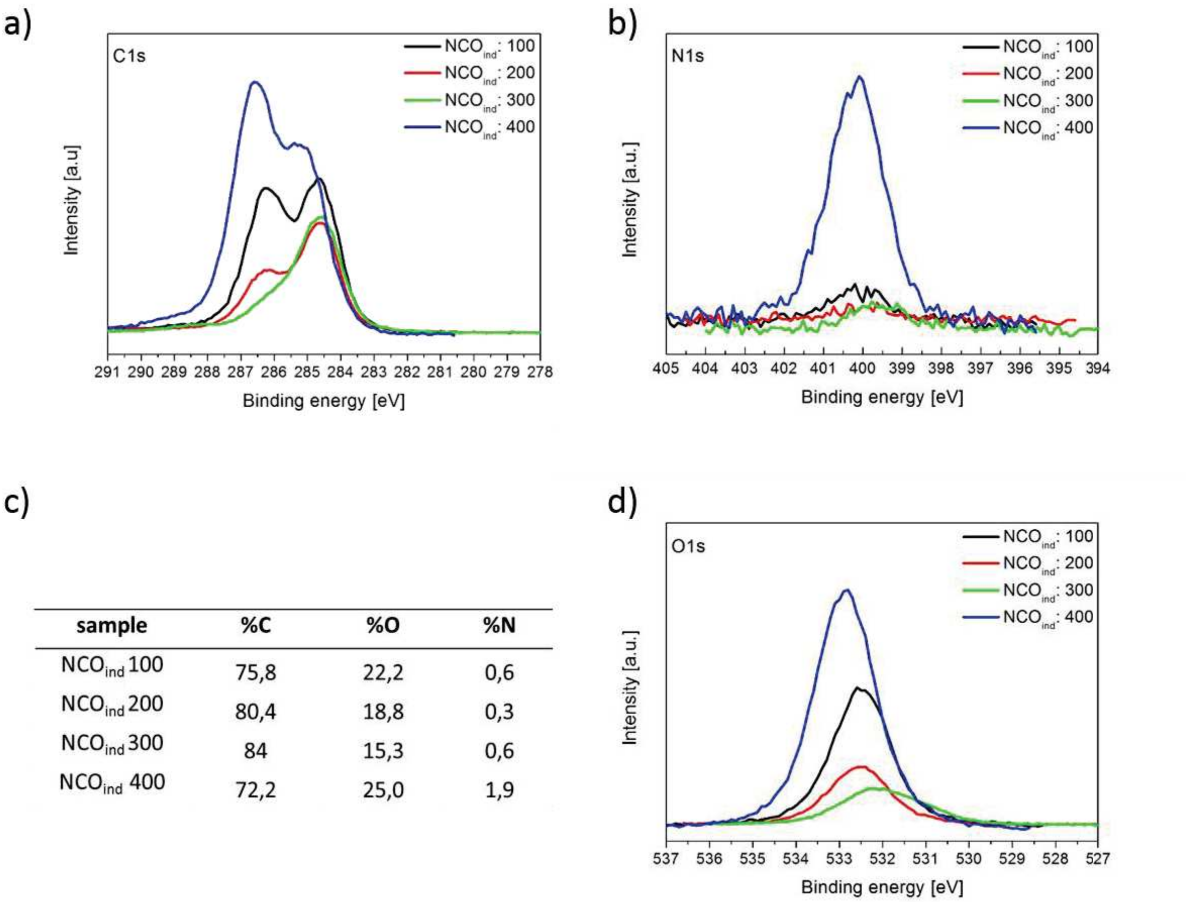

sample	%C	%O	%N
NCO_{ind} 100	75,8	22,2	0,6
NCO_{ind} 200	80,4	18,8	0,3
NCO_{ind} 300	84	15,3	0,6
NCO_{ind} 400	72,2	25,0	1,9

Figure 4-14: XPS spectra of PU film surfaces at energies corresponding to orbitals C_{1s} in a), N_{1s} in b), O_{1s} in d), and their elemental composition in c).

We also performed contact angle measurements of water drops deposited on the PU surfaces (Figure 4-15). Contact angles progressively increase from 48° to 96° for increasing NCO index up to an NCO index of 300, i.e. the samples are becoming increasingly hydrophobic. Beyond this value, the contact angle seems constant at 100 °. Since the only parameter that was varied is the ratio of isocyanate to hydroxyl function in the PU synthesis, differences in contact angle values can be correlated to changes in isocyanate content from one sample to another. Furthermore, aromatic rings, being hydrophobic compounds, contained in the polyMDI are assumed to contribute to the enhanced hydrophobicity. As the contribution to the contact angle value can be originated from both surface chemistry and roughness, we also investigated the surface roughness by AFM measurement. The surface roughness of each sample is summarized in Table 4-2.

Table 4-2 : Summary of the RMS roughness obtained by AFM for PU films with various isocyanate indexes.

NCO index	roughness (RMS)
75	12.9 nm
100	6.29 nm
200	2.89 nm
300	2.6 nm
400	1.6 nm

The root mean square values show a maximum at 12.9 nm for an NCO index of 75 and 1.6 nm for an NCO index of 400. Therefore, the contact angle value can depend either on differences in the surface chemistry and/or on surface roughness. This is contradictory with XPS analysis were surface chemistry was shown to be the same regardless of the NCO index. We assume that surface rearrangement at the PU/water interface differs from the PU/air interface.

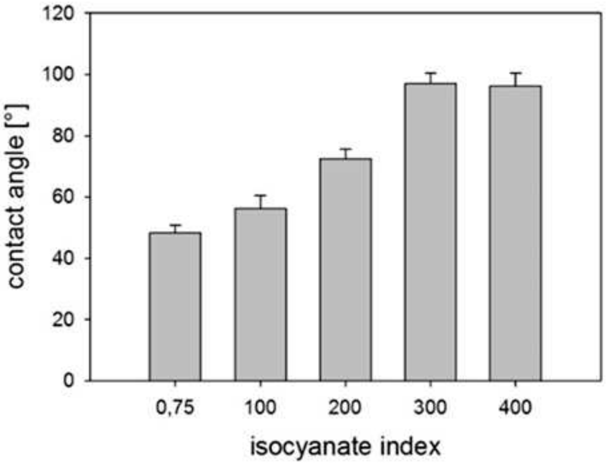

Figure 4-15 : Static contact angle measurement of ultrapure water for PU films with various isocyanate indexes.

We also investigated the structure of the PU films using both WAXS/SAXS methods. The details of the experimental protocols and the data treatments can be found in Section 2.23. Figure 4-16a shows the combined results from both techniques. The region corresponding to WAXS (i.e. for q > 0.3 Å^{-1}) displays a unique and similar halo for every sample indicating an amorphous system. Indeed, no Bragg peak appears in this q-range whatever the NCO index, indicating the absence of measurable crystalline structures. This can be explained by the steric hindrance of PPO chains and the oligomeric nature of polyMDI compared to its monomeric form MDI which is known to be able to cristallize[34].

From the SAXS measurements (i.e. for q < 0.3 Å^{-1}) shown in Figure 4-16a a clear evidence of micro phase separation can be observed as attested by the peaks around 0.08 Å^{-1}. The maximum value of the peaks is slightly shifted when the isocyanate is increased from 0.086 Å^{-1} to 0.079 Å$^{-1.}$ This can be interpreted as resulting from the presence of small domains separated by 7.7 nm (NCO $_{\mathrm{ind}}$: 75) and 7.9 nm (NCOind: 400) respectively which is quite similar. We interpret this as the signature of the hard domains embedded in the soft domains[35,36]. The peak intensity increases with increasing isocyanate index. No second- or third-order peaks are visible, ruling out the possibility that hard domains display translational order within the soft segments matrix. If the interface between the hard and soft domains was sharp, one would expect a decrease of the tail of the curve for small angles (i.e. q < 0.3 Å^{-1}) proportional to q^{-4} according to Porod law[37]. Using the Porod's invariant Q[37], one would expect that

$$Q = \frac{1}{2\pi^2}\int_0^\infty q^2 I(q)dq, \tag{42}$$

and

$$Q = \Delta\rho^2 \phi_s \phi_h = \Delta\rho^2 \phi_s (1 - \phi_s), \tag{43}$$

where q is the scattering vector, ϕ_s and ϕ_h are the volume fraction of the soft and hard domains, respectively, and $\Delta\rho^2 = (\rho_s - \rho_h)^2$ is the square of the difference of the scattering length density of the electrons between hard and soft domains. We do not observe this slope because the peak associated with the density fluctuations at 1.5 Å^{-1} starts very close to the peaks associated with the phase separation. Therefore, we suppose that the contribution of the second peak at large angles ($q \approx$ 0.076-08 Å^{-1}) may overlap the peak associated with the phase separation. However, by subtracting the contribution of the density fluctuations (see Section 2.23.1) , one can obtain curves in which the tail of the SAXS region is decreasing as q^{-4} since

$$\lim_{q\to\infty} I(q) = 2\pi\Delta\rho^2 \frac{S}{V}\frac{1}{q^4}, \tag{44}$$

where S/V is the total area of the interfaces divided by the total volume of the sample. By plotting $q^4 I(q)$ as a function of q (Figure 4-16b), one should therefore obtain a plateau for the q values > q_{peaks} when the two phases are separated by sharp interfaces. This plateau is observed for samples having an isocyanate index of 300 and 400, as seen in Figure 4-16b. This plateau starts at q ≈ 0.15 Å^{-1} and is quite short.

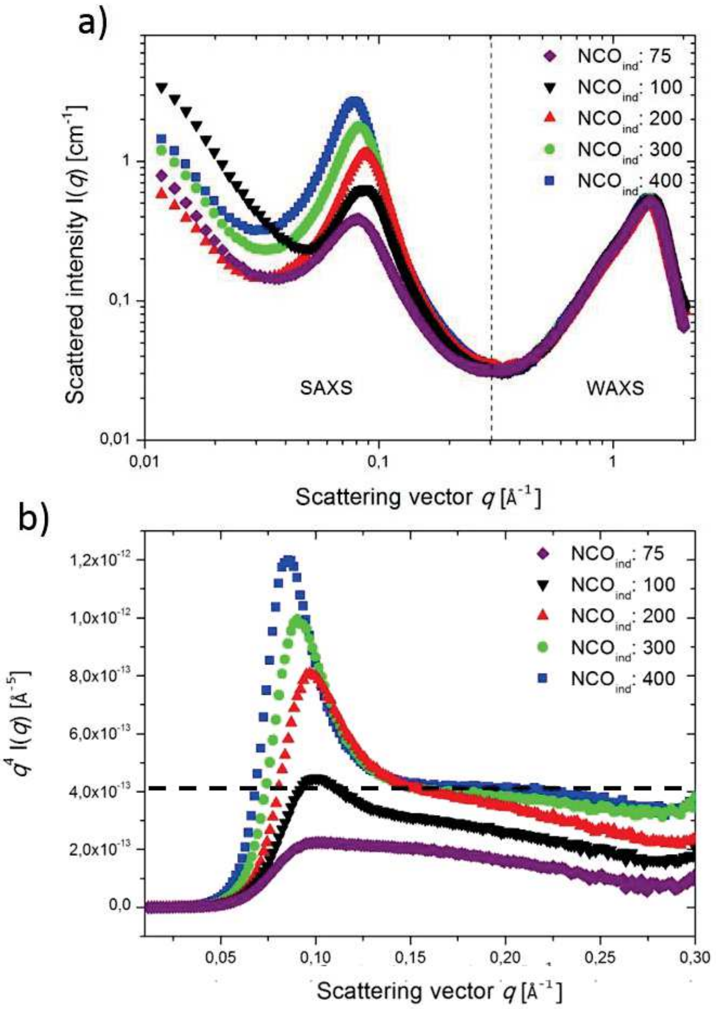

Figure 4-16 : a) Evolution of the scattered intensity (log scale) measured by SAXS/WAXS for PU samples with various isocyanate indexes). The dashed line indicates the SAXS/WAXS transition. b) Porod representation for the different samples. The dashed line indicates the plateau.

Even samples with NCO indexes of 300 and 400 show a decrease of their respective $q^4I(q)$ *versus* q curves at a given point around 0.22 Å. This means that some diffuse interfaces are also present within these systems but to a much lower extend. According to Buckley *et al.*[38] , interfaces are diffuse when hard and soft segments are interpenetrating and the separation between hard and soft domains is not sharp anymore. For diffuse interfaces, the evolution of the tail of the curves of $I(q)$ obeys the following law[39]

$$\lim_{q \to \infty} q^4 I(q) = 2\pi \Delta\rho^2 \frac{S}{V} \exp(-q^2\sigma^2), \qquad (45)$$

or,

$$\lim_{q \to \infty} ln[q^4 I(q)] = ln\left[2\pi \Delta\rho^2 \frac{S}{V}\right] - q^2\sigma^2, \qquad (46)$$

where σ is related the average width l of the diffuse interface between the hard and soft domains by $l = \sqrt{2\pi\sigma}$. Nevertheless, even samples with NCO indexes of 300 and 400 show a decrease of their respective $q^4 I(q)$ *versus* q curves at a given point around 0.22 Å. This means that some diffuse interfaces are also present within these systems but to a much lower extend. From Equ. (46), by plotting $ln[q^4 I(q)]$ as a function of q^2 (Figure 4-17), we obtain curves whose slope is related to the width of the diffuse interface. As seen in Figure 4-17, the width of the interface is increasing when the NCO index is decreasing. This is in accordance with our observations in Figure 4-16 since samples with NCO indexes of 300 and 400 display a plateau consistent with a sharp interface and thus a more complete phase separation. We find that the width of the interface of these two samples is l = 3.8 and 5.3 Å respectively. Samples with lower NCO indexes have a more diffuse interface whose thickness increases from 7.6 Å (NCO_{ind} : 300) to 9.9 Å (NCO_{ind} : 75).

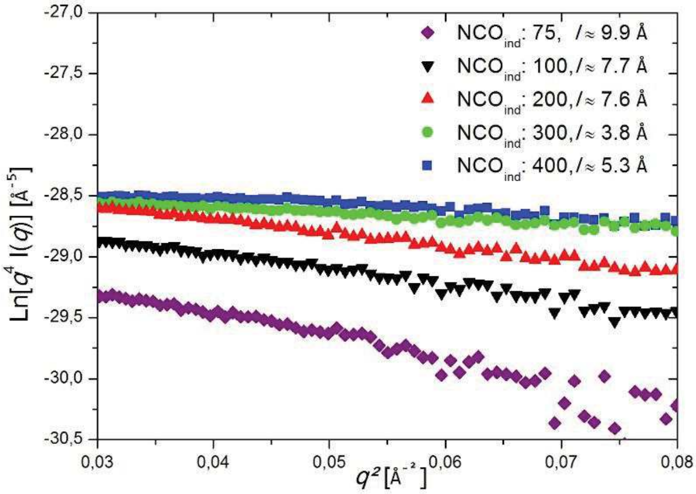

Figure 4-17 : Evolution of ln [$q^4 I(q)$] as a function of q^2 for samples with NCO indexes of 75 to 400. The slope of each curve provides the square width l^2 of the diffuse interface; the calculated width l is provided in the caption for each sample.

From the knowledge of the height of the plateau in Figure 4-16, one can determine the total surface area S of the interfaces divided by the volume of the sample V. Moreover, from the product of volume fractions of hard and soft segments $\phi_s\phi_h$ injected in the batch (see Section 0 in the Supplementary Informations) one can provide the Porod inhomogeneities length L_p (see Equ. 48 in the Supplementary Informations) which correspond to an average radius of the domains. We determined L_p to to be 27 and 23 Å for an NCO index of 400 and 300, respectively. The absence of a plateau for samples with NCO indexes below 300 prevents us to extract from the curves in Figure 4-16 an accurate value of S/V, hence, no value for the radius of the domains in samples with NCO indexes below 300 can be provided in this study.

A schematic representation of the PU microstructure with sharp and diffuse interfaces is shown in Figure 4-18a and b.

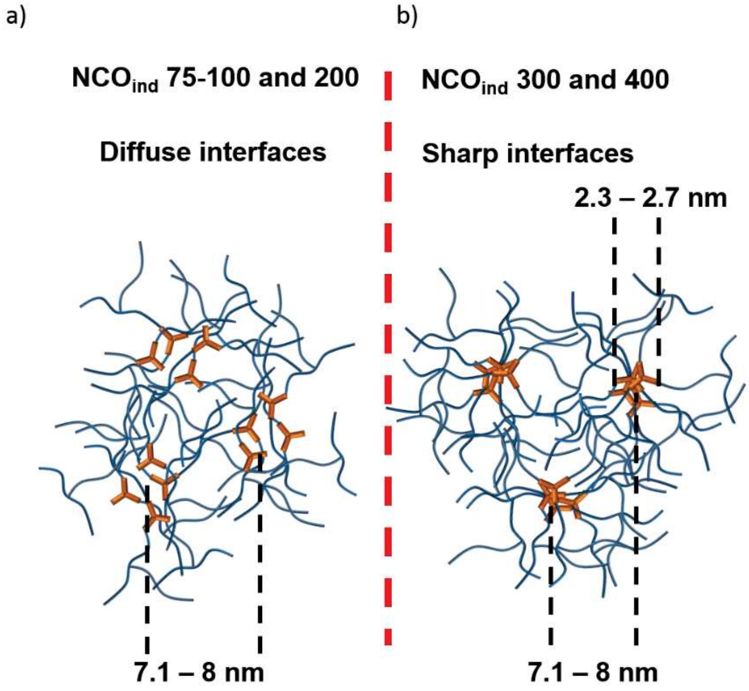

Figure 4-18 : Schematic representation of PU structure with phase separation when the interface between hard and soft segments is diffuse a) and sharp b).

Moreover, by integrating the curves $q^2I(q)$ versus q (see Figure S 8) one can obtain the Porod invariant Q expressed in Equ. (42), and compare this value to the experimental one (see Table 4-3 in Supplementary informations). We estimated $\Delta\rho^2$ from the book of Van Krevelen *et al.*[21] (Table 2-5) and $\phi_s\phi_h$ both by calculation from Equ. (47) and experimentally (see Table 4-3). The experimental value of $\phi_s\phi_h$ allows us to determine the Porod invariant which would be found in an ideal case (i.e. system with only sharp interfaces). We found that $\phi_s\phi_h$ (experimental)= 0.166 and 0.138 for samples NCO_{ind}: 400 and 300 respectively and $\phi_s\phi_h$ obtained by the treatment of our curves were 0.137 and 0.113 respectively for NCO_{ind}: 400 and 300 . We find that the Porod invariant obtained from Figure S 8 provides a lower value due to the fact that interfaces are not perfectly sharp for samples with NCO indexes of 300 and 400. Moreover, the applied corrections to estimate the integral value may not be perfect (see Section 0 in Supplementary Informations). Again, the lack of sharp interfaces in samples with NCO indexes below 300 prevent us to calculate the Porod invariant since the Q-calculation is only appropriate when the tail of the curve for small angles in Figure 4-16a shows a decrease proportional to q^{-4}.

An approximation of the degree of phase separation could therefore be deduced for samples with NCO indexes of 300 and 400. If we consider that the PU can switch from four main states which are (i) a homogenous system without phase separation, (ii) a system with diffuse interfaces (iii) a system with a mix of diffuse and sharp interfaces and (iv) system completely phase-separated. This degree of phase separation is the *Q-value* obtained from our samples expressed as percentage of the ideal *Q-value* (purely sharp interfaces). From Table 4-3, we obtained respectively 81 and 82 % for NCO indexes of 300 and 400. This demonstrates again that sharp interfaces coexist with diffuse interfaces, but the degree of phase separation is high enough to form domains that support cell adhesion.

4.2.4 Discussion

The adhesion of cells on a synthetic substrate is not straightforward since these materials lack the binding motifs that are found in the ECM. The use of surface modifications or coatings is widespread to improve the surface bioactivity regarding cell behavior inside the body or *in-vitro.* Such approaches tend to be time consuming and rarely cost efficient, which hampers their applications in the medical domain. However, some synthetic materials can promote cell adhesion and subsequently support cell proliferation. The understanding of the intrinsic properties of such materials is important for applications in regenerative medicine or tissue engineering. We proposed here to tailor the isocyanate index as a simple way to modulate the adhesion of both WJMSCs and 3T3 fibroblasts. In particular, we show that a clear threshold exists in the isocyanate index beyond which both cells types adhere easily on the surface. Naively, one may expect that for NCO indexes below 100, the excess of hydroxyl groups would render the material more hydrophilic and thus increase the cellular adhesion. Indeed, several studies report that hydrophilic surfaces are more likely to allow cell attachment[40], but the correlation between contact angle value and the cellular adhesion is still under debate[41]. Here we showed that the more hydrophobic surfaces (i.e. NCO indexes of 300 and 400) allow both cell types to adhere on our PU films. The cell adhesion appears at a threshold value of the NCO index between 200 and 300. As the interaction of cells with the substrate is directed by the outermost surface, we evaluated the changes in surface chemistry associated with changes in NCO index.

As shown in our XPS measurements (Figure 4-14) , chemical species are the same for all samples and the outmost layer is enriched in soft segments. This is consistent with the studies of Hearn *et al.*[42] who conclude that the difference in composition between the surface and the bulk material is due to surface rearrangements to minimize the surface energy. However, care must be taken in this assumption since XPS are conducted under ultra-high vacuum and these conditions cannot capture the “real” surface arrangement when samples are in aqueous conditions. Moreover, several other authors reported[43,44] that the PU surface is a dynamic environment and that undergoes rearrangements that depend on the hydration time.

Protein adsorption is also a key element that is of importance in the adhesion process. We showed that the amount of proteins adsorbed onto the material surface is nearly the same for all the samples except for the ones with lower NCO index (100 and 75). We expect that in these later cases some free ethylene glycol groups repel the adsorption of proteins[45]. Nevertheless, samples with NCO indexes of 200, 300 and 400 have similar quantities of proteins adsorbed onto the PU substrate. Hence the modulation of cell adhesion cannot be explained with the argument of protein adsorption.

Another argument that could explain the cell response described in this study could be the segmented structure of the polyurethane. Indeed, it is well-known that the polyurethane microstructure is well described as a biphasic system where hard segments form distinct micro domains scattered within a matrix of soft segments[46]. This phase separation can be controlled by several parameters such as the molecular weight of polyols[47], the type of chain extender[48] or the amount of isocyanate used in the formulation. Hsu *et al.* [43] demonstrated that phase separation in poly(carbonate urethane) is important to support endothelial cells adhesion and proliferation compared to PU where hard and soft segments are homogenously mixed and therefore do not form any domains. Therefore, when a PU surface displays clear nanodomains, cells may sense these heterogeneities and preferentially attached to these hard domains. Using WACS and SAXS, we demonstrated that our PUs exhibit microphase separation for all our experimental conditions. Nalluri *et al.* [15] showed that PU having hard segment domains separated with non-adherent PEG soft segment allowed for MSCs to spread and adhere on the surface on the contrary to PUs that do not exhibit any phase separation. The same trend was observed by Yuan *et al.*[14] for endothelial cells. Furthermore, Hao *et al.*[16] produced thermoplastic polyurethane and showed that 3T3 fibroblasts were able to adhere better on PU with high hard segments content than on those having smaller hard segment content. They also demonstrated that protein adsorption was higher when decreasing the amount of hard segments even though cells could not adhere on those surfaces.

Our present study comes to the same conclusion as the examples cited above. We demonstrate that the presence of hard-segment micro domains is a key feature to allow cell adhesion on the PU surface. We confirm that phase separation in PU can be controlled by the NCO index (i.e. the relative amount of isocyanate to hydroxyl functions). We used SAXS and WAXS methods to analyze the degree of phase separation within the polymer and we demonstrate that even if phase separation is confirmed for all the samples, the degree of phase separation between hard and soft segments is different. Our analysis shows that the existence of domains enriched with either hard or soft segments within the polymer is not enough to promote cellular adhesion, but that the “quality” of phase separation is the important feature. Indeed, by using Porod's law[39], we showed that samples with NCO indexes of 300 and 400 display sharp interfaces, indicatinga more complete phase separation. This is attested by the plateau in Figure 4-17b which indicates that $I(q) \propto q^{-4}$ at the tail of the SAXS curve which is consistent with sharp interfaces or system with more complete phase separation[38,49]. On the other hand, samples with NCO indexes of 75, 100 and 200 exhibit a more pronounced decrease of the tail of the peak at small angles by looking at the curves in Figure 4-17b which indicates that the interfaces between hard and soft segments are diffuse. Therefore, hard domains are not only composed of hard segments but also of soft segments that are interpenetrated. The dependence of the degree of phase separation on the NCO index was already shown by Saiani *et al.* [50].

Modulation of the NCO index is a versatile way to adjust the mechanical properties of PU samples. Moreover, the isocyanate index is also contributing to the extent of phase separation within the system.

When the degree of phase separation is high enough, interfaces are sharp and the separation between hard and soft domains is clear. These domains form islets that allow the cells to adhere on the surface. It was already demonstrated that for copolymers that undergo phase separation, the dispersed phase can be used as islet to allow cells to forms focal contacts while the continuous phase (non-adhesive) contributes to the overall mechanical properties of the polymer[51]. Besides, the domains in this study are disorganized in space. This is, in fact, an advantage for cell adhesion as Dalby *et al.*[52] demonstrated that randomly distributed nano pits are more likely to promote cell adhesion and MSCs osteogenesis compared to organized pit (i.e. in square and hexagonal).

The exact mechanism by which cells can attach on PU surface via nanodomains has still to be elucidated. The wettability properties of a given material affects drastically protein adsorption and conformation as demonstrated by Tzoneva *et al.*[53], therefore, we hypothesize that microdomains induce conformational changes on the adsorbed proteins which in turns mediate cell adhesion. For example, Groth *et al.*[54] showed that fibronectin or Human Serum Albumine (HSA) adsorption was also increased when more hard segments were introduced in the synthesis but the authors showed that platelet activation was decreased when the amount of hard segments increased indicating that despite more protein were adsorbed, their conformation was affected by the hard segment content. This indicates that hard segments and hard domains that ensue from the phase separation may contribute to modify the conformation of the adsorbed proteins and subsequently the cellular adhesion.

4.2.5 Conclusion

We generated polyurethane films with controlled NCO indexes. We showed that both 3T3 fibroblasts and WJMSCs were able to attach on the PU surfaces which have an NCO index higher than 200. We further characterized our substrates in terms of surface wettability, surface chemistry, tensile modulus and structure properties. We demonstrated that the NCO index influences the degree of phase separation within the polymer. For NCO index of 300 and 400, phase separation is more complete and interfaces are sharp whereas for NCO indexes below 300, the interfaces are diffuse. This implies that in this later case the hard domains are not only composed of hard segments but also contain a fraction of soft segments. This may explain why cells adhere only on PU with indexes higher than 300 since it is the hard domains that were already found to favor cell adhesion. We finally extrapolated these results from flat surfaces to a tridimensional scaffold. We showed that this cell adhesiveness is also maintained when cultured in 3D which is a promising way to combine a controlled microarchitecture of the scaffold with nano-cues to support cells adhesion for tissue engineering applications.

4.2.6 References

1. Hynes, R. O. Integrins: versatility, modulation, and signaling in cell adhesion. *Cell* **69,** 11–25 (1992).
2. Sonntag, M. H., Schill, J. & Brunsveld, L. Integrin-Targeting Fluorescent Proteins: Exploration of RGD Insertion Sites. *ChemBioChem* **18,** 441–443 (2017).
3. Hersel, U., Dahmen, C. & Kessler, H. RGD modified polymers: biomaterials for stimulated cell adhesion and beyond. *Biomaterials* **24,** 4385–4415 (2003).
4. Wilson, C. J., Clegg, R. E., Leavesley, D. I. & Pearcy, M. J. Mediation of Biomaterial–Cell Interactions by Adsorbed Proteins: A Review. *Tissue Eng.* **11,** 1–18 (2005).
5. Siow, K. S., Britcher, L., Kumar, S. & Griesser, H. J. Plasma methods for the generation of chemically reactive surfaces for biomolecule immobilization and cell colonization-a review. *Plasma Process. Polym.* **3,** 392–418 (2006).
6. Guelcher, S. A. Biodegradable Polyurethanes: Synthesis and Applications in Regenerative Medicine. *Tissue Eng. Part B Rev.* **14,** 3–17 (2008).
7. Vermette, P., Griesser, H. J., Laroche, G. & Guidoin, R. *Biomedical applications of polyurethanes*. **6,** (Landes Bioscience Georgetown, TX, 2001).
8. Jhon, Y.-K., Cheong, I.-W. & Kim, J.-H. Chain extension study of aqueous polyurethane dispersions. *Colloids Surfaces A Physicochem. Eng. Asp.* **179,** 71–78 (2001).
9. Lee, H. S. & Hsu, S. L. An analysis of phase separation kinetics of model polyurethanes. *Macromolecules* **22,** 1100–1105 (1989).
10. Abouzahr, S. & Wilkes, G. L. Structure property studies of polyester- and polyether-based MDI–BD segmented polyurethanes: Effect of one- vs. two-stage polymerization conditions. *J. Appl. Polym. Sci.* **29,** 2695–2711 (1984).
11. Tyler, B. J., Ratner, B. D., Castner, D. G. & Briggs, D. Variations between Biomer^{TM} lots. I. Significant differences in the surface chemistry of two lots of a commercial poly (ether urethane). *J. Biomed. Mater. Res.* **26,** 273–289 (1992).
12. Li, Y., Gao, T. & Chu, B. Synchrotron SAXS studies of the phase-separation kinetics in a segmented polyurethane. *Macromolecules* **25,** 1737–1742 (1992).
13. Ng, H. N., Allegrezza, A. E., Seymour, R. W. & Cooper, S. L. Effect of segment size and polydispersity on the properties of polyurethane block polymers. *Polymer (Guildf).* **14,** 255–261 (1973).
14. Yuan, Y. *et al.* Engineering of endothelial cell response on biphasic polyurethane matrix. *Technology* **4,** 139–151 (2016).
15. Nalluri, S. M. *et al.* Hydrophilic polyurethane matrix promotes chondrogenesis of mesenchymal stem cells. *Mater. Sci. Eng. C* **54,** 182–195 (2015).
16. Mi, H.-Y. *et al.* Properties and fibroblast cellular response of soft and hard thermoplastic polyurethane electrospun nanofibrous scaffolds. *J. Biomed. Mater. Res. Part B Appl. Biomater.* **103,** 960–970 (2015).

17. Hepburn, C. *Polyurethane elastomers*. (Springer Science & Business Media, 2012).

18. Modesti, M. & Lorenzetti, A. An experimental method for evaluating isocyanate conversion and trimer formation in polyisocyanate--polyurethane foams. *Eur. Polym. J.* **37,** 949–954 (2001).

19. Aubert, L. *et al.* Collagen-based medical device as a stem cell carrier for regenerative medicine. *Int. J. Mol. Sci.* **18,** (2017).

20. Lindner, P. & Zemb, T. Neutron, X-ray and light scattering: introduction to an investigative tool for colloidal and polymeric systems. (1991).

21. Van Krevelen, D. W. & Te Nijenhuis, K. *Properties of polymers: their correlation with chemical structure; their numerical estimation and prediction from additive group contributions*. (Elsevier, 2009).

22. Lutzweiler, G. *et al.* Modulation of Cellular Colonization of Porous Polyurethane scaffolds via the control of pore interconnection size and nanoscale surface modifications. *ACS Appl. Mater. Interfaces* (2019).

23. Zdrahala, R. J., Gerkin, R. M., Hager, S. L. & Critchfield, F. E. Polyether-based thermoplastic polyurethanes. I. Effect of the hard-segment content. *J. Appl. Polym. Sci.* **24,** 2041–2050 (1979).

24. Discher, D. E., Janmey, P. & Wang, Y. Tissue cells feel and respond to the stiffness of their substrate. *Science (80-.).* **310,** 1139–1143 (2005).

25. Clemitson, I. R. *Castable polyurethane elastomers*. (CRC Press, 2015).

26. Bernal, M. M., Lopez-Manchado, M. A. & Verdejo, R. In situ foaming evolution of flexible polyurethane foam nanocomposites. *Macromol. Chem. Phys.* **212,** 971–979 (2011).

27. Okuto, H. Studies on the structure of polyurethane elastomers. II. High resolution NMR spectroscopic determination of allophanate and biuret linkages in the cured polyurethane elastomer: Degradation by amine. *Die Makromol. Chemie* **98,** 148–163 (1966).

28. Yoon, S. C. & Ratner, B. D. Surface and bulk structure of segmented poly (ether urethanes) with perfluoro chain extenders. 2. FTIR, DSC, and X-ray photoelectron spectroscopic studies. *Macromolecules* **21,** 2392–2400 (1988).

29. Lin, H.-B. *et al.* Endothelial cell adhesion on polyurethanes containing covalently attached RGD-peptides. *Biomaterials* **13,** 905–914 (1992).

30. Deslandes, Y., Pleizier, G., Alexander, D. & Santerre, P. XPS and SIMS characterisation of segmented polyether polyurethanes containing two different soft segments. *Polymer (Guildf).* **39,** 2361–2366 (1998).

31. Kim, B. S., Jeong, H. Y. & Kim, B. K. Surface characterizations of polyurethanes having different types of soft segment. *Colloids Surfaces A Physicochem. Eng. Asp.* **268,** 60–67 (2005).

32. Nakamae, K., Nishino, T., Asaoka, S. & others. Microphase separation and surface properties of segmented polyurethane—Effect of hard segment content. *Int. J. Adhes. Adhes.* **16,** 233–239 (1996).

33. Chattopadhyay, D. K., Sreedhar, B. & Raju, K. V. S. N. Influence of varying hard segments on the properties of chemically crosslinked moisture-cured polyurethane-urea. *J. Polym. Sci. Part B Polym. Phys.* **44,** 102–118 (2006).

34. Ning, L., De-Ning, W. & Sheng-Kang, Y. Crystallinity and hydrogen bonding of hard segments in segmented poly(urethane urea) copolymers. *Polymer (Guildf).* **37,** 3577–3583 (1996).

35. Ryan, A. J. *et al.* Dynamics of (micro)phase separation during fast, bulk copolymerization: some synchrotron SAXS experiments. *Macromolecules* **24,** 2883–2889 (1991).

36. Velankar, S. & Cooper, S. L. Microphase separation and rheological properties of polyurethane melts. 1. Effect of block length. *Macromolecules* **31,** 9181–9192 (1998).

37. Koberstein, J. T. & Stein, R. S. Small-angle X-ray scattering studies of microdomain structure in segmented polyurethane elastomers. *J. Polym. Sci. Polym. Phys. Ed.* **21,** 1439–1472 (1983).

38. Buckley, L. J., Hammond, P. T. & Rubner, M. F. A morphological investigation of polyurethane/diacetylene segmented copolymers. *Macromolecules* **26,** 2380–2382 (1993).

39. Garrett, J. T., Lin, J. S. & Runt, J. Influence of preparation conditions on microdomain formation in poly (urethane urea) block copolymers. *Macromolecules* **35,** 161–168 (2002).

40. Kim, C. H., Khil, M. S., Kim, H. Y., Lee, H. U. & Jahng, K. Y. An improved hydrophilicity via electrospinning for enhanced cell attachment and proliferation. *J. Biomed. Mater. Res. Part B Appl. Biomater.* **78B,** 283–290 (2006).

41. Alexander, M. R. & Williams, P. Water contact angle is not a good predictor of biological responses to materials. *Biointerphases* **12,** 02C201 (2017).

42. Hearn, M. J., Ratner, B. D. & Briggs, D. SIMS and XPS studies of polyurethane surfaces. 1. Preliminary studies. *Macromolecules* **21,** 2950–2959 (1988).

43. Hsu, S. & Kao, Y.-C. Cell Attachment and Proliferation on Poly(carbonate urethanes) with Various Degrees of Nanophase Separation. *Macromol. Biosci.* **4,** 891–900 (2004).

44. Xu, L.-C., Runt, J. & Siedlecki, C. A. Dynamics of hydrated polyurethane biomaterials: Surface microphase restructuring, protein activity and platelet adhesion. *Acta Biomater.* **6,** 1938–1947 (2010).

45. Archambault, J. G. & Brash, J. L. Protein repellent polyurethane-urea surfaces by chemical grafting of hydroxyl-terminated poly (ethylene oxide): effects of protein size and charge. *Colloids Surfaces B Biointerfaces* **33,** 111–120 (2004).

46. Kwei, T. K. Phase separation in segmented polyurethanes. *J. Appl. Polym. Sci.* **27,** 2891–2899 (1982).

47. Wang, T.-L. & Hsieh, T.-H. Effect of polyol structure and molecular weight on the thermal stability of segmented poly(urethaneureas). *Polym. Degrad. Stab.* **55,** 95–102 (1997).

48. Gisselfält, K. & Helgee, B. Effect of soft segment length and chain extender structure on phase separation and morphology in poly (urethane urea) s. *Macromol. Mater. Eng.* **288,** 265–271 (2003).

49. Van Bogart, J. W. C., Gibson, P. E. & Cooper, S. L. Structure-property relationships in polycaprolactone-polyurethanes. *J. Polym. Sci. Polym. Phys. Ed.* **21,** 65–95 (1983).

50. Saiani, A. *et al.* Origin of multiple melting endotherms in a high hard block content polyurethane. 2. Structural investigation. *Macromolecules* **37,** 1411–1421 (2004).

51. Dalby, M. J., Riehle, M. O., Johnstone, H. J. H., Affrossman, S. & Curtis, A. S. G. Polymer-Demixed Nanotopography: Control of Fibroblast Spreading and Proliferation. *Tissue Eng.* **8,** 1099–1108 (2002).

52. Dalby, M. J. *et al.* The control of human mesenchymal cell differentiation using nanoscale symmetry and disorder. *Nat. Mater.* **6,** 997 (2007).

53. Tzoneva, R. *et al.* Fibrinogen adsorption and platelet interactions on polymer membranes. *J. Biomater. Sci. Polym. Ed.* **13,** 1033–1050 (2002).

54. Groth, T. H. *et al.* Protein adsorption, lymphocyte adhesion and platelet adhesion/activation on polyurethane ureas is related to hard segment content and composition. *J. Biomater. Sci. Polym. Ed.* **6,** 497–510 (1995).

4.2.7 Appendix

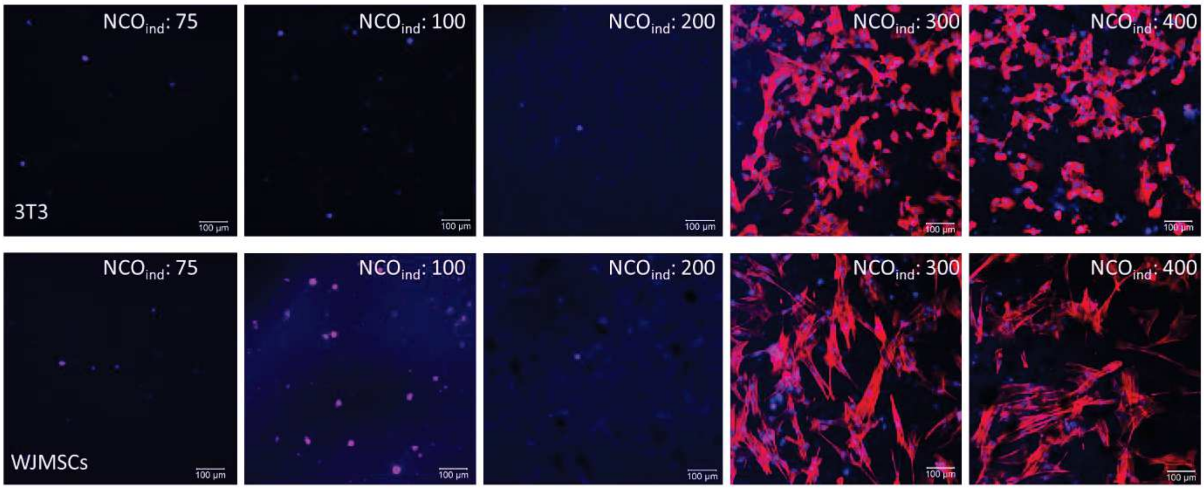

Figure S 5 : Images taken under a confocal microscope of NIH 3T3 fibroblasts (top row) and WJMSCs (bottom row) seeded on PU films having different NCO indexes (from 75 to 400). Images were taken after 24 hours of culture. Cells were stained respectively with DAPI (blue) and phalloidin (red).

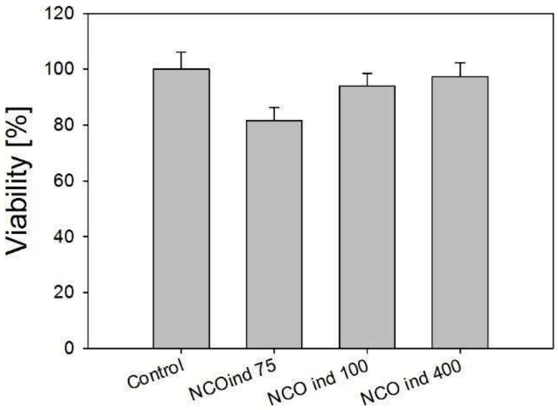

Figure S 6 : Evaluation of the cytotoxicity of PU films while changing the NCO indexes. Values were obtained by MTT method.

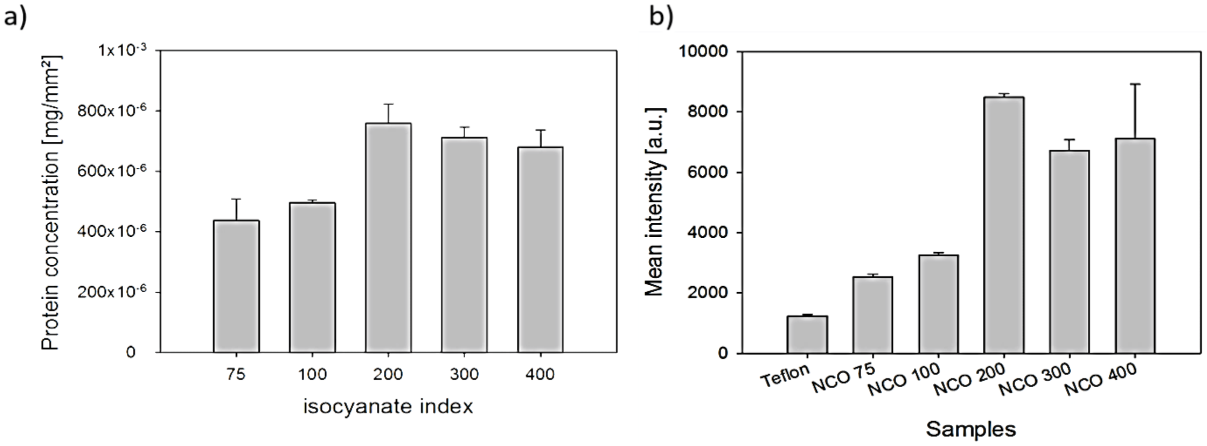

Figure S 7 : Measurement of protein adsorption for PU films when varying isocyanate indexes. Two methods were employed for comparison, a) Bradford method and b) by measuring the fluorescence intensity of adsorbed FITC-BSA under a confocal microscope. Teflon was used as a negative control.

4.2.7.1 Porod's invariant and degree of phase separation

The experimental evaluation of Q allows measuring the scattering length density inhomogeneity in the sample, i.e. the degree of microphase separation in a two-phase system. As the contrast factor, $\Delta\rho^2$, and volume fractions, ϕ_s and ϕ_h are available, the ratio of the experimental evaluation of Q, via Equ.42, and its theoretical value, obtained through Equ. 43, thus yields this degree of microphase separation. However, the integration in Equ. 42 must be properly carried out. Here, because we do not have the values of ϕ_s and ϕ_h, we will proceed differently. The experimental value of Q allows us to evaluate the product $\phi_s \phi_h$ using Eq. 43.

A Kratky representation of the corrected scattered intensities ($q^2 I(q)$ vs. q) for all studied copolymer films is proposed in Figure S 8. The Porod's invariant of each sample is then related to the area under the corresponding curve, $q^2 I(q)$. We note that Q is decreasing when we are going from the samples 400 to 75. In practice, these areas correspond however to integrations over a finite q-range ($q_{\mathrm{min}} < q < q_{max}$). So, extrapolations of data are necessary for extending the integration over all the reciprocal space ($0 < q < \infty$). Here, for neglecting the heterogeneities, or upturns at small q-values, the integrations of the experimental curves, $q^2 I(q)$, were first achieved over the range $0.02 < q < 0.3$ Å^{-1}. Then, they were completed by: at smaller q-values, the triangle areas defined by half the product $q_{\mathrm{min}} y_{\mathrm{min}}$, with q_{min}=0.02 Å^{-1} and $y_{\mathrm{min}} = q_{\mathrm{min}}^2 I_{\mathrm{coh}}(q_{\mathrm{min}})$; at higher q-values ($q > q_{\mathrm{max}}$=0.3 Å^{-1}), the areas under extrapolated curves based on scattered intensities scaling as q^{-6}. This latter correction corresponds to $A \int_{q_{max}\cdot}^{\infty} \frac{dq}{q^4} = \frac{A}{3q_{max}^3}$, A being defined by $\frac{A}{q_{max}^6} = I(q_{max})$, for each sample.

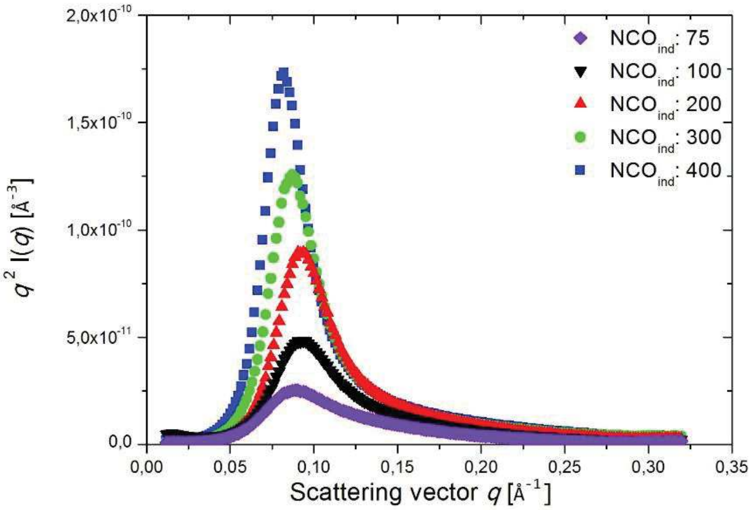

Figure S 8 : Kratky representation of all corrected SAXS scattered intensities. Porod's invariants are evaluated through integrations over all the reciprocal space of such curves

The obtained Q-values (cm^{-4}) are listed in Table 4-3. From them and with the contrast factor $\Delta\rho^2 = (\rho_s - \rho_h)^2 = 3.2761\ 10^{20}$ cm^{-4} that assumes an amorphous state for both phases, we evaluate the products of volume fractions $\phi_s\phi_h = \phi_s(1-\phi_s)$ and therefore volume fractions themselves, using Equ. 43. Of course, these values are only approximate since they are based on the existence of sharp interfaces. But, we have shown in Figure 4-17, that it is not the case. Interfaces are diffuse at the resolution of our SAXS experiments (20 Å).

Diffuse boundaries actually affect the Porod's invariant, Q. Indeed, its value would rather be smaller than the one given by Equ. 43 since the deviation in the scattering length density fluctuations is smaller inside the diffuse interface zones than when interfaces are sharp. In a first approximation, we can replace Equ. 43 by:

$$Q = \Delta\rho^2\Phi_1\Phi_2(1-\frac{l}{l_P}) = \Delta\rho^2\Phi_1(1-\Phi_1)(1-\frac{l}{l_P}), \qquad (47)$$

where l is the effective thickness of the diffuse interface defined by Equ. 48; l_P, the Porod's length inhomogeneity defined by:

$$l_p = \frac{4\Phi_h\Phi_s}{S/V}. \qquad (48)$$

The reduction in Q associated with the diffuse character of interfaces is equal to the ratio of the interface thickness, l, to the average microdomain size, l_P.

The corrections for the volume fractions associated with the corrected Eq. 47 could only be achieved for the Samples 400 and 300 for which a specific interface area, S/V, could be measured. They are also listed in Table 4-3 (Corr values). The respective density of the polyol and the isocyanate were measured experimentally by weighting a known volume of each compound at 25°C. We obtained density values of 1.23 g/ml and 1.17 g/ml for the isocyanate and the polyol respectively. The experimental values of of $\phi_s \phi_h$ are shown in Table 4-3 ($\phi_s \phi_h$ Exp) and the corresponding Porod invariant that would be obtained in an ideal case Q_{ideal} .

Table 4-3 : Structural characteristics of all the copolymer films from analyses of SAXS data.

Film	d (Å)	S/V ($Å^{-1}$)	Q (10^{16} cm^{-4})	$\phi_s\phi_h$	ϕ_s	l_P (Å)	$\phi_s\phi_h$ Corr	ϕ_s Corr	$\phi_s\phi_h$ Exp	Q_{ideal} (10^{16} cm^{-4})
400	79.5	0.0202	4500+/-250	0.137	0.63	27.2	0.170	0.78	0.166	5441
300	74.8	0.0194	3700+/-250	0.113	0.66	23.2	0.135	0.84	0.138	4546
200	71.4		2900+/-150	0.089	0.70				0.103	
100	73.1		1950+/-150	0.060	0.76				0.065	
75	77.6		1150+/-75	0.035	0.81				0.047	

Chapter 5. Combination of a self-assembled peptide hydrogel with porous PU scaffolds to promote proliferation and differentiation of WJMSCs

5.1 Résumé

Dans le Chapitre 3 nous avons étudié l'influence de paramètres morphologiques d'un matériau poreux (taille des pores et dimension des interconnexions) sur la colonisation cellulaire. Nous avons également testé l'influence de deux traitements de surfaces. Cependant la prolifération des cellules dans notre matériau restait limitée.

Afin d'améliorer la colonisation cellulaire et d'influencer la différenciation, nous avons également fonctionnalisé le matériau poreux avec un gel de peptides qui s'auto-assemblent au contact d'ions divalents présents dans les milieux de culture. La différenciation cellulaire n'a pas encore été abordée au cours de cette thèse. C'est un objectif courant en ingénierie tissulaire car les sources de cellules souches en provenance des patients sont limitées ou interdites par l'éthique. La capacité à régénérer un tissu à partir de cellules souches reste un défi important. L'approche classique consiste à utiliser des agents biochimiques comme les facteurs de croissance. Bien que leur capacité à promouvoir la différentiation est avérée, il faut noter que les facteurs de croissance sont régulés finement dans l'espace et le temps dans le corps, chose qu'il est difficile de reproduire *in-vitro*. De plus, les applications ciblées par les implants poreux concernent entre autres le remplacement de parties du corps retirées à cause de tumeurs. Hors, il est difficilement concevable d'introduire des facteurs de croissance chez des patients atteints de cancers, l'apport de telles molécules pouvant relancer la maladie.

Dans le chapitre suivant, nous avons choisi de conserver la structure du matériau poreux en PU considéré comme optimale Section 4.1, à savoir un diamètre moyen des pores de 133 µm et d'interconnexions de 52 µm, préparée par la méthode de "sphere templating". L'indice d'isocyanate du PU étant également un paramètre important au regard de l'adhésion cellulaire (Section 4.2), nous avons formulé le polyuréthane pour obtenir un indice d'isocyanate de 400.

Nous avons utilisé un gel commercial de peptides auto-assemblés dans lequel nous ensemençons les cellules. L'idée est de fournir un environnement proche de la matrice extracellulaire qui permette de promouvoir (i) la prolifération des cellules dans les poreux car nous avons montré dans la Section 4.1.3.2 que la prolifération était limitée dans le poreux seul. (ii) Nous avons ensuite évalué si ce gel pouvait induire la différentiation des cellules en l'absence de facteurs de croissance.

Dans ce chapitre, nous comparons trois conditions expérimentales : sans gel où les cellules de la gelée de Wharton (WJMSCs) sont ensemencées dans le poreux (nommée « SCAFFOLD »), un cas où les WJMSCs sont intégrées d'abord au gel, puis injectées dans le matériau (« SCAFFOLD+GEL ») puis un dernier cas ou les cellules sont ensemencées dans le gel seul (« GEL »).

Le gel formé de tri-peptides avec, à l'une de leurs extrémités, un groupement Fmoc (fluorénylméthoxycarbonyle), permet d'introduire plus de cellules au sein du matériau en comparaison au cas où les cellules sont ensemencées dans le poreux en l'absence de gel. En effet nous avons constaté

(Section 2.7.1) que les cellules n'adhèrent que très peu au polyuréthane puisque celui-ci ne possède pas de site d'adhésion spécifiques. Les cellules sédimentent donc au fond du puits de culture alors que lorsqu'elles sont intégrées dans le gel, elles restent davantage piégées dans le matériau.

Le gel est composé d'un réseau fibreux qui offre une architecture ressemblant au réseau protéique de la matrice extracellulaire. Cet environnement semble propice pour permettre aux cellules de proliférer. Néanmoins, le gel se dégrade rapidement et la dissolution est visible dès le septième jour de culture. Nous avons montré que cette perte d'intégrité entraine la migration des cellules vers les parois des pores. Les cellules intégrées dans le gel seul meurent. Néanmoins, lorsque les cellules sont intégrées au gel puis injectées dans le matériau (SCAFFOLD+GEL), elles prolifèrent davantage que lorsqu'elles sont ensemencées dans le matériau seul (SCAFFOLD).

Nous avons également évalué les sécrétions de collagène de type II ainsi que des glycosaminoglycanes sulfatés (sGAGs) qui sont des indicateurs connus de la différentiation des cellules souches mésenchymateuses en chondrocytes (i.e. les cellules de tissus cartilagineux). Les cellules ensemencées dans le gel seul (GEL) sécrètent nettement plus de sGAGs que les cellules dans le poreux. Le collagène de type II semble en revanche être peu sécrété ou retenu dans le matériau et aucune différence n'est visible entre les différentes conditions.

Nous faisons l'hypothèse que la surproduction de sGAGs dans le cas où les cellules sont ensemencées dans le gel seul est due à un mécanisme de compensation en réponse à la dégradation du gel. Il a été démontré que les cellules sécrètent une matrice péri cellulaire (i.e. dans l'environnement local de la cellule) à laquelle les cellules adhèrent. Les protéines sécrétées interagissent à leur tour avec l'environnement local (adsorption, changement de conformations etc.…). Les cellules adhèrent aux protéines et sentent la réponse mécanique de la protéine adsorbée sur le matériau. Ainsi, la réponse mécanique doit être une combinaison des propriétés mécanique du matériau et des protéines adsorbées.

Enfin, le gel ne permet pas pour le moment d'induire une différenciation des WJMSCs en cellules cartilagineuses. L'optimisation des propriétés de dégradation est nécessaire pour permettre des études sur le long-terme. Ces résultats restent préliminaires mais constituent une base pour de futurs développements.

5.2 Introduction

Tissue-engineered scaffolds are widespread nowadays due to their ability to create a three-dimensional environment for cells. Current techniques offer a broad variety of possibilities to generate scaffolds with relevant features such as optimum porosity, interconnection and pore sizes[1,2]. Several studies have been conducted both *in-vitro* and *in-vivo.* They revealed that despite the fact that cell colonization throughout the entire porous structure can be achieved, the tissue ingrowth remains mostly immature, and nonfunctional. This scar tissue formation results from an uncontrolled immune response but also because scaffolds failed to mimic efficiently the complex architecture of the extracellular matrix (ECM)[3,4]. This is because cells are often coating the pore walls rather than organising in a three-dimensional manner. They dedifferentiate as if they were cultured on flat surfaces, and the ECM molecules synthesised by the cells are not easily restrained within the scaffold[5,6]. One option to overcome this issue would be to provide an environment which is more suitable for the cells. An excellent example are hydrogels, since they provide fibrous structures which are closer to the extracellular matrix protein assembly. Hydrogels can be obtained from purely synthetic molecules such as poly(ethyleneglycol) PEG[7] or poly(2-hydroxy ethyl methacrylate)[8], but they can also be derived from natural sources, examples being alginate, chitosan or silk fibrin[9–11]. Other examples are ECM-derived hydrogels from which fibers are originated from extracellular matrix such as collagen[12], hyaluronic acid[13] or Matrigel®[14]. These are of great interest because they are not only biocompatible, but also bioactive since they can support cell adhesion, proliferation, migration and differentiation[15]. Despite their numerous advantages, the use o naturally-derived hydrogels is often limited by the batch-to-batch variability which complicates their transfer into clinic applications[16,17]. Hydrogels composed of self-assembled peptides (SAPs) have gained particular interest during the last decade. These gels are usually formed by small sequences (mainly di or tripeptides), because they can be synthesised easily and in a highly reproducible manner. Moreover, peptides can be end-capped with aromatic groups such as 9-fluorenylmethyloxycarbonyl (Fmoc), or carbazole[18] which promote self-assembling by π-π stacking or via hydrophobic interactions. Self-assembly can also be initiated enzymatically[19]. Frederix *et al.*[20] screened 8000 combinations of tripeptides based on the 20 amino acids and found some tripeptides combinations that can self-organise without the need of protecting them with Fmoc or other functional groups that promote self-assembly. SAPs can be tuned in terms of Young Modulus[21] or viscoelasticity[22] to provide physical cues that approach those of the ECM. Such control of the mechanical properties can be a powerful tool to control the fate of stem cells via mechanostransduction[23–25]. Moreover, SAP hydrogels can include binding motifs that allow cells to be anchored[26]. Other peptide sequences are useful since they own sites that can be degraded by enzymes such as matrix metalloproteinase (MMP) and subsequently enhance cell migration[27]. Biogelx Limited is a company which supplies SAP hydrogels based on small di-tri peptides end-capped with Fmoc-phenylalanine which can self-assemble into nanofibers when culture media is added. Divalent cations such as calcium crosslink the structure in physiological conditions[28]. These products are interesting candidates for regenerative medicine and tissue engineering since they can be tuned in terms of mechanical properties. Moreover they can be functionalised with specific peptide sequences, for example RGD (arg-gly-asp), to provide adhesion sites for the cells[29]. However, hydrogels alone suffer from their poor mechanical strength when injected in load-bearing areas and avoiding their degradation can also be a challenging task *in-vivo*[30,31].Thus, the combination of SAP hydrogel with a porous scaffold is a promising option, in which cells are embedded in a suitable tridimensional network of fibers while the overall structure is mechanically stabilized by the scaffold.

In this study, we used the sphere templating technique developed in Chapter 3 to obtain porous polyurethane (PU) scaffolds. The obtained scaffolds are combined with a hydrogel (Biogelx-S) composed of SAPs. Wharton's Jelly-derived mesenchymal stem cells (WJMSCs) are embedded in the hydrogel and subsequently injected inside the pores of the scaffold. We investigated both the proliferative activity of the cells and the ability of the gel to provide physical properties that could induce the differentiation of WJMSCs toward chondrocytes in the absence of induction media.

5.3 *Results*

We first examined if the gel was able to penetrate and to form within the porous structures. As the pre-gel solution is a viscous liquid, it could enter into the pores simply under the action of capillarity. The gelation could then occur when the culture media was added (see Section 2.7.1). The gel was able to form into the scaffold and was homogeneously distributed throughout the whole sample, as is shown in Figure 5-1. Fibers can be seen inside the pores, this is a result of the self-assembly of the peptides with the addition of divalent cation from the media.

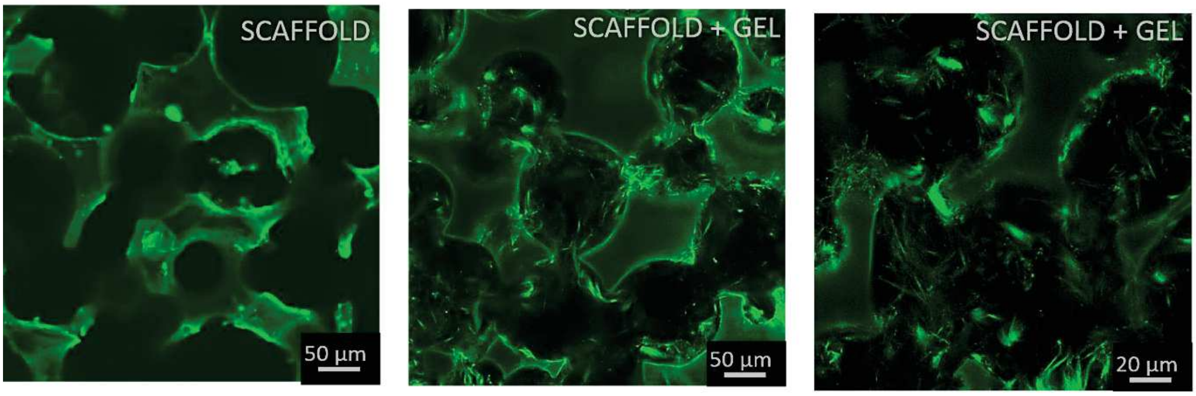

Figure 5-1 : Images taken with a confocal microscope of PU scaffolds stained with FITC-conjugated BSA to stain the hydrogel. Left image corresponds to the raw scaffold. The image in middle shows the scaffold with the gel. The same sample is shown with a higher magnification in the image in the right. Images were taken in the centre of the samples.

To evaluate whether the hydrogel alone (named "GEL"), the scaffold alone (named "SCAFFOLD") or the combination of the hydrogel with the scaffold (named "SCAFFOLD+GEL") has some benefits on cell viability, we cultured WJMSCs in these three conditions for 21 days *in-vitro*. The viability/proliferation of WJMSCs relative to each condition is shown in Figure 5-2. Intensities are normalised by the value at day 1 to detect if cells were able to proliferate. One can first observe that after 7 days cells proliferate best when embedded in the SCAFFOLD+GEL. While the WJMSCs cultured in the GEL alone appear to offer the most suitable environment to the cells at day 7, they suffer from a drastic decrease in viability from day 7 to day 21. It is not surprising that the SCAFFOLD alone does not promote cellular proliferation, since the PU is poorly adhesive to cells as we demonstrated in Chapter 3. Therefore, in the pure SCAFFOLD cells need to first secrete ECM components to which they can attach and cells start to proliferate after, between day 1 and day 21. However, cells that were embedded in the SAP hydrogel, had the same "local" environment than the ones embedded in the SCAFFOLD+GEL but the evolution of viability/proliferation is always different for the whole experiment.

We may note that the reduction of resazurin into resorufin is correlated to mitochondria activity which implies that a higher intensity does not always mean that the cell number is actually increasing. This was already reported by Surmaitis *et al.*[33] who showed that when 3T3 fibroblasts were cultured on poorly adhesive surface, the metabolic rate was increased compared to cells cultured on classical culture plastic which promote cell adhesion. They demonstrate that the metabolic activity of fibroblasts was enhanced for the first 6 days of culture before reaching the value of fibroblasts cultured on adherent plates. The increased mitochondrial activity is associated to the upregulation of ECM component synthesis that will provide some adhesive motifs to the cells. If we follow this statement, that would mean that the gel on itself does not support properly the adhesion of WJMSCs.

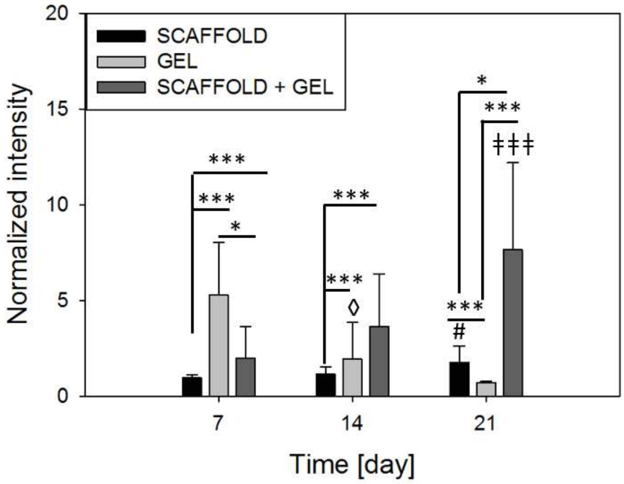

*Figure 5-2 : Evaluation of cell viability as a function of time for WMSCs cultured in the PU SCAFFOLD alone, in the GEL alone, or in the SCAFFOLD+GEL by measuring the fluorescence intensity with the spectrofluorimeter. Intensity values are normalised by the intensity measured on day 1 of culture to assess the proliferation. The statistical analysis was obtained by two ways ANOVA with Holm-Sidak method for pairwise comparisons. Symbol: ◊ correspond to a p-value $< 0,05$ for comparison between WJMSCs in the gel at day 14 and 7, # stands for the comparison of WJMSCS in the scaffold between day 14 and day 21, $p < 0,05$. The symbols: ⧻ correspond to p-value $< 0,001$ and to the comparison between WJMSCs seeded in the scaffold + gel between day 14 and day 21. Comparison between the different samples are given by *, ** and *** corresponding to p-value $p < 0,05$, $p < 0,01$ and $p < 0, 001$ respectively, n=3.*

To gain more insight into the behaviour of cells in the different conditions, we performed confocal microscopy. The corresponding images after 21 days are shown in Figure 5-3. When cells were seeded in the PU SCAFFOLD alone (Figure 5-3a), one can see that cells are scattered across the samples. Cells are able to bridge the pore to create cell-cell contacts. The low density of cells is in agreement with the recorded intensity in Figure 5-2. Since the proliferation is delayed by the need to secrete a primary ECM, one can expect a better colonisation for longer period of culture. Cell density is on the other hand much higher on samples SCAFFOLD+GEL (Figure 5-3b) . WJMSCs are more concentrated at the periphery of the gel (shown with the white arrow) and some cells are also directly attached to the PU. We noticed that the gel started to degrade after 7 days, this weakening of the overall network may promote cell migration toward the PU surface. As can be seen in Figure 5-3b, the gel is located only at some areas (pointed by the dashed arrow) while some space are empty. If one compares with Figure 5-1 where the gel was more homogeneously distributed within the scaffold, this attests for that the gel is degrading over time. Interestingly, some cells are adhering on the PU substrate devoided of gel which reinforces the hyphothesis that WJMSCs may migrate toward the wall of the pores. In the case where cells were embedded only in the GEL, cells show a more rounded morphology and a low density for images taken at day 21 (Figure 5-3c). This results corroborate the drop in intensity at day 21 in Figure 5-2.

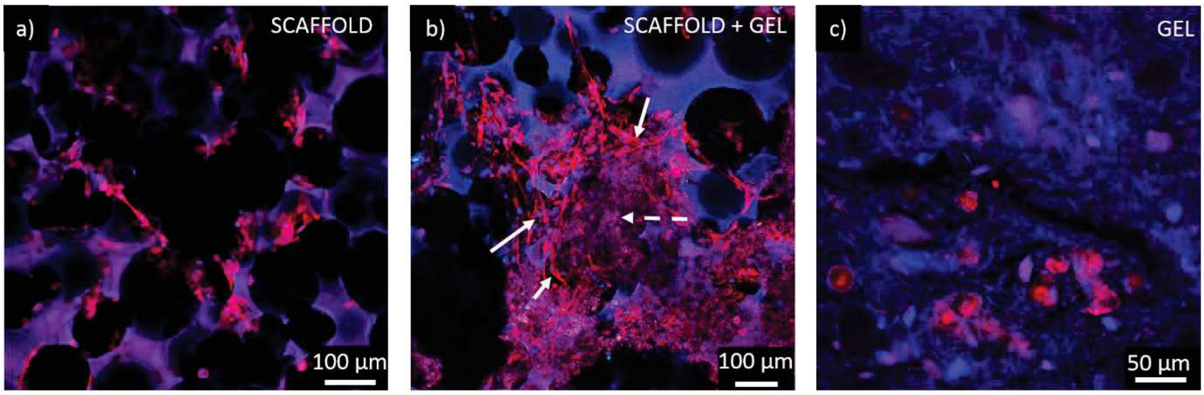

Figure 5-3 : Confocal images of WJMSCs after 21 days of culture in a) PU SCAFFOLD alone, b) SCAFFOLD+GEL and c) the GEL alone. Cells were stained to visualise both F-actin filaments with Fluorescent phalloidin (red) and the nucleus with DAPI (blue). The white dashed arrow points to the gel within the scaffold and the full arrows show the cells.

From the results presented above, we can conclude that the gel alone is not a suitable solution for long-term culture of WJMSCs. Since the degradation of the gel arises within seven days, cells that were embedded in the gel and subsequently seeded in the scaffold could migrate on the PU surface when the gel started to degrade. Nevertheless, when the gel was still intact, the fluorescent intensity showed the highest value (day 7 on Figure 5-2) which indicates that the seeding efficiency is improved. Besides, when the hydrogel degrades, the Young modulus generally decreases as well. We choose to prepare a gel having a Young Modulus E ~ 8 - 9,2 kPa and the Young Modulus of our PU was around 8 MPa as shown in (Section 4.2), hence we cannot exclude that the migration of the cells from the gel toward the PU surface seen in Figure 5-3b is not related to differences in moduli.

Additionally, as WJMSCs are known for their ability to differentiate in several lineages, we investigated whether one or more of our conditions could initiate the differentiation of cells toward chondrocytes. As differentiation markers, we evaluated both the secretions of sulphated glycosaminoglycans (sGAGs) using the kit Blyscan (see Section 2.13.2) and type II collagen (Section 2.11.5).

The evolution of sGAG over 21 days is shown in Figure 5-4. Glycosaminoglycans are much more important within the GEL compared to the other conditions at any moment. In each case, sGAG secretions increased only slightly from day 14 to day 21, even if the values for WJMSCs cultured in both the SCAFFOLD alone and in the SCAFFOLD+GEL remained low. It is known that the differentiation of MSCs can be induced by physical cues[34] such as the stiffness of the substrate or by the organisation of the surrounding ECM. Although the amount of cells cultured within the GEL only is decreasing, one could expect that the gel could direct the fate of stem cells. As the degradation of the gel progresses, the cells may secrete some extracellular proteins to form a capsule that surrounds them to compensate[35]. One hypothesis would be that this upregulation of ECM could be due to the counterbalance of the loss of the integrity of the gel.

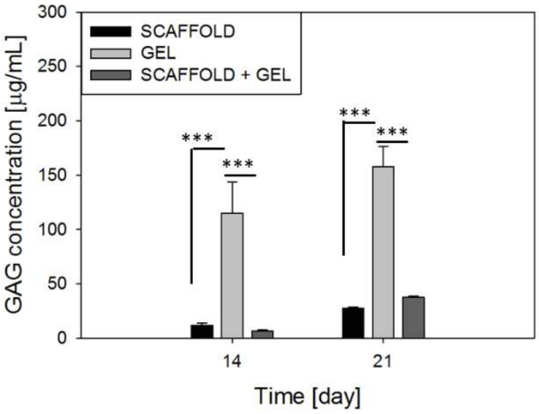

*Figure 5-4: Evolution of the concentration of sulphated-glycosaminoglycans sGAGs with time. Two-ways ANOVA with Holm-Sidak method was used for statistical analysis, *, ** and *** correspond to p-values p< 0,05, p < 0,01 and p < 0,001 respectively.*

Type II collagen was stained and visualised under the confocal microscope after 21 days. The results are shown Figure 5-5 for all three sample types. For all the conditions, we observe that only little type II collagen is present across the samples. Some residues are pointed by the white arrows on Figure 5-5a and b. We can see that for the condition where WJMSCs were seeded into the PU SCAFFOLD only, the collagen appears to be close to the cells (inset Figure 5-5a) and tends to form some aggregates. Some aggregates are also seen for the case of SCAFFOLD+GEL, but those collagen residues are more likely located in the hydrogel but not necessarily close to the cells. The inset Figure 5-5b supports that finding, indeed, no collagen fibers or aggregates are observed near the cells. For WJMSCs seeded into the gel alone, type II collagen was seen near the cells but no significant difference can be seen from our observations between the three conditions.

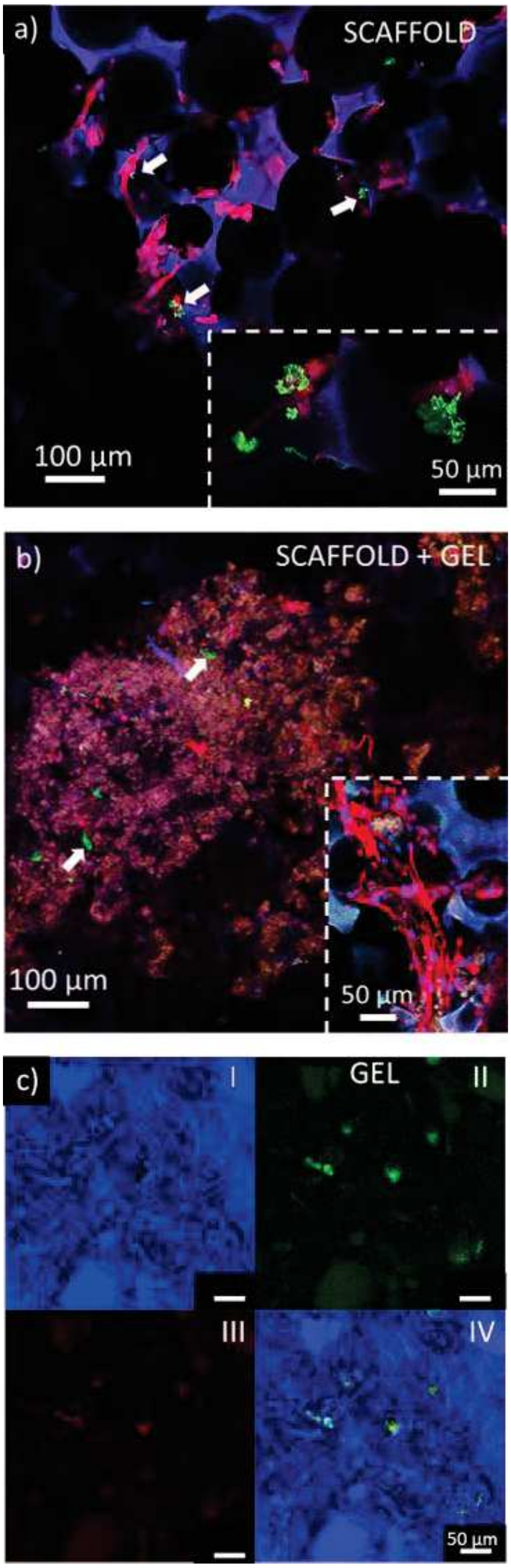

Figure 5-5 : Confocal images of WJMSCs seeded in a) PU SCAFFOLD, b) PU SCAFFOLD+GEL and c) the GEL only. Images were taken after 21 days of culture. F-actin filaments were stained with fluorescent phalloidin (red), nuclei were stained with DAPI (blue) and type II collagen was stained with Oregon Green® 488. On c), image I was taken with the blue channel only, the green one for image II, the red one for image III and the superposition is shown on image IV. Collagen is pointed with an arrow.

5.4 Discussion

We proposed here to use a SAP hydrogel as a cell carrier and as an ECM-like environment to see whether proliferation and differentiation of WJMSCs could be promoted without the need of bioactive molecules such as growth factors and hormones. Regarding proliferation, the combination of the gel with the scaffold accelerates the rate of proliferation compared to the raw PU scaffold, hence, the cellular density was higher with the hydrogel. These results are consistent with the work of Im *et al.*[36] who injected a SAP hydrogel seeded with fibroblasts within a poly(L-lactide-co-ε-caprolactone) (PLCL) and noticed an increase in proliferative activity for the samples where SAP hydrogel was combined with the scaffold compared to the scaffold alone. However, the authors did not investigate the effect of the hydrogel alone on the cells. The same tendency was observed by Bokhari *et al.*[37] where osteoblasts showed an increase in proliferation within a scaffold coated with a commercial SAP (PuraMatrix™) hydrogel instead of being cultured in the scaffold only. We must nonetheless emphasise that the enhanced proliferation promoted by the hydrogel is not restricted to the case of SAPs, indeed, others studies conducted with synthetic or natural hydrogels showed similar behaviour regarding the proliferation of cells[5,38,39].

We aim now to discuss a few examples where cells were cultured only in a hydrogel without scaffold to determine whether a hydrogel alone can represent a realistic cell carrier on its own. Kisiday *et al.*[40] embedded chondrocytes in a SAP hydrogel (without scaffold) and observed that cells were able to proliferate within the gel and their ECM component synthesis was enhanced, which, in turn, increased the compressive modulus of the gel. This stiffening of the hydrogel is attributed to the densification of the network by ECM molecules secreted by the cells combined with the traction exerted by the cells on the fibers. Even if the gel was not the same as ours, these results are opposed to our findings since our hydrogel lose his integrity (we expected a decrease of the Young Modulus as well) after 7 days. Therefore, an optimisation of the initial peptide concentration is needed for further studies. Besides, Zhou *et al.* [26] showed that fibroblasts embedded in a SAP hydrogel composed of Fmoc-diphenylalanine (Fmoc-FF) have a decreased viability over time in the absence of RGD motifs even if the environment is close to the one of the ECM. Conversely, cells proliferate well when RGD sequences were added into the SAPs. Therefore, the lack of RGD sequences may impact negatively the viability of WJMSCs within the hydrogel. This is also supported by the confocal images (Figure 5-3b) which shows that cells are more located at the periphery of the hydrogel and tends to attach rather to the polyurethane substrate. Another hypothesis would be that the Young modulus difference between the hydrogel (8-9 kPa) and the PU (8 MPa) could promote cells migration toward the stiffer substrate by durotaxis[41].

We also used the hydrogel to see if we could induce chondrogenesis without external sources (i.e. growth factors). We evaluated the amount of s-GAGs and type II collagen as markers for chondrogenesis[42,43]. The Young modulus of the substrate was already shown to act as a physical cue that can direct the differentiation pathway of stem cells[34]. We used a hydrogel having a Young Modulus $E \sim 8 - 9.2$ kPa, it is close to the value obtained by Alakpa *et al.*[29] who demonstrated that for gels having a Modulus $E \sim 13$ kPa, the chondrogenic marker *SOX*9 was upregulated for pericytes cultured in only basal media. We could clearly observe that sGAGs were upregulated for WJMSCs in the GEL alone (Figure 5-4) compared to SCAFFOLD and SCAFFOLD+GEL samples. Due to the soft nature of the gel (which softens with time), cells may increase the synthesis of ECM molecules to compensate the loss of stiffness in their local environment. Ferreira *et al.*[35] demonstrated that cells secreted extracellular components when cultured in poorly adhesive substrate. Indeed, cells create a pericellular matrix which forms a local "capsule" to which cells attach. Therefore, the current hydrogel may prevent the formation of stable adhesion which promotes an upregulation of extracellular components. Furthermore, Loebel *et al.*[44] visualized the nascent proteins secreted by MSCs in hydrogels at early times after seeding. They demonstrate that cells interact rather with these nascent proteins which somehow screen the effect of the hydrogel. Moreover, they showed that the thickness of this pericellular matrix increases when the gel softens, this could explain the upregulation of sGAGs for WJMSCs seeded in the Gel. However, cells are located in different environments in each sample; the gel alone, the PU substrate alone and a combination of both. Therefore, the nature of the ECM components secreted may differ as well as the way how cells can attach and remodel this pericellular matrix. The differentiation of WJMSCs toward cartilage cells seems to be not efficient or restricted to the early stages in this simplified approach especially because no biochemical factors were added. Some studies showed that MSCs differentiation is more pronounced with induction media[45,46] whereas others demonstrate that the substrate alone could induce the differentiation[47,48]. Such discrepancies arise from the fact that the underlying mechanism by which cells interact with a material, or with the proteins adsorbed on a material surface is difficult to elucidate, furthermore, the evolution of MSCs toward chondrogenesis is not a single step but cells undergo instead several stages of differentiation running from prechondrocytes to chondrocytes[49] and the position achieve on this fresco is not often investigated.

5.5 Conclusion and Outlooks

We demonstrated the synergetic effect of combining a polyurethane scaffold with a SAP hydrogel to support cellular adhesion and function *in-vitro.* A truly beneficial effect of the hydrogel in the scaffold was shown regarding the proliferation of WJMSCs. However, the hydrogel started to degrade after 7 days of culture which decreased the viability of the embedded cells or promotes their migration toward the walls of the scaffold. We quantified type II collagen and sulphated glycosaminoglycans to evaluate the ability of WJMSCs to differentiate into chondrocytes. SGAGs were significantly higher for cells embedded in the GEL alone compared to the SCAFFOLD and the SCAFFOLD+GEL samples. Conversely , type II collagen was not found to be different between the samples. We hypothesise that the nature of the protein secreted is triggered by the external environment and by the way how cells can remodel and anchor to this pericellular matrix. Protein conformation is also affected by the underlying substrate and the subsequent feedback received by the cells when exerting pulling/stretching may trigger different signalling pathways which could direct their fate.

Future works could be done on the evaluation of the gene expression to shed light on which particular proteins are expressed in each condition. Further works on the optimisation of the gel degradation rate or formulation could allow to reach more beneficial effects regarding the long-term culture.

5.6 References

1. Lutzweiler, G. *et al.* Modulation of Cellular Colonization of Porous Polyurethane scaffolds via the control of pore interconnection size and nanoscale surface modifications. *ACS Appl. Mater. Interfaces* (2019).

2. Murphy, C. M., Haugh, M. G. & O'Brien, F. J. The effect of mean pore size on cell attachment, proliferation and migration in collagen–glycosaminoglycan scaffolds for bone tissue engineering. *Biomaterials* **31**, 461–466 (2010).

3. Sadtler, K. *et al.* Developing a pro-regenerative biomaterial scaffold microenvironment requires T helper 2 cells. *Science (80-.).* **352**, 366–370 (2016).

4. Anderson, J. M. Biological responses to materials. *Annu. Rev. Mater. Res.* **31**, 81–110 (2001).

5. Eyrich, D. *et al. In Vitro* and *In Vivo* Cartilage Engineering Using a Combination of Chondrocyte-Seeded Long-Term Stable Fibrin Gels and Polycaprolactone-Based Polyurethane Scaffolds. *Tissue Eng.* **13**, 2207–2218 (2007).

6. Grad, S., Kupcsik, L., Gorna, K., Gogolewski, S. & Alini, M. The use of biodegradable polyurethane scaffolds for cartilage tissue engineering: Potential and limitations. *Biomaterials* **24**, 5163–5171 (2003).

7. Imaninezhad, M., Hill, L., Kolar, G., Vogt, K. & Zustiak, S. P. Templated Macroporous Polyethylene Glycol Hydrogels for Spheroid and Aggregate Cell Culture. *Bioconjug. Chem.* **30**, 34–46 (2018).

8. Atzet, S., Curtin, S., Trinh, P., Bryant, S. & Ratner, B. Degradable poly (2-hydroxyethyl methacrylate)-co-polycaprolactone hydrogels for tissue engineering scaffolds. *Biomacromolecules* **9**, 3370–3377 (2008).

9. Tibbitt, M. W. & Anseth, K. S. Hydrogels as extracellular matrix mimics for 3D cell culture. *Biotechnol. Bioeng.* **103**, 655–663 (2009).

10. Ahmed, S. & Ikram, S. Chitosan based scaffolds and their applications in wound healing. *Achiev. life Sci.* **10**, 27–37 (2016).

11. Andersen, T., Auk-Emblem, P. & Dornish, M. 3D cell culture in alginate hydrogels. *Microarrays* **4**, 133–161 (2015).

12. Glowacki, J. & Mizuno, S. Collagen scaffolds for tissue engineering. *Biopolym. Orig. Res. Biomol.* **89**, 338–344 (2008).

13. Searle, S. *et al.* Hyaluronic acid based hydrogel droplets: A potential injectable cell culture scaffold. in *EUROoC, Stuttgart, Germany. 24 and 35 May, 2018.* (2018).

14. Kaiser, A., Kale, A., Novozhilova, E. & Olivius, P. The effects of Matrigel®on the survival and differentiation of a human neural progenitor dissociated sphere culture. *Anat. Rec.* (2019).

15. Yan, C. & Pochan, D. J. Rheological properties of peptide-based hydrogels for biomedical and other applications. *Chem. Soc. Rev.* **39**, 3528–3540 (2010).

16. Zhu, M. *et al.* Gelatin methacryloyl and its hydrogels with an exceptional degree of controllability and batch-to-batch consistency. *Sci. Rep.* **9**, (2019).

17. Ekerdt, B. L. *et al.* Thermoreversible Hyaluronic Acid-PNIPAAm Hydrogel Systems for 3D Stem Cell Culture. *Adv. Healthc. Mater.* **7**, 1800225 (2018).

18. Martin, A. D., Robinson, A. B. & Thordarson, P. Biocompatible small peptide super-hydrogelators bearing carbazole functionalities. *J. Mater. Chem. B* **3**, 2277–2280 (2015).

19. Criado-Gonzalez, M. *et al.* Enzyme-assisted self-assembly within a hydrogel induced by peptide diffusion. *Chem. Commun.* **55**, 1156–1159 (2019).

20. Frederix, P. W. J. M. *et al.* Exploring the sequence space for (tri-) peptide self-assembly to design and discover new hydrogels. *Nat. Chem.* **7**, 30 (2015).

21. Adams, D. J., Mullen, L. M., Berta, M., Chen, L. & Frith, W. J. Relationship between molecular structure, gelation behaviour and gel properties of Fmoc-dipeptides. *Soft Matter* **6**, 1971–1980 (2010).

22. Cox, H., Cao, M., Xu, H., Waigh, T. A. & Lu, J. R. Active Modulation of States of Prestress in Self-Assembled Short Peptide Gels. *Biomacromolecules* **20**, 1719–1730 (2019).

23. Jacob, R. S. *et al.* Self healing hydrogels composed of amyloid nano fibrils for cell culture and stem cell differentiation. *Biomaterials* **54**, 97–105 (2015).

24. Sieminski, A. L., Semino, C. E., Gong, H. & Kamm, R. D. Primary sequence of ionic self-assembling peptide gels affects endothelial cell adhesion and capillary morphogenesis. *J. Biomed. Mater. Res. Part A An Off. J. Soc. Biomater. Japanese Soc. Biomater. Aust. Soc. Biomater. Korean Soc. Biomater.* **87**, 494–504 (2008).

25. Kopesky, P. W., Vanderploeg, E. J., Sandy, J. S., Kurz, B. & Grodzinsky, A. J. Self-assembling peptide hydrogels modulate in vitro chondrogenesis of bovine bone marrow stromal cells. *Tissue Eng. Part A* **16**, 465–477 (2009).

26. Zhou, M. *et al.* Self-assembled peptide-based hydrogels as scaffolds for anchorage-dependent cells. *Biomaterials* **30**, 2523–2530 (2009).

27. Galler, K. M., Aulisa, L., Regan, K. R., D'Souza, R. N. & Hartgerink, J. D. Self-assembling multidomain peptide hydrogels: designed susceptibility to enzymatic cleavage allows enhanced cell migration and spreading. *J. Am. Chem. Soc.* **132**, 3217–3223 (2010).

28. Harper, M. M. *et al.* Biogelx: Cell Culture on Self-Assembling Peptide Gels BT - Peptide Self-Assembly: Methods and Protocols. in (eds. Nilsson, B. L. & Doran, T. M.) 283–303 (Springer New York, 2018).

29. Alakpa, E. V *et al.* Tunable supramolecular hydrogels for selection of lineage-guiding metabolites in stem cell cultures. *Chem* **1**, 298–319 (2016).

30. Alini, M. *et al.* The potential and limitations of a cell-seeded collagen/hyaluronan scaffold to engineer an intervertebral disc-like matrix. *Spine (Phila. Pa. 1976).* **28**, 446–453 (2003).

31. Jin, R. & Dijkstra, P. J. Hydrogels for tissue engineering applications. in *Biomedical applications of hydrogels handbook* 203–225 (Springer, 2010).

32. Aubert, L. *et al.* Collagen-based medical device as a stem cell carrier for regenerative medicine. *Int. J. Mol. Sci.* **18**, (2017).

33. Surmaitis, R. L., Arias, C. J. & Schlenoff, J. B. Stressful Surfaces: Cell Metabolism on a Poorly Adhesive Substrate. *Langmuir* **34**, 3119–3125 (2018).

34. Engler, A. J., Sen, S., Sweeney, H. L. & Discher, D. E. Matrix Elasticity Directs Stem Cell Lineage Specification. *Cell* **126**, 677–689 (2006).

35. Ferreira, S. A. *et al.* Bi-directional cell-pericellular matrix interactions direct stem cell fate. *Nat. Commun.* **9**, 4049 (2018).

36. Im, H., Kim, S. H., Kim, S. H. & Jung, Y. Skin regeneration with a Scaffold of predefined shape and bioactive peptide hydrogels. *Tissue Eng. Part A* **24**, 1518–1530 (2018).

37. Bokhari, M. A., Akay, G., Zhang, S. & Birch, M. A. The enhancement of osteoblast growth and differentiation in vitro on a peptide hydrogel—polyHIPE polymer hybrid material. *Biomaterials* **26**, 5198–5208 (2005).

38. Rustad, K. C. *et al.* Enhancement of mesenchymal stem cell angiogenic capacity and stemness by a biomimetic hydrogel scaffold. *Biomaterials* **33**, 80–90 (2012).

39. Jiang, J. *et al.* Bioactive Stratified Polymer Ceramic-Hydrogel Scaffold for Integrative Osteochondral Repair. *Ann. Biomed. Eng.* **38**, 2183–2196 (2010).

40. Kisiday, J. *et al.* Self-assembling peptide hydrogel fosters chondrocyte extracellular matrix production and cell division: Implications for cartilage tissue repair. *Proc. Natl. Acad. Sci.* **99**, 9996 LP – 10001 (2002).

41. Isenberg, B. C., DiMilla, P. A., Walker, M., Kim, S. & Wong, J. Y. Vascular Smooth Muscle Cell Durotaxis Depends on Substrate Stiffness Gradient Strength. *Biophys. J.* **97**, 1313–1322 (2009).

42. Mwale, F., Stachura, D., Roughley, P. & Antoniou, J. Limitations of using aggrecan and type X collagen as markers of chondrogenesis in mesenchymal stem cell differentiation. *J. Orthop. Res.* **24**, 1791–1798 (2006).

43. Grogan, S. P. *et al.* Identification of markers to characterize and sort human articular chondrocytes with enhanced in vitro chondrogenic capacity. *Arthritis Rheum. Off. J. Am. Coll. Rheumatol.* **56**, 586–595 (2007).

44. Loebel, C., Mauck, R. L. & Burdick, J. A. Local nascent protein deposition and remodelling guide mesenchymal stromal cell mechanosensing and fate in three-dimensional hydrogels. *Nat. Mater.* (2019).

45. Shah, R. N. *et al.* Supramolecular design of self-assembling nanofibers for cartilage regeneration. *Proc. Natl. Acad. Sci.* **107**, 3293–3298 (2010).

46. Ranga, A. *et al.* 3D niche microarrays for systems-level analyses of cell fate. *Nat. Commun.* **5**, 4324 (2014).

47. Ustun, S., Tombuloglu, A., Kilinc, M., Guler, M. O. & Tekinay, A. B. Growth and differentiation of prechondrogenic cells on bioactive self-assembled peptide nanofibers. *Biomacromolecules* **14**, 17–26 (2012).

48. Kim, J. E. *et al.* Effect of self-assembled peptide--mesenchymal stem cell complex on the progression of osteoarthritis in a rat model. *Int. J. Nanomedicine* **9**, 141 (2014).

49. Goldring, M. B., Tsuchimochi, K. & Ijiri, K. The control of chondrogenesis. *J. Cell. Biochem.* **97**, 33–44 (2006).

Conclusion générale

La pose de prothèses et d'implants devient un acte majeur dans le domaine médical. Les accidents ainsi que les maladies dues au vieillissement de la population sont les causes majeures du remplacement de certaines parties du corps. Les implants classiquement utilisés peuvent néanmoins induire des complications telles que des inflammations chroniques, une perte de densité osseuse dans le cas d'implant poreux, etc.

L'ingénierie tissulaire offre une perspective prometteuse en vue de générer de nouveaux implants mieux acceptés par le corps et ayant donc une meilleure efficacité. Le principe général est d'utiliser des matériaux poreux qui permettent aux tissus environnants de croitre au sein de l'implant. Ceci permet d'avoir une régénération partielle de la zone ciblée voire une régénération totale si le matériau constituant le poreux est également biodégradable. Dans ce cas, le tissu remplace progressivement l'implant.

Cependant, nous sommes encore loin d'une maîtrise parfaite de l'interaction matériau/tissu biologique. De nombreux paramètres sont à prendre en compte pour moduler au mieux la réponse cellulaire dans le matériau poreux. Parmi eux, la taille des pores et des interconnexions. Alors que la taille des pores ainsi que la porosité (qui en dépend) sont largement étudiées dans la littérature, nous avons choisi d'étudier l'influence de la taille des interconnexions sur des fibroblastes ainsi que sur des cellules souches mésenchymateuses.

Dans un premier temps, nous avons conçu un matériau poreux dans lequel la taille des pores et des interconnexions peut être contrôlée indépendamment. La méthode de « sphere templating » s'est révélée être une bonne candidate (Chapitre 3). Bien que largement utilisée dans la littérature et ce même dans des domaines différents de l'ingénierie tissulaire, cette approche reste néanmoins peu prédictive. Nous avons généré des matériaux poreux avec différentes tailles de pores et d'interconnexions en variant les conditions de préparation, notamment, le frittage qui permet aux microsphères de paraffine de partiellement fusionner formant un négatif de la structure poreuse finale. Alors que la théorie du frittage est généralement bien décrite par le modèle de Frenkel, nous avons démontré qu'un autre modèle proposé par Scott Milner permet de mieux décrire nos résultats. Le modèle de Milner propose une évolution du frittage en deux temps par un mécanisme d'écoulement visco-élastique. Nous avons pu démontrer que le modèle de Milner pouvait être amélioré en prenant en compte le caractère viscoélastique de la paraffine.

Cette approche nous a permis de développer des matériaux poreux sur une large gamme de tailles de pores et d'interconnexions de manière reproductible et prédictible. La technique de « sphere templating » est également simple à mettre en œuvre et peu onéreuse.

Les matériaux ainsi obtenus ont ensuite été testés comme support tridimensionnels pour deux types de cellules : les fibroblastes (NIH 3T3) et les cellules souches mésenchymateuses issues de la gelée de Wharton (WJMSCs).

Nous avons évalué l'influence des interconnexions sur la capacité des cellules à survivre, à coloniser et à synthétiser leur matrice extracellulaire dans les matériaux poreux (voir Section 4.1).

Les matériaux ont été au préalable traités par deux méthodes : le traitement au plasma et le revêtement par la polydopamine afin de les rendre hydrophiles.

Nous avons montré que les cellules répondent différemment aux traitements de surface selon leur type. Les fibroblastes montrent une meilleure viabilité dans les matériaux revêtus de polydopamine alors que les cellules souches colonisent d'avantage les matériaux traités au plasma. Le rôle des interconnexions est en revanche commun aux deux types cellulaires. Les grandes interconnexions favorisent les contacts intercellulaires amenant à une meilleure colonisation et survie des cellules à long terme alors que les petites interconnexions induisent la mort progressive des cellules spécialement au centre du matériau.

Afin de s'affranchir d'un traitement de surface induisant une étape supplémentaire dans le processus de fabrication des poreux, nous avons modifié également la formulation du polyuréthane en variant le ratio isocyanate/polyol ou indice d'isocyanate (NCO index). La variation de ce ratio induit des changements dans la microstructure du polymère comme montré dans la Section 4.2. Le polyuréthane présente une microstructure biphasique, avec des segments rigides (isocyanates) regroupés en micro-domaines. L'augmentation de l'indice d'isocyanate permet d'atteindre une meilleure séparation de phase (i.e. l'interface entre les segments rigides et mous) et plus franche alors qu'elle est diffuse lorsque l'indice est plus faible. Cette 'qualité' de la séparation de phase modifie drastiquement les propriétés d'adhésion des cellules. Nous avons montré qu'il existe un indice d'isocyanate à partir duquel les cellules peuvent adhérer au matériau. En dessous de cet indice, le matériau est non-adhérent pour nos cellules. Nous avons corrélé ce comportement au fait que les matériaux ayants un indice d'isocyanate permettant l'adhésion cellulaire sont aussi ceux qui possèdent des interfaces franches. Cela implique que les micro domaines « rigides » forment des nano-ilots servant probablement de points d'ancrage aux cellules. Cette méthode est simple à mettre en œuvre et permet d'avoir un contrôle à l'échelle nanoscopique.

Il faut noter que le mélange du polyol et de l'isocyanate est une étape importante car l'isocyanate est insoluble dans le polyol, ainsi un mélange manuel laisse des gouttes d'isocyanate et le mélange n'est pas homogène ce qui impacte probablement la microstructure du PU. On peut voir que cela impacte l'adhésion des cellules (Figure S 1 et Figure S 2 du Chapitre 4) où malgré un indice d'isocyanate de 400, les cellules n'adhèrent pas au substrat contrairement au cas où les précurseurs sont mélangés à l'Ultra Turrax (Section 4.2).

Nous pouvons conclure que la capacité des cellules à coloniser un poreux dépend de la morphologie, de la chimie mais aussi de la méthode d'ensemencement. Nous avons présenté Section 2.7.1 les différentes approches pour ensemencer les cellules dans le poreux. Les traitements de surface rendent le matériau temporairement ou définitivement hydrophile permettant une meilleure pénétration de la suspension cellulaire. Le poreux seul est très hydrophobe comme montré dans la Section 4.1.3.1, mais la formulation avec un indice d'isocyanate de 400 permet une adhésion complète des cellules (Section 4.2). Ainsi il est nécessaire d'adapter les méthodes d'ensemencement en conséquence, une pré-inbubation du poreux dans du sérum permet une pré-adsorption des protéines ou bien la méthode des deux seringues présentée Section 2.7.1 permet de forcer le milieu de culture dans les poreux et de chasser l'air.

Enfin, nous avons injecté dans le matériau poreux un gel de peptides auto-assemblés dans lequel les WJMSCs étaient encapsulées (Chapitre 5). Le gel avait pour objectif de mimer la matrice extracellulaire présente dans les tissus. Nous avons pu montrer que la prolifération des cellules dans le gel+ le poreux était améliorée. Nous avons aussi regardé si les cellules pouvaient se différencier dans le gel en l'absence de facteurs de croissance, notamment par mécanotransduction. Cependant, le gel se dégradant rapidement, nous n'avons pas pu différencier les WJMSCs.

En perspective il serait intéressant d'optimiser la culture dynamique sous perfusion pour voir si la prolifération et la colonisation dans les matériaux peuvent être augmentées sur le long terme. Les premiers résultats présentés dans la partie expérimentale (voir Section 2.7.2) étant préliminaires, un développement plus approfondi serait intéressant. De plus, une optimisation du gel de peptides serait aussi un axe de développement nécessaire principalement pour augmenter la stabilité du gel et donc la survie cellulaire à long terme. Une génération en une seule étape du matériau combiné au gel via une émulsion et notamment par une approche de polyHIPE (High Internal Phase Emulsion), une émulsion dont la phase dispersée (le gel ou le pré-gel) représente au moins 74 % du volume total ce qui garantit que les gouttes sont en contact et donc que le matériau est interconnecté. Cette approche nécessite toutefois de trouver un agent qui puisse stabiliser efficacement l'émulsion.

Des études plus approfondies en biologie moléculaire permettraient de mieux comprendre l'influence du matériau et de sa structure sur la réponse cellulaire. Notamment l'étude des gènes exprimés lorsque les cellules sont ensemencées dans les poreux, avec les différents traitements de surface ainsi les différents indices d'isocyanate. Cela permettrait de voir si les cellules s'engagent vers une différentiation ou une dédifférenciation ou encore si les WJMSCs peuvent demeurer à l'état de cellules souches. Des analyses histologiques permettraient également de visualiser la quantité et l'organisation de la matrice extracellulaire.

Enfin, des tests in-vivo permettraient d'évaluer si les paramètres architecturaux (tailles des pores et des interconnexions) des poreux trouvés dans ce mémoire comme optimum resteraient valables dans un environnement biologique.

UNIVERSITÉ DE STRASBOURG

Gaëtan

LUTZWEILER

ECOLE DOCTORALE pcp

Résumé

Les matériaux poreux représentent une solution idéale en ingénierie tissulaire car leur structure peut offrir un environnement tridimensionnel aux cellules similaire à leur matrice extracellulaire tout en maintenant de bonnes propriétés mécaniques. Une première partie de cette thèse consiste à développer des matériaux poreux en polyuréthane (PU), dont l'architecture est contrôlée pour favoriser au mieux la survie et la croissance des cellules. Ces matériaux sont combinés à des traitements de surface (revêtement de polydopamine (PDA) et traitement plasma) pour augmenter notamment l'adhésion des cellules. Nous avons pu démontrer que le diamètre des interconnexions (i.e. l'ouverture connectant deux pores adjacents) impacte profondément la survie et l'organisation des cellules à long terme dans le matériau. Le revêtement de PDA s'est révélé efficace pour des cellules de type fibroblaste, alors que le traitement plasma favorise la colonisation des cellules souches mésenchymateuses (MSCs). Par ailleurs, nous avons étudié l'influence de la formulation du PU sur les capacités d'adhésion des cellules au matériau. Nous avons démontré que pour un ratio donné entre les réactifs, l'adhésion des cellules peut être exclue ou permise. Finalement, nous avons mis un gel de peptides auto-assemblés dans les pores du matériau pour fournir aux cellules un environnement similaire à leur matrice extracellulaire. Nous avons pu montrer que le gel permet d'augmenter la prolifération des MSCs.

Mots clés : matériaux poreux, diamètre d'interconnexion, revêtement de surface, polyuréthane, cellules souches mésenchymateuses, polydopamine

Résumé en anglais

Porous materials are an ideal solution in tissue engineering since they can provide a three-dimensional environment to the cells that is close to their extracellular matrix while keeping suitable mechanical properties. In the first part of this Thesis we develop porous materials made from polyurethane (PU) whose architecture is controlled to allow cells colonisation and growth. These materials are subsequently surface-treated (polydopamine coating and plasma treatment) to enhance the adhesion of the cells. We were able to show that the interconnection diameter (i.e. the aperture connecting two adjacent pores) has an important impact on the long-term cell survival and organization in the material. Polydopamine (PDA) coating was shown to be efficient for fibroblasts, whereas plasma treatment promoted mesenchymal stem cells (MSCs) colonisation. Besides, we also studied the influence of the PU formulation on the adhesion capacity of the cells. We demonstrated that at a given ratio between the reactants, cell adhesion could be allowed or prevented. Finally, we put a hydrogel of self-assembled peptides inside the pores of the material to provide an environment close to the extracellular matrix for the cells. We could show that the gel increases the proliferation ability of MSCs. In summary, this Thesis puts forward the important interplay between material properties and morphology of porous scaffolds.

Keywords: porous materials, interconnection diameter, surface functionalisation, polyurethane, mesenchymal stem cells, polydopamine